

A Holistic Modelling Approach to Simulate Catchments-Estuary-Coastal System Behaviour at Macro Time Scales

Rajapaksha Mudiyanseelage Janaka Bamunawala

**A HOLISTIC MODELLING APPROACH TO SIMULATE
CATCHMENT-ESTUARY-COASTAL SYSTEM
BEHAVIOUR AT MACRO TIME SCALES**

Rajapaksha Mudiyansele Janaka Bamunawala

A HOLISTIC MODELLING APPROACH TO SIMULATE
CATCHMENT-ESTUARY-COASTAL SYSTEM BEHAVIOUR
AT MACRO TIME SCALES

DISSERTATION

to obtain
the degree of doctor at the University of Twente,
on the authority of the rector magnificus,
Prof.dr. T. T. M. Palstra,
on account of the decision of the graduation committee,
to be publicly defended
on Thursday the 16th of April 2020 at 12:45 hour

by

Rajapaksha Mudiyansele Janaka Bamunawala

born on the 06th of September 1984
in Kurunegala, Sri Lanka.

This dissertation has been approved by:

Supervisor: Prof.dr. R. W. M. R. J. B. Ranasinghe

Co-supervisors: Dr. A. J. F. van der Spek

Dr.ir. A. Dastgheib

This research was conducted under the auspices of the Graduate School for Socio-Economic and Natural Sciences of the Environment (SENSE).

Copyright © 2020 by Rajapaksha Mudiyanseelage Janaka Bamunawala.

All rights reserved. No parts of this thesis may be reproduced, stored in a retrieval system or transmitted, in any form or by any means, without the prior permission in writing from the author.

Cover photo credit: NASA Global Climate Change

ISBN: 978-90-365-4988-2

URL: <https://doi.org/10.3990/1.9789036549882>

Printed by: Veenman +, The Netherlands

Graduation Committee

| | |
|---------------------------------------|---|
| Prof.dr. G. P. M. R. Dewulf | University of Twente - Chairman/secretary |
| Prof.dr. R. W. M. R. J. B. Ranasinghe | University of Twente / IHE Delft - Promotor |
| Dr. A. J. F. van der Spek | Deltares - Co-promotor |
| Dr.ir. A. Dastgheib | IHE Delft - Co-promotor |
| | |
| Prof.dr. R. J. Nicholls | University of East Anglia, United Kingdom |
| Prof.dr. K. M. Wijnberg | University of Twente |
| Prof.dr. J. C. J. Kwadijk | University of Twente / Deltares |
| Prof.dr.ir. A. E. Mynett | TU Delft / IHE Delft |

Summary

The coastal zone is the dynamic link that connects land and oceans and is often of great importance to the society, given that about 10% of the world's population inhabit these areas. In addition to providing habitat, the coastal zone is heavily utilized for a wide range of activities that are of great importance to society. Due to the predicted population growth, economic development and urbanization, human pressures on coasts and coastal ecosystems will increase significantly over the 21st century. Furthermore, projected climate change driven variations in mean sea level, wave conditions, intensity and frequency of storm surges, temperature and river flow will also affect the coast in many ways.

Among different classifications of world's coastline, open sandy coasts are considered to be one of the most complex coastal systems with respect to its geomorphological behaviour, because they are continually varying due to the influences of both natural and anthropogenic drivers. The majority of these sandy coasts is interrupted by inlets. The long term (50-100 year) evolution of these inlet-interrupted coasts is driven by both oceanic and terrestrial processes. Coastal retreat due to Bruun effect and basin infilling demand are the most significant forms of sea-level rise driven coastline recessions. Besides these recessions, future changes in temperature, precipitation and anthropogenic activities at catchment scale would alter the fluvial sediment supply received by the coasts, which in turn affect the long-term evolution of inlet-interrupted coasts. Such changes will significantly increase the socio-economic risks associated along the inlet-interrupted coasts. Thus, understanding the long-term evolution of inlet-interrupted coasts is essential for coastal zone planners and managers. There are significant uncertainties in future climate change and anthropogenic activities driven impacts that would affect the evolution of sandy shorelines. As a result (in addition to the uncertainties associated with the modelling technique(s) adopted), projections of inlet-interrupted coastline changes will inherit the variabilities related to the climate change impacts and anthropogenic activities (i.e., input uncertainties) considered. Therefore, it is desirable to quantify the uncertainties associated with the shoreline change projections to manage the climate change impacts and anthropogenic activities driven socio-economic losses along the inlet-interrupted coasts.

In this regards, a Reduced Complexity (RC) modelling technique was developed to probabilistically simulate the climate-change driven evolution of inlet-interrupted coasts at macro (50-100 year) time scales, while taking into account the contributions from catchment-estuary-coastal systems in a holistic manner. In this new RC model, the evolution of inlet-interrupted coasts is determined by (1) computing the variation of total sediment volume exchange between the inlet-estuary system and its adjacent coast (ΔV_T), and (2) distributing the computed ΔV_T along the inlet-interrupted coast as a spatially and

temporally varying quantity. The exchange volume ΔV_T , as computed here, consists of three major components: variation in fluvial sediment supply (ΔV_{FS}), basin infilling due to the sea-level rise-induced increase in accommodation space (ΔV_{BI}), and estuarine sediment volume change due to variations in river discharge (ΔV_{BV}).

This modelling technique was first applied at four barrier estuary systems (Alsea estuary, OR, USA, Dyfi estuary, Wales, UK, Kalutara inlet, Sri Lanka, and Swan river system, Australia) and barrier island coast at Chandeleur Islands, LA, USA. The findings of these model applications indicate that the selected mainland inlet-interrupted coasts are likely to strive for sediment by the end of this century. However, the governing processes and the relative contributions of different sediment volume component (i.e., ΔV_{FS} , ΔV_{BI} , and ΔV_{BV}) were found to vary markedly due to their differences in geomorphic settings and projected climate conditions. The projected coastline change adjacent to Alsea estuary is affected by both ΔV_{FS} and ΔV_{BI} , in which, the latter process governs the overall behaviour of the system. The projected coastline change along Dyfi estuary and Kalutara inlet are governed by ΔV_{BI} and ΔV_{BI} , respectively, whereas the evolution of inlet-interrupted coast at the Swan river is dominated by ΔV_{BV} . The evolution of the barrier island coast along the Chandeleur Islands in Louisiana, USA is predominantly governed by the sediment volume demand due to basin infilling (ΔV_{BI}). The projected changes of Chandeleur Islands over the 21st century indicate that the barrier islands could survive without drowning under the future sea-level rise scenarios. However, some reductions of its freeboard are projected after the mid-century period.

Application of the developed RC modelling technique at 41 barrier estuary systems across six continents shows that coasts adjacent to 93% of the systems studied may erode under changing climate conditions. Depending on the projected climatic conditions (i.e., arid or non-arid conditions) and the characteristics of the attached river catchment, both basin infilling and fluvial sediment supply could affect the evolution of the inlet-interrupted coasts. Further scrutiny of the global application results indicates that the overall behaviour of the barrier estuary systems can be approximated with the ratio between the estuary surface area and the river catchment area. This first-order approximation indicates that the long-term evolution of inlet-interrupted coasts attached to non-arid river catchments are affected by both ΔV_{BI} (due to sea-level rise) and ΔV_{FS} (due to variation in temperature and river discharge), if the ratio between the estuary surface area and river catchment is less than 0.01. The coastline changes under different percentiles of ΔV_T indicate the uncertainties associated with the future climatic forcing projections, and hence the necessity of a probabilistic modelling approach to evaluate long-term evolution of inlet-interrupted coasts.

Acknowledgement

Completion of a PhD is quite a challenge that would not be possible to accomplish without the help and support of others. I want to express my sincere gratitude to those who helped me since 2015 to achieve that challenge.

Firstly, I would like to express my sincere gratitude to my promotor Professor Roshanka Ranasinghe. Rosh, thank you very much for giving me the opportunity to investigate this new exciting research idea as a PhD at the University of Twente and IHE Delft. It was a great pleasure for me to work under your supervision and my heartfelt appreciation for your patience, support, and motivation given throughout my PhD research. Your guidance, critical comments, innovative insights, and profound knowledge and understanding are the cornerstone of this successful PhD dissertation. Thank you very much for always motivating me to improve my work and to focus on achieving the level of quality that is needed.

Besides my promotor, I would like to thank my co-promotors Dr Ad van der Spek and Dr Ali Dastgheib. Ad, thank you very much for funding my research through Deltares. Your guidance, critical comments and in-depth knowledge gave me the much-needed support to my research, especially when finalizing this dissertation. Ali, thank you very much for all the scientific inputs, brainstorming (and non-scientific) conversations, constructive comments and suggestions. I greatly value your enthusiastic support and encouragements, which helped me to finalize my research and scientific publications.

I am sincerely thankful to Associate Professor Shreedhar Maskey for his guidance, support and scientific contribution given to this research. Your in-depth knowledge and expertise provided me with the support needed to successfully complete this research.

Special thanks to all the members of the evaluating committee. It is an honour for me to have all of you assessing my dissertation.

A special thanks go to Professor Dano Roelvink, for your kindness and support throughout my PhD at the CESPd chair group in IHE Delft. Your critical comments and suggestions were invaluable in finalizing this research and dissertation. Mick, Johan, and Ap, thank you very much for the insightful conversations and enjoyable time in the CESPd research group.

Assela, thank you very much for your great company, insightful conversations on broader scientific perceptions, politics, and culture!! Both you and your wife were most generous to facilitate (frequent) gatherings at your place to discuss all those over drinks and dinner, which made my life in Delft much enjoyable. Thanks very much!

Jeewanthi, many thanks to you for the help and support given to me during my PhD. Your kindness and ever-reliable supportiveness made my life in Delft much more comfortable. Thank you very much!!

Life at Delft would not be so enjoyable without the company of the colleagues at IHE. Mohaned, Ha, Abdi, Uwe, Adele, Hesham, Sebrian, Duoc, Vo, Hieu, Liqin, Jakia, Nguyen, Mohan, Maria, Clara, Iosif, Polpat, Aftab, and Swagatham, thank you all for the nice memories that we shared in Delft. Shahnoor, you were there with me ever since I started my PhD. Thank you very much for your great company, help and support given throughout my stay in Delft. Together, we managed to stay afloat during all the hard times that passed by. I hope the friendship will continue for many more years to come. Trang, a special thanks to you for your kindness and help given during my PhD. All your scientific inputs, encouragement and friendly non-scientific conversations are greatly valued.

I would express my deepest gratitude to my parents and my loving wife, who have been giving me never-ending encouragement, support and unconditional love. Thank you very much for tolerating my stubbornness and for facilitating me to be away from Sri Lanka over the last 5 years to pursue my own ambitions. Thank you very much for all your support and love.

Table of content

| | |
|--|------------|
| Summary | VII |
| Acknowledgement | IX |
| Table of content | XI |
| 1 Introduction | 1 |
| 1.1 Background and motivation | 1 |
| 1.2 Sediment pathway from source to the coast | 4 |
| 1.3 Types of inlet-interrupted coasts | 7 |
| 1.4 Main drivers that affect the long-term evolution of inlet-interrupted coasts | 11 |
| 1.4.1 Projected changes in temperature and runoff | 12 |
| 1.4.2 Projected changes in global sea level | 13 |
| 1.4.3 Projected changes in regional relative sea-level change | 16 |
| 1.4.4 Anthropogenic activities | 17 |
| 1.5 Modelling of the long-term evolution of inlet-interrupted coasts | 17 |
| 1.6 Overarching objectives and research questions | 21 |
| 1.7 Outline of this thesis | 21 |
| 2 Probabilistically simulating climate change-driven coastline change along inlet-interrupted coasts: model development | 23 |
| 2.1 Introduction | 23 |
| 2.2 Determining changes in total sediment volume exchange between a barrier-estuary system and its inlet-interrupted coast | 24 |
| 2.2.1 Basin infilling volume due to sea-level rise-induced increase in accommodation space | 25 |
| 2.2.2 Basin volume change due to variation in river flow | 26 |
| 2.2.3 Change in Fluvial Sediment Supply | 28 |
| 2.2.4 Reference climatic conditions for baseline simulations | 30 |
| 2.3 Probabilistic assessment of change in total sediment volume exchange at barrier-estuary tidal inlets | 30 |

| | | |
|----------|--|-----------|
| 2.4 | Determining the coastline change along inlet-interrupted coastlines ----- | 35 |
| 2.4.1 | Inlet-affected coastline lengths ----- | 35 |
| 2.4.2 | Alongshore variable coastline change estimation ----- | 38 |
| 2.4.3 | Determining the final coastline position----- | 42 |
| 2.5 | Modelling future changes in barrier island coastlines ----- | 43 |
| 2.6 | Probabilistic assessment of future changes in barrier island coastlines----- | 47 |
| 2.7 | Model hindcasts for the 1986-2005 period ----- | 49 |
| 3 | Probabilistically simulating coastline change along inlet-interrupted coasts ---- | 51 |
| 3.1 | Introduction ----- | 51 |
| 3.2 | Case study sites ----- | 52 |
| 3.3 | Alsea estuary system ----- | 56 |
| 3.3.1 | Stochastic model inputs ----- | 56 |
| 3.3.2 | Future variations of change in total sediment volume exchange between the estuary and the inlet-affected coast----- | 60 |
| 3.3.3 | Projected changes in coastline position----- | 63 |
| 3.4 | Dyfi estuary system ----- | 65 |
| 3.4.1 | Stochastic model inputs ----- | 65 |
| 3.4.2 | Future variations of change in total sediment volume exchange between the estuary and the inlet-affected coast----- | 69 |
| 3.4.3 | Projected changes in coastline position----- | 72 |
| 3.5 | Kalutara inlet system ----- | 74 |
| 3.5.1 | Stochastic model inputs ----- | 74 |
| 3.5.2 | Future variations of change in total sediment volume exchange between the estuary and the inlet-affected coast----- | 78 |
| 3.5.3 | Projected changes in coastline position----- | 81 |
| 3.5.4 | Future variations of change in total sediment volume exchange between the estuary and the inlet-affected coast (Excluding river sand mining effect)----- | 83 |
| 3.6 | Swan River System----- | 85 |
| 3.6.1 | Stochastic Model Inputs ----- | 85 |
| 3.6.2 | Future variations of change in total sediment volume exchange between the estuary and the inlet-affected coast----- | 89 |
| 3.6.3 | Projected changes in coastline position----- | 92 |

| | | |
|----------|--|------------|
| 3.7 | Comparison of the modelled results at the barrier-estuary systems ----- | 94 |
| 3.8 | Chandeleur Islands----- | 95 |
| 3.8.1 | Stochastic model inputs and other input parameters----- | 95 |
| 3.8.2 | Projected changes in the barrier island ----- | 97 |
| 3.8.3 | Projected changes of the barrier island under hypothetical initial conditions ----- | 99 |
| 3.9 | Summary and conclusions ----- | 101 |
| 3.10 | A note on the uncertainties associated with the model projections ----- | 103 |
| 4 | Global applications of the model ----- | 105 |
| 4.1 | Introduction----- | 105 |
| 4.2 | Data sources ----- | 105 |
| 4.3 | Projected change in total sediment volume exchange between the estuary and the inlet-affected coast by 2100 ----- | 109 |
| 4.4 | Approximated inlet-affected coastline changes ----- | 116 |
| 4.5 | Summary and conclusions ----- | 122 |
| 5 | General conclusions ----- | 125 |
| 5.1 | Introduction----- | 125 |
| 5.2 | Synthesis and main conclusions of this study ----- | 126 |
| 5.3 | Implications of the study and possible future research initiatives ----- | 130 |
| A | Annexes ----- | 133 |
| A.1 | The GCMs used in the study ----- | 134 |
| A.2 | Properties of the selected barrier estuary systems ----- | 135 |
| A.3 | Projected change in total sediment volume exchange at the selected barrier estuary systems ----- | 138 |
| A.4 | Projected inlet-affected coastline change adjacent to the selected barrier estuary system ----- | 141 |
| B | Bibliography ----- | 145 |
| C | List of figures ----- | 155 |

Chapter 1

Introduction

1.1 Background and motivation

The coastal zone is the dynamic link that connects the land and oceans. In general, there is no single definition to demarcate the coastal zone. However, the term *Low Elevation Coastal Zones (LECZ)* is one of the widely used definition in recent years (Wong et al., 2014), which is referred to a specific area near the coast up to 10 m elevation above mean sea level (Vafeidis et al., 2011). These LECZs are of great importance to society because approximately 10% of the world's population inhabit these areas. LECZs provided habitats to more than 600 million people in the year 2000, which was more than 10% of the world's population by that time (Vafeidis et al., 2011). Globally, more people live in urban areas than in rural areas, with 54% of the world's population residing in urban areas in 2014 (United Nations, 2015). Many of these urban settlements are clustered into megacities of over 10 million inhabitants. Fifteen of the world's 20 megacities are located within low elevation coastal zones (World Bank, 2010). In addition to providing habitat, the coastal zone is heavily utilized for a wide range of activities that are of great importance to society. These uses of the coastal zone include navigation, defence and military, tourism, use of various marine/ecosystem resources and services, waste disposal, development of various coastal infrastructures, research, art, and recreational activities (McGranahan et al., 2007; Neumann et al., 2015; Wong et al., 2014).

Due to the predicted population growth, economic development and urbanization, human pressures on coasts and coastal ecosystems will increase significantly over the 21st century (Wong et al., 2014). Such multiple pressures would inevitably lead to depleting most coastal resources while damaging its ecosystems as well. On the other hand, projected climate-change driven variations in mean sea level, wave conditions, intensity and frequency of storm surges, and river flow will affect the coastal zone in many ways (Brown et al., 2014; FitzGerald et al., 2008, 2014; Ranasinghe, 2016; Ranasinghe and Stive, 2009; Spencer et al., 2016; Syvitski et al., 2009; Syvitski and Kettner, 2008; Wong et al., 2014; Woodruff et al., 2013; Zhang et al., 2004). Rising sea level is likely to inundate many of the low elevated coastal areas by the end of this century (Ranasinghe, 2016). Changes in wave and storm conditions, in conjunction with rising sea level, would result in more frequent and intense coastal inundations. Changes in future river flow will have direct implications on the amount of sediment received by coasts. Such changes in sediment supply would affect the level of inundation of low-lying coastal areas (Besset et al., 2019; Syvitski et al., 2009). The potential socio-economic impacts of such changes in the coastal zone are likely to be enormous if adaptive measures are not implemented (Hallegatte et al., 2013; Hinkel et al., 2013).

Owing to these socio-economic significances, the coastal zone has attracted the interest of various scientific disciplines such as coastal engineering, oceanography, hydrology and geology. Coasts are highly varied and complex systems; thus, the variety of coastal classifications is large and often subjected to the perception of interest. In this regard, a vast majority of the world's coastlines fall in the 'open coast' category, in which the coastlines are exposed to the direct impacts from the oceans. These open coasts contain estuaries, cliffed and sandy coasts and gravel beaches, in which open sandy coasts comprise about one-third of world's coastlines (Le Cozannet et al., 2019; Luijendijk et al., 2018; Ranasinghe, 2016), and are extensively subjected to human utilization (Davenport and Davenport, 2006). Sandy coasts are considered to be one of the most complex coastal systems with respect to its geomorphological behaviour because they are continually varying due to the influences of both natural and anthropogenic drivers (Anthony et al., 2015; Besset et al., 2019; Ranasinghe, 2016; Stive, 2004; Toimil et al., 2017). The majority of these sandy coasts is interrupted by inlets (Aubrey and Weishar, 1988; Davis-Jr. and FitzGerald, 2003; Duong et al., 2016; FitzGerald et al., 2015; McSweeney et al., 2017; Woodroffe, 2003). The dynamic nature of these inlet-interrupted coasts is caused by both oceanic and terrestrial processes. As it was mentioned previously, climate-change driven impacts and anthropogenic activities in the coastal zone (in general) would also exert substantial changes to the complex and dynamic behaviour of the inlet-interrupted coasts as well. These changes along the inlet-interrupted coasts are likely to be associated with significant socio-economic impacts (Hinkel et al., 2013; Spencer et al., 2016). Therefore, it is essential to understand the physical responses of inlet-interrupted coasts under any substantial variations in environmental forcing and anthropogenic activities.

Potential impacts due to climate change on inlet-interrupted coasts vary non-linearly on both spatial and temporal scales. According to Ranasinghe (2016), climate-change impacts on sandy coasts can be classified as short-term (hours to days), medium-term (years to decadal), and long-term (decades to century). In the same study, it was also mentioned that changes in sea level, wave conditions and storm surges, and river flow condition are the main contributors that govern the climate-change driven impacts on sandy coasts. Owing to the slow nature of rising sea level, almost all the impacts on inlet-interrupted coasts that are driven by sea-level rise would fall under the long-term impacts that span over 50-100 year time periods. Under the Bruun effect (Bruun, 1962), the coast would retreat to accommodate the rising sea level. Additionally, previous studies have shown that the inlet-interrupted coasts would undergo an additional extent of coastal recession due to sea-level rise driven basin infilling as well (Ranasinghe et al., 2013; Stive, 2004; Stive et al., 1998, 1990). Besides these recessions, future changes in temperature, precipitation and anthropogenic activities at catchment scale would alter the fluvial sediment supply received by the coasts (Overeem and Syvitski, 2009; Ranasinghe et al., 2019b; Syvitski et al., 2009; Syvitski and Milliman, 2007), which in turn have significant implications on inlet-interrupted coasts (Bamunawala et al., 2018a). Such long-term coastal recessions will significantly increase the socio-economic risks associated along inlet-interrupted coasts. Therefore, understanding the long-term variation of inlet-interrupted coasts is essential for decision-makers and managers.

There are significant uncertainties in future climate change and anthropogenic activities driven impacts that would affect the shoreline changes along sandy coasts (Le Cozannet et al., 2019; Ranasinghe, 2016). As a result, (in addition to the uncertainties associated with the modelling technique(s) adopted, (i.e., forcing uncertainties)), projections of future changes along inlet-interrupted coastlines will inherit the variabilities related to the climate change impacts and anthropogenic activities (i.e., input uncertainties) considered. Therefore, it is desirable to quantify the uncertainties associated with the shoreline change projections to manage the future climate change impacts and anthropogenic activities driven socio-economic losses along the inlet-interrupted coasts. Such risk-based measures will avoid the unnecessary restrictions associated with the conventional deterministic estimates of future coastline changes, thus enabling optimum utilization of the highly valuable land areas along the coasts (Dastgheib et al., 2018; Jongejan et al., 2016). The significance of such a risk-based coastal zone planning and management strategies (e.g., economically optimal setback lines) was clearly illustrated in the Probabilistic Coastal Recession (PCR) model applications at the Narrabeen Beach, Sydney, Australia (Jongejan et al., 2016), along the eastern coast of Sri Lanka (Dastgheib et al., 2018), and at Hozaki, Japan (Dastgheib et al., (forthcoming)). Although the above PCR applications were only focused on the coastal retreat due to sea-level rise and storm erosions, its results emphasise the need for probabilistic estimates of coastline change by the coastal zone planners and managers to implement effective land-use planning strategies. Probabilistic estimates of

coastline changes along inlet-interrupted coasts under climate-change impacts and anthropogenic activities require multiple realizations under stochastic model inputs (i.e., Monte Carlo simulations).

Under ideal circumstances, such modelling applications are to be undertaken with a coupled process-based coastal and catchment model for the entire period considered, so that the episodic (e.g., storms, surges, extreme river flows), medium-term (e.g., changes in river flow/mean wave conditions) and long-term impacts (e.g., sea-level rise, changes in fluvial sediment supply and longshore sediment transport capacity) due to climate change are accounted for in assessing the changes along inlet-interrupted coasts. However, such process-based modelling techniques are presently not available, mainly due to the accumulation of numerical errors within the computational domain during long-term simulations, which in turn lead to morphological instabilities (Duong et al., 2016; Ranasinghe, 2016). Even if such a multi-scale process-based modelling technique is developed, the computational demand and the simulation time per each model realization would likely to make it impractical to be used in a Monte Carlo framework of probabilistic estimates of coastline changes along inlet-interrupted coasts (Ranasinghe, 2016). An alternative approach to overcome these drawbacks in long-term process-based modelling methods is the use of reduced-complexity models to project the changes along the sandy coasts. Such models are proven to be computationally efficient and thus can be easily applied within a probabilistic framework to quantify the uncertainties in future changes along inlet-interrupted coastlines. Moreover, reduced-complexity models have proven to be very useful in obtaining insights of long-term coastal zone evolutions at regional scales (Ranasinghe, 2016; Ranasinghe et al., 2013; van Maanen et al., 2016).

From this point of view, this research study attempts to develop a suitable modelling technique that can provide probabilistic estimates on the long-term evolution of inlet-interrupted coasts under climate-change driven impacts.

1.2 Sediment pathway from source to the coast

Coastlines in the vicinity of tidal inlets (i.e., inlet-interrupted coasts) are shaped and affected not only by oceanic processes (e.g., mean sea-level change, tides and waves, longshore sediment transport), but also by terrestrial processes (e.g., such as river flow, fluvial sediment supply, land use/agricultural patterns, and land management) (Cowell et al., 2003; Green, 2013; Syvitski et al., 2009). The following figure (Figure 1-1) illustrates the sediment pathway from its source to the coast.

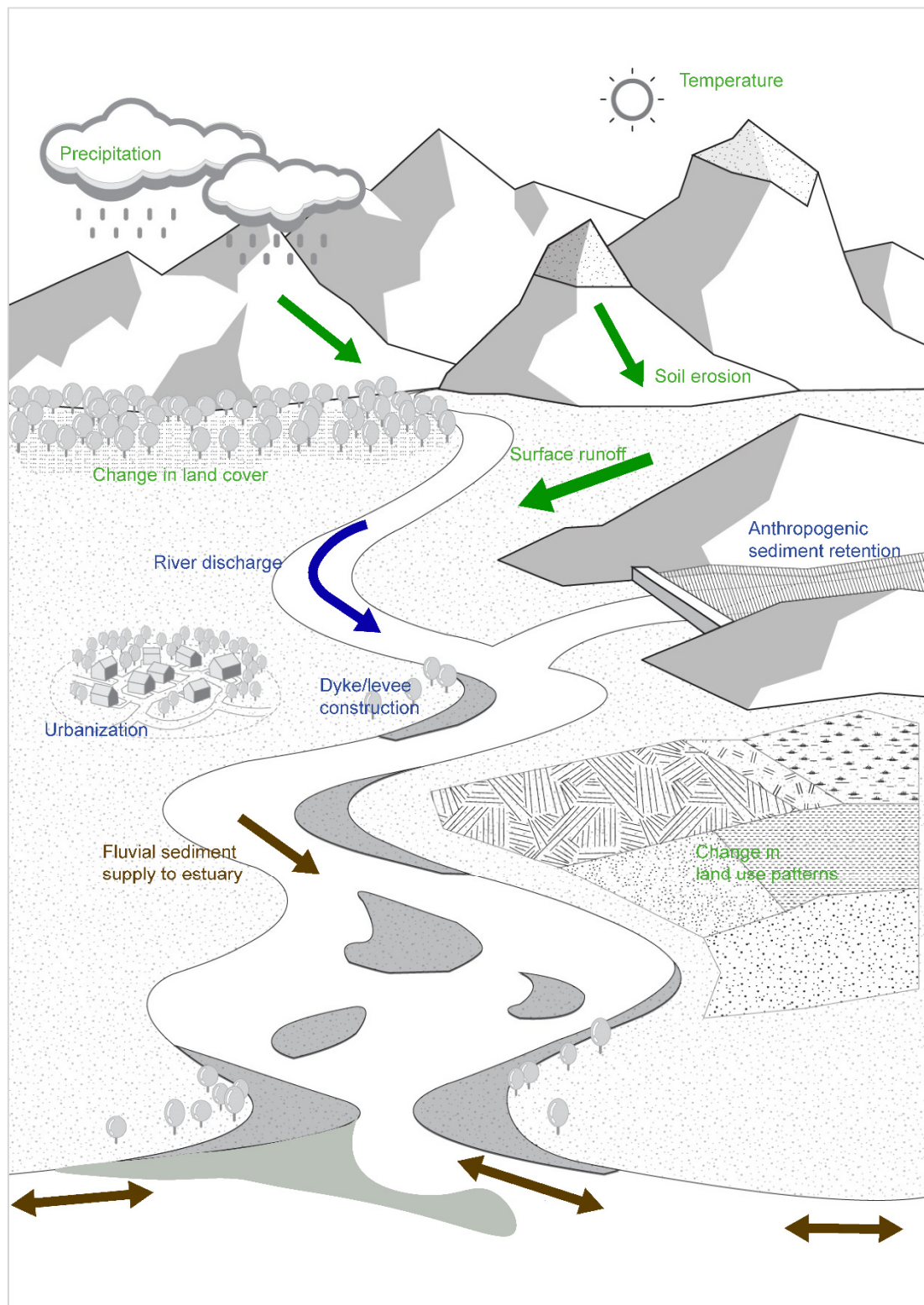


Figure 1-1: Schematic representation of the sediment pathway from its source to the coast adjacent to a mainland barrier estuary. Three colours used in the figure denote the major components (i.e., zones) related to this sediment pathway; (1) catchment scale sediment production zone through soil erosion (in green), (2) transition zone through sediment throughput (in blue), and (3) deposition and redistribution zone through sediment exchange between an estuary and its adjacent coast (in brown). Two-way arrows in brown denote sediment volume exchange between the estuary and its adjacent inlet-interrupted coast.

According to the above figure, there are three major components to be considered in the sediment pathway from source to the coasts; (1) the catchment scale sediment production zone through weathering and soil erosion, (2) the transition zone through fluvial sedimentation and reworking, and (3) the deposition and redistribution zone through sediment exchange between an estuary and its adjacent coast. The long-term evolution of the inlet-interrupted coastlines is affected by the processes that govern the behaviour of the above-mentioned zones of the sediment pathway. The following paragraphs describe the overall behaviour of those three zones and their relative importance in the long-term evolution of inlet-interrupted coasts.

Globally, rivers contribute about 95% of the sediment received by the oceans (Syvitski, 2003). Generation of this sediment starts at the mountain level, where the rocks are weathered into sediment through mechanical, chemical and biological processes (Syvitski and Milliman, 2007). Projected changes in climate would most likely to result in increased temperature (Stocker et al., 2013b). The increased temperature would affect both chemical and mechanical weathering, thus increasing the rate of soil erosion at the catchment scale (Syvitski et al., 2003; Syvitski and Milliman, 2007). Future changes in precipitation will also affect the amount of soil eroded at catchment scales. The combined effect of increased temperature and diminished precipitation would create water stresses to plant and reduce their growth. This, in turn, increases soil erosion at catchment scales. The combination of increased precipitation and temperature would enhance the growth of trees, which in turn reduces the soil erosion in the river catchments (Shrestha et al., 2013). The rate of sediment generation at the catchment scale also depends on anthropogenic activities, such as land clearance for agriculture, urbanization, road construction and reforestation (Overeem et al., 2013; Syvitski et al., 2009; Syvitski and Milliman, 2007). Engineering work such as inter-basin water diversions will reduce the effective catchment area, which in turn result in decreased sediment generation from a given watershed area. All these climate-change driven impacts and anthropogenic activities would alter the magnitude of sediment production at the catchment scale, which, in turn, affects the sediment volume received by the coasts, and the subsequent long-term evolution of inlet-interrupted coasts.

Sediment generated at the catchment scale is transported to the coasts and oceans by the rivers. Climate-change driven variations in future precipitation will alter the river discharge, thus affecting the throughput of eroded soil at catchment scale (Kettner et al., 2005; Shrestha et al., 2013; Syvitski et al., 2003). Anthropogenic activities would exert significant influences on the sediment throughput at the catchment scale in both positive and negative manner. Negative impacts comprise anthropogenic sediment retention, river sand mining, reduction in sedimentation area due to levee/dyke construction, and reduction in river flow due to water withdrawal for irrigation/drinking water supply. River flow regulation, increased surface runoff due to urbanization and deforestation are

considered as the anthropogenic activities that would increase the fluvial sediment transport capacity at catchment scale (Chu, 2014; Dunn et al., 2019; Overeem et al., 2013; Ranasinghe et al., 2019b; Syvitski, 2005; Syvitski et al., 2009; Syvitski and Milliman, 2007; Syvitski and Saito, 2007; Verstraeten and Poesen, 2001; Vörösmarty et al., 2003; Walling, 1999). These anthropogenic activities and climate-change driven impacts would change the total fluvial sediment throughput, which in turn will affect the long-term evolution of the inlet-interrupted coasts.

The final part of the sediment pathway from source to sink is the deposition and redistribution of sediment within the estuary and its adjacent inlet-interrupted coast. The estuarine accommodation volume is affected by both the sediment throughput from the river, and the volume of sediment exchanged between the estuary and its adjacent coast. Climate-change induced sea-level rise will increase the volume of accommodation space within the estuary. If the sediment supply from the river flow is negligible, the sediment demand caused by the increased accommodation space will be supplied from the adjacent coast, which in turn result in eroding the inlet-interrupted coast. In situations where future riverine sediment throughput is sufficiently large, part of the increased estuarine sediment demand will be fulfilled by the fluvial sediment supply. This will decrease the sediment volume imported to the estuary from its adjacent inlet-interrupted coast, and the extent of the subsequent coastline recession associated. If the future riverine sediment throughput is higher than the increased estuarine sediment demand, the resulting surplus sediment volume will be exported to the adjacent coast, which in turn result in progradation of the inlet-interrupted coast (Ranasinghe, 2016; Ranasinghe et al., 2013). These sediment volume exchanges between the estuary and the adjacent coast are closely linked with the longshore sediment transport capacity in the vicinity, which is related to the contemporary wave condition, and other inlet processes.

1.3 Types of inlet-interrupted coasts

Inlet-interrupted coasts include both mainland and barrier island coasts. Therefore, the deposition and redistribution part of sediment pathways (described above) would vary with the type of inlet-interrupted coast. For inlet-interrupted coasts along the mainland, sediment deposition and redistribution processes are closely linked with the type of estuary they are attached with (FitzGerald et al., 2014; Ranasinghe et al., 2013). One commonly-used classification of estuaries is based on its geomorphology, in which they are categorized as bar-built, fjord, tectonic, and coastal plain estuaries (FitzGerald et al., 2014).

Bar-built (barrier) estuaries are commonly found along sandy coasts located in wave-dominated, microtidal environments. These systems are comprised of shore-parallel

sandbars, spit platforms and spits, which are supported by longshore sediment transports near the estuary mouth. High flow velocities at estuary mouth tend to diminish rapidly towards the headland as its cross-sections are widened in the same direction. These estuaries are usually shallow and contain extensive lagoons/waterways within it. Examples of bar-built estuaries can be seen along the eastern coast of USA (near mid-latitudes), the Gulf of Mexico, Australia, Brazil, India, and in the Amazon and Nile River regions.

Coastal plain estuaries, which are also known as drowned river valleys, are characterized by relatively small river flow compared to the tidal prism and hence have relatively small fluvial sediment supply. Most estuaries resemble river courses with large width-to-depth ratios. These estuaries are typically shallow (~10 meters), but wide (several kilometres). The width of these estuaries get wider and deeper towards the mouth, and hence the cross-sectional area exponentially increases in the same direction. Few examples for this type of estuary can be found along the eastern coasts of USA and Canada (e.g., Chesapeake Bay and Delaware (USA) and Miramachi and St Lawrence (Canada)), western coast of Europe (e.g., Gironde (France) and Thames (UK)), New South Wales coast in Australia (e.g., Botany Bay), and the western coast of Africa (e.g., Orange River Mouth (Namibia)).

Barrier islands represent about 7% of the world's inlet-interrupted coasts (Stutz and Pilkey, 2011), and are often densely populated areas subjected to potentially conflicting interests of economy, and coastal safety. Barrier island systems can be classified in different ways, such as; attachment versus detachment, wave or tide dominance, open water or fetch limited exposure, drift or swash alignment, single or multiple barrier planform and island length or inlet width. Detached barriers form islands. In contrast, attached barriers form different forms of barrier systems (e.g., tombolos and double tombolos, barrier spits, welded barriers, looped barriers, pocket barriers, baymouth barriers, and cusped barriers) (van Heteren, 2014).

McBride et al. (1995) identified eight forms of barrier behaviours (Figure 1-2), which include both shore-normal and -parallel movements. Barrier island behaviours are categorised as progradation/retrogradation, dynamic equilibrium, or lateral movement if the open-water shorelines show substantial variations compared to its back-barrier shorelines. Barrier island behaviours such as rotational instability, in-place narrowing, landward rollover, and breakup are observed when both the open water and back-barrier coasts show significant movements.

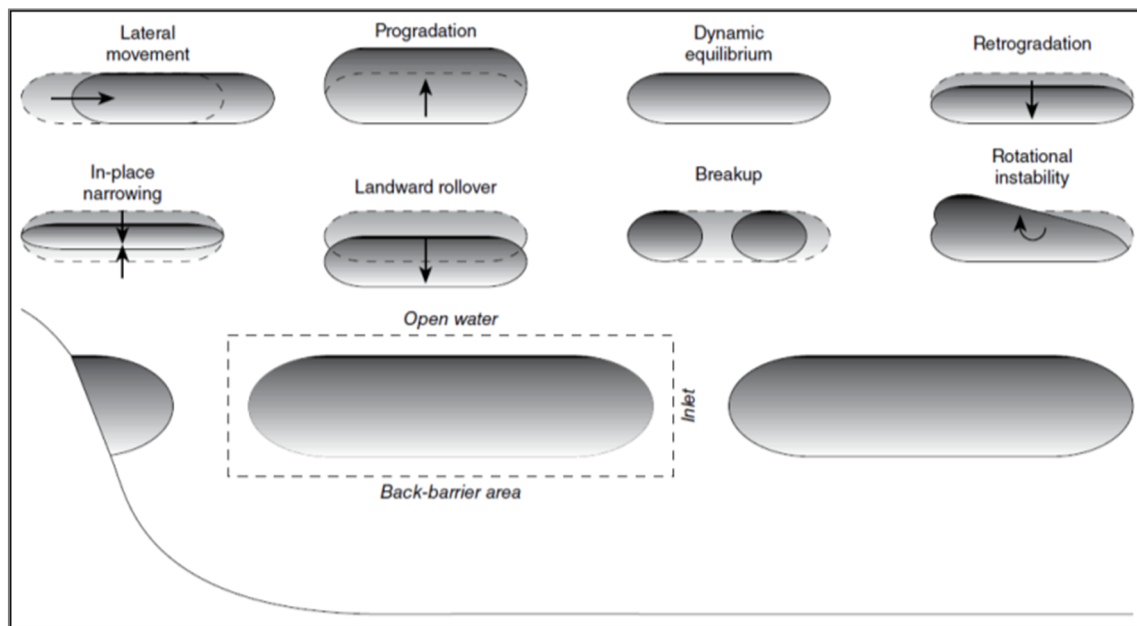


Figure 1-2: Different modes of barrier island behaviour Source: van Heteren (2014); after McBride et al. (1995).

In the shore-parallel direction, barrier spits and islands may accrete and migrate very rapidly in both up-drift and down-drift directions. Progradational and retrogradational behaviours are the main shore-normal movements of barrier islands. Stable barriers are the ones that in dynamic equilibrium, and hence may show in-place narrowing behaviour or minimal changes in its shorelines. Overall recession (i.e., barrier rollover) and landward movement of the open-water shoreline are the demarcating features of retrogradational behaviour of barrier islands. For barrier rollover to take place, the barrier islands should be narrowed down to a certain critical width and height. These rollover rates are in the order of tens of metres per year, which is highly dependent on the nature of the back-barrier system and frequency and magnitude of extreme events. Both subtidal lagoons and intertidal marshes tend to slow down the barrier rollovers, where the former has a higher impact on barrier movement. Rotational instability is the non-uniform behaviour of the barrier islands, which results in local progradation along one end of the barrier, while the rest of the barrier remains stable or move landward due to berm-ridge and neap-berm developments, and swash-bar welding. This behaviour may result in *drumstick* barrier island development and/or a change in barrier orientation. Barrier island breakup may occur if there is no longer a sufficient sand volume and relief above sea level to prevent inundation during storms.

The above discussion indicates that the long-term evolution of barrier island and mainland inlet-interrupted coasts should be investigated separately, because of the noticeable differences in their behaviour. Long-term evolution of inlet-interrupted coasts along the mainland is also varied markedly with the type of attached estuary. Thus, developing a model that can successfully determine the long-term evolution of coastline at all the inlet-

interrupted coasts is beyond the scope of this study. Therefore, as the first step to accomplish this challenging task, it is necessary to narrow down the scope of the study into specific coastal types, which in turn, enable the identification of the applicable climate-change driven impacts that influence the future behaviour of the selected types of inlet-interrupted coastlines.

Owing to the above mentioned diversity in the behaviour of different types of coastal systems, the scope of this study is restricted to determine the long-term evolution of inlet-interrupted coastlines attached to bar-built (barrier) estuaries and barrier island coasts. For the mainland systems, coastlines interrupted by both estuaries with low-lying margins and small tidal inlets are considered in this study. Estuaries with low-lying margins contain tidal flats and salt marshes along their margins as well as banks with mild slopes. If the salt marshes fail to keep up their areal extent by vertical accretion, such wetlands will be transformed into intertidal and/or subtidal environments under the rising sea level. The back-barrier salt marshes in mixed energy environments are demarcated by a very mild sloped topography that extends over a large area. The tidal prism may increase significantly within this unique hypsometry if the supratidal marsh surfaces are flooded or eroded due to rising sea level (FitzGerald et al., 2014). Tidal prism may also increase in the back-barrier if the marshlands are converted into open water bodies under future sea level. Similarly, at estuaries surrounded by mildly sloping banks, increased sea level would lead to a significant increase in surface area, leading to an increase in the tidal prism, and consequently, inlet cross-section area (O'Brien, 1969). Small tidal inlets can be considered as a unique category of the above. Those estuaries generally have little or no intertidal flats, backwater marshes or ebb-tidal deltas (Ranasinghe et al., 2013). A definitional figure of the coastal types that are being studied is presented in Figure 1-3.

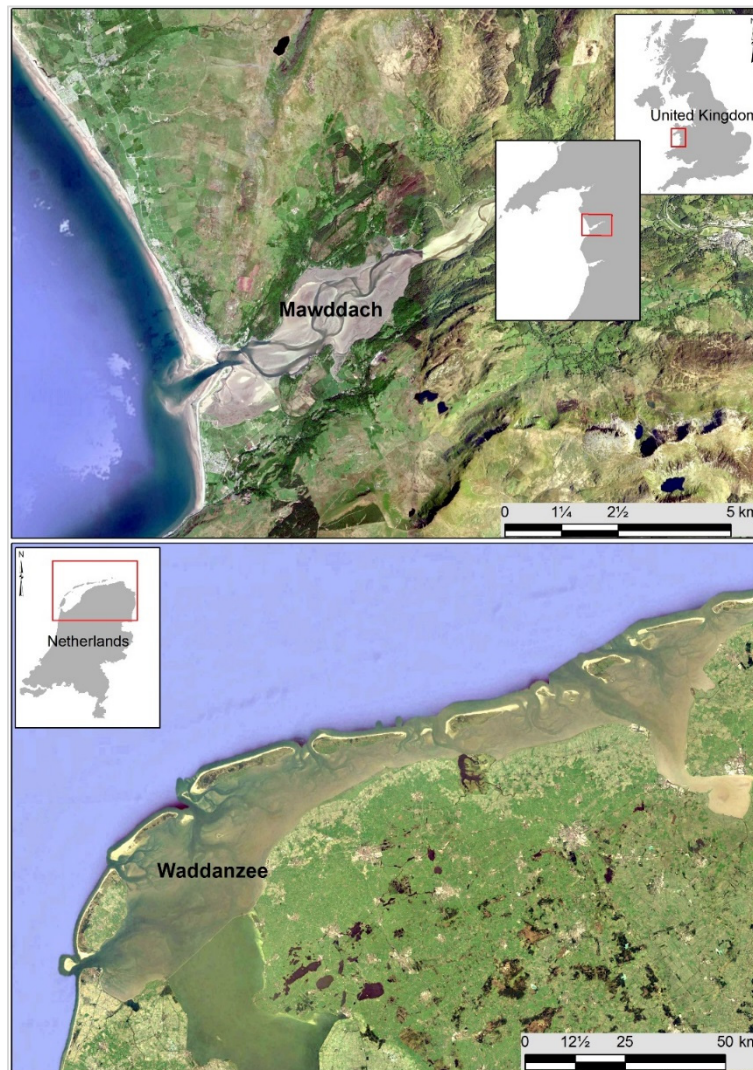


Figure 1-3: A definitional figure of the coastal types considered in this study. Mainland barrier estuary (top, represented by Mawddach estuary, Wales, UK) and barrier-island coast (bottom, represented by the barrier islands along the Waddanee, Netherlands).

1.4 Main drivers that affect the long-term evolution of inlet-interrupted coasts

According to the above description of the sediment pathway from source to the coasts, four drivers were identified as the main contributors to the long-term behaviour of inlet-interrupted coasts; temperature, runoff, change in sea level, and anthropogenic activities (e.g., dam construction and/or removal, urbanization, deforestation). Within the mentioned climatic variables, temperature is considered as the main driver, whereas runoff and sea-level rise were considered to vary with future changes in temperature. Temperature is considered as the main driver because of its correlation with sea-level change and the link to the fluvial sediment supply (via the BQART model). These relationships are described

in detail under Section 2.3. Change in anthropogenic activities was considered as an independent driver when assessing the long-term changes along inlet-interrupted coasts. The following sub-section illustrates the future projections of temperature, runoff and change in sea level and the dataset used to approximate the anthropogenic activities at the catchment scale.

1.4.1 Projected changes in temperature and runoff

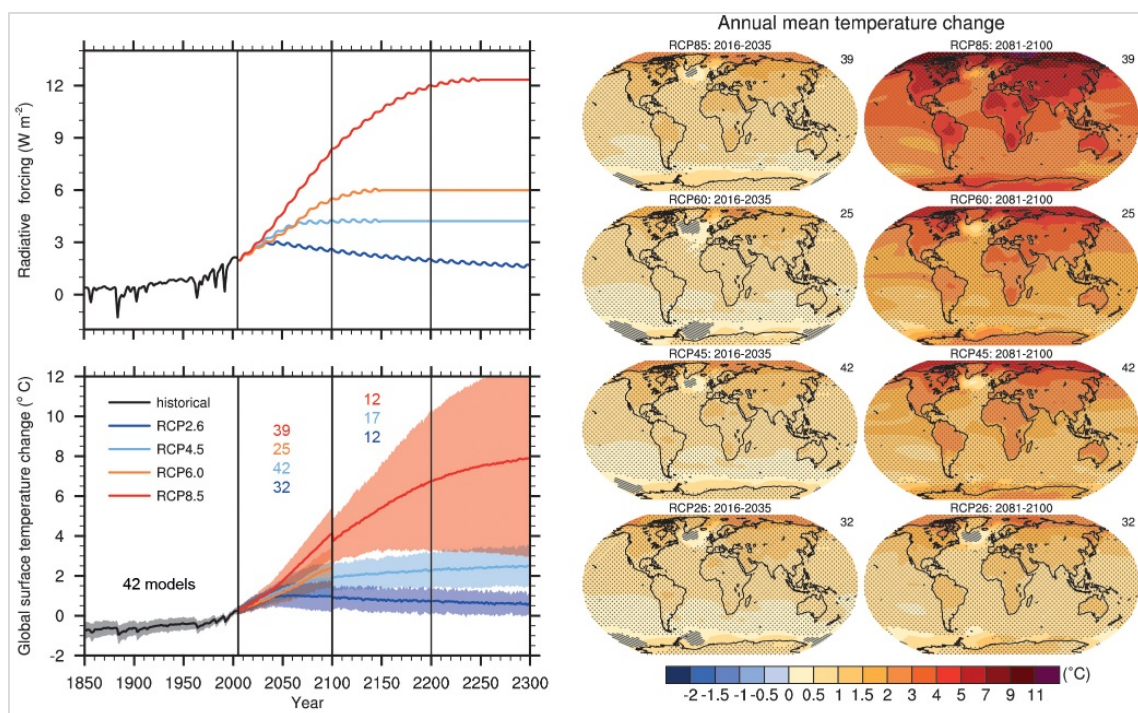


Figure 1-4: Projected average of annual mean surface air temperature change (relative to 1986–2005) for the four RCPs. Hatching indicates regions where the multi-model mean signal is less than one standard deviation of internal variability. Stippling indicates regions where the multi-model mean signal is greater than two standard deviations of internal variability and where 90% of the models agree on the sign of change. The number of CMIP5 models used is indicated in the upper right corner of each panel. (Top left) Total global mean radiative forcing for the four RCPs based on the Model for the Assessment of Greenhouse-gas Induced Climate Change (MAGICC) energy balance model. (Bottom left) Time series of global annual mean surface air temperature anomalies (relative to 1986–2005) from CMIP5 concentration-driven experiments. (Source: Figure TS.15 of Stocker et al. (2013a)).

According to Stocker et al. (2013a), global mean temperatures will continue to rise over the 21st century under all emission scenarios that are summarized in Representative Concentration Pathways (RCPs). These trends become highly sensitive to the RCPs after the mid-21st century, where the rate of global warming is projected to increase rapidly under RCP 6.0 and 8.5. Projected global change in annual mean temperature for 2016-2035 and 2081-2100 periods are shown in Figure 1-4.

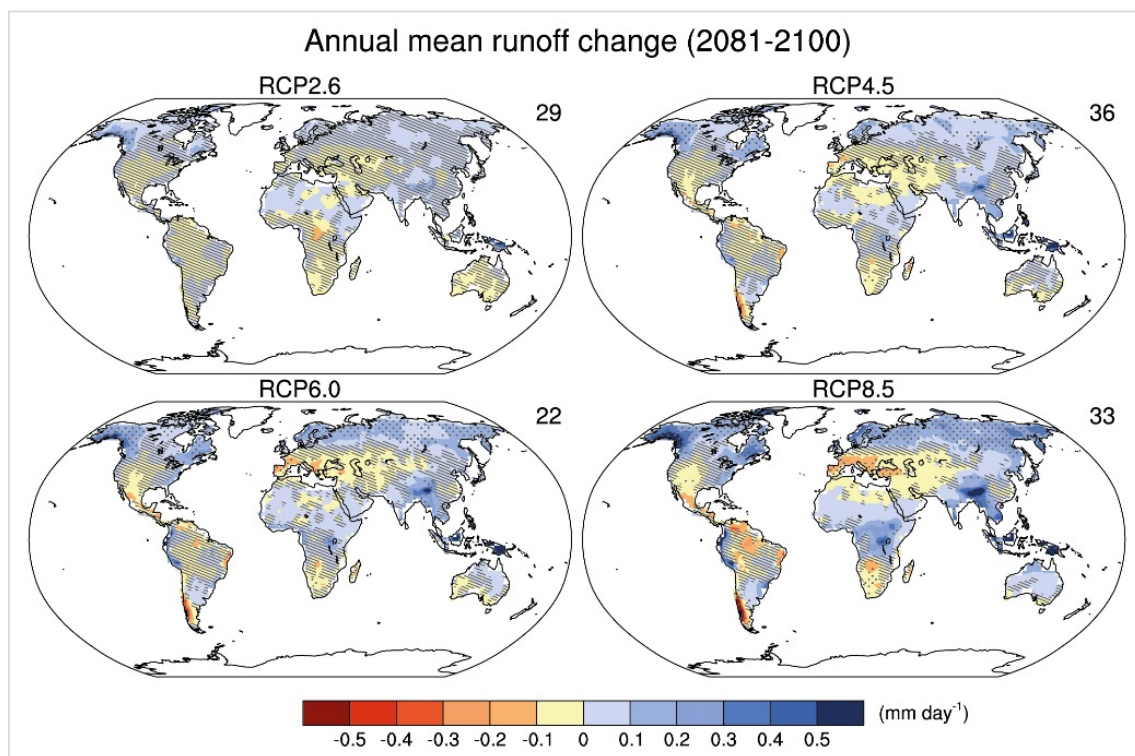


Figure 1-5: Projected change in annual mean runoff for 2081–2100 (relative to 1986–2005). Hatching indicates regions where the multi-model mean change is less than one standard deviation of internal variability. Stippling indicates regions where the multi-model mean change is greater than two standard deviations of internal variability and where at least 90% of models agree on the sign of change. The number of CMIP5 models used is indicated in the upper right corner of each panel (Source: Figure 12.24 of Collins et al. (2013)).

Projected changes in precipitation and temperature are likely to result in changes in runoff patterns, which in turn affect the riverflows across the globe. Collins et al. (2013) have projected decreased mean annual runoff in parts of southern Europe, Middle East, southern Africa and western parts of North America, whereas high northern latitudes and east and south Asian regions are projected to have increased runoff for all RCPs by the end of the 21st century (relative to 1986-2005) (Figure 1-5).

1.4.2 Projected changes in global sea level

Due to the increasing oceanic temperature and loss of continental glaciers in the polar regions, global mean sea level is expected to increase during the 21st century (Stocker et al., 2013b). IPCC projections presented by Stocker et al., (2013a) indicate that the global mean sea level rise for the late 21st century (2081-2100) is likely to be in the range of 0.26 m to 0.82 m (relative to 1986-2005) (Figure 1-6).

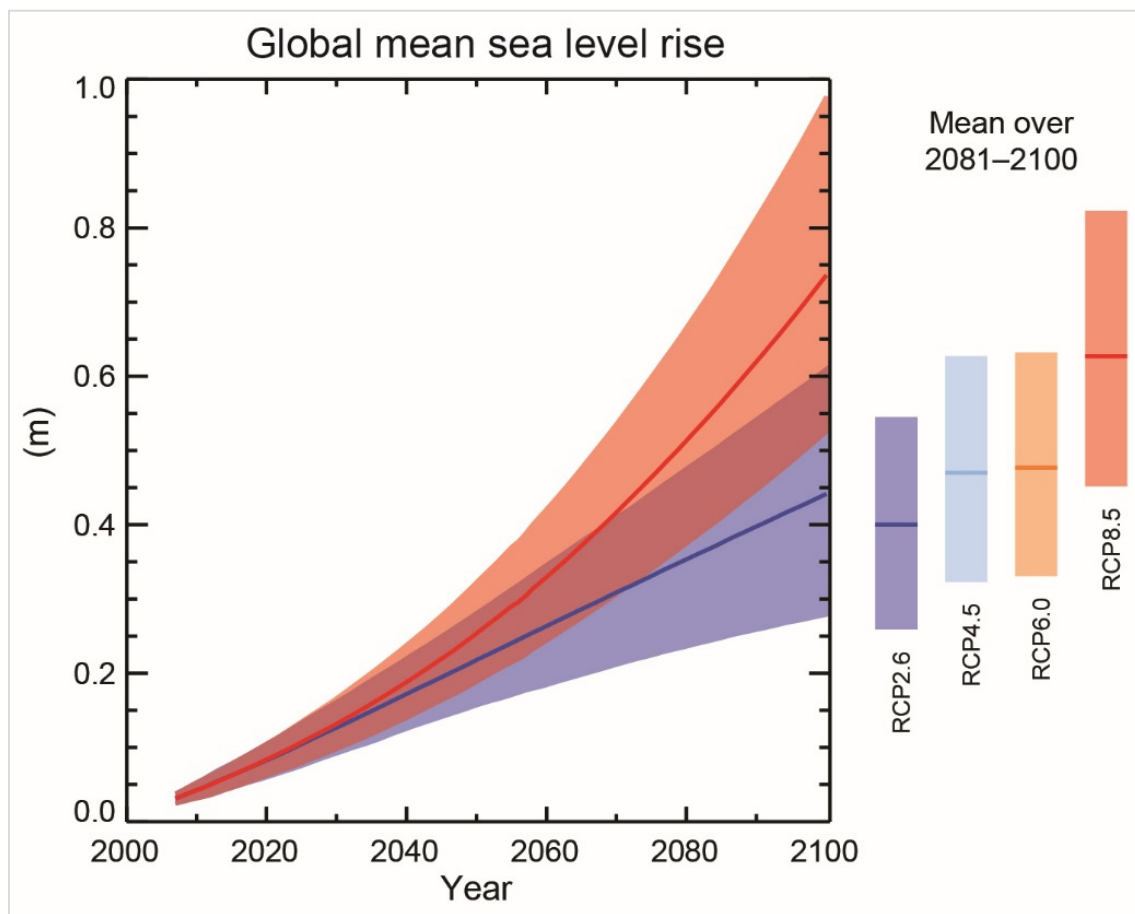


Figure 1-6: Projections of global mean sea-level rise over the 21st century (relative to 1986–2005). The assessed likely ranges for RCP2.6 and RCP8.5 are shown as shaded bands. Vertical bars indicate the likely ranges of mean over the period 2081–2100 for all RCP scenarios with median values are indicated as horizontal lines (Source: Figure SPM.9 of Stocker et al. (2013b))

Nicholls et al. (2014) have presented an equation to determine global sea-level changes as a time series over the 21st century. Global sea-level rise predictions used in this study were computed according, by the use of the following equation [1-1]:

$$\Delta SL_G = a_1 t + a_2 t^2 \quad [1-1]$$

where ΔSL_G is the change in global sea level (m) since 2000, ' t ' is the number of years since 2000, a_1 is the trend in sea level change (m/yr), and a_2 is the change in the rate of sea-level change trend (m/yr²).

Mehvar et al. (2016) have presented the relevant coefficients for all four RCPs, which are indicated in the following table (Table 1-1).

Table 1-1: Trends and rate of change in trends of global sea-level rise for IPCC RCP scenarios

| Forcing | a_1 (m/yr) | | | a_2 (m/yr ²) | | |
|---------|--------------|----------|----------|----------------------------|------------------------|------------------------|
| | Lower | Middle | Upper | Lower | Middle | Upper |
| RCP 2.6 | 0.003400 | 0.004426 | 0.004934 | -6.94×10^{-6} | -1.22×10^{-6} | 1.206×10^{-5} |
| RCP 4.5 | 0.002977 | 0.003953 | 0.004570 | 6.939×10^{-6} | 1.366×10^{-5} | 2.589×10^{-5} |
| RCP 6.0 | 0.003010 | 0.003965 | 0.004544 | 7.776×10^{-6} | 1.486×10^{-5} | 2.82×10^{-5} |
| RCP 8.5 | 0.002675 | 0.003279 | 0.003349 | 6.451×10^{-5} | 4.131×10^{-5} | 2.598×10^{-5} |

Projections for minimum, mean and maximum change in global sea level under all RCPs are shown in the following figure (Figure 1-7).

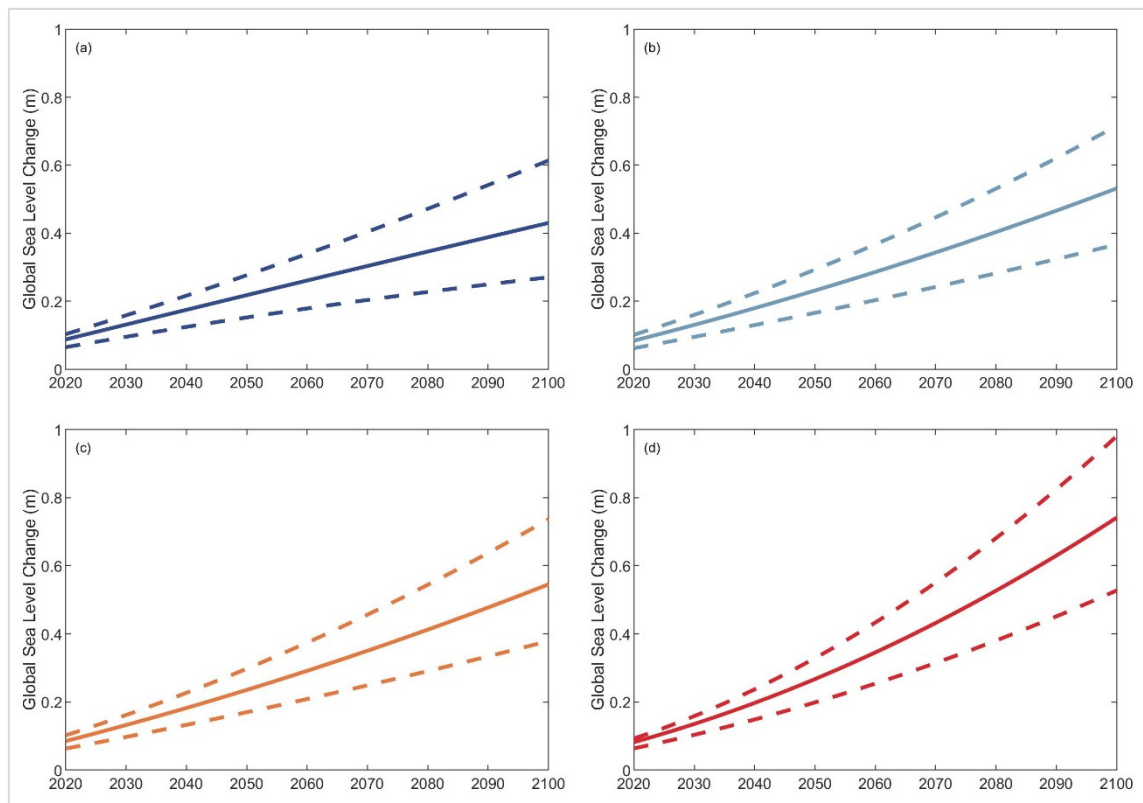


Figure 1-7: Projected maximum, mean and minimum global sea-level changes for 2020-2100 (relative to 1986-2005). Subplots (a), (b), (c), and (d) are corresponding to RCP 2.6, RCP 4.5, RCP 6.0, and RCP 8.5 forcing, respectively

1.4.3 Projected changes in regional relative sea-level change

According to Stocker et al. (2013a), strong regional patterns are projected for the change in sea level by the end of the 21st century under all RCPs (Figure 1-8), which are different to the global change in mean sea level projections during the same period (2081-2100).

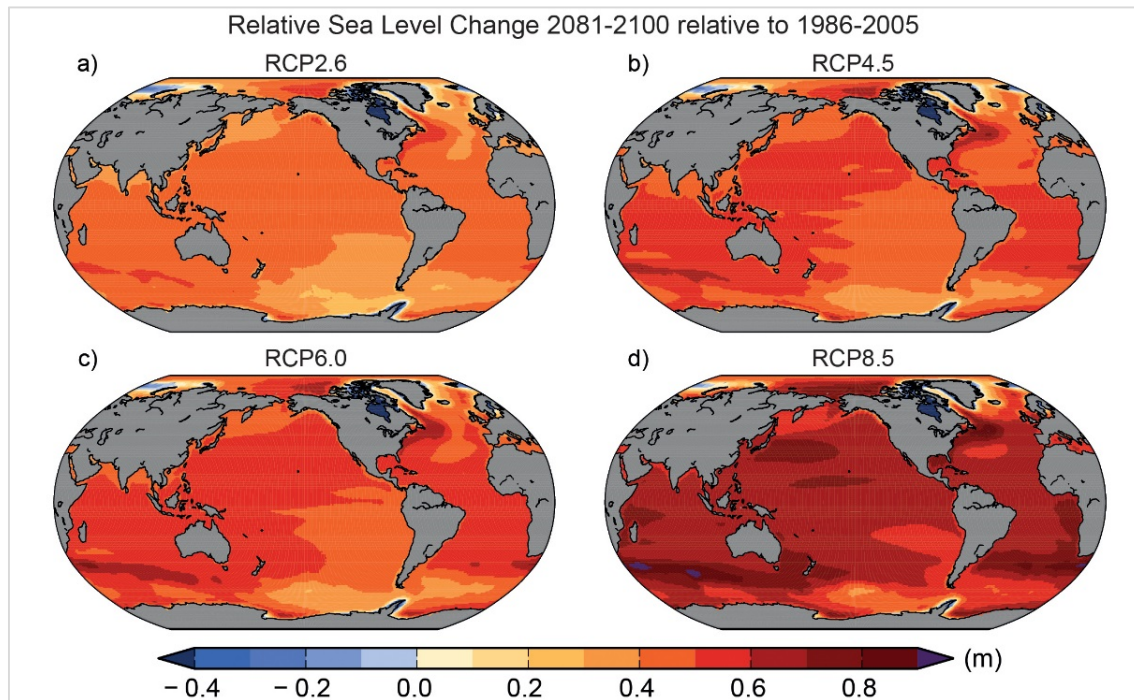


Figure 1-8: Regional relative sea-level change for 2081-2100 (relative to 1986-2005). Each map includes effects of atmospheric loading, plus land-ice, glacial isostatic adjustment and terrestrial water sources. (Source: Figure TS.23 of Stocker et al. (2013a)).

The above regional relative sea-level change projections are obtained according to the following equation [1-2].

$$\Delta RSL = \Delta SL_G + \Delta SL_{RM} + \Delta SL_{RG} + \Delta SL_{VLM} \quad [1-2]$$

where ΔRSL is the change in relative sea level, ΔSL_G is the change in global mean sea level, ΔSL_{RM} is the regional variation in sea level from the global mean due to meteorological factors, ΔSL_{RG} is the regional variation in sea level due to changes in the earth's gravitational field, and ΔSL_{VLM} is the change in sea level due to vertical land movement, all values are in metres.

Intermediate projections of regional relative sea-level change

For a given location, the regional relative sea-level change projections by 2100 (ΔRSL) were obtained from Figure 1-7, while the corresponding global mean sea level change (ΔSL_G) per each RCP was obtained from Table SPM. 2 of Stocker et al. (2013b). The

difference between those two sets of values provide the cumulative contribution of ΔSL_{RM} , ΔSL_{RG} , and partly ΔSL_{VLM} for 2100.

1.4.4 Anthropogenic activities

In this study, the Human FootPrint Index (HFPI) dataset presented by Wildlife Conservation Society - WCS and Center for International Earth Science Information Network - CIESIN - Columbia University. (2005) was used to approximate present-day anthropogenic activities at the river catchment scale. The human footprint index is developed by using several global datasets such as population distribution, urban areas, roads, navigable rivers, electrical infrastructures and agricultural land use. This dataset is available at a spatial resolution of 30 arc-seconds and is regionally normalized to account for the interaction between the natural environment and human influences (Sanderson et al., 2002). Global and continental scales raster files of HFPI data are available at <https://doi.org/10.7927/H4M61H5F>. The global map of the HFPI dataset is shown in Figure 1-9.

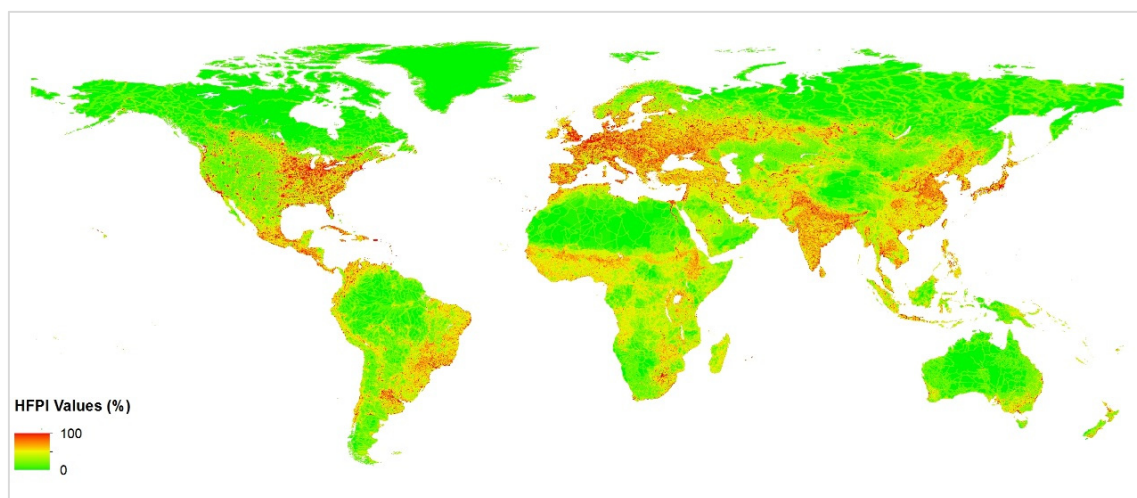


Figure 1-9: Global map of Human FootPrint Index (HFPI). The HFPI dataset was published by Wildlife Conservation Society - WCS and Center for International Earth Science Information Network - CIESIN - Columbia University. (2005). The global raster dataset was obtained from <https://doi.org/10.7927/H4M61H5F>.

1.5 Modelling of the long-term evolution of inlet-interrupted coasts

The evolution of inlet-interrupted coasts can be hypothesized as a result of a change in sediment volume (i.e., sediment budget) between the inlet-estuary system and its adjacent shoreline (Ranasinghe et al., 2013; Stive, 2004; Stive et al., 1998, 1990). The concept of

sediment budget is discussed in detailed and presented in several studies. This includes the generic sediment budget concept for coastal engineering, erosion and management issues presented by Komar (1998, 1976), sand budget based analysis of littoral processes that affect the coast from Pismo to Santa Barbara (Bowen and Inman, 1966), review of available sediment budget concepts and application of an more reliable conception for Long Island, New York, and Ocean City Inlet, Maryland (Rosati, 2005), mesoscale sediment budget application for Long Island, New York (Kana, 1995), study on the sand budget at the Santa Barbara coast in California (Patsch and Griggs, 2008), and a preliminary assessment of the sediment budget for Humber estuary in the UK (Townend and Whitehead, 2003). However, most of the above mentioned studies have only considered the coastal processes in their analysis of sediment budget. One of the most comprehensive discussions of the sediment budget for both open and inlet-interrupted coasts is presented by (Cowell et al., 2003), who introduced the “Coastal Tract” concept.

The long-term evolution of inlet-interrupted coasts is affected by a variety of processes in river catchment that govern sediment generation and transportation and processes within an estuary and its adjacent coasts that influence the sediment deposition and redistribution as well. Therefore, any modelling technique that investigates the long-term evolution of inlet-interrupted coasts could be better supported by considering the holistic behaviour of catchment-estuary-coastal systems, which are closely associated with the sediment pathway from its source to the coast. However, only a limited number of studies to date have considered this holistic behaviour when assessing the long-term evolution of inlet-interrupted coasts.

In the assessment of shoreline variations of Poverty Bay, New Zealand, Smith (1988) had mostly considered the variations in land use patterns and management, while ignoring the other anthropogenic activities and climate change-driven impacts associated with sediment generation and transportation at the catchment scale. Work presented by Kettner et al. (2009) investigates the evolution of the Poverty Shelf (North Island, New Zealand) through a coupled numerical modelling technique (HydroTrend and SedFlux). In this study, catchment processes related to fluvial sedimentation were considered in a simplified manner, where the variation in sediment throughput was computed by only considering the natural and anthropogenic changes in catchment land cover. In the study, no considerations were given to potential coastline progradations or sediment dispersal within Poverty Bay. The modelling approach presented by Shennan et al. (2003) to simulate the evolution of the Humber estuary in the UK, consideration was only given to the changes in precipitation and vegetation (in terms of deforestation) at the catchment scale to assess the variation in fluvial sediment supply. However, in this assessment of sediment dynamics of the Humber estuary, attention was given to both estuarine and coastal processes by the means of tidal regimes and sea-level changes, respectively. Nevertheless, this study does not consider the nearshore morphodynamics to account for the changes along the adjacent

coastline. The work presented by Green (2013) proposes a conceptual mechanism that fulfils the estuarine sediment demands at Pauatahanui Inlet, New Zealand. Despite that the possibility of fulfilling the estuarine sediment demands by multiple sources was recognized, this study has only considered the catchment management options to achieve the desired sediment supply to the estuary.

Work presented by Fanos (1995) correlates variations of the Nile delta shoreline with the riverine sediment throughput. However, in this assessment, variations in the volume of sediment received by the coast were only considered due to reservoir sediment retention and river flow regulations within the catchment, while omitting the influences due to other applicable anthropogenic activities and changes in climatic conditions. Angamuthu et al. (2018) present multi-decadal Delft 3D simulations of an idealized large delta system under different climatic and human activities. In their study, the evolution of an idealized delta system was investigated under different rates of fluvial sediment supply, river discharge, relative sea-level and selected human interventions. Although this study does not investigate the impacts of river-delta system evolution on its adjacent coast, their findings emphasize the influence of both natural and human drivers on delta morphodynamics.

The coupled watershed-coastal modelling technique presented by Samaras and Koutitas (2014) is focused on evaluating the climate change impacts on sediment transportation and morphological changes along a sandy coast in Northern Greece. The proposed modelling technique utilizes the Soil Water Assessment Tool (SWAT) and a shoreline evolution model (PELNCON-M) to investigate the evolution of the integrated catchment-coastal system under climate change-driven impacts. Future climatic variations considered in this study are restricted to increases in precipitation and wave extremes to represent changes in terrestrial and oceanic processes, respectively. Therefore, this study does not account for the estuarine processes and anthropogenic activities at the catchment scale in assessing the long-term evolution of the coastline. However, findings of this study emphasize the importance of an integrated modelling approach in investigating long-term coastline evolution under changing climatic conditions. Guo et al. (2015) have investigated the impacts of river discharge/sediment load variations on the long-term estuarine morphodynamic equilibrium of the Yangtze River, China using three schematized river discharge hydrographs. Their findings show that a long-term estuarine morphodynamic equilibrium can be achieved if the annually-averaged sediment transport gradients along the estuary are diminished, and the sediment received from the river flow and the outflux to the sea is to be balanced. Although the study considered the sediment exchange between the estuary and its adjacent coast, only the tide-river flow interaction was accounted as the contributing oceanic process, while acknowledging the necessity of including the impacts of anthropogenic activities and change in sea-level when examining the long-term evolution of estuarine morphodynamics. CoSMoS-COAST (Coastal One-line Assimilated Simulation Tool) presented by Vitousek et al. (2017) is a transect-based model that

predicts both the short- and long-term behaviour of coastline due to waves and sea-level rise driven variations in longshore and cross-shore sediment transport. This process-based numerical model was applied along 500 km of Southern California in the USA, which represents a variety of geomorphic settings. However, this modelling technique only accounts for some key processes such as fluvial sediment throughput, regional sediment supply, and long-term coastal erosion that contribute to the long-term evolution of coastlines in an implicit manner. This implicit consideration of other sediment transport processes is achieved during the model parameter calibration through data assimilation from historical shoreline positions. Despite these restrictions, findings of this study emphasize the need for an integrated modelling approach to evaluate the long-term evolution of shorelines and the uncertainties that are associated with the future projections of coastline positions.

As was mentioned in Section 1.1, it is desirable to quantify the uncertainties associated with the long-term shoreline change projections to manage the climate change impacts and anthropogenic activities driven socio-economic losses along the inlet-interrupted coasts. Therefore, reduced complexity modelling techniques are preferred in investigating the long-term evolution of inlet-interrupted coasts, because their computing time efficiency (i.e., fast model simulations) enables quantifying the uncertainties associated in the model projections through a probabilistic approach (i.e., Monte Carlo framework).

Such a simplified modelling technique that can simulate long-term coastal evolution at the regional scale (The Cascade model) was presented by Larson et al. (2003), in which the focus was given to the volume of sediment transferred around the inlets through the inlet-shoal complex. This model accounts for several processes involved in terms of sediment sources/sinks; including beach nourishment, cliff erosion, and overwash. An improved version of this model (Cascade Version 2) was presented by Larson et al. (2007), where the attention was given to improve the representation of physical processes that are involved in sediment storage and transfer, highlighting the beach morphology response and inlet shoal growth and bypassing. Although these two models account for estuarine and coastal processes related to sediment deposition and redistribution, the omission of the riverine sediment throughputs can be identified as their major drawback in determining the long-term evolution of estuary-coastal systems.

In this perspective, the Scale-aggregated Model for Inlet-interrupted Coasts (SMIC) presented by Ranasinghe et al. (2013) is the first of its kind that treats Catchment-Estuary-Coastal (CEC) systems in a holistic manner, while giving due consideration to the description of physics governing the behaviour of the integrated system. Although SIMC provides a robust platform to probe into CEC systems holistically, limitation in its applicability to small tidal inlets, simplified method adopted in quantifying the fluvial sediment supply, omission of spatial variation in coastline change and the deterministic

nature of its future projections are the major drawbacks associated in the long-term evolution of inlet-interrupted coasts under climate change impacts and anthropogenic activities.

Thus, this research attempts to address this knowledge gap by developing a reduced complexity modelling tool that can probabilistically simulate the climate-change driven evolution of inlet-interrupted coasts at macro (50-100 year) time scales, while taking into account the contributions from Catchment-Estuary-Coastal (CEC) systems in a holistic manner.

1.6 Overarching objectives and research questions

The main objective of this PhD research is to gain new insights in the climate-change driven variation of inlet-interrupted coastlines at macro time scales (50-100 year) in a probabilistic manner, while giving due considerations to the terrestrial processes that govern fluvial sedimentation and dominant oceanic processes, by development and strategic application of a rapidly executable reduced complexity model.

This research study endeavours to answer the following specific research questions, which will assist the quest of achieving the above research objective.

- 1) How can macro time scale coastline change along inlet-interrupted coasts be effectively numerically modelled in a probabilistic manner?
- 2) How would the selected different catchment-estuary-coastal systems behave under future climate change-driven impacts?
- 3) What are the relative contributions of different climatic forcing to the projected coastline changes?
- 4) How would the world's inlet-interrupted coasts evolve under future climate change-driven impacts?

1.7 Outline of this thesis

The content of this dissertation is structured into five chapters, as summarized below:

Chapter 1 constitutes the introduction to this study, which consists of motivation and research background with a description of sediment pathway from its source to the coast, a review on different types of inlet-interrupted coasts, main climatic drivers that affect the long-term evolution inlet-interrupted coasts and their projected variations across the 21st century, and a review on different modelling techniques adopted in assessing climate-change driven impacts on inlet-interrupted coasts, their shortcomings and limitation. It

also introduces the overarching research objective and specific research questions considered in this study.

Chapter 2 introduces the reduced-complexity modelling technique developed to probabilistically assess the evolution of inlet-interrupted coasts under climate change-driven impacts and (relevant) anthropogenic activities at macro (50-100 year) time scales. It comprises the methods of probabilistically determining the variations in total sediment volume exchanged between the inlet-interrupted coasts and the respective barrier estuaries they are connected to, and a conceptual framework to distribute the impacts of the computed variations in total sediment volume exchanged along the inlet-interrupted coastline. This chapter also provides a modelling framework to probabilistically assess the evolution of barrier island coasts at macro time scales, by considering climate change-driven impacts and (relevant) anthropogenic activities.

Chapter 3 presents the application of the proposed reduced-complexity modelling technique at four selected mainland (barrier estuary) systems (Alesha estuary, OR, USA; Dyfi estuary, Wales, UK; Kalurata inlet, Sri Lanka; and Swan river system, Australia) and one barrier island (Chandeleur Islands, LA, USA). Descriptions of the selected case study sites are provided at the beginning of this chapter. It is followed by the model applications at the selected barrier estuary systems, which are in three sequential steps: (1) Development of stochastic variables, (2) Computation of the variation in total sediment volume exchanged, and (3) Assessment of total coastline change by distributing the above (2) computed variation in total sediment volume exchange along the inlet-affected coast. This is followed by a comparison between the projected changes at the selected barrier estuary systems. Model applications at the selected barrier island are presented in two steps: (1) Development of stochastic variables and (2) Determination of barrier migration distance and assessing the final freeboard height. Finally, an assessment of initial barrier island conditions that contribute to barrier drowning is also evaluated by applying the same modelling technique with hypothetical initial barrier island characteristics.

Chapter 4 demonstrates the generic applicability of the proposed reduced-complexity modelling technique at mainland inlet-interrupted coasts via applications at 41 representative barrier estuary systems sampled across six continents. It also consists of first-order probabilistic approximations on inlet-interrupted coastline change due to climate change-driven impacts. A broad classification of the selected barrier estuary systems is also suggested, by considering the relative contributions of the processes that govern the long-term evolution of their inlet-interrupted coasts.

Chapter 5 presents the general conclusions of this study and the suggestions for future research initiatives.

Chapter 2

Probabilistically simulating climate change-driven coastline change along inlet-interrupted coasts: model development

2.1 Introduction

As mentioned in Chapter 1, present-day process-based modelling approaches are unable to simulate long-term evolution of inlet-interrupted coasts in a probabilistic manner, while taking into account the contributions from the complete catchment-estuary-coastal system in a holistic way. Hence, the attention was given to develop a fast, reduced-complexity model to investigate the long-term evolution of inlet-interrupted coasts.

This chapter describes the development of a reduced-complexity modelling technique that can probabilistically assess the evolution of inlet-interrupted coasts at macro time scales by considering both climate change-driven forcing and anthropogenic activities. The proposed modelling approach deals with two systems; mainland inlet-estuary systems and barrier-island systems. The modelling framework for the mainland inlet-estuary systems consists of two major components: (1) computing variation in total sediment exchange between the inlet-estuary system and its adjacent coast and (2) determining the evolution of the bounding inlet-interrupted coast.

This chapter is structured in the following sequence: Section 2.2 presents the deterministic modelling approach of computing the total change in sediment volume exchanged between the mainland barrier estuary and its adjacent inlet-interrupted coast, and the baseline climatic conditions used in sediment volume calculations. Section 2.3 presents the probabilistic framework adopted to determine the volume changes in total sediment exchange in barrier-estuary systems. It is followed by the presentation of a conceptual modelling framework to probabilistically (to allow uncertainty quantification) determine the resulting coastline change at mainland inlet-estuary systems (Section 2.4). Section 2.5 presents the proposed deterministic modelling framework to assess barrier island evolution at macro time scales, and Section 2.6 describes the probabilistic framework for determining barrier island evolution over multi-decadal to century time periods. Finally, Section 2.7 presents a comparison of model hindcasts with the observed coastline changes over 1986-2005 period.

2.2 Determining changes in total sediment volume exchange between a barrier-estuary system and its inlet-interrupted coast

Part of the multi-decadal coastline change at tidal inlets driven by climate change and anthropogenic activities is governed by changes in the net volume of sediment exchanged between inlet-estuary systems and their adjacent coast (Stive et al., 1998). Discretization of this sediment volume (i.e., inlet-estuary system response to future climate change-driven impacts and anthropogenic activities) yields three components: (1) basin infilling volume due to sea level rise-induced increase in accommodation space, (2) basin volume change due to variation in river discharge, and (3) change in net annual fluvial sediment supply (Ranasinghe et al., 2013). Depending on whether the estuary is in sediment importing or exporting mode (relative to the ocean side of the estuary), and the magnitude of the above three sediment budget components, an inlet-affected coastline will be subsequently subjected to a certain amount of coastal recession or progradation. In addition to this change in the coastline position, sea-level rise tends to drive the coastline landward (i.e., the Bruun effect) which will influence the coastal sediment budget.

As a first step in determining the evolution of an inlet-interrupted coastline, the net annual volume of sediment exchanged between the inlet-estuary system and its adjacent coast needs to be computed. This calculation presumes that any given inlet-estuary system would strive to and eventually reach its natural equilibrium. Hence, any excess amount of sediment would be exported to its adjacent coast. If there is a deficit in sediment, an inlet-estuary system would import sand from its adjacent coast. This sediment volume can be computed by summation of three different processes, given by the following equation:

$$\Delta V_T = \Delta V_{BI} + \Delta V_{BV} + \Delta V_{FS} \quad [2-1]$$

where ΔV_T is the cumulative change in the total sediment-volume exchange between the estuary and its adjacent coast, ΔV_{BI} is the sea-level rise-driven change in basin volume, ΔV_{BV} is the change in basin infill sediment volume due to variation in river discharge, and ΔV_{FS} is the change in fluvial sediment supply due to combined effects of climate change and anthropogenic activities, all volumes in m^3 .

The schematic diagram presented below (Figure 2-1) shows the connections between these processes and the sediment-volume components associated with ΔV_T .

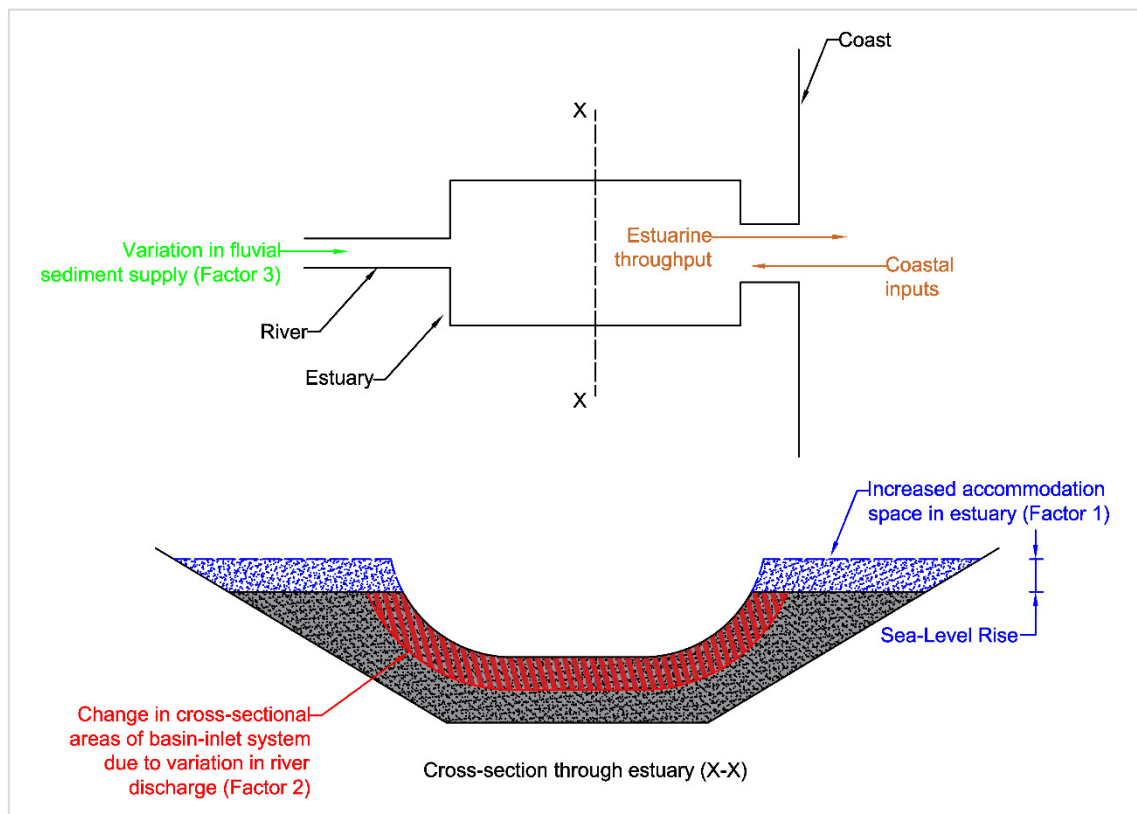


Figure 2-1: Schematic illustration of the connections between sediment volume components associated with the change in total sediment-volume exchange (ΔV_T) between inlet-estuary system and its adjacent coast.

2.2.1 Basin infilling volume due to sea-level rise-induced increase in accommodation space

Accommodation space is the additional volume created within the basin due to a given increment in regional relative mean sea level (ΔRSL (m)). This volume ($A_b \Delta RSL$; where, A_b is the basin surface area (m^2)) results in a sediment demand in the estuary (ΔV_{BI} (m^3); Factor 1 of Figure 2-1). There is a hysteresis relation between sea-level rise (hydrodynamic forcing) and its associated basin infilling (morphological response), in which the latter is the lagging process. According to Ranasinghe et al. (2013), this lag in morphological response is estimated to be about 50% of the volume required by the

corresponding forcing conditions. This can be expressed as equation [2-2], where the negative sign indicates sediment imported into the inlet-estuary system from the coast.

$$\Delta V_{BI} = -\text{fac}(A_b \Delta RSL) \quad [2-2]$$

where ‘fac’ ($0 < \text{fac} < 1$) accounts for the morphological response lag. In this study, it is set to be 0.5 (adopted from Ranasinghe et al. (2013)) for all the simulations.

2.2.2 Basin volume change due to variation in river flow

Changes in river discharge (ΔQ_R (m^3)) will affect the infill volume of the estuary. Such changes in river discharge would alter the tidal flow volume during the ebbing phase of the tide, and subsequently, the estuarine and inlet velocities. Due to the tendency of velocities in basin-inlet system (averaged over the net cross section) to approach an equilibrium value, the basin-inlet system will change its cross section by either scouring or accretion, until the equilibrium cross section is reached. Depending on the sign of change in future river discharge (i.e., increase (+)/decrease (-)), a particular volume of sediment (ΔV_{BV} (m^3); Factor 2 in Figure 2-1) would be exchanged between the inlet-basin system and its adjacent coast to accommodate this basin-inlet cross-sectional change. This volume of sediment (ΔV_{BV}) can be computed as the following [2-3]:

$$\Delta V_{BV} = \frac{\Delta Q_R V_B}{(P + Q_R)} \quad [2-3]$$

where Q_R is the present river flow into the basin during ebb (m^3), ΔQ_R is the climate change-driven variation in river flow during ebb (m^3), V_B is the present basin volume (m^3), and P is the mean equilibrium ebb-tidal prism (m^3).

Determining equilibrium tidal prism for estuaries with low-lying margins

The above sediment volume ΔV_{BV} depends on the contemporary equilibrium tidal prism. This equilibrium tidal prisms in estuaries with low-lying margins are linked with the concurrent sea level and cross-sectional area of the tidal inlet and channels in the basin (Section 1.2). Given that the sea level is progressively increasing (Stocker et al., 2013b), it is necessary to determine the equilibrium tidal prism at these inlet-estuary systems for the concurrent mean sea level, so that the corresponding basin volume change (Section 2.2.2) and subsequent amount of sediment exchange can be estimated. Figure 2-2 illustrates the flowchart of this non-linear, iterative calculation procedure, followed by a description of the relevant physical processes associated. The resulting equilibrium tidal-prism values were used in equation [2-3] to determine ΔV_{BV} .

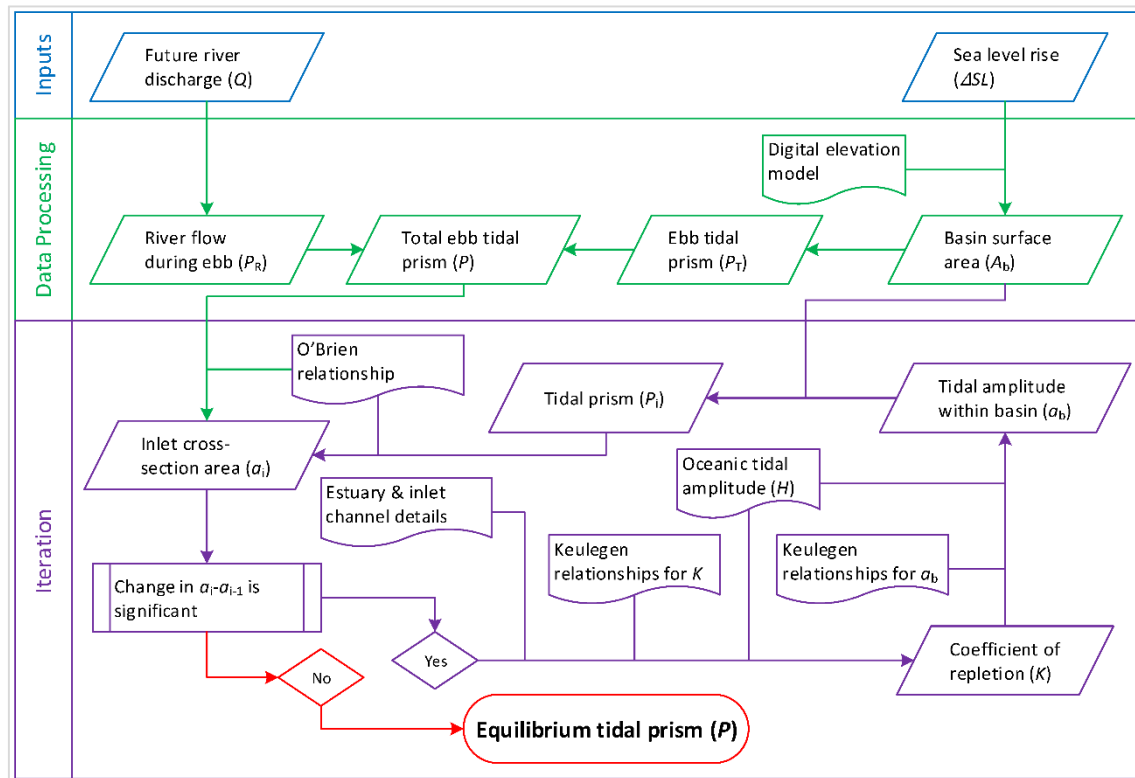


Figure 2-2: Flowchart of the iteration procedure to determine equilibrium tidal prism at estuaries with low-lying margins.

The total ebb-tidal prism (P) consists of two components: (1) the volume of water flowing out of the estuary system due to tidal forcing alone, which is known as the ebb-tidal prism (P_T), and (2) the volume of water supplied by the river flow during the ebb (P_R).

$$P = P_T + P_R \quad [2-4]$$

Owing to the geomorphic settings of these systems, the basin surface area of the estuary (A_b) may change with sea-level rise. Therefore, a lookup table for the basin surface area is developed with the aid of a suitable Digital Elevation Model (DEM), to determine the new basin surface area (A_b) under a given sea-level condition.

Assuming there is no phase lag in tidal elevations within the systems (Dronkers (1964); a reasonable assumption for not-very-long estuaries), the ebb-tidal prism (P_T) corresponding to this new basin surface area can be calculated according to the relationship presented in Keulegan (1951).

$$P_T = A_b(2a_b) \quad [2-5]$$

where A_b is the surface area of the estuary and a_b is the mean tidal amplitude within the estuary.

Tidal inlets throughout the world exhibit several consistent relationships that have allowed coastal engineers and marine geologists to formulate predictive models. One such widely-known relationship is O'Brien's relationship between inlet channel cross-sectional area (a (ft²)) and tidal prism (P (ft³)) (O'Brien, 1969).

$$a = c_1 P^{c_2} \quad [2-6]$$

where c_1 and c_2 are empirical coefficients.

Thus, the inlet cross-sectional area could be changed to accommodate the changes in the tidal prism. According to Keulegan (1951), such changes in the inlet cross-sectional area could, however, also affect tidal attenuation characteristics in the inlet channel as attenuation is a function of the inlet-channel geometry.

Table 2 of Keulegan (1951) provides a lookup table for an expression (left-hand side of [2-7]), which includes the coefficient of repletion (K), basin surface area (A_b (ft²)), inlet channel cross-sectional area (a (ft²)) and oceanic tidal amplitude (H (ft)) for a given inlet-channel length (L_c (ft)), inlet-channel hydraulic radius (r (ft)) and Manning's roughness (n).

$$\frac{A_b K \sqrt{H}}{a} \times 10^{-4} = f(n, r, L_c) \quad [2-7]$$

This relationship allows determining the coefficient of repletion (K). The resulting tidal amplitude within the basin (a_b (ft)) can be computed according to the following equation [2-8].

$$\frac{a_b}{H} = \sin(\tau) \quad [2-8]$$

where $\sin(\tau)$ is a function of the coefficient of repletion (K), which can be determined through another lookup table (Table 4) provided in Keulegan (1951).

Use of the above computed tidal amplitude in [2-5] will result in a new tidal prism, which will result in different inlet cross-sectional area through O'Brien's relationship [2-6]. A new inlet cross-sectional area will have a different coefficient of repletion (K) and, thus a new tidal amplitude within the basin. Therefore, the above relationships are used iteratively, until the difference between two subsequent inlet cross-sectional area is less than 1% of the former value (Figure 2-2).

2.2.3 Change in Fluvial Sediment Supply

Climate change and anthropogenic activities could result in significant changes in the annual fluvial sediment volume (ΔQ_S (m³)) supplied to the coast (Palmer et al., 2008; Ranasinghe et al., 2019b; Syvitski, 2005; Vörösmarty et al., 2003). Subsequently, these changes would affect the total volume of sediment exchanged between the inlet-estuary system and its neighbouring coast (ΔV_{FS} (m³); Factor 3 in Figure 2-1) over the period

considered (t (in years)). The changes in fluvial sediment volume can be calculated as follows [2-9]:

$$\Delta V_{FS} = \int_0^t \Delta Q_S(t) dt \quad [2-9]$$

Assessment of fluvial sediment supply to coasts

Sediment generation and fluvial sediment throughput at catchment scale are affected by both climate change-driven impacts and anthropogenic activities (Section 1.2).

Bamunawala et al. (2018a) have illustrated that the empirical BQART model presented by Syvitski and Milliman (2007) can be used to assess the annual fluvial sediment supply to the coast, by considering both climate change-driven impacts and human activities. This empirical model is based on 488 globally-distributed datasets. For catchments with mean annual temperature greater than or equal to 2°C, the BQART model estimates the annual sediment volume (Q_S) supplied to the coast by the following equation [2-10]:

$$Q_S = \omega B Q^{0.31} A^{0.5} R T \quad [2-10]$$

where ω is 0.02 or 0.0006 for the sediment volume (Q_S), expressed in kg/s or MT/year, respectively, Q is the annual river discharge from the catchment considered (km^3/yr), A is the catchment area (km^2), R is the relief of the catchment (km), and T is the catchment-wide mean annual temperature (°C).

Term ‘B’ in the above equation [2-10] represents the catchment sediment production and comprises glacial erosion (I), catchment lithology (L) that accounts for its soil type and erodibility, a reservoir trapping-efficiency factor (T_E), and human-induced erosion factor (E_h), which is expressed as follows [2-11]:

$$B = IL(1 - T_E)E_h \quad [2-11]$$

Glacial erosion (I) in the above equation [2-11] is expressed as follows [2-12]:

$$I = 1 + (0.09A_g) \quad [2-12]$$

where A_g is the percentage of ice cover of the catchment area.

Syvitski and Milliman (2007) have indicated that the human-induced erosion factor (E_h ; anthropogenic factor) of the above equation [2-11] depends on land-use practices, socio-economic conditions and population density. In this study, E_h values were approximated by the Gross National Product (per capita) and population density. Based on the global dataset used, the optimum range of E_h was suggested as 0.3 to 2.0. Instead of using countrywide estimates of GNP/capita and population density to estimate the human-induced soil erosion factor (E_h), high-resolution spatial information published by the Wildlife Conservation Society - WCS and the Center for International Earth Science Information Network - CIESIN - of Columbia University in 2005 in the form of a human

footprint index (HFPI) can be used, so that the anthropogenic influences on sedimentation are better represented (Balthazar et al., 2013; Bamunawala et al., 2018a).

2.2.4 Reference climatic conditions for baseline simulations

The reduced-complexity modelling technique presented in Section 2.2 computes the total volume change in sediment exchange between the inlet-estuary systems and its adjacent coastline for the 2020-2100 period. In order to compute these future changes in total sediment exchange, first, baseline conditions need to be established. Since the model projections are for the 2020-2100 period, catchment-estuary-coastal conditions by 2019 were used to approximate the reference conditions in all sediment-volume computations. Similarly, all the future changes in sea level over the interval 2020-2100 were computed by using the 2019 mean sea level as the baseline for this study. Given that both mean annual temperature (T) and river discharge (Q) show significant inter-annual variability, use of the T and Q values specifically for the individual year 2019 would result in a biased representation of the reference conditions. Therefore, T and Q values of the last decade (2010-2019) were used to obtain the reference conditions for these variables in 2019.

2.3 Probabilistic assessment of change in total sediment volume exchange at barrier-estuary tidal inlets

The reduced-complexity modelling technique presented in Section 2.2 requires four input parameters for its simulations: annual mean temperature (T) and river discharge (Q), change in regional relative sea-level (ΔRSL), and a human-induced erosion factor (E_h). Use of unique sets of input parameters (for the reference and future periods) will provide deterministic projections of future changes in total volume exchange between the inlet-estuary systems and its adjacent coastline. Probabilistic assessments of the evolution of inlet-interrupted coasts are preferred over deterministic estimates so that the uncertainties associated with the shoreline projections can be quantified (described in Section 1.1). As the initial step in achieving this target, it is necessary to probabilistically determine the change in total sediment volume exchange at tidal inlets. This section presents the procedure used here for probabilistically estimating that change in sediment exchange between the estuary and its inlet-interrupted coast.

The logical sequence of the probabilistic modelling approach adopted is presented in Figure 2-3, followed by a description of the different computational steps involved.

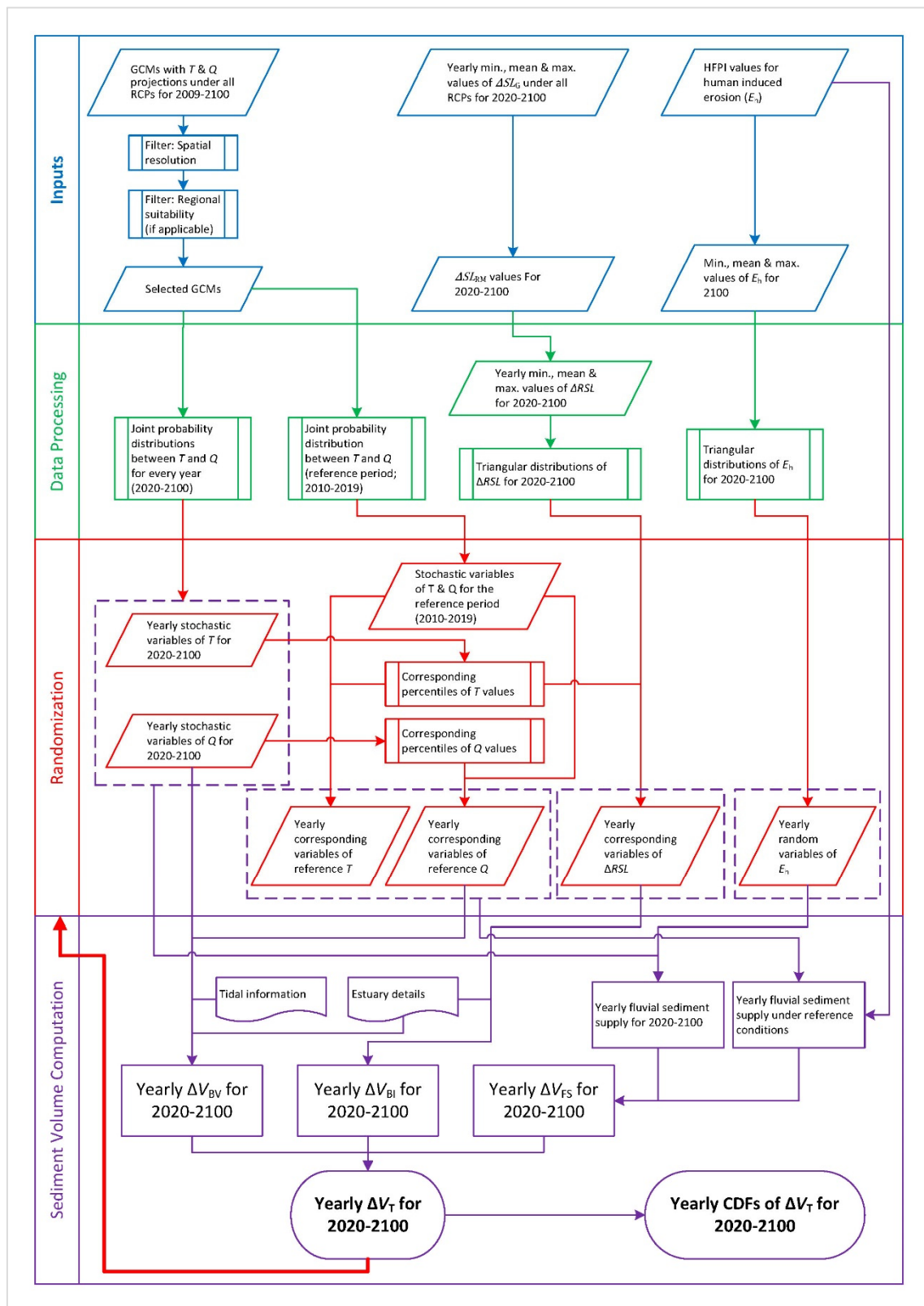


Figure 2-3: Flowchart of the proposed modelling approach of determining the change in total sediment volume exchange between a barrier-estuary system and its adjacent inlet-interrupted coast.

Step 1: Input data selection

The initial steps of this proposed probabilistic modelling framework consist of data source selection (blue coloured section of Figure 2-2). Temperature and run-off data for the 2009-2100 period (including the 2010-2019 reference period) was obtained from the General Circulation Models (GCMs) available from the Coupled Model Intercomparison Project Phase 5 (CMIP5 data portal; Earth System Grid-Centre for Enabling Technologies (ESG-CET); available on the webpage <http://pcmdi9.llnl.gov/>). Projected daily/monthly values of temperature and surface runoff were obtained for the all four Representative Concentration Pathways (RCPs) of applicable GCMs. Initially, the GCMs with both temperature and surface runoff projections for all RCPs over the 2020-2100 period were considered as data sources. Out of the above-considered data sources, GCMs with spatial resolution finer than 2.5° were selected to obtain the necessary climate inputs (T and Q). If available, the suitability of the above-selected data sources was assessed regionally, by considering the guidelines published on the suitability of GCMs in respective areas (e.g., CSIRO and Bureau of Meteorology (2015) for Australia).

Yearly minimum, mean, and maximum values of global sea-level change (ΔSL_G) were calculated according to the method presented in Section 1.4.2 (equation [1-1]). Intermediate values of the cumulative contribution of ΔSL_{RM} , ΔSL_{RG} , and partly ΔSL_{VLM} were approximated according to the method adopted by Mehvar et al. (2016), where the temporal variation was assumed to vary linearly from 2000 to 2100. Use of these interpolated values and the intermediate global sea-level changes computed from equation [1-1] provided the projected maximum, mean and minimum regional relative sea-level changes at any given location for the period 2000-2100.

The human-induced erosion factor (E_h), which contributes to catchment scale sediment generation is here represented via the Human FootPrint Index (HFPI). HFPI values within the catchment were rescaled linearly to fit the optimum scale of E_h suggested by Syvitski and Milliman (2007). These rescaled HFPI values were then averaged over the catchment to determine a representative factor for human-induced erosion (E_h). Given the contemporary rate of population growth and urbanization, it is safe to assume that E_h will have increased by 2100. Owing to numerous uncertainties associated in such projections (e.g., Veerbeek (2017)), the increment of E_h by 2100 was assumed to follow a triangular distribution with a mean, minimum and maximum of respectively 15, 10 and 20 percent of its present-day values.

Step 2: Data processing

The next step of the proposed modelling framework involves data preparation (green colour section of Figure 2-2). Precipitation, evapotranspiration, and runoff are the main components of the total water budget at the catchment scale, with temperature,

evapotranspiration, and precipitation being closely correlated parameters. In order to capture the correlation between T and Q , joint probability distributions were generated for every year between 2020 and 2100 to determine the annual mean temperature and cumulative runoff values at the catchment scale. Joint probability distributions for 2020-2100 period were created by the use of annual mean temperature and cumulative runoff values obtained from the selected GCMs. A joint probability distribution of T and Q for the reference conditions was also generated by the use of annual mean temperature and cumulative surface runoff values for the 2010-2019 period. These T and Q values over the reference period were also obtained from the above selected GCMs.

The yearly values of ΔRSL were used to fit triangular distributions to represent ΔRSL for each year (2020-2100). The above-adopted minimum, mean, and maximum increments of the human-induced erosion factor (E_h) by 2100 were assumed to increase linearly from 2020. Based on these values, triangular distributions were fitted to represent yearly E_h values for the interval 2020-2100.

It should be noted that the Human activities that may exert changes to the natural environment vary on various dimensions (e.g., population growth, urbanization, and economic development). However, it is (almost) certain that the population and extent of the urbanized area would only increase over the 21st century. Therefore, it is reasonable to assume increments in HFPI by 2100. The underlying objective of the adopted linearly increasing, triangular distributions of HFPI is to accommodate the above trends and uncertainties in the proposed modelling framework. Use of different methods of translating present-day HFPI into the future will almost certainly result in different projections of fluvial sediment supply from the river catchment. Future studies that look into the details of socio-economic growth of the societies may provide detailed representations of this increased human-induced impacts on the environment, but taking this aspect into account was not possible within this study due to time constraints.

Step 3: Generating stochastic model inputs

The third stage of the proposed probabilistic modelling framework is related to generating the stochastic model input for temperature, runoff, regional relative sea-level change, and the human-induced erosion factor (i.e., Randomization; red colour section of Figure 2-2). The fitted joint probability distributions for T and Q for were then used to generate stochastic model inputs for temperature and runoff for each year of the study period (2020-2100) considered (as described above). Percentiles of each of the T and Q values over the period 2020-2100 were calculated for every year so that the reference temperature and runoff values could be related to the same probability of occurrence. Stochastic input values of T and Q for the reference period (2010-2019) were generated from the fitted joint probability distribution (as described above). These reference values and the above-

computed percentile values of temperature and runoff for 2020-2100 were then used to determine the reference T and Q values for each year with the same probability of occurrence (i.e., same percentiles).

Two significant causes of global sea-level rise are thermal expansion caused by warming of the oceans and increased melting of land-based ice, such as glaciers and ice sheets (Stocker et al., 2013b). Both of these factors are directly related to increasing temperature. Therefore, in all the model applications, a direct relationship was assumed between annual mean temperatures (T) and change in regional relative sea-level (ΔRSL). In order to achieve this direct relationship, percentiles of each annual mean temperature value obtained through the fitted joint probability models (as described above) were calculated. Fitted triangular distributions that represent the regional relative sea-level change (ΔRSL) for each year between 2020 and 2100 were used in conjunction with the above-computed percentiles of annual mean temperature values to generate stochastic variables of ΔRSL for the period 2020-2100.

Fitted triangular distributions that represent the human-induced erosion factor (E_h) were used to generate stochastic variables of E_h for 2020-2100.

Step 4: Computing sediment volumes

All the above computed stochastic model input and other corresponding model inputs were then used in the final phase of the proposed probabilistic modelling framework to determine the change in total sediment volume exchange (ΔV_T) between the mainland barrier estuaries and their adjacent inlet-interrupted coasts (i.e., Sediment volume computation; purple colour section of Figure 2-3). The above-computed future and reference stochastic variables of runoff values and the corresponding estuarine and tidal information were used to calculate the variations in sediment volume due to changes in basin volume (ΔV_{BV} ; equation [2-3]) over the interval 2020-2100. Stochastic variables of regional changes in relative sea-level were used together with the relevant estuarine information to determine the sediment volume demands due to basin infilling (ΔV_{BI} ; equation [2-2]) for 2020-2100 period. Changes in fluvial sediment supply (ΔV_{FS}) were computed by the use of stochastic model input of future and reference T and Q values, stochastic variables of the human-induced erosion factor, and other corresponding river catchment information in equation [2-10]. These three sediment volume components were then used in equation [2-1] to determine the total change in sediment volume exchange. These values were used to obtain the empirical cumulative distributions of the change in total sediment volume exchange (ΔV_T) for each of the years over the 2020-2100 period.

A selected percentile value of this ΔV_T was used to determine the subsequent coastline change along the inlet-interrupted coasts as described in Section 2.4.

2.4 Determining the coastline change along inlet-interrupted coastlines

Changes in the total sediment volume exchange between barrier estuaries and their adjacent inlet-interrupted coasts will result in coastline recession or progradation (as described in Section 2.2). The extent and magnitude of such variations are closely related to the concurrent wave/current conditions and alongshore sediment transport capacity in the vicinity. Many studies have indicated that potential climate-change impacts during the 21st century may result in changing mean wave conditions across the oceans (Casas-Prat et al., 2018; Hemer et al., 2013; Mori et al., 2010; Morim et al., 2019; Semedo et al., 2013). Such changes in wave conditions could result in variations in longshore sediment transport rates (and gradients therein), which may subsequently affect the extent and magnitude of coastline change along inlet-interrupted coasts.

However, all available wave projections only provide mean changes of wave conditions (i.e., not for individual RCPs) over the last two/three decades of the 21st century (i.e., not for the entire 21st century). Therefore, in this study, which considers all RCPs over the entire 21st century, it is assumed that the ambient rates of longshore sediment transport remain invariant throughout the 21st century. Thus, the projected changes in coastlines are computed based on the current longshore sediment transport rates. The conceptual framework used to compute the spatio-temporal variations of inlet-affected coastlines is described in the following sections.

2.4.1 Inlet-affected coastline lengths

The maximum extent of inlet-affected coastline in both up-drift and down-drift directions from a given inlet-estuary system is confined by the existence of headlands, rock outcrops or by a prominent change in mean shoreline orientation. Following the method adopted in the SMIC applications by Ranasinghe et al. (2013), the maximum extent of this inlet-affected coastline distance was considered to be ~25km. If there is no known gradient in the net annual alongshore sediment transport rate along the coastline (i.e., both up- and down-drift directional coastline from the inlet), it can be assumed that the coastal cell (i.e., estuary-coastal system) is presently in equilibrium at annual time scales.

First, to decide whether the inlet-interrupted coastline will recede or prograde, the sign of the change in total sediment volume exchange between the estuary and coast is considered. A positive volume means that the inlet-estuary system would export its excess sediment volume to the coast, which would result in coastline progradation. If the net change in total sediment volume exchange is negative, the inlet-estuary system would import sand from its adjacent coasts, (in the absence of prominent ebb deltas, a necessary assumption made in this study), resulting in coastal recession. However, both the extent and magnitude of coastal recession adjacent to a sediment-importing system is also a

function of the difference between the magnitudes of net longshore sediment transport (LST) and the sediment demand by the estuary system.

Here, three different forms of coastline behaviour are considered:

- Type A: Coastline change under a positive sediment budget (Figure 2-4)
- Type B: Coastline change under a negative sediment budget, which is smaller than the net annual longshore sediment transport capacity (Figure 2-5)
- Type C: Coastline change under a negative sediment budget, which is larger than the annual longshore sediment transport capacity (Figure 2-6)



Figure 2-4: Conceptual framework for distributing a positive sediment budget. V_0 is the net longshore sediment transport capacity, V_1 is the sediment volume supplied to the coast by the inlet-estuary system, the dotted black line is the initial coastline position, light brown lines indicate the final coastline position.

Under the first category, an inlet-estuary system will annually provide a certain amount of sediment (V_1) to the coast. In order to maintain the equilibrium of the coastal cell, this additional sediment volume should be distributed along the coast, eliminating the imbalances of the system. Distribution of this sediment would occur along the down-drift coastline, which in turn would result in a certain amount of coastal progradation, as shown in Figure 2-4.



Figure 2-5: Conceptual framework for distributing a negative sediment budget (case 1). V_0 is the net longshore sediment transport capacity, $V_1 (< V_0$ in magnitude) is the sediment volume demand from the inlet-estuary system, the dotted black line is the initial coastline position, light brown lines indicate the final coastline position.

In the other two scenarios, the inlet-estuary system annually imports a particular sediment volume from the coast. Conceptualizing the mechanism of subsequent coastline recession due to this sediment import is closely tied to the net Longshore Sediment Transport (LST) capacity along the adjacent coast. If the ambient longshore sediment transport capacity is greater than or equal to the volume of sediment demanded by the estuary, LST will supply the total sediment volume demanded by the inlet-estuary system. Thus, the inlet acts as a sink for the ambient LST and will, therefore, create a deficit in longshore sediment transferred along the down-drift coast (i.e., LST up-drift of inlet $>$ LST down-drift of inlet). Given that the coastal cell containing the inlet is considered to be in equilibrium with no gradient in longshore sediment transport rate, the system would strive to achieve its equilibrium by eroding sand from its down-drift coast, resulting in coastal recession near the inlet (Figure 2-5). The annual erosion along the down-drift coast will be restricted by the annual longshore sediment transport capacity, where the maximum possible coastal recession would correspond with the net annual longshore sediment transport capacity (in the absence of any sediment supply from ebb deltas or farther offshore).

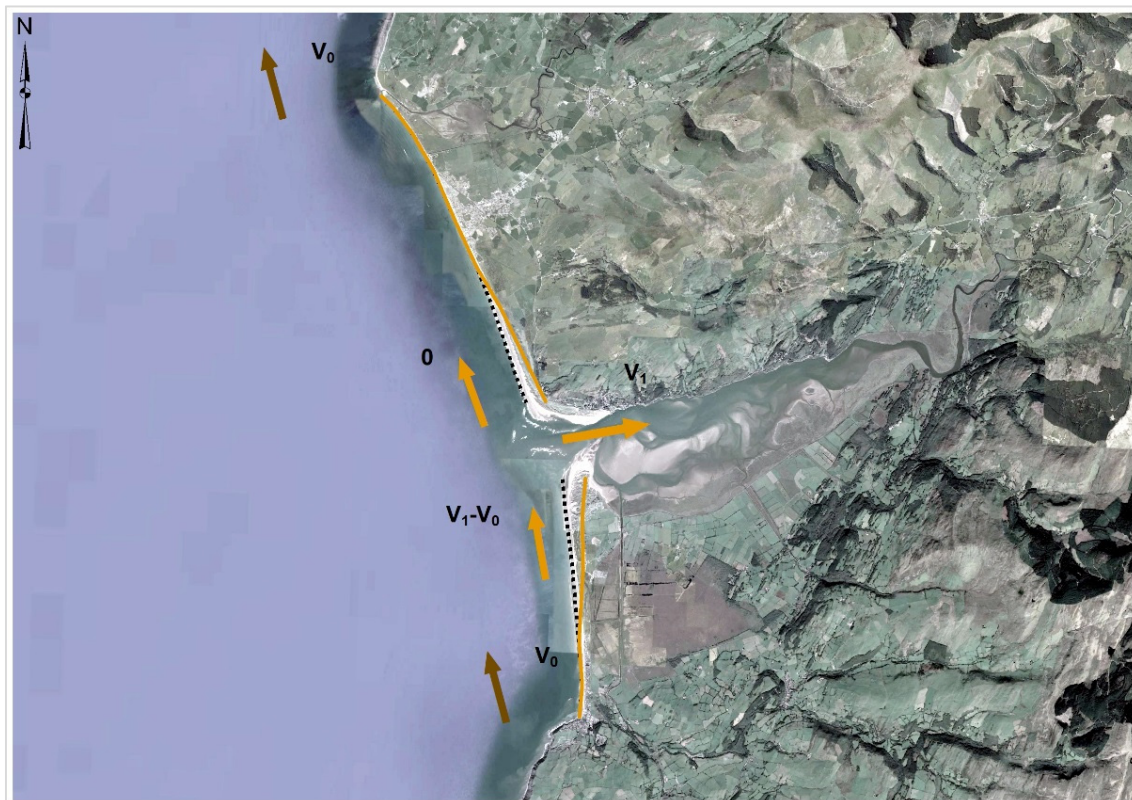


Figure 2-6: Conceptual framework for distributing a negative sediment budget (case 2). V_0 is the net longshore sediment transport capacity, $V_1 (> V_0$ in magnitude) is the sediment volume demand from the inlet-estuary system, the dotted black line is the initial coastline position, light brown lines indicate the final coastline position.

Longshore sediment transport alone would not be sufficient to fulfil the total volume of sediment demanded by an inlet-estuary system in situations where the yearly demand by the estuary is larger than the net annual longshore sediment transport capacity. In such situations, erosion along the down-drift coast would be constrained to the aforementioned maximum possible extent. The deficit sediment volume ($|V_1 - V_0|$) required by the estuary may be taken from the up-drift coast, which would result in coastline erosion along the up-drift coast as well (Figure 2-6).

2.4.2 Alongshore variable coastline change estimation

Once the type of the inlet-affected coast(s) is identified (i.e., Type A, B, or C), it is necessary to determine the alongshore variability of the coastline(s). This can be achieved by the use of a suitable coastline model. Generally, coastline models invoke the assumption of invariant cross-shore profile (usually the area between the top of the dune to the depth of closure) (Larson et al., 1987; Roelvink and Reniers, 2011). Out of many such models currently available (e.g., GENESIS, LITPACK, UNIBEST-LT/CL, BEACHPLAN), selection of a suitable technique is subjected to the spatial and temporal

scales considered, availability of necessary data, and the desired output accuracy (Roelvink and Reniers, 2011).

Following the overarching objective of this study (Section 1.6), a simplified framework of a generically applicable coastline model that provides first-order estimates of coastline variations at macro time scales was developed and presented herewith. This framework only represents the general changes of the inlet-affected coastline by considering the total change in sediment volume exchange between the inlet-estuary system and its adjacent coast (Section 2.2), while assuming uniform shoreline orientations along up- and down-drift coasts and the lack of any coastal structures.

One-line model

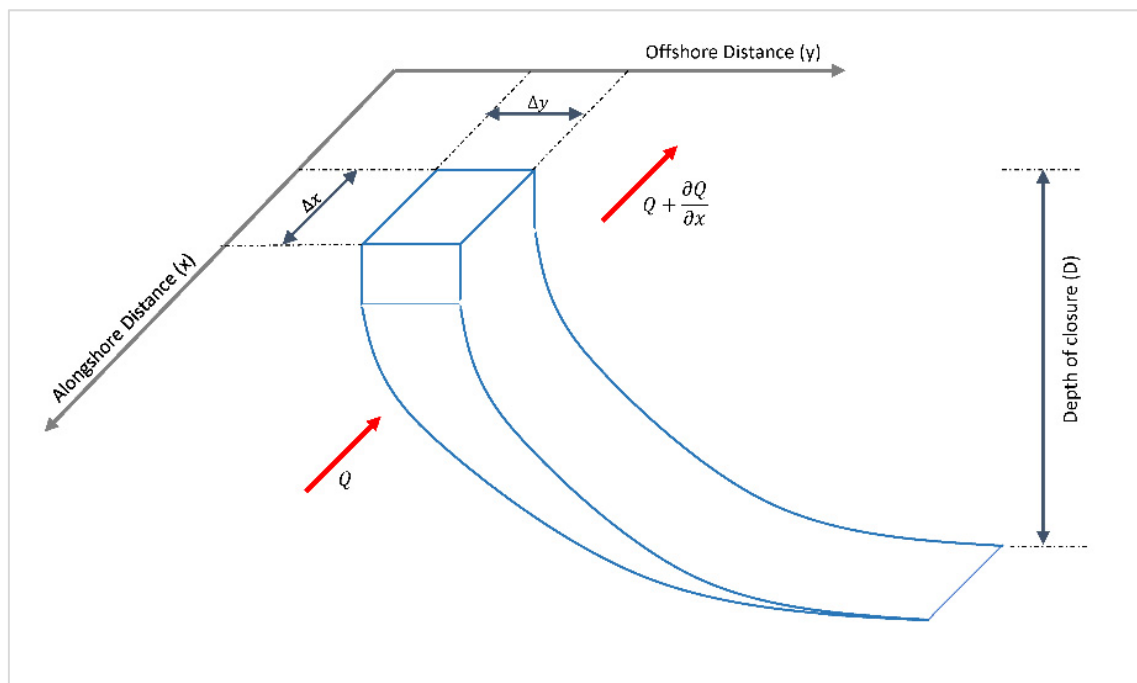


Figure 2-7: Schematic illustration of a hypothetical equilibrium cross-shore profile

Within the development of this simplified model, it is assumed that the longshore sediment transport occurs uniformly over the entire cross-shore profile. Figure 2-7 illustrates the hypothetical equilibrium cross-shore profile. Given that the change in total sediment volume exchange (ΔV_T) was computed annually, that sediment volume was then divided into a number of equal fragments so that the resulting coastline change can be computed. This volume fragment ($V_{fr} = \frac{\Delta V_T}{n_v}$) was then distributed along the respective coastline(s). Depending on the equivalent longshore transport capacity ($\Delta Q_{LST} = \frac{Q_{LST}}{n_v}$), all or part of this volume fragment is transported along the coast. Following the assumption of a balanced sediment budget within the coastal cell, any volume of sediment that gets transported in the down-drift direction will result in coastal progradation at the farthestmost

section of the down-drift coast. If the volume fragment is larger than the equivalent longshore transport capacity (ΔQ_{LST}), the deficit volume ($\Delta V = V_{fr} - \Delta Q_{LST}$) will result in changing the coastline position (Δy) within the considered alongshore distance (Δx) (Figure 2-7). Assuming that the shoreline moves cross-shore parallel to itself while maintaining its equilibrium profile, the following relationship [2-13] can be derived to determine the resulting change in coastline position (Δy).

$$\min(\Delta V, V_{fr}) = \Delta x(D\Delta y) \quad [2-13]$$

where D is the depth of closure.

The above procedure is repeated n_v times, so that the total change in sediment volume exchange between the estuary and adjacent coast (ΔV_T) is fully distributed. These computations are closely related with an expression to represent the longshore sediment transport rate, which, in turn, is closely related to the longshore current generated by the breaking waves that are obliquely incident to the shoreline. This can be presented as the following [2-14]:

$$Q_{LST} = Q_0 \sin(2\alpha_b) \quad [2-14]$$

where Q_0 is the amplitude of the longshore sediment transport rate (m^3/yr), and α_b is the breaking wave angle, which can be expressed as the following under small-angle approximation.

$$\alpha_b = \alpha_0 - \frac{\Delta y}{\Delta x} \quad [2-15]$$

where α_0 (rad) is the angle of breaking wave crests.

Since the local coastline position (Δy) would be updated with the distribution of each volume fragment, breaking wave angle (α_b) and subsequent longshore sediment transport rate (Q_{LST}) are also updated after completion of the distribution of each volume fragment.

If the information on initial longshore sediment transport rate and the corresponding angle of breaking wave crest (α_0) is available, the above-described procedure (i.e., description under *One-line model*) can be implemented to determine the spatial variation of up- and down-drift coastlines. If such information is not available, the amplitude of longshore sediment transport rate (Q_0) and the angle of breaking wave crest (α_0) can be computed based on the respective coastal environmental conditions, which are described in the following sub-sections.

Computing longshore sediment transport potential

There are numerous methods available to compute the longshore sediment transport rate, which includes both process-based modelling approaches and empirical transport formulas. Process-based modelling approaches incorporate a variety of coastal processes in determining the longshore sediment transport rate, but they demand a large number of

input parameters and case-specific calibration. Bulk longshore sediment transport equations (e.g., the CERC formula (CERC, 1984), the Kamphuis formula (Kamphuis, 1991), and the Bayram formula (Bayram et al., 2007)) can provide reasonable estimates of longshore sediment transport rates with a limited number of input parameters (Mil-Homens et al., 2013). In this study, the formulation from the US Army corps, Coastal Engineering Research Centre (CERC), published in the Shore Protection Manual (1984) is used to compute the longshore sediment transport potential [2-16].

$$Q_0 = \frac{0.77\sqrt{g}}{32 \times (1-p) \times \left(\frac{\rho_s}{\rho} - 1\right) \times \sqrt{\gamma_b}} \times H_{sb}^{2.5} \quad [2-16]$$

where H_{sb} is the significant wave height at breaker line (m), γ_b is the breaking parameter for irregular waves (0.55), ρ_s is the density of sand ($\cong 2,650 \text{ kg/m}^3$), ρ is the density of seawater ($\cong 1,030 \text{ kg/m}^3$), p is the porosity of sand (0.4), and g is the gravitational acceleration (9.81 m/s^2).

The CERC formula was selected in this study because it requires the least number of site-specific input parameters to calculate the longshore sediment transport potential (which will become essential in the global application of the model presented in Chapter 4).

Determining representative breaking wave parameters

The above-described computation of longshore sediment transport potential requires representative (schematized) breaking-wave parameters of the location considered. A schematized wave condition should be able to replicate comparable sediment transportation capabilities by reproducing a similar longshore sediment transport capacity as the full-wave conditions (Dastgheib, 2012; Lesser, 2009). In this study, the following method was used to schematize the wave conditions.

The schematization of the waves starts with a manual discretization of deep-water wave climate into a number of height classes and directional bins. Following the principle of computing the longshore sediment transport potential mentioned above [2-16], the representative wave height of each bin is calculated according to the following relationship [2-17].

$$H_{s,rep} = \left(\frac{\sum P_i H_s^{2.5}}{\sum P_i} \right)^{1/2.5} \quad [2-17]$$

where $H_{s,rep}$ is the representative significant wave height of the directional bin considered (m), P_i is the probability of wave height classes in the directional bin considered, and H_s is the significant wave height of waves within each height class (m).

The representative wave direction and period are calculated according to the following equations:

$$dir_{rep} = \frac{\sum dir_j}{\sum n_i} \quad [2-18]$$

$$T_{rep} = \frac{\sum T_j}{\sum n_i} \quad [2-19]$$

where dir_j and T_j represent wave direction and period within the selected bin, respectively, and n_i is the number of waves within each wave height class of the selected bin.

The above-identified representative wave condition is then transferred to its breaking point by using linear wave theory. This transformation provides the necessary inputs (breaking wave height (H_{sb}) and the angle of breaking wave crest (α_0)) to compute the longshore sediment transport rate using the equation [2-16].

2.4.3 Determining the final coastline position

In addition to the above-described coastline change due to variation in total sediment volume exchange between the estuary and its adjacent coast, sea-level, if not compensated by sediment supply, will shift the active cross-shore profile upward and landward, which results in coastal recession as well (Bruun, 1962). The magnitude of the above coastal recession is expressed according to equation [2-20] as follows:

$$\Delta C_{BE} = \frac{\Delta RSL}{\tan(\beta)} \quad [2-20]$$

where ΔC_{BE} is the resulting coastal recession (m), ΔRSL is the sea-level rise (m), and β is the slope of the active beach profile.

This simple two-dimensional model of shoreline response to sea-level rise has been widely applied since its inception. However, the validity and accuracy of its estimations have been debated by numerous researchers (e.g., Cooper and Pilkey (2004); Ranasinghe et al. (2012); Ranasinghe and Stive (2009)).

In this study, a selected percentile of change in total sediment volume exchange (ΔV_T) between the estuary and its adjacent coast was used to determine the changes along the inlet-affected coastline. Therefore, the same percentile of sea-level rise was used in the above equation [2-20] to determine the coastal recession due to the Bruun effect. The final coastline position was obtained by superimposing the Bruun-estimated coastal recession on the computed coastline evolution driven from the change in total sediment volume exchange (ΔV_T) between the estuary and the coast. A flowchart of this modelling approach to determine the final coastline position is shown in Figure 2-8.

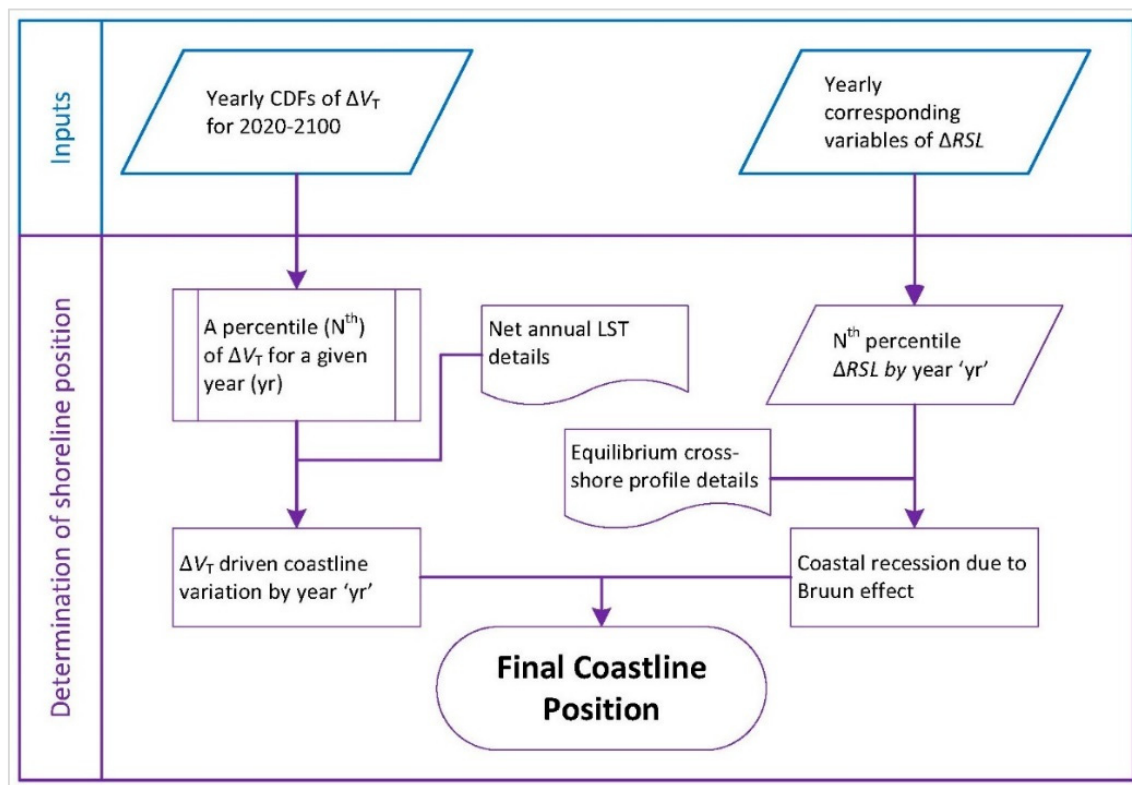


Figure 2-8: Flowchart of the conceptual modelling framework for determining the final coastline position along inlet-interrupted coastlines. Note: Yearly empirical cumulative distributions (CDFs) are obtained from the resulting sediment volume computations (as explained under Section 2.3; Step 4: Computing sediment volumes).

2.5 Modelling future changes in barrier island coastlines

Evolution of barrier islands under the influence of both climate change and anthropogenic influences at macro time scales is based on the concepts of sediment conservation and invariant shoreface and barrier profiles. This is similar to the concepts adopted in the numerical model presented by Moore et al. (2007) and Stolper et al. (2005), in which the initial equilibrium barrier island morphology is assumed to maintain its vertical position with respect to rising sea level. Given the macro (50-100 years) time scales considered in this study and an adequate sand volume to maintain their volume and profile, it is assumed that barrier islands would eventually recover from the impact of episodic events such as storm surges, extreme waves and winds.

As a first step of the modelling framework, it is necessary to identify an initial equilibrium barrier island profile(s) that can adequately represent the average conditions of the study area. Once this equilibrium profile is identified, it is possible to determine the initial barrier island profile volume (V_{BIP-i} in m^3/m), which provides the basis to compute future equilibrium barrier profile volume(s) under climate change impacts and anthropogenic activities (Figure 2-9).

According to the time scales considered in this study, the sea-level rise-driven accommodation space requirement and if applicable, the variation in fluvial sediment supply, are the most prominent factors that affect the equilibrium barrier island profile volume. Computation of the sediment demand due to basin infilling (ΔV_{BI}) at barrier island systems could be done in the same way as for mainland inlet-estuary systems (Eq. [2-2] in Section 2.2.1). If a prominent fluvial sediment source is present in its vicinity, the future changes in fluvial sediment supply could also be computed in the same way as for mainland inlet-estuary systems (Eq. [2-9] to [2-12] in Section 2.2.3).

Another primary source of sediment that contributes to the evolution of barrier island systems is the longshore sediment drift. Following the assumptions made in Section 2.4, the ambient longshore sediment drift is assumed to remain invariant throughout the entire future period considered. Thus, the contemporary gradient in longshore sediment transport at the barrier island system provides the marine sediment inputs (V_{LST}) to the overall sediment budget, which can be expressed as:

$$V_{BIP-f} = V_{BIP-i} - \left(\frac{V_{BI} - nV_{LST}}{L_{BIS}} \right) \quad [2-21]$$

where V_{BIP-f} is the final barrier island profile volume (m^3/m), V_{LST} is the marine sediment supply from the existing longshore sediment transport gradient (m^3/yr), n is the number of years, and L_{BIS} is the length of the barrier island (m).

Equation [2-21] can be used to determine barrier island volume at future time step(s). This final volume is passed to a lookup table containing barrier island profile volumes, computed at different barrier crest positions. The lookup table is composed by considering the initial equilibrium barrier profile and the mean underlying substrate slope over which the barrier island migrates. The vertical and horizontal resolutions of this lookup table are kept at reasonably fine (0.01 m, and 10 m, respectively) so that the final barrier position could be determined accurately.

The principle of using the lookup table mentioned above is that the equilibrium barrier island morphology is assumed to maintain its vertical position with respect to the rising sea level. Thus, if the considered magnitude of regional relative sea-level change is known, the vertical position of the barrier island can be determined. This provides the vertical grid position of the lookup table. The model then searches for the most suitable V_{BIP-f} along the horizontal grid points of the lookup table and interpolates (if necessary) to determine the final horizontal position of the barrier island profile (Figure 2-10).

However, cross-shore migration of barrier islands is restricted by an applicable maximum barrier-migration rate. The maximum barrier-migration rate (m/yr) is a site-specific value, which mostly depends on the size and the width of the equilibrium barrier island profile. Barrier island systems with larger volumes (m^3/m) will have less mobility (in terms of barrier migration rate), because more energy is required to transport the larger sediment volumes cross-shore. This maximum barrier migration rate can be differentiated with

respect to the system width, because of the difference in energy required to transport the sediment eroded from its shoreface to the back-barrier area. In addition to the aforementioned factors, aeolian transport also contributes to the reduction of the mobility of barrier islands by adding more sand to the system (Morton and Miller, 2005; Twichell et al., 2013).

Consequently, the maximum migration rate applies a threshold to the possible barrier movement. Thus, the model subsequently performs a check to determine whether the migration distances computed above would displace the barrier island beyond the acceptable threshold of migration over a given period. If the threshold is exceeded, then the model forces the barrier profile to reduce its freeboard, so that the new equilibrium position will be at a reduced vertical position with respect to the new sea level. To enable this reduction of the vertical position of the barrier island crest, the lookup table is used (via a search routine) at different vertical grid positions to determine the new horizontal position of the barrier island that does not exceed the applied maximum barrier-migration threshold (Figure 2-11).

Figures 2-9 to 2-11 illustrate the above-described computation sequence of barrier island evolution. Figure 2-9 shows an initial equilibrium barrier-island profile (i.e., the hatched area) and its freeboard (H_0) under present-day sea level (blue line). This equilibrium profile is used to calculate the initial barrier island profile volume (V_{BIP-i} in m^3/m).

Figure 2-10 shows the barrier migration under future sea-level conditions (solid blue line). This new cross-shore position of the barrier-island profile is shown by the solid red line. The barrier island maintains its initial freeboard (H_0) by freely migrating in the landward direction. Initial sea level and barrier island profile are shown in dashed red and black lines, respectively.

Figure 2-11 shows the final equilibrium barrier island profile (green line) after restricting its cross-shore migration distance under the maximum barrier-migration threshold concept. The figure also indicates the final barrier freeboard (H_1), which is less than its initial value (H_0). This reduction in barrier freeboard (i.e., H_0-H_1) is forced by the model to accommodate the applicable maximum barrier-migration threshold. The figure also indicates the reduced barrier-migration distance due to the application of the threshold for maximum migration. Initial sea level and the barrier island profile are indicated by dashed blue and black lines, respectively. The intermediate position of the barrier island is shown by the dashed red line.

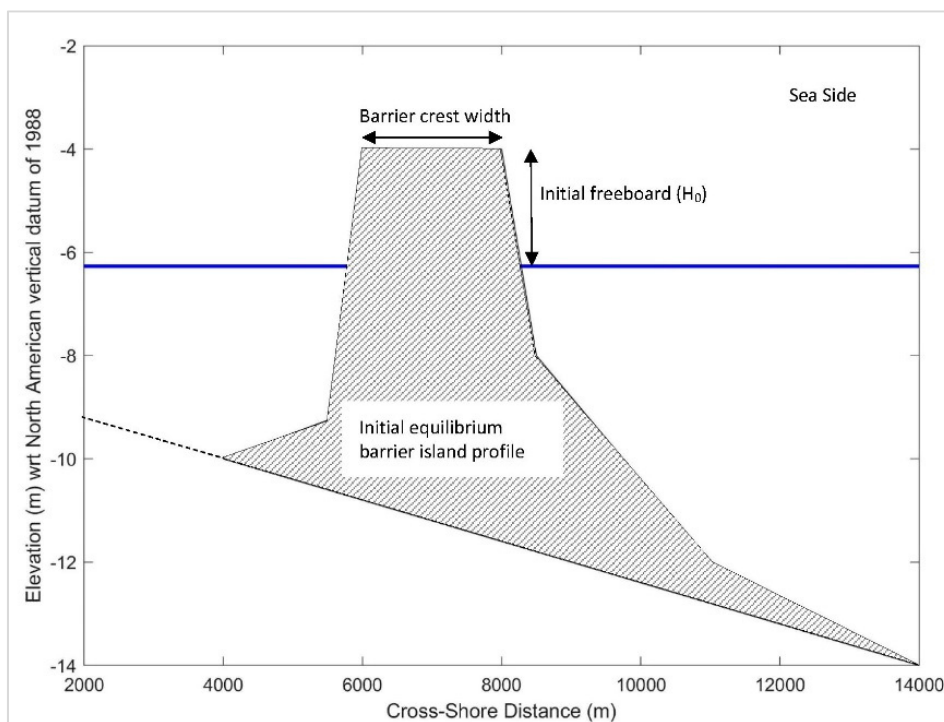


Figure 2-9: An illustrative plot of the Initial equilibrium barrier island profile and the present-day sea level. The hatched area indicates the equilibrium barrier island profile, while the present-day sea level is indicated by the blue line.

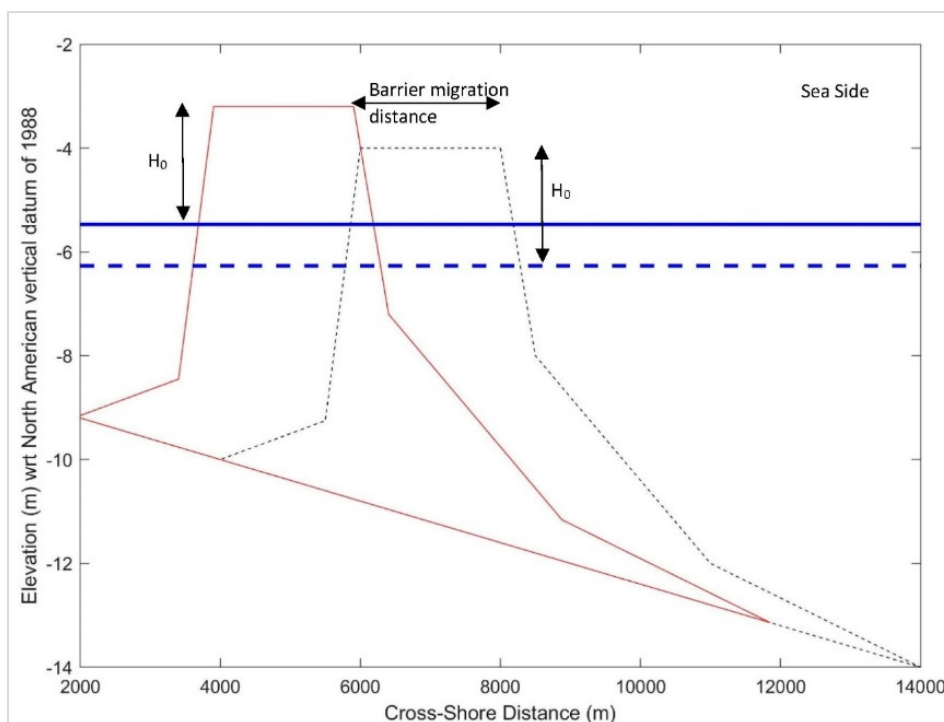


Figure 2-10: An illustrative plot of the intermediate barrier island profile under future sea-level conditions (computed without a threshold on maximum barrier migration rate). Initial and future barrier island profiles are indicated by the dashed black line and solid red line, respectively. H_0 is the initial barrier freeboard (maintained under future sea level). Initial and future sea levels are indicated in dashed and solid blue lines, respectively.

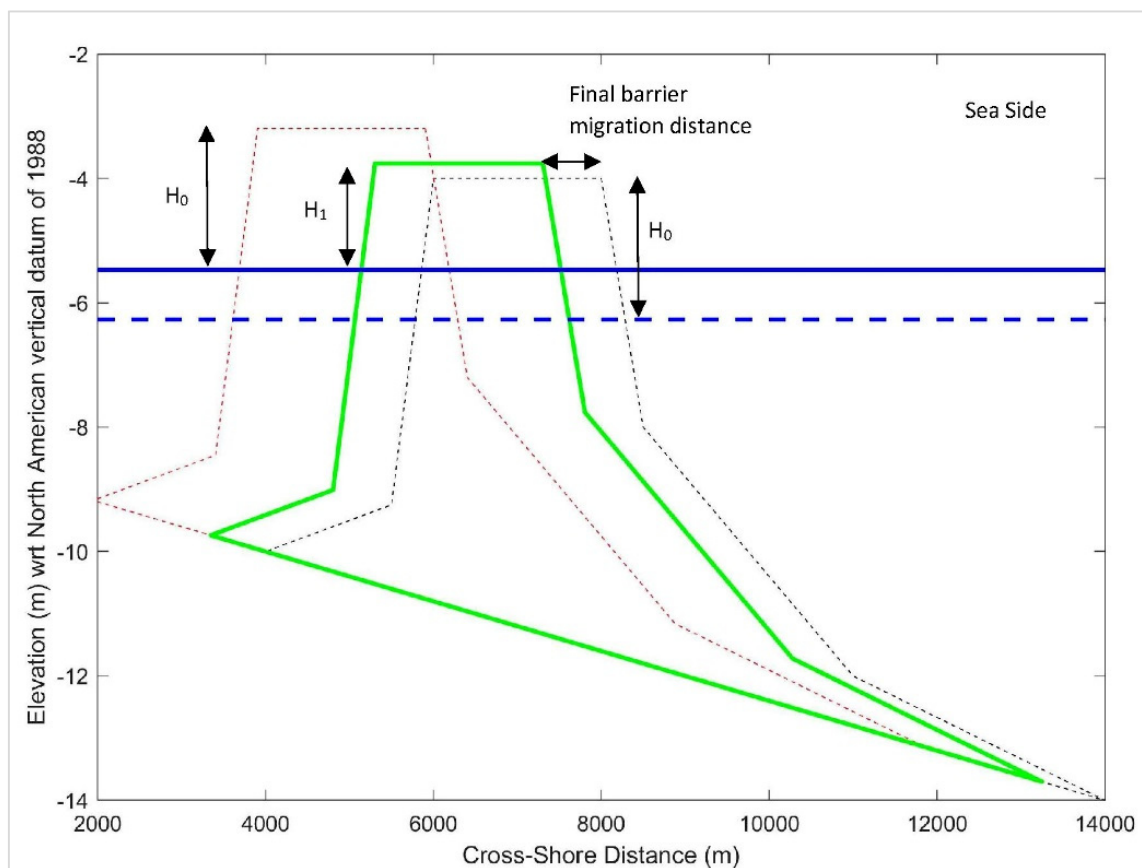


Figure 2-11: An illustrative plot of the final barrier island profile under future sea-level conditions (computed with a threshold on maximum barrier migration rate). Initial, intermediate and final barrier island profiles are indicated by dashed black, dashed red, and solid green lines, respectively. H_0 and H_1 are the initial and future barrier freeboard, respectively. Initial and future sea levels are indicated by dashed and solid blue lines, respectively.

2.6 Probabilistic assessment of future changes in barrier island coastlines

The modelling approach described in Section 2.5 requires initial barrier island characteristics and three model inputs: (1) regional relative change in sea level (ΔRSL), (2) maximum barrier island migration rate, and (3) marine sediment availability (and other applicable sediment sources/sink data) to simulate the future evolution of the barrier island. Use of unique sets of model inputs will provide deterministic predictions of future changes in barrier islands. Probabilistic assessments of the evolution of inlet-interrupted coasts are preferred over deterministic estimates, which provide essential inputs to coastal zone planners and managers by quantifying the uncertainties associated with the projected coastline changes (described in Section 1.1).

The flowchart of the proposed probabilistic modelling framework that simulates the future changes in barrier islands is shown in Figure 2-12, followed by the descriptions of the different computational steps involved in it.

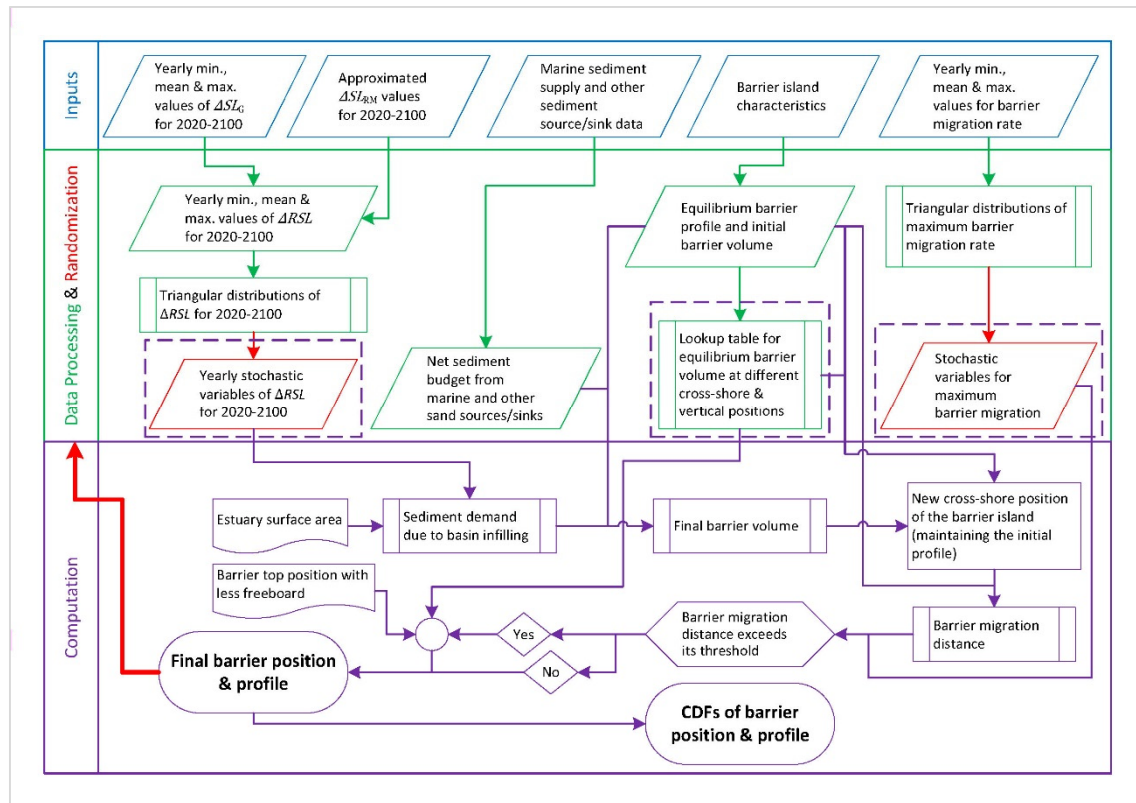


Figure 2-12: Flowchart of the proposed probabilistic modelling framework to determine future changes in barrier islands

The first step of the proposed modelling approach is the identification of data sources and the initial equilibrium barrier-island profile. Stochastic model inputs of regional relative sea-level change (ΔRSL) were computed according to the same method described in Section 2.4, in which triangular distributions were fitted to represent the yearly ΔRSL values for the 2020-2100 period. The net sediment volume that contributes to the final barrier island volume was calculated based on the marine sediment supply to longshore sediment transport (LST) gradients and other applicable sediment sinks/source data. If a prominent fluvial sediment source is available, the future changes in fluvial sediment supply could also be computed according to the methods adopted for the mainland inlet-estuary systems (described in Section 2.4). Initial barrier volume and the lookup table of equilibrium barrier volume were computed based on the initial barrier island characteristics. Stochastic model inputs for maximum barrier-migration rate were generated from the fitted triangular distribution that represents the applicable yearly barrier migration distances. This triangular distribution was fitted using approximated

values of minimum, mean, and maximum barrier migration rates for a given case study site.

Final barrier island volume values were computed by the use of above generated stochastic model inputs of ΔRSL , available marine sediment volume, and the initial barrier island volume (equation [2-21]). Then the potential cross-shore positions of the barrier island were determined according to the method described in Section 2.5. The fitted triangular distribution of maximum barrier-migration rates was used to generate potential maximum barrier-migration distances. These stochastic model inputs of maximum barrier migration rate were used to determine whether the above computed horizontal positions have exceeded the applicable threshold for migration distance. For those instances where the barrier migration threshold was found to be exceeded, new equilibrium positions of the barrier island were computed following the method described in Section 2.5.

2.7 Model hindcasts for the 1986-2005 period

As a model validation exercise, the above-presented modelling technique was applied to a historical period (1986-2005) to compare the model hindcasts with observed shoreline change at the studied mainland barrier estuary systems. To achieve this objective, the following simplifications were made when obtaining the model inputs/reference conditions.

- For the historical period (1986-2005), an ensemble of GCMs was used to obtain the yearly values of temperature (T) and runoff (Q).
- The reference conditions for the temperature (T) and runoff (Q) were taken as the mean value of the same GCM ensemble over the 1976-1985 period.
- The rate of global mean sea-level rise was taken as 2.1 mm/yr for the 1986-2005 period, following the projections presented in Chapter 4 of the IPCC Special Report on the Ocean and Cryosphere in a Changing Climate (i.e., Oppenheimer et al. (2019)).
- The present value of HFPI was considered as a constant throughout the historical time period.
- The hindcast coastline changes at the respective locations were compared with satellite-image based shoreline change rates presented by Luijendijk et al. (2018).

The results of the comparison are shown in Table 2-1. This comparison indicates that the modelled coastline change at all four systems for the validation period compare well with those observed over the same period, providing confidence in the model.

Table 2-1: Comparison of the hindcasts rates of coastline change over 1986-2005 with the observed rates of coastline change obtained from Luijendijk et al. (2018). Negative rates of coastline change indicate coastal recession.

| CEC System | Rate of coastline change over 1986-2005 (m/yr) | |
|-------------------------------|--|-------------------|
| | Luijendijk et al. (2018) | RC model hindcast |
| Alsea estuary (USA) | -0.7 | -0.5 |
| Dyfi estuary (UK) | -1.0 | -0.8 |
| Kalutara estuary (Sri Lanka) | -1.0 | -0.7 |
| Swan River system (Australia) | -1.0 | -1.2 |

Chapter 3

Probabilistically simulating coastline change along inlet-interrupted coasts

3.1 Introduction

This chapter describes the application of the reduced-complexity modelling techniques introduced in Chapter 2 at four selected barrier-estuary systems and one barrier island coast. The selected mainland inlet-interrupted coasts represent both barrier estuaries with low-lying margins (Alesha estuary, Oregon, USA, and Dyfi estuary, Wales, UK) and small tidal inlets (Kalutara inlet, Sri Lanka and Swan river system, Australia). Each of these sub-categories consists of an arid and non-arid river catchment so that their behaviour under different climatic conditions can be investigated. The Chandeleur Islands, part of the Mississippi River Delta in Louisiana, USA are selected as the case-study site for barrier island coasts.

The contents of this chapter are structured as follows: Section 3.2 provides a brief description of the selected case-study sites. Model applications and results at the selected barrier-estuary systems are presented in Sections 3.3 to Section 3.6. Each of the above four sections comprises descriptions of the stochastic model inputs, computed future projections of change in total sediment volume exchange between the estuary and its adjacent inlet-interrupted coast, and the resulting final coastline change. Section 3.7 provides a comparison between the four barrier estuary case studies and discusses the differences in their future evolution. Section 3.8 presents the model applications and

results at the selected barrier island case study site, and Section 3.9 presents the summary and conclusions of this chapter. A description of the uncertainties associated with the model results is presented in Section 3.10.

3.2 Case study sites

Alsea Estuary (OR, USA)

Located in the state of Oregon, USA, the Alsea estuary-inlet system annually drains about 1.4 km^3 of water to the Pacific Ocean. This water volume is collected over its river catchment area of about $1,200 \text{ km}^2$. Surface area and the average depth of the Alsea estuary are about 9 km^2 and 2 m , respectively. This estuary system consists of inter-tidal marshes and wetlands, providing habitats to many species. The direction of longshore sediment transport around the Alsea estuary is highly seasonal, with a northwards net annual longshore sediment transport rate of about $50,000 \text{ m}^3/\text{yr}$ (Ruggiero et al., 2013).

Dyfi Estuary (Wales, UK)

Located along the mid-Wales coast in the United Kingdom, the Dyfi estuary connects the Dovey river/Afon Dyfi to the Irish Sea. Its surface area is about 17 km^2 and the average depth is 2.5 m . The Dyfi estuary is considered as a national nature reserve in Wales due to its extensive inter-tidal flats and rich bio-diversity. The watershed area of the river system is relatively small ($\sim 700 \text{ km}^2$), and thus drains less than 1 km^3 of water per annum. The northward net annual longshore sediment transport rate near the inlet is about $45,000 \text{ m}^3$ (Motyka and Brampton, 1993).

Kalutara Inlet (Sri Lanka)

Located along the western coast of the island, Kalutara inlet drains Sri Lanka's second-largest annual riverflow volume ($\sim 3.8 \text{ km}^3/\text{yr}$) to the Indian Ocean. This inlet is connected to a relatively small lagoon with a surface area of about 2 km^2 and an average depth of 3 m . The watershed area of the Kalu River is about $2,800 \text{ km}^2$. The southbound net annual longshore sediment transport rate in the vicinity of the inlet is about $200,000 \text{ m}^3/\text{yr}$ (Ranasinghe et al., 2019a). Fluvial sediment supply to the coast by the Kalu River is significantly hindered by river sand mining activities. According to published literature, its magnitude is $\sim 650,000 \text{ m}^3/\text{yr}$ (Bamunawala et al., 2018b).

Swan River (Australia)

The Swan river reaches the Indian Ocean via an inlet-estuary system located near Perth, Australia. The surface area of this estuary is around 52 km^2 , it has a mean depth of $\sim 5 \text{ m}$,

resulting in a basin volume $\sim 312 \times 10^6 \text{m}^3$. Despite its large watershed size (121,000 km²), the Swan rive drains only a small volume of water to the ocean ($\sim 0.5 \text{ km}^3/\text{yr}$) due to the arid nature of its catchment. The net longshore sediment transport rate in the vicinity of the inlet is about 50,000 m³/yr towards the north.

Chandeleur Islands (LA, USA)

The Chandeleur Islands is a chain of barrier islands located in the Gulf of Mexico, LA, USA. This 80 km long island chain provides shelter to the mainland Louisiana state by attenuating the intensity of waves and storm surges. The unique environmental conditions along the extensive back-barrier estuary area of the Chandeleur Islands ($\sim 8,750 \text{ km}^2$) is rich in biodiversity and of great economic importance as well. The freeboard of the barrier islands is about 2.3 m, and the barrier crest width is $\sim 2 \text{ km}$. The net annual longshore sediment transport towards the south has a long-term averaged gradient of 5.7 m³/m/yr (Lavoie, 2009).

Figure 3-1 shows the locations of the four barrier-estuary case-study sites and their respective watershed areas and Table 3-1 summarises the main properties of these systems.

Table 3-1: Properties of the selected mainland inlet-estuary systems

| Parameter | Mainland Inlet-Estuary System | | | |
|---|-------------------------------|-------|----------|---------|
| | Alesa | Dyfi | Kalutara | Swan |
| River discharge (Q in km ³ /yr) | 1.430 | 0.789 | 3.782 | 0.500 |
| Temperature (T in °C) | 11.3 | 8.2 | 26.0 | 23.0 |
| Mean ebb-tidal prism (P in 10 ⁶ m ³) | 9.0 | 71.1 | 6.2 | 2.6 |
| Basin surface area (A _b in 10 ⁶ km ²) | 9.1 | 17.3 | 1.75 | 52.0 |
| Basin volume (V _b in 10 ⁶ m ³) | 20.0 | 44.98 | 5.25 | 312 |
| Catchment area (A in km ²) | 1,225 | 670 | 2,778 | 121,000 |
| Catchment relief (R in km) | 1.25 | 0.66 | 2.25 | 0.53 |
| Lithology factor (L) | 1.0 | 0.75 | 0.5 | 0.5 |
| Anthropogenic factor (E _h) | 0.67 | 0.93 | 0.93 | 0.58 |
| Beach profile slope (tan β) | 0.02 | 0.02 | 0.02 | 0.01 |
| Depth of closure (h _{D_{0C}} in m) | 15 | 15 | 15 | 20 |

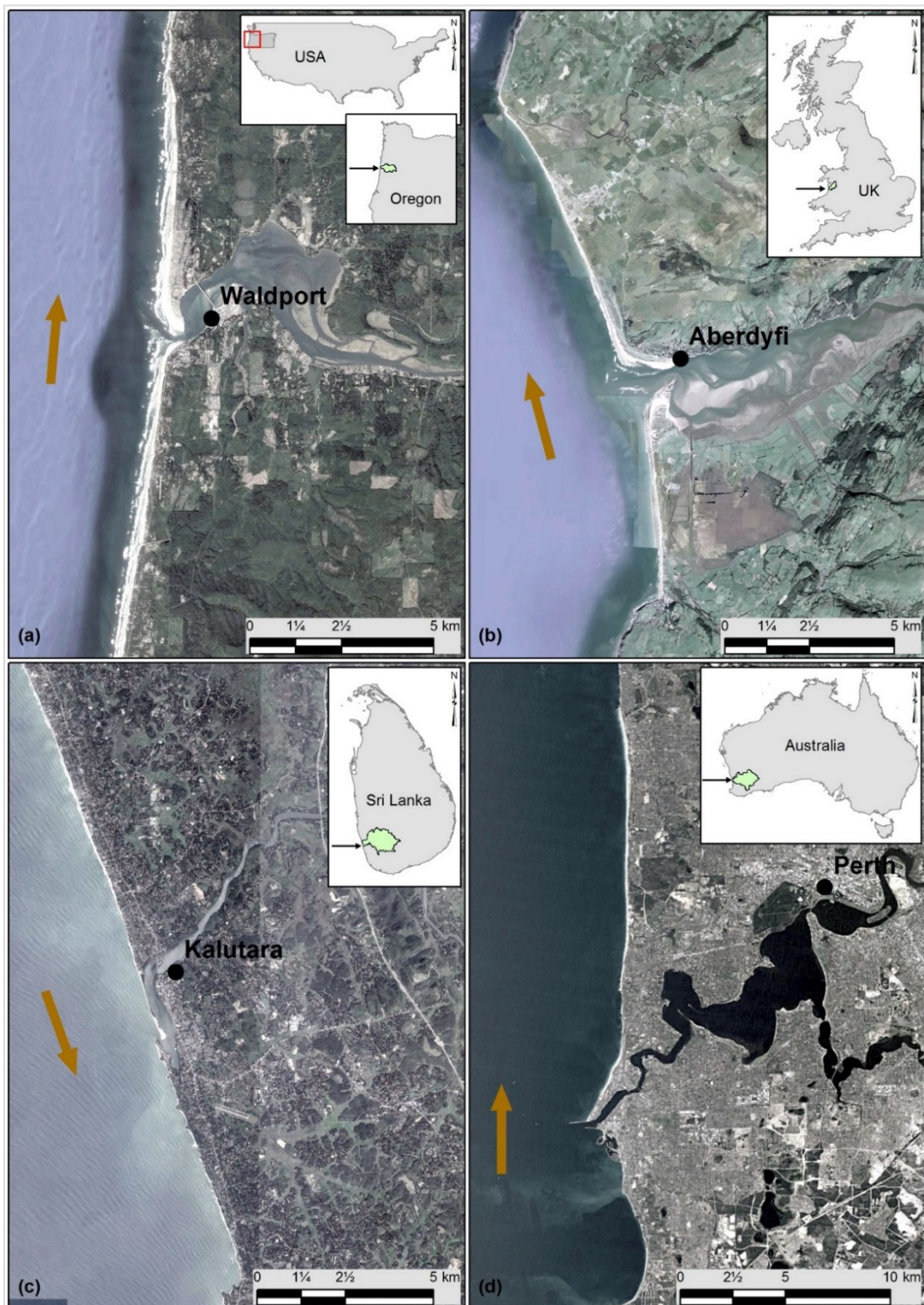


Figure 3-1: Locations of the selected mainland inlet-estuary systems (a) Alsea estuary, OR, USA; (b) Dyfi estuary, Wales, UK; (c) Kalutara inlet, Sri Lanka and (d) Swan river system, Australia. Horizontal black arrows in the insert location maps indicate the inlet locations, while the catchment areas are shaded in green; brown arrows in the main figures indicate the direction of net annual longshore sediment transport. Each subplot shows the extent of the inlet-interrupted coastlines (in both the up- and down-drift directions) of the respective systems.

Figure 3-2 shows the location of the selected barrier-island chain.

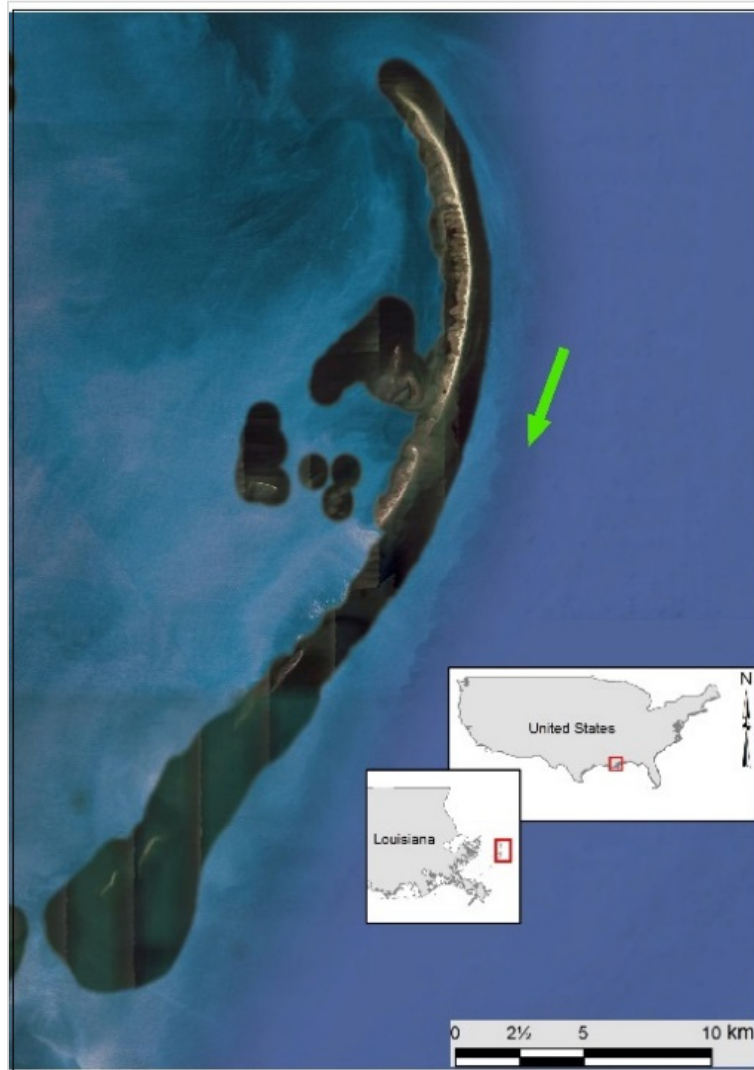


Figure 3-2: Location of the selected barrier-island system (Chandeleur Islands) in Louisiana, USA The green arrow indicates the direction of net annual longshore sediment transport.

3.3 Alesa estuary system

3.3.1 Stochastic model inputs

The stochastic model inputs of annual mean temperature and annual cumulative river discharge were generated from the fitted joint probability distributions (as described in Section 2.3). Inputs for these joint probability distributions were obtained from 7 GCMs with daily/monthly projections of temperature and runoff over the Alesa river catchment. These projections were yearly averaged to compute the inputs of the above fitted joint probability distributions. Details of the GCMs used are provided in Annex A.1.

Figure 3-3 shows the projected variations of annual mean temperature at the Alesa river catchment over the three decadal periods considered (2021-2030, 2056-2065, and 2091-2100). Similar to the globally averaged temperature variation published by Stocker et al. (2013), the 50th percentile annual mean temperature values in Alesa river catchment show hardly any change during mid- and end-century periods for RCP 2.6. The projected maximum and minimum increments of the 50th percentile annual mean temperature values by 2100 are ~3.0°C and ~0.5°C for RCP 8.5 and 2.6, respectively.

Figure 3-4 shows the projected variations in annual cumulative river discharges of the Alesa river over the same three decadal periods, indicating trivial variations in river discharge over the 21st century for all RCPs. Except for RCP 8.5, projected annual cumulative river discharges are slightly increased by 2100, where the maximum and minimum increments in the 50th percentile values are ~0.2 km³/yr and <0.1 km³/yr for RCP 2.6 and 4.5, respectively. The projected 50th percentile value of the annual cumulative river discharge by 2100 is marginally decreased (<0.1 km³/yr) for RCP 8.5.

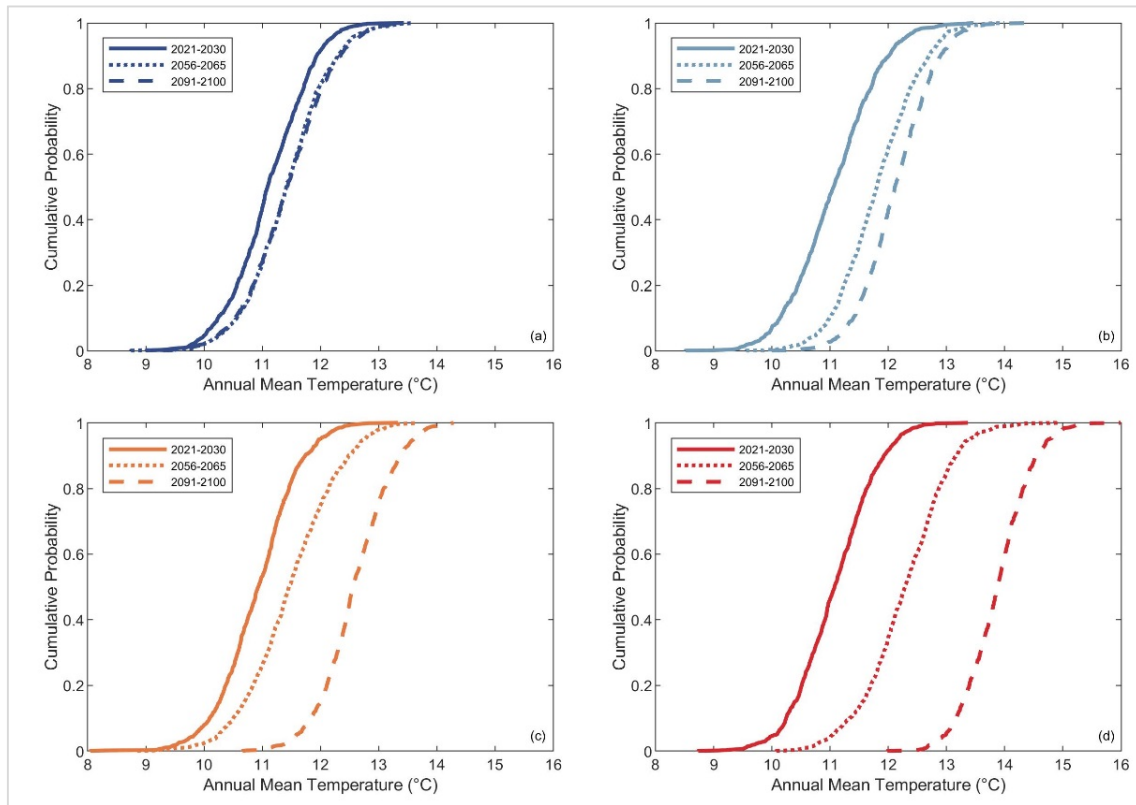


Figure 3-3: Empirical cumulative distributions of averaged annual mean temperature in the Alesia river catchment, OR, USA. Subplots (a), (b), (c), and (d) are for the RCPs 2.6, 4.5, 6.0, and 8.5, respectively.

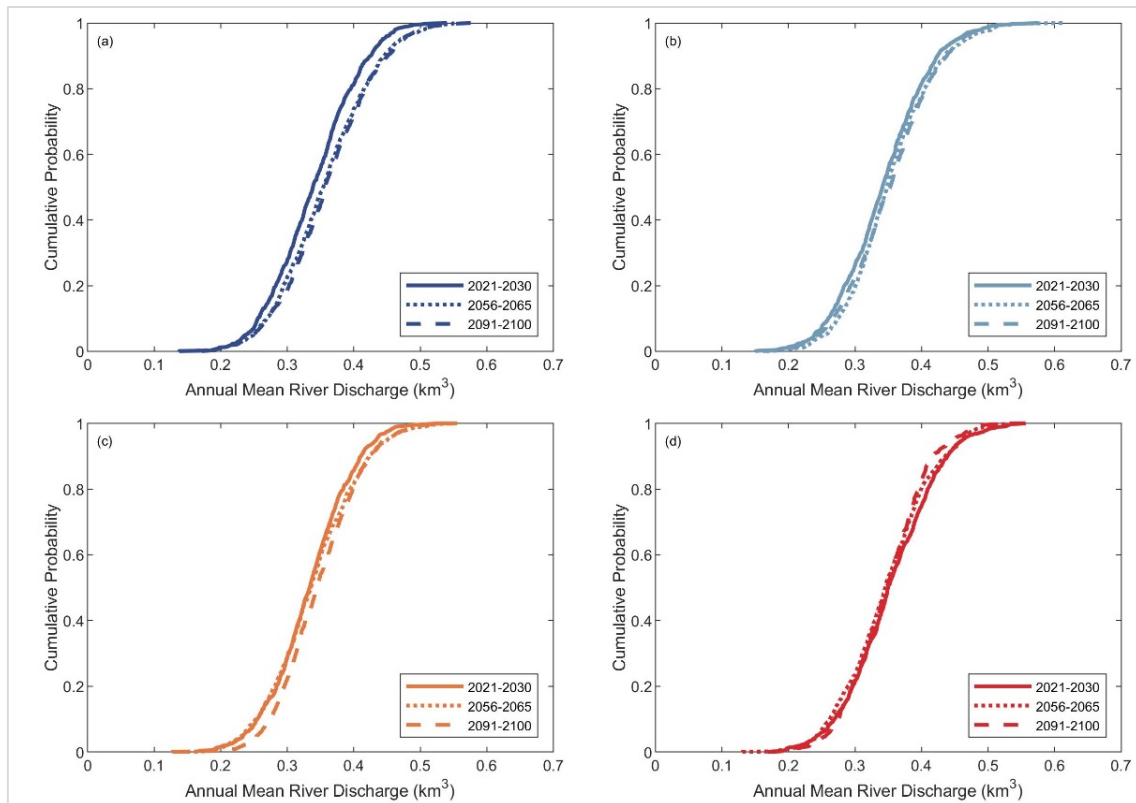


Figure 3-4: Empirical cumulative distributions of averaged annual cumulative river discharge at the Alesia estuary, OR, USA. Subplots (a), (b), (c), and (d) are for the RCPs 2.6, 4.5, 6.0, and 8.5, respectively.

Figure 3-5 shows the projected regional relative sea-level changes (ΔRSL) in the vicinity of the Alsea estuary for 2021-2100 period. Intermediate values for mean, maximum, and minimum relative regional sea-level changes (Figure 3-5) were computed by using the values shown in Table 3-2. The projected maximum and minimum changes in mean ΔRSL by 2100 are ~ 0.60 m, and ~ 0.35 m for RCP 8.5 and 2.6, respectively.

Table 3-2: Projected changes in regional relative sea-level change and its components in the vicinity of Alsea estuary by 2100

| | RCP 2.6 | RPC 4.5 | RCP 6.0 | RCP 8.5 |
|---|---------|---------|---------|---------|
| Global mean sea level change (ΔSL_G in m) | 0.40 | 0.47 | 0.48 | 0.63 |
| Regional variation (ΔSL_{RM} in m) | 0.05 | -0.02 | -0.03 | -0.08 |
| Regional relative sea level change (ΔRSL in m) | 0.45 | 0.45 | 0.45 | 0.55 |

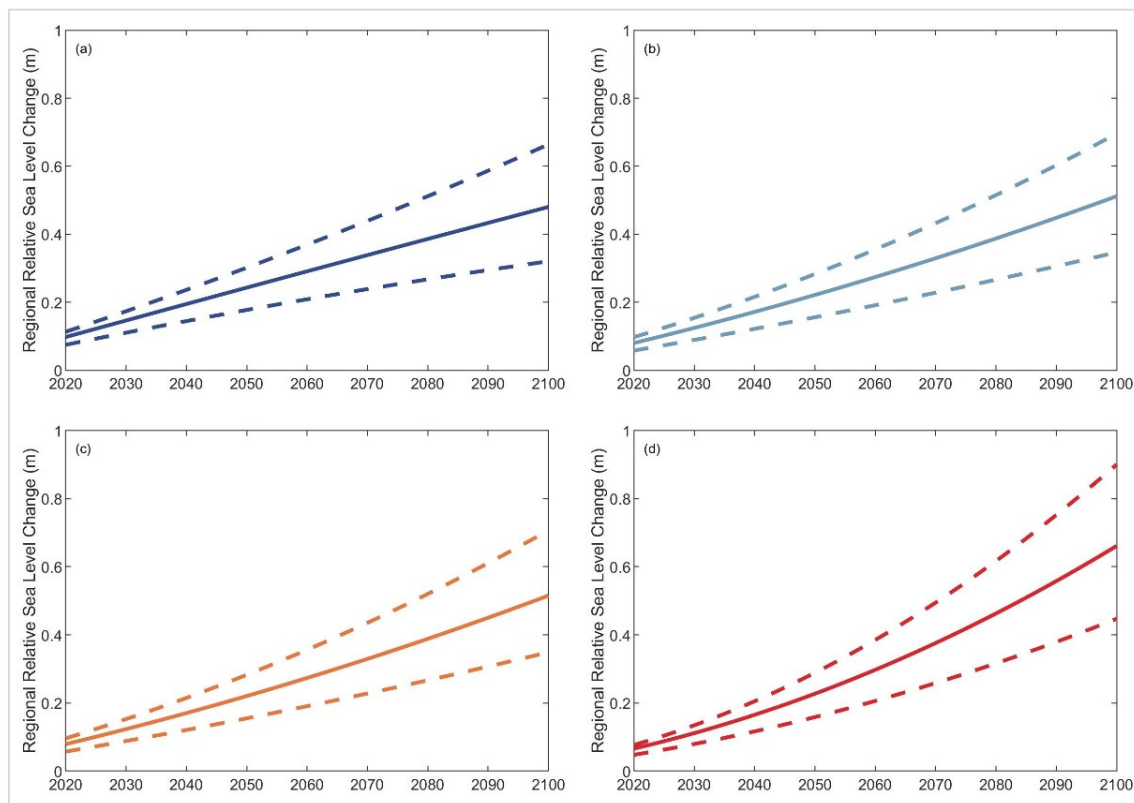


Figure 3-5: Projected changes in regional relative sea level at the Alsea estuary, OR, USA. Subplots (a), (b), (c), and (d) are for the RCPs 2.6, 4.5, 6.0, and 8.5, respectively. The solid line indicates the mean change, while the two dashed lines indicate the maximum and minimum variations of ΔRSL .

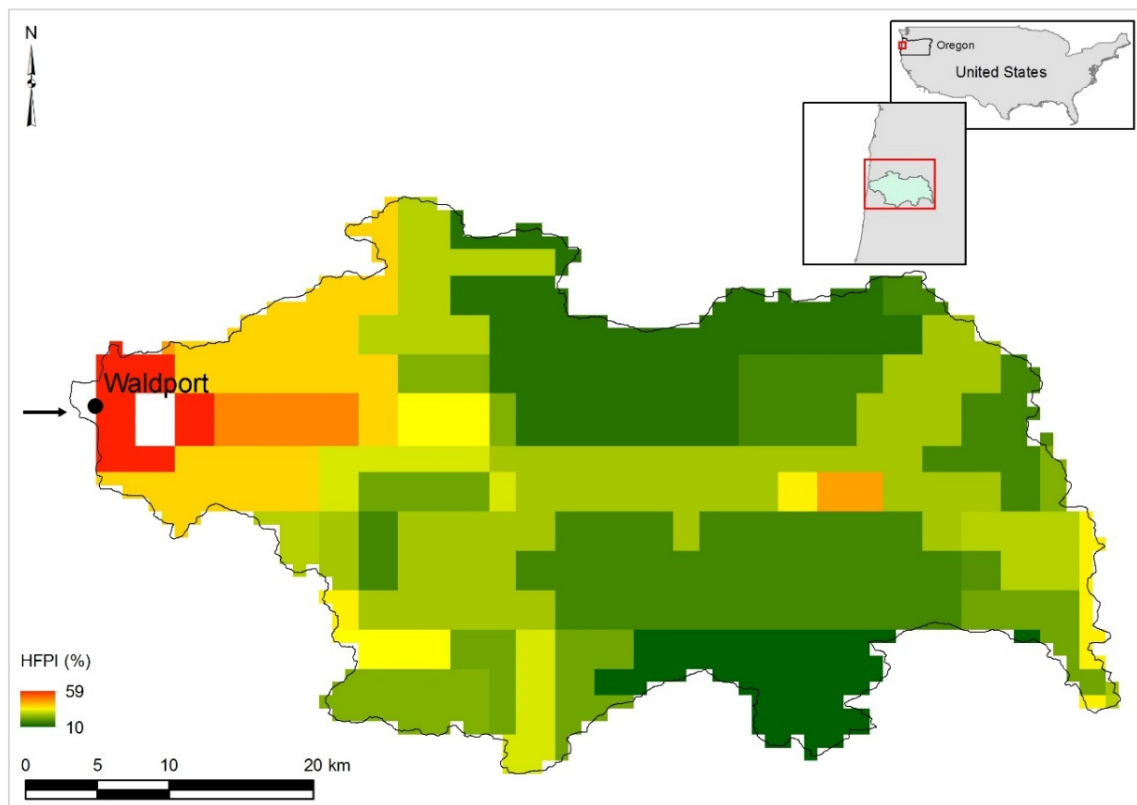


Figure 3-6: Human FootPrint Index (HFPI) of the Alsea river catchment, OR, USA. The black arrow in the main figure shows the inlet locations, while the catchment area is shaded in green within the insert location maps.

Figure 3-6 shows the Human FootPrint (HFPI) of the Alsea river catchment, OR, USA. The catchment-averaged HFPI value was used as the reference conditions of human-induced erosion factor (E_h in equation [2-11]) and fitted triangular distributions were used to generate yearly stochastic variables of E_h (as described in Section 2.3) to compute the changes in fluvial sediment supply.

Results of the reduced-complexity model application at the Alsea estuary are presented in sub-section 3.3.2 (Future variations of change in total sediment volume exchange between the estuary and the inlet-affected coast) and sub-section 3.3.3 (Projected changes in coastline position).

3.3.2 Future variations of change in total sediment volume exchange between the estuary and the inlet-affected coast

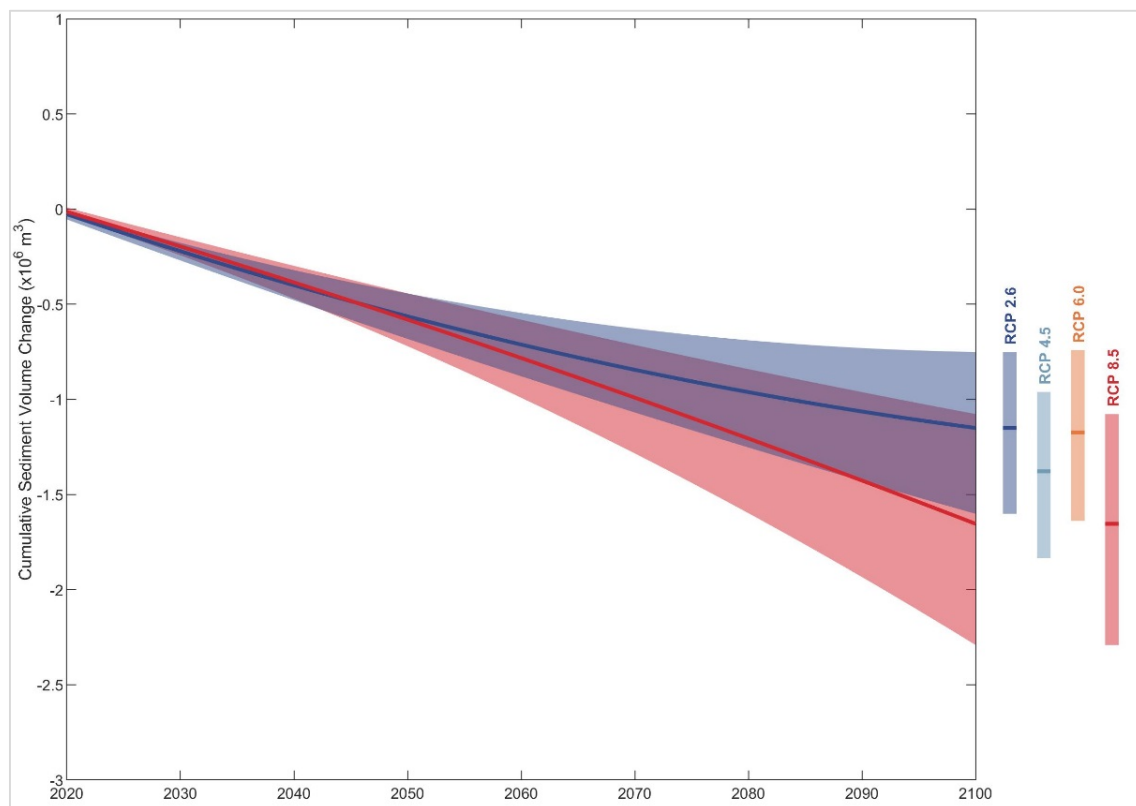


Figure 3-7: Projected variations of change in total sediment volume exchange (ΔV_T) between the Alsea estuary and its inlet-interrupted coast over the 21st century. The projected ranges between 10th and 90th percentile are shown as shaded bands with the variation of the 50th percentile values indicated by the solid lines for RCP 2.6 (blue) and RCP 8.5 (red). Vertical bars indicate the projected ranges between the same percentiles by 2100 for all RCPs with the 50th percentile values indicated as horizontal lines.

The above figure (Figure 3-7) shows the projected variations in the change in total sediment volume exchange (ΔV_T) between the Alsea estuary and its inlet-interrupted coast over the 21st century. The computations of ΔV_T were based on the methods presented under Section 2.2 and Section 2.3.

According to these results, both RCP 2.6 and 8.5 scenarios result in similar ranges of uncertainty and 50th percentile values of ΔV_T (~ -0.5 Million Cubic Meters (MCM) by 2050) during 2020-2050. From that point onwards, the projected uncertainty ranges and the 50th percentile values of ΔV_T under RCP 8.5 tend to deviate from those under RCP 2.6 and result in a more substantial median value by 2100 (~ -1.7 MCM). The projected uncertainties of ΔV_T by 2100 are quite similar for all but RCP 8.5. Figure 3-7 also indicates that the projected 50th percentile ΔV_T by 2100 is similar for both RCP 2.6 and 6.0 (~ -1.1 MCM). The above variations in ΔV_T are closely related to the differences in projected sea level, annual mean temperature, and annual cumulative river discharge values among the different RCPs, and are discussed in more detail below.

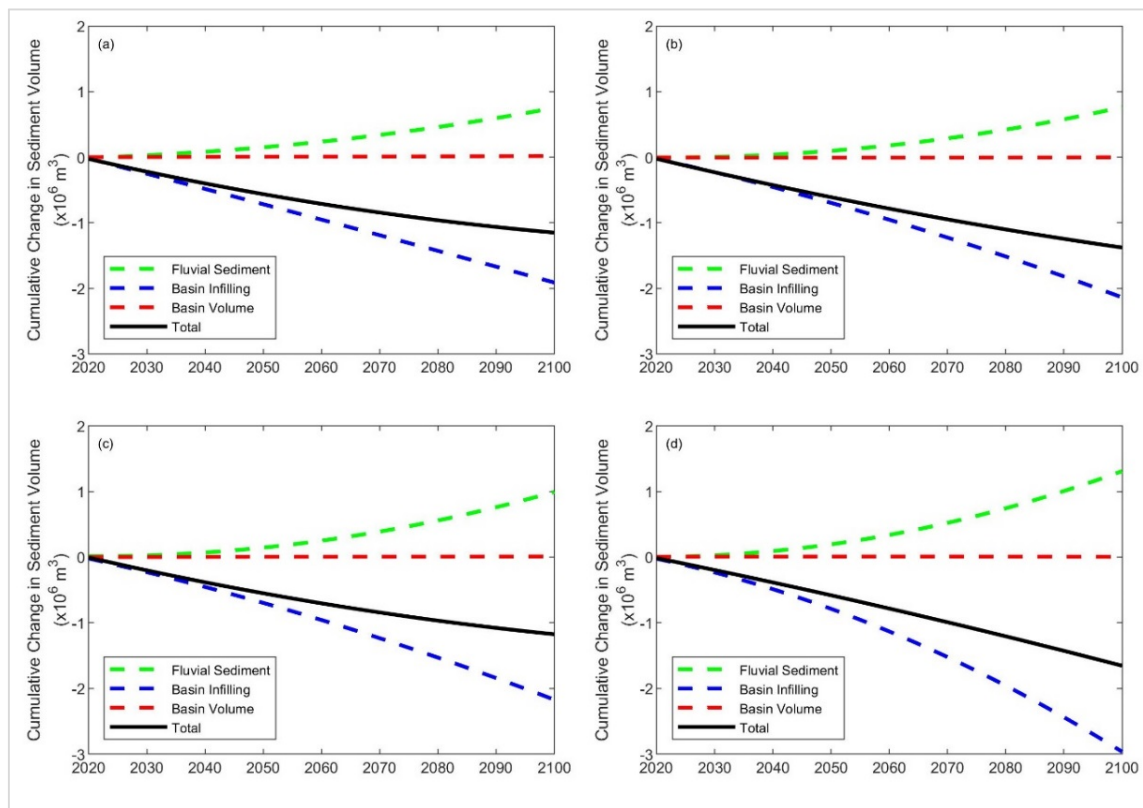


Figure 3-8: Variations of the projected 50th percentile values of change in total sediment volume exchange (ΔV_T) and the different contributing processes at the Alesja estuary over the 21st century. Subplots (a), (b), (c), and (d) are for the RCPs 2.6, 4.5, 6.0, and 8.5, respectively.

Figure 3-8 shows the variations of the projected 50th percentile values of change in total sediment volume exchange (ΔV_T) and the different contributing processes (basin infilling volume (ΔV_{BI}), basin volume change (ΔV_{BV}) and change in fluvial sediment supply (ΔV_{FS})) at Alesja estuary for the entire study period of 2021-2100 under all RCPs. The results presented in the above figure indicate that ΔV_T at Alesja estuary system is predominantly governed by the basin infilling volume (ΔV_{BI}). The results also indicate that the projected variations of ΔV_{BV} have trivial impacts on ΔV_T for all RCPs.

The sediment demand due to basin infilling (ΔV_{BI}) is projected to increase rapidly under RCP 8.5 condition during the late 21st century, thus resulting in the most significant 50th percentile cumulative sediment volume deficit by 2100 (~3 MCM). This is driven by the projected changes in sea level during the same period (Figure 3-5). Projected changes in mean annual temperature (Figure 3-3), and the fitted increments in human-induced erosion factor (E_h) contribute positively to increase the fluvial sediment supply (ΔV_{FS}) from the river catchment towards late 2100 for all RCPs. These fluvial sediment surpluses reduce the sea-level-rise-driven basin infilling volume requirements (ΔV_{BI}) over the late 21st century. Therefore, the most significant 50th percentile value of ΔV_T in the Alesja estuary system by 2100 is projected to be ~-1.5 MCM.

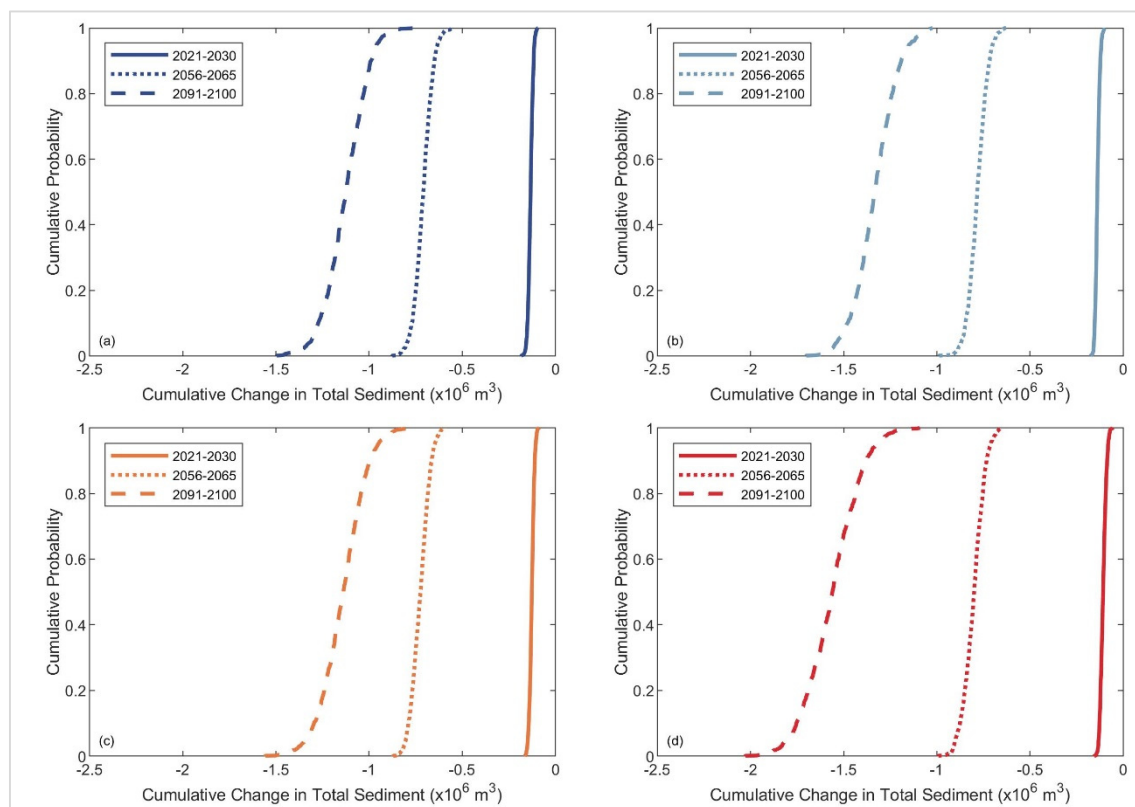


Figure 3-9: Empirical cumulative distributions of the projected change in total sediment volume exchange between the Alsea estuary and its inlet-interrupted coast. Subplots (a), (b), (c), and (d) are for the RCPs 2.6, 4.5, 6.0, and 8.5, respectively.

Figure 3-9 shows the empirical cumulative distributions (CDFs) of the projected change in total sediment volume exchange (ΔV_T) at Alsea estuary over the three decadal periods considered (2021-2030, 2056-2065, and 2091-2100) for all RCPs. The above CDFs were created by averaging the projected ΔV_T values over the indicated three decadal periods. These CDF plots indicate the total uncertainties associated with the projected ΔV_T at the Alsea estuary system (in contrast to the selected range between 10th and 90th percentiles presented in Figure 3-7).

During the first decadal period, there is very little uncertainty in the ΔV_T projections under all four RCPs. These uncertainties increase slightly over the mid-century period for all RCPs (<0.25 MCM), increasing to considerable uncertainties by the end-century period, in which the least (~0.75 MCM) and the most (~1 MCM) variations by 2100 are projected for RCP 4.5 and 8.5, respectively.

The above CDFs of change in total sediment volume exchange (ΔV_T) provide the input needed by coastal zone planners/managers to implement effective land-use planning strategies to manage the future climate change impacts and anthropogenic activities driven socio-economic losses along the inlet-interrupted coasts. In this study, the 50th percentile values of ΔV_T were selected to compute the projected coastline change near the Alsea estuary, and the results are presented in the following sub-section.

3.3.3 Projected changes in coastline position

The modelling framework presented in Section 2.4 was applied to project the changes along the inlet-affected coastline at the Aalsea estuary by 2040, 2060, 2080, and 2100. The projected 50th percentile cumulative change in total sediment volume exchange (ΔV_T) between the estuary and its adjacent coast by the same periods are presented in Table 3-3. These projections of ΔV_T indicate that the Aalsea estuary is likely to import sediment from its adjacent coast during the periods considered (i.e., by 2040, 2060, 2080, and 2100) for all RCPs. A comparison of the above ΔV_T and the net annual longshore sediment transport capacity near the inlet was made to identify the applicable form(s) of coastline behaviour (i.e., Type A, B, or C) presented in Section 2.4.1 so that the coastline change due to the variations in sediment volume exchange can be determined using the method presented in Section 2.4.2.

The above comparison indicates that the coastline evolution at the Aalsea estuary is Type-B behaviour (i.e., LST is greater than or equal to the sediment volume demand of the estuary; described in Section 2.4.1). Therefore, the down-drift coast will be subjected to additional coastal recession driven by the change in total sediment volume exchange (ΔV_T), other than that due to the Bruun effect. The up-drift coast is only affected by the coastline recession due to the Bruun effect.

Table 3-3: The 50th percentile values of the cumulative change in total sediment volume exchange considered for coastline change projections at the Aalsea estuary. Note: Negative signs denote sediment demand in the estuary

| Year | Cumulative Change in Total Sediment Volume ($\Delta V_T \times 10^6 \text{ m}^3$) | | | |
|------|---|---------|---------|---------|
| | RCP 2.6 | RCP 4.5 | RCP 6.0 | RCP 8.5 |
| 2040 | -0.40 | -0.43 | -0.38 | -0.39 |
| 2060 | -0.71 | -0.78 | -0.71 | -0.78 |
| 2080 | -0.96 | -1.11 | -0.97 | -1.21 |
| 2100 | -1.15 | -1.38 | -1.17 | -1.65 |

The projected 50th percentile changes of the inlet-affected coastline at the Aalsea estuary are shown in Figure 3-10.

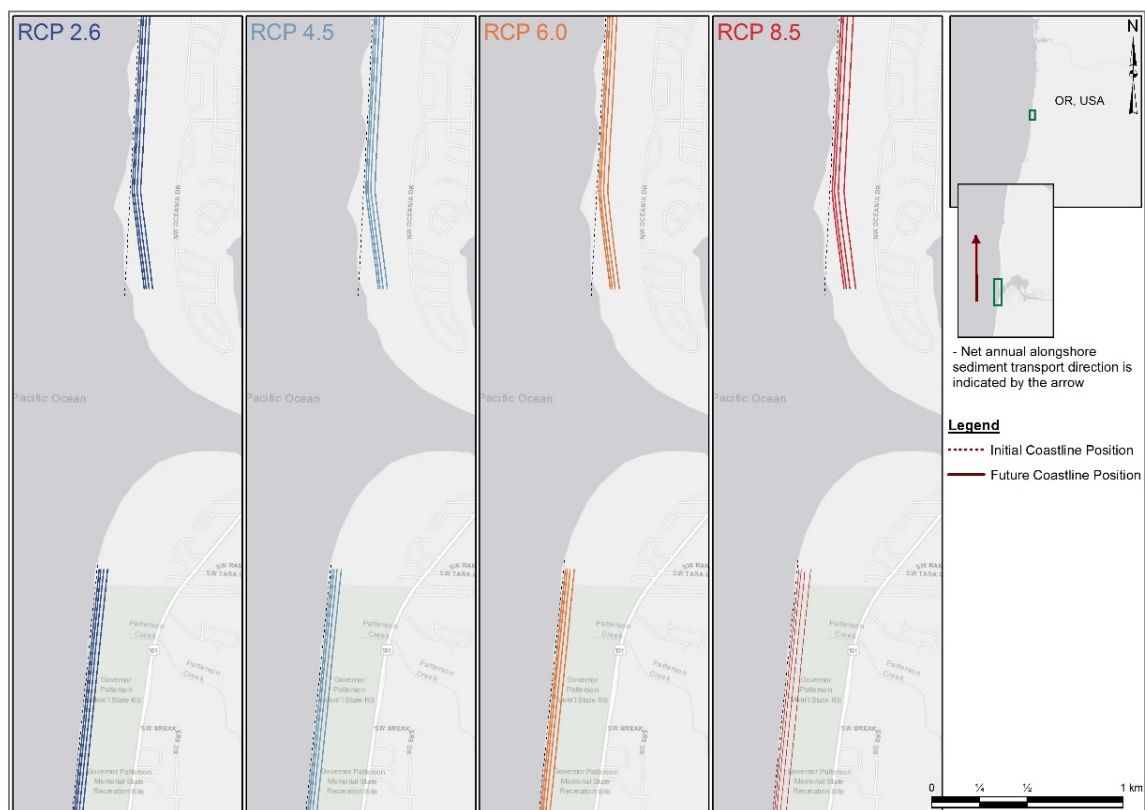


Figure 3-10: Projected changes of the inlet-affected coastline at the Alsea estuary. The four solid lines in each subplot represent the final coastline position by 2040, 2060, 2080 and 2100 (in the same order, moving landward from the most seaward line).

The model results indicate that the down-drift coast at the Alsea estuary may erode between ~67 m (RCP 2.6) and ~86 m (RCP 8.5) by 2100 (i.e., ~-1 m/yr rate of erosion). The up-drift coast is only affected by the coastal recession due to Bruun effect and hence projected to be eroded between ~54 m (RCP 2.6) and ~72 m (RCP 8.5) by 2100 (i.e., ~-1 m/yr rate of erosion). The coastline change projections presented by Vousdoukas et al. (2020) indicate ~50 m erosion along both up-and down-drift coast by 2100 for RCP 8.5. It should, however, be noted that this global assessment of sandy coastline variation presented by Vousdoukas et al. (2020) does not consider the estuarine effects and also incorporates a correction factor for Bruun effect-driven coastline recession.

3.4 Dyfi estuary system

3.4.1 Stochastic model inputs

Figure 3-11 shows the projected variations of annual mean temperature at the Dyfi River catchment over the three decadal periods considered (2021-2030, 2056-2065, and 2091-2100). Unlike the globally-averaged temperature variation published by Stocker et al. (2013), the 50th percentile annual mean temperature values in the Dyfi river catchment show differences during mid- and end-century periods for RCP 2.6, in which the latter period (i.e., 2091-2100) projection is ~0.5°C warmer than the former duration. The projected maximum and minimum increments of the 50th percentile annual mean temperature values by 2100 are ~2.5°C and ~0.5°C for RCP 8.5 and 2.6, respectively.

Figure 3-12 shows the projected variations in annual cumulative river discharge of the Dyfi River over the same three decadal periods, indicating trivial variations in river discharge over the 21st century for all RCPs. Except for RCP 6.0, the projected annual cumulative river discharges are slightly increased by 2100. However, all these projected variations (i.e., both reductions and increments) are quite trivial, and thus only result in minor variations of annual cumulative river discharge (<0.05 km³/yr) of the Dyfi river over the 21st century.

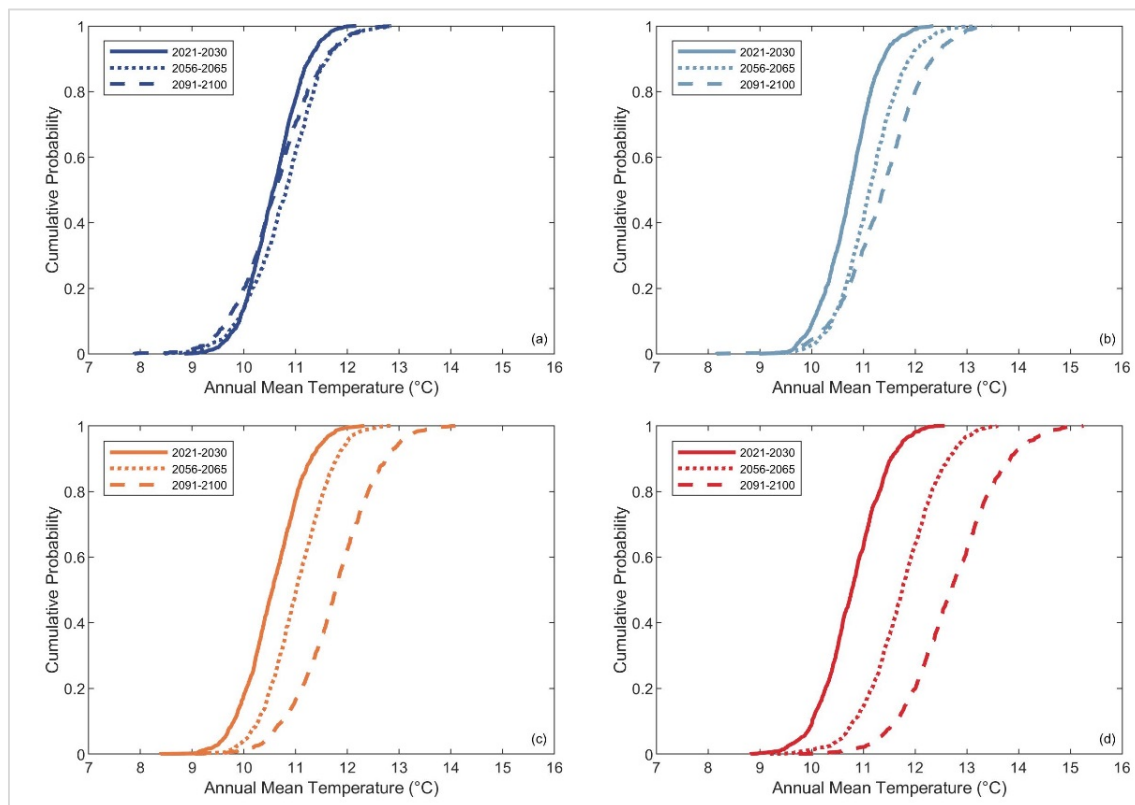


Figure 3-11: Empirical cumulative distributions of averaged annual mean temperature in the Dyfi river catchment, Wales, UK. Subplots (a), (b), (c), and (d) are for the RCPs 2.6, 4.5, 6.0, and 8.5, respectively.

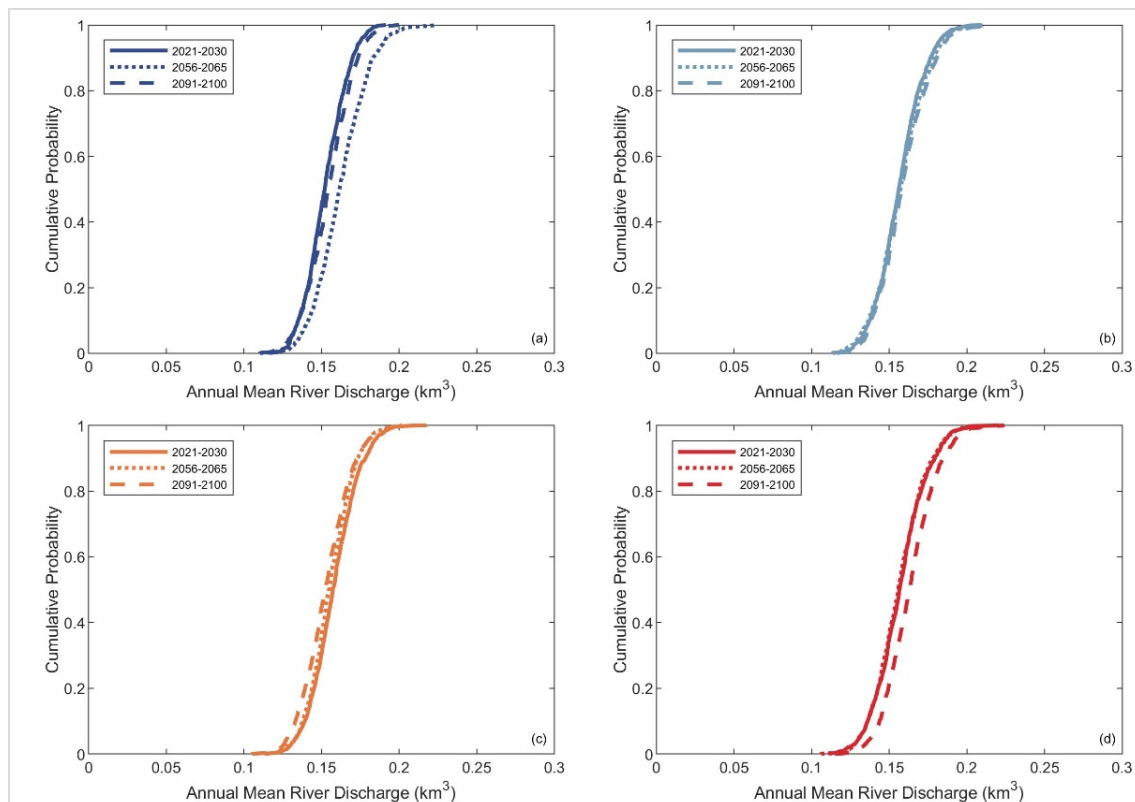


Figure 3-12: Empirical cumulative distributions of averaged annual cumulative river discharge at the Dyfi estuary, Wales, UK. Subplots (a), (b), (c), and (d) are for the RCPs 2.6, 4.5, 6.0, and 8.5, respectively.

Figure 3-13 shows the projected regional relative sea-level changes (ΔRSL) in the vicinity of the Dyfi estuary for 2021-2100 period. The projected maximum and minimum changes in mean ΔRSL by 2100 are ~ 0.60 m, and ~ 0.30 m for RCP 8.5 and 2.6, respectively.

Table 3-4: Projected changes in regional relative sea-level change and its components considered at the vicinity of the Dyfi estuary by 2100.

| | RCP 2.6 | RPC 4.5 | RCP 6.0 | RCP 8.5 |
|---|---------|---------|---------|---------|
| Global mean sea level change (ΔSL_G in m) | 0.40 | 0.47 | 0.48 | 0.63 |
| Regional variation (ΔSL_{RM} in m) | -0.05 | -0.02 | -0.03 | -0.08 |
| Regional relative sea level change (ΔRSL in m) | 0.35 | 0.45 | 0.45 | 0.55 |

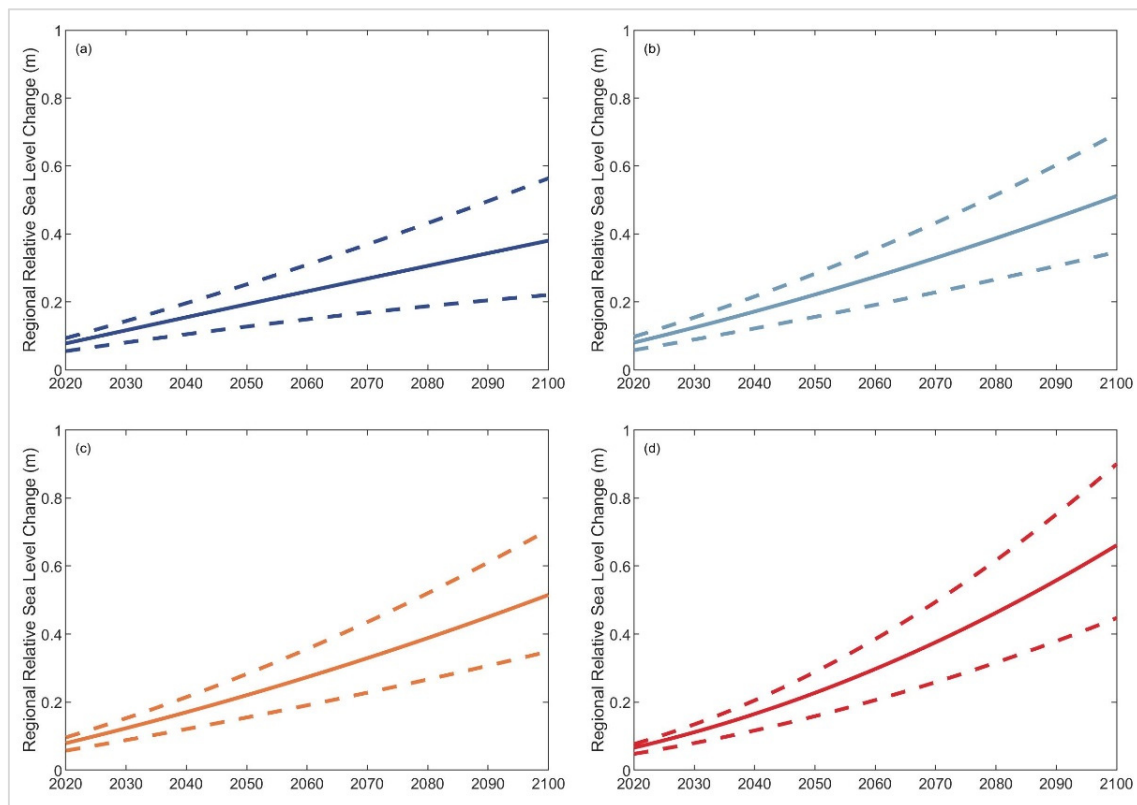


Figure 3-13: Projected changes in regional relative sea level at the Dyfi estuary, Wales, UK. Subplots (a), (b), (c), and (d) are for the RCPs 2.6, 4.5, 6.0, and 8.5, respectively. The solid line indicates the mean change, while the two dashed lines indicate the maximum and minimum variations of ΔRSL .

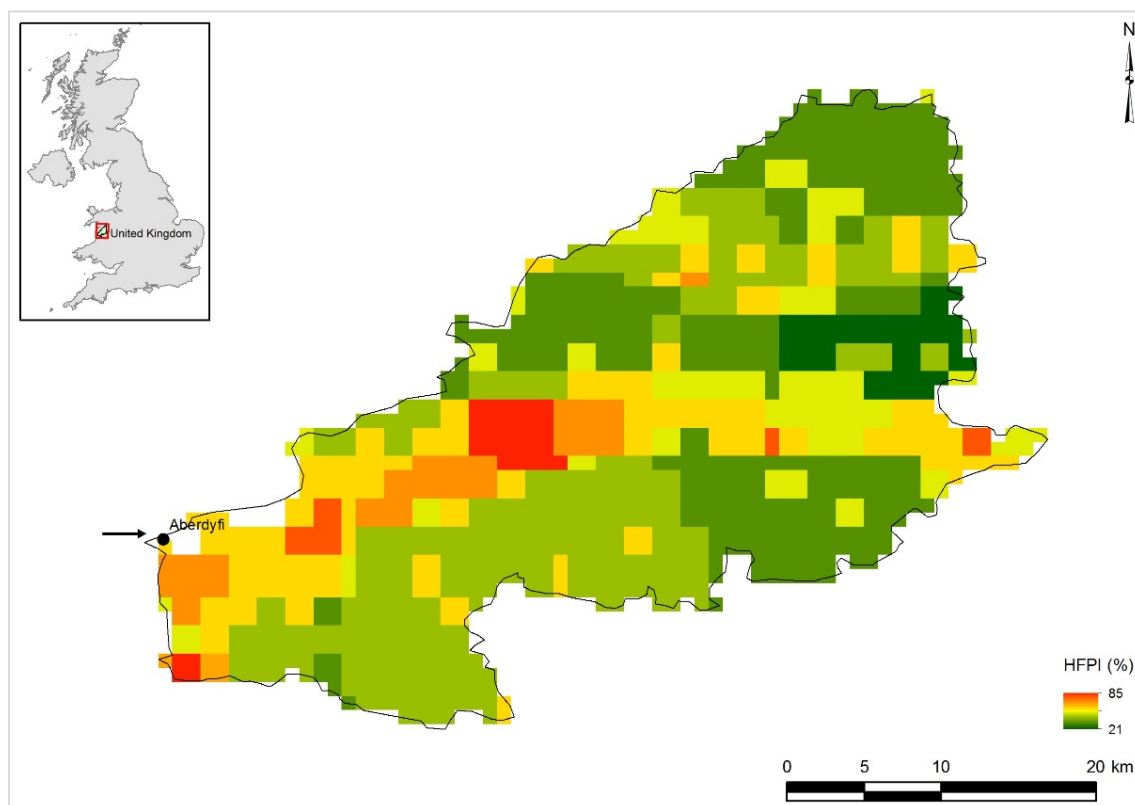


Figure 3-14: Human FootPrint Index (HFPI) of the Dyfi river catchment, Wales, UK. The black arrow in the main figure indicates the inlet location, while the catchment area is shaded in green within the insert location maps.

Figure 3-14 shows the Human FootPrint (HFPI) of the Dyfi river catchment, Wales, UK, which was used to compute the changes in fluvial sediment supply.

Results of the reduced-complexity model application at Dyfi estuary are presented in sub-section 3.4.2 (Future variations of change in total sediment volume exchange between the estuary and the inlet-affected coast) and sub-section 3.4.3 (Projected changes in coastline position).

3.4.2 Future variations of change in total sediment volume exchange between the estuary and the inlet-affected coast

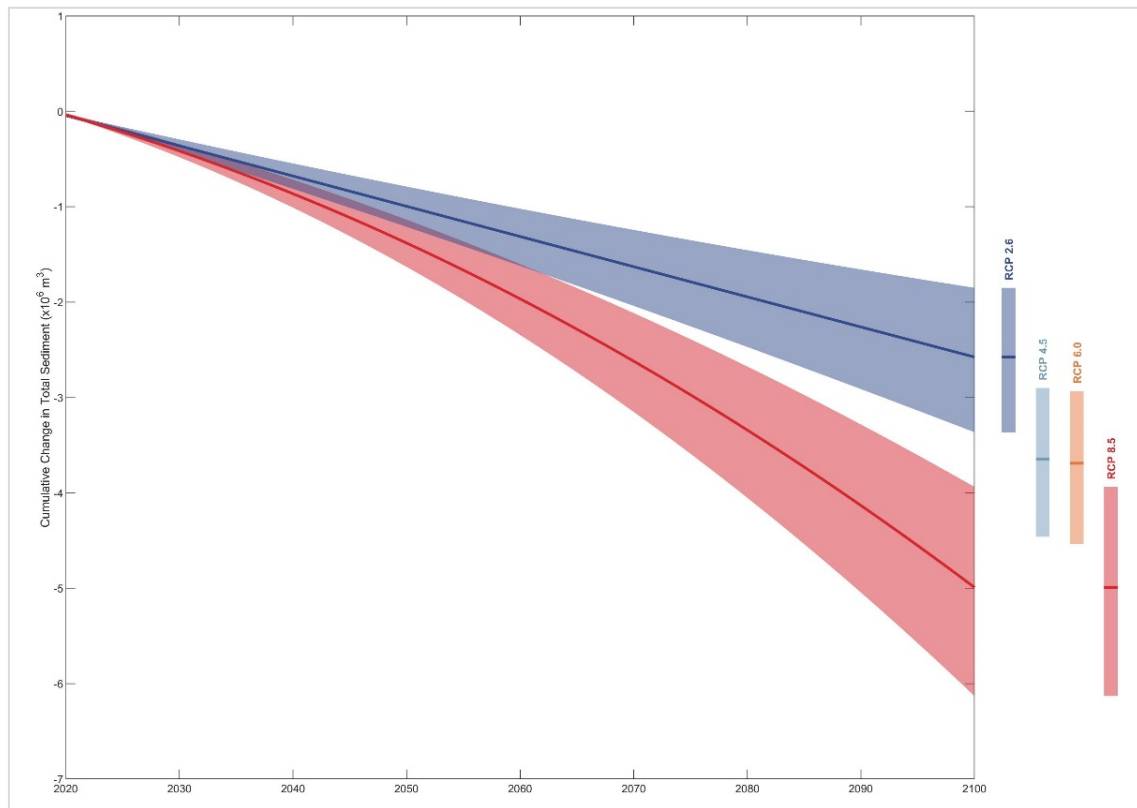


Figure 3-15: Projected variations of change in total sediment volume exchange (ΔV_T) between the Dyfi estuary and its inlet-interrupted coast over the 21st century. The projected ranges between 10th and 90th percentile are shown as shaded bands with the variation of the 50th percentile values indicated by solid lines for RCP 2.6 (blue) and RCP 8.5 (red). Vertical bars indicate the projected ranges between the same percentiles by 2100 for all RCPs with the 50th percentile values indicated as horizontal lines.

The above figure (Figure 3-15) shows the projected variations in the change in total sediment volume exchange (ΔV_T) between the Dyfi estuary and its inlet-interrupted coast over the 21st century.

According to these results, both RCP 2.6 and 8.5 scenarios result in similar ranges of uncertainty during the 2020-2050 period. However, the magnitude of the 50th percentile value of ΔV_T for RCP 8.5 (~-1.5 MCM) is ~50% larger than that for RCP 2.6 (~-1.0 MCM) by 2050. From that point onwards, projected uncertainty ranges and the 50th percentile values of ΔV_T under RCP 8.5 tend to deviate from those under RCP 2.6 and result in a larger median value by 2100 (~-5.0 MCM). Figure 3-15 indicates that the projected 50th percentile of ΔV_T by 2100 is similar under RCP 4.5 and 6.0 (~-3.5 MCM), but smaller for RCP 2.6 (~-2.5 MCM). The above variations in ΔV_T are closely related to the differences in projected sea level, annual mean temperature, and annual cumulative river discharge values among the different RCPs, and are discussed in more detail below.

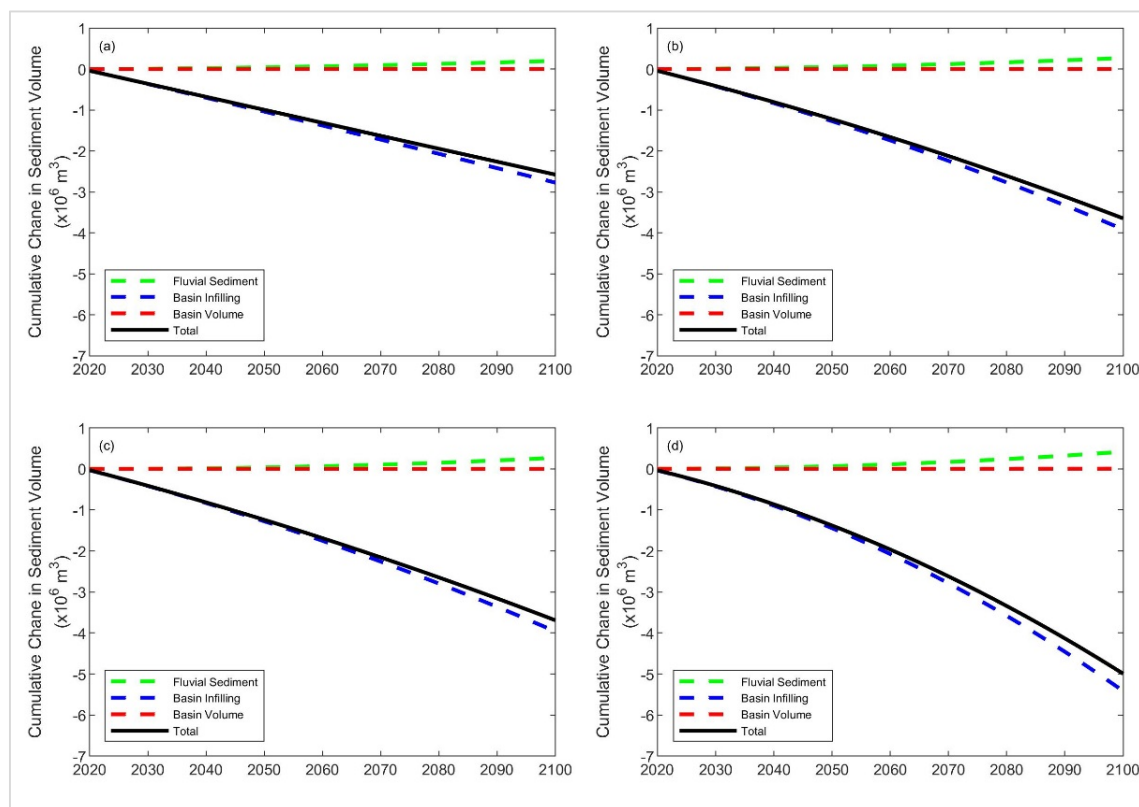


Figure 3-16: Variations of the projected 50th percentile values of change in total sediment volume exchange (ΔV_T) and the different contributing processes at the Dyfi estuary over the 21st century. Subplots (a), (b), (c), and (d) are for the RCPs 2.6, 4.5, 6.0, and 8.5, respectively.

Figure 3-16 shows the variations of the projected 50th percentile values of change in total sediment volume exchange (ΔV_T) and the different contributing processes (basin infilling volume (ΔV_{BI}), basin volume change (ΔV_{BV}) and change in fluvial sediment supply (ΔV_{FS})) at Dyfi estuary for the entire study period of 2021-2100 under all RCPs. The results presented in the above figure indicate that ΔV_T at Dyfi estuary system is governed by the basin infilling volume (ΔV_{BI}) for all RCPs. The results also indicate that projected variations of ΔV_{BV} and ΔV_{FS} have trivial impact on ΔV_T for all RCPs.

The sediment demand due to basin infilling (ΔV_{BI}) is projected to increase rapidly under RCP 8.5 condition during the late 21st century, thus resulting in the most significant 50th percentile cumulative sediment volume deficit by 2100 (~5.5 MCM). This is driven by the projected changes in sea level during the same period (Figure 3-13). The relative contributions from ΔV_{BV} and ΔV_{FS} on projected variation in ΔV_T are trivial for all RCPs. Therefore, the maximum and minimum 50th percentile values of ΔV_T at Dyfi estuary system by 2100 are projected to be ~-2.5 MCM and ~-5.0 MCM for RCP 2.6 and 8.5, respectively.

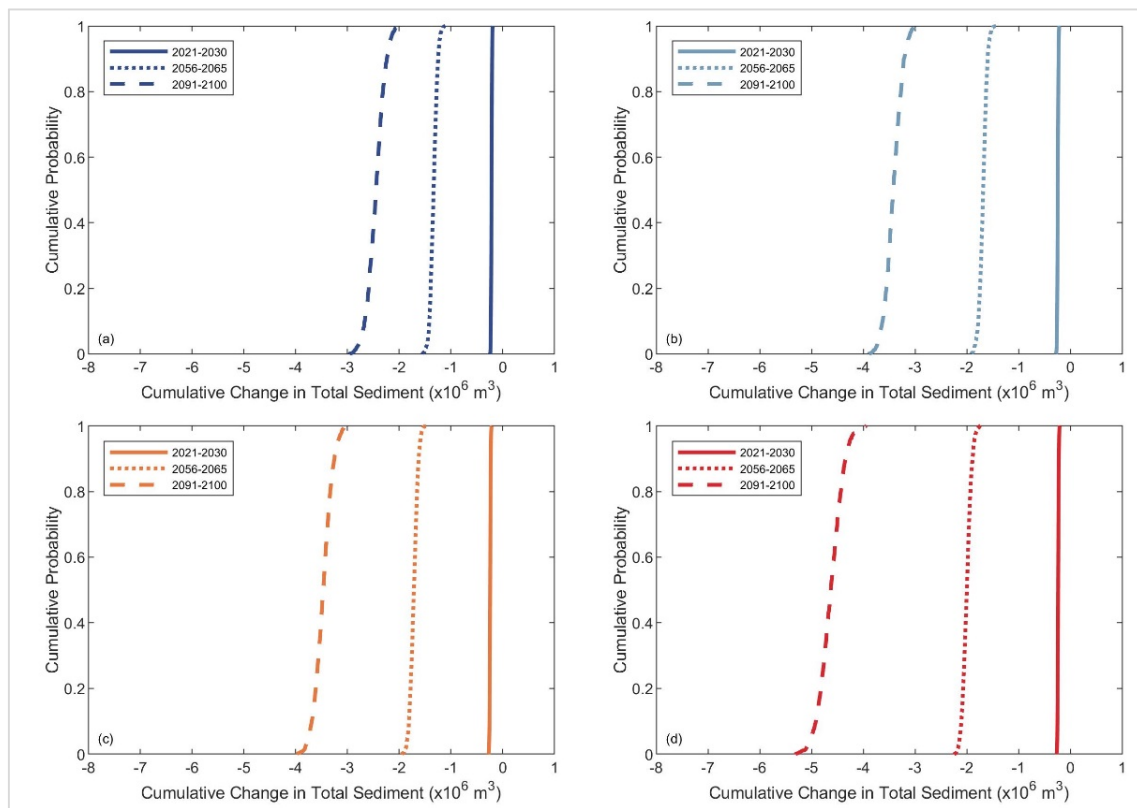


Figure 3-17: Empirical cumulative distributions of the projected change in total sediment volume exchange between the Dyfi estuary and its inlet-interrupted coast. Subplots (a), (b), (c), and (d) are for the RCPs 2.6, 4.5, 6.0, and 8.5, respectively.

Figure 3-17 shows the empirical cumulative distributions (CDFs) of the projected change in total sediment volume exchange (ΔV_T) at Dyfi estuary over the three decadal periods considered (2021-2030, 2056-2065, and 2091-2100) for all RCPs.

During the first decadal period, ΔV_T at this inlet-estuary system shows very little uncertainty under all four RCPs. These uncertainties increase slightly over the mid-century period for all RCPs (~ 0.5 MCM), increasing to considerable uncertainties by the end-century period, in which the largest (~ 1.5 MCM) variations by 2100 was projected for RCP 8.5.

The coastline changes associated with the 50th percentile values of ΔV_T for the Dyfi estuary are presented in the following sub-section.

3.4.3 Projected changes in coastline position

The projected 50th percentile cumulative change in total sediment volume exchange (ΔV_T) between the estuary and its adjacent coast by the same periods are presented in Table 3-5. Those projections of ΔV_T indicate that the Dyfi estuary is likely to import sediment from the adjacent coast during the periods considered (i.e., by 2040, 2060, 2080, and 2100) for all RCPs. A comparison of the above ΔV_T and the net annual longshore sediment transport capacity near the inlet indicates that the coastline evolution at Dyfi estuary could be projected as Type-C behaviour (i.e., LST is less than the sediment volume demand by the estuary; described in Section 2.4.1). Therefore, both the up- and the down-drift coast will be subjected to additional coastal recession driven by the change in total sediment volume exchange (ΔV_T), on top of that due to the Bruun effect. The extent of additional coastal recession along the down-drift coastline is constrained by the longshore sediment transport capacity. The additional coastal erosion along the up-drift coast corresponds to the deficit sediment volume (i.e., the difference between the estuarine sediment demand (Table 3-5) and longshore sediment transport capacity; as described in Section 2.4.1).

Table 3-5: The 50th percentile values of the cumulative change in total sediment volume exchange considered for coastline change projections at the Dyfi estuary. Note: Negative signs denote sediment demand in the estuary.

| Year | Cumulative Change in Total Sediment Volume ($\Delta V_T \times 10^6 \text{ m}^3$) | | | |
|------|---|---------|---------|---------|
| | RCP 2.6 | RCP 4.5 | RCP 6.0 | RCP 8.5 |
| 2040 | -0.68 | -0.81 | -0.82 | -0.86 |
| 2060 | -1.31 | -1.66 | -1.69 | -1.97 |
| 2080 | -1.95 | -2.61 | -2.65 | -3.34 |
| 2100 | -2.58 | -3.64 | -3.69 | -4.99 |

The projected 50th percentile changes of the inlet-affected coastline at the Dyfi estuary are shown in Figure 3-18.

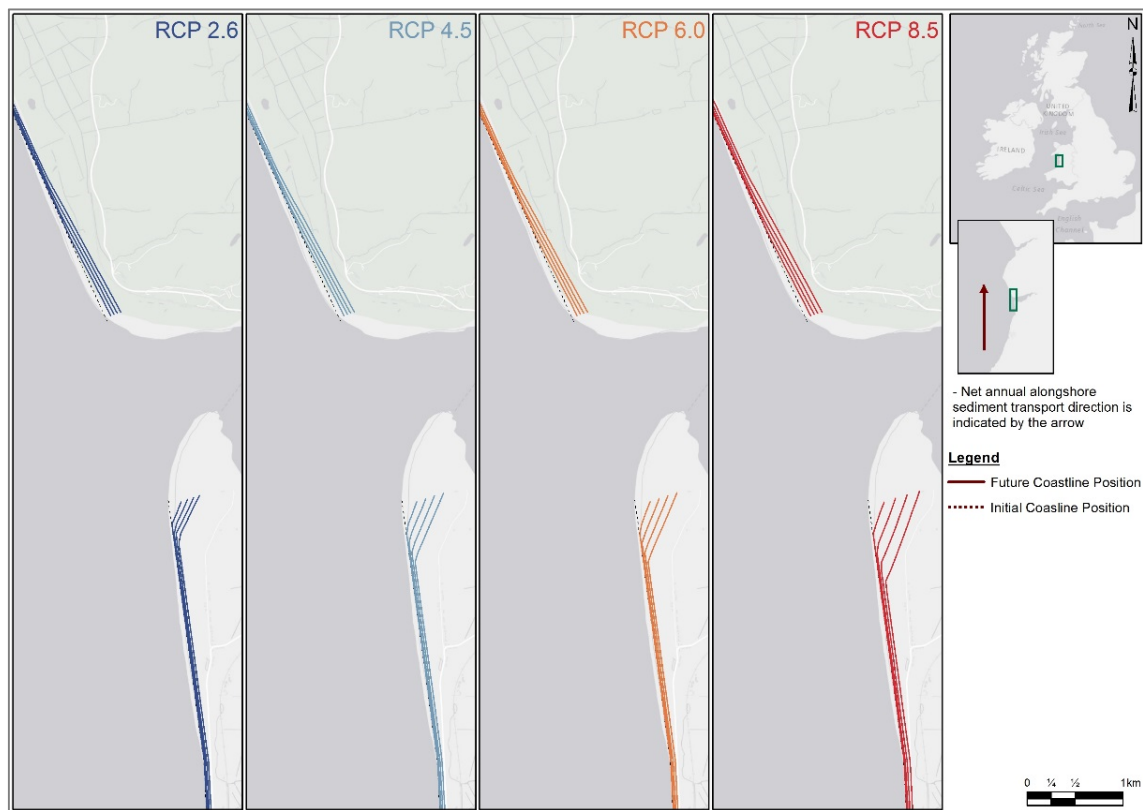


Figure 3-18: Projected changes of the inlet-affected coastline at the Dyfi estuary. The four solid lines in each subplot represent the final coastline position by 2040, 2060, 2080 and 2100 (in the same order, moving landward from the most seaward line).

The model results indicate that the down-drift coast at the Dyfi estuary may erode by ~75 m (RCP 2.6) to ~92 m (RCP 8.5) by 2100 (i.e., ~-1 m/yr rate of erosion). However, the up-drift coast is projected to be eroded between ~95 m (RCP 2.6) and ~152 m (RCP 8.5) by 2100 (i.e., ~-1.5 m/yr rate of erosion). The coastline-change projections presented by Vousdoukas et al. (2020), which excludes the effects of the estuary, indicate ~100 m erosion along both up-and down-drift coast by 2100 for RCP 8.5.

3.5 Kalutara inlet system

3.5.1 Stochastic model inputs

Figure 3-19 shows the projected variations of annual mean temperature at the Kalu River catchment over the three decadal periods considered (2021-2030, 2056-2065, and 2091-2100). Unlike the globally-averaged temperature variation published by Stocker et al. (2013), the 50th percentile annual mean temperature values in the Kalu River catchment show differences during mid- and end-century periods for RCP 2.6, in which the latter period (i.e., 2091-2100) projection is ~0.25°C warmer than the former. The projected maximum and minimum increments of the 50th percentile annual mean temperature values by 2100 are ~2.5°C and < 0.5°C for RCP 8.5 and 2.6, respectively.

Figure 3-20 shows the projected variations in annual cumulative river discharges of the Kalu River over the same three decadal periods, indicating increased river discharge over the 21st century for all RCPs. Except for RCP 2.6, the projected annual cumulative river discharges are increased by 2050 as well. The projected maximum and minimum increments in the 50th percentile values by 2100 are ~0.75 km³/yr and ~0.25 km³/yr for RCP 8.5 and 2.6, respectively. The projections for RCP 8.5 indicated a small likelihood (~1% probability of exceedance) of extreme discharges (~3 km³/yr) over the latter part of the 21st century, which is about twice the magnitude of the 50th percentile value over the same period.

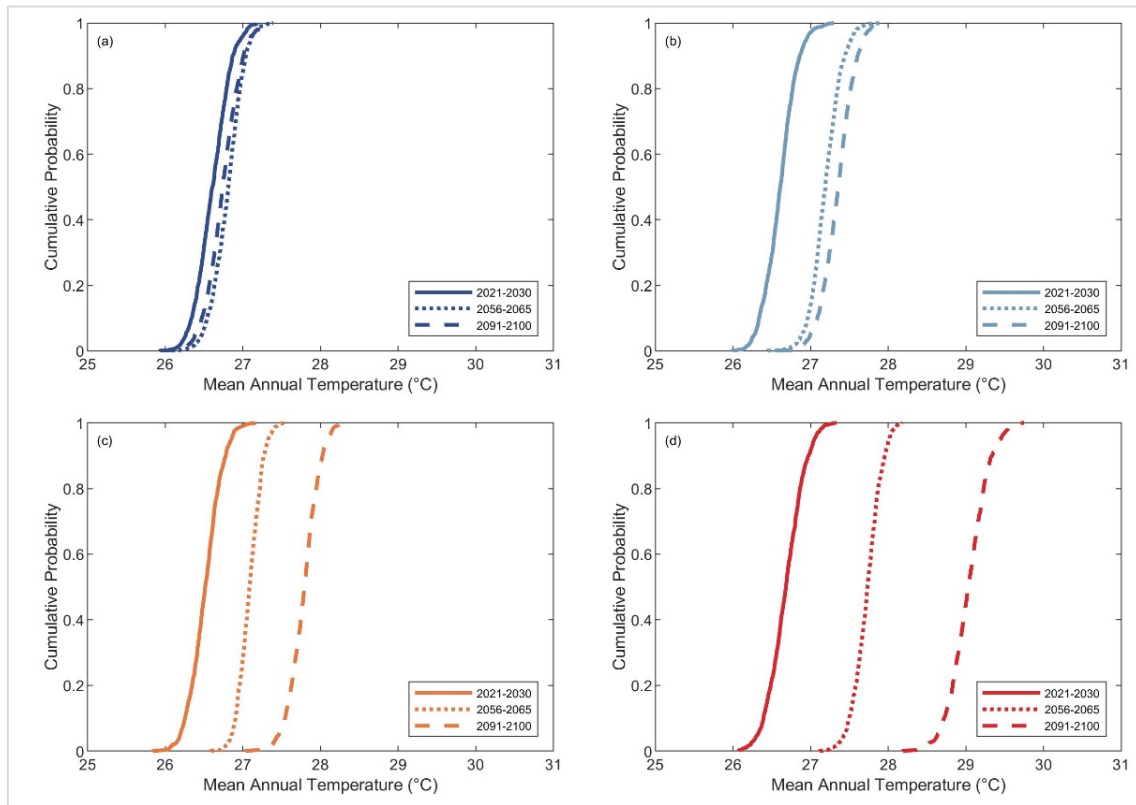


Figure 3-19: Empirical cumulative distributions of averaged annual mean temperature in the Kalu river catchment, Sri Lanka. Subplots (a), (b), (c), and (d) are for the RCPs 2.6, 4.5, 6.0, and 8.5, respectively.

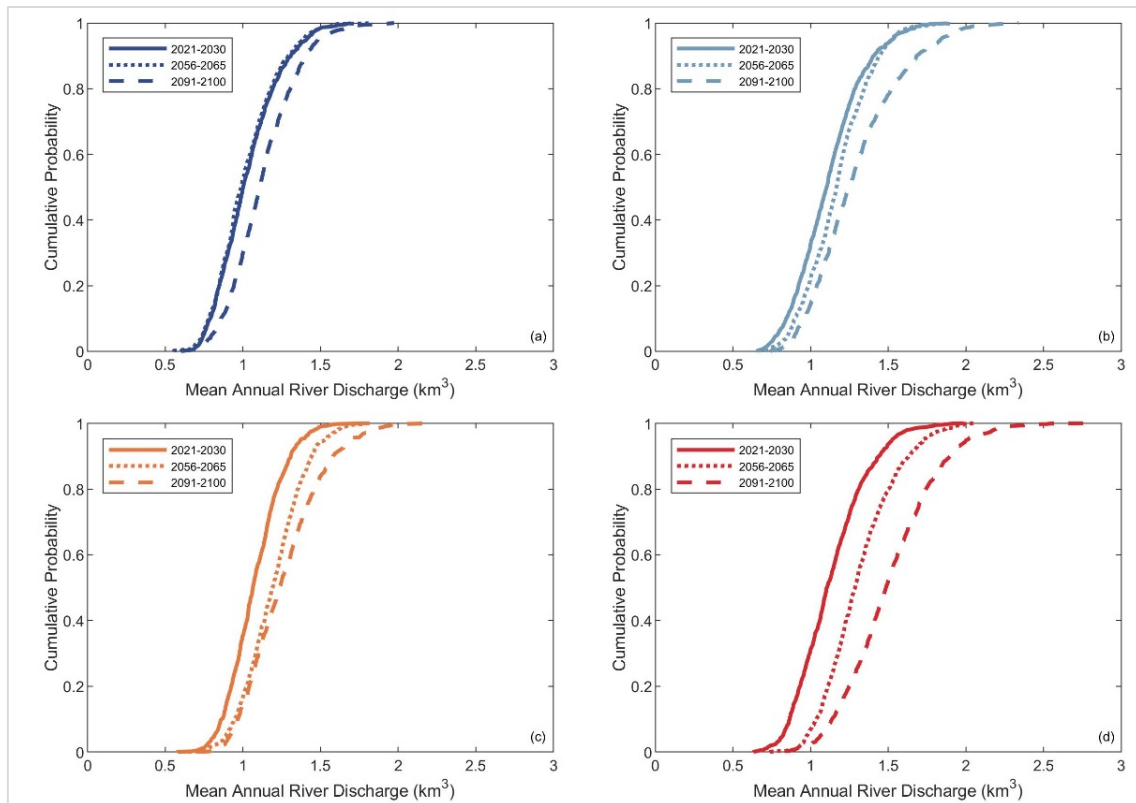


Figure 3-20: Empirical cumulative distributions of averaged annual cumulative river discharge at the Kalutara estuary, Sri Lanka. Subplots (a), (b), (c), and (d) are for the RCP 2.6, 4.5, 6.0, and 8.5, respectively.

Figure 3-13 shows the projected regional relative sea-level changes (ΔRSL) in the vicinity of the Kalutara estuary for 2021-2100 period. The projected maximum and minimum changes in mean ΔRSL by 2100 are ~ 0.65 m, and ~ 0.30 m for RCP 8.5 and 2.6, respectively.

Table 3-6: Projected changes in regional relative sea-level change and its components considered at the vicinity of Kalutara estuary by 2100

| | RCP 2.6 | RPC 4.5 | RCP 6.0 | RCP 8.5 |
|---|---------|---------|---------|---------|
| Global mean sea level change (ΔSL_G in m) | 0.40 | 0.47 | 0.48 | 0.63 |
| Regional variation (ΔSL_{RM} in m) | -0.05 | -0.02 | -0.03 | 0.02 |
| Regional relative sea level change (ΔRSL in m) | 0.35 | 0.45 | 0.45 | 0.65 |

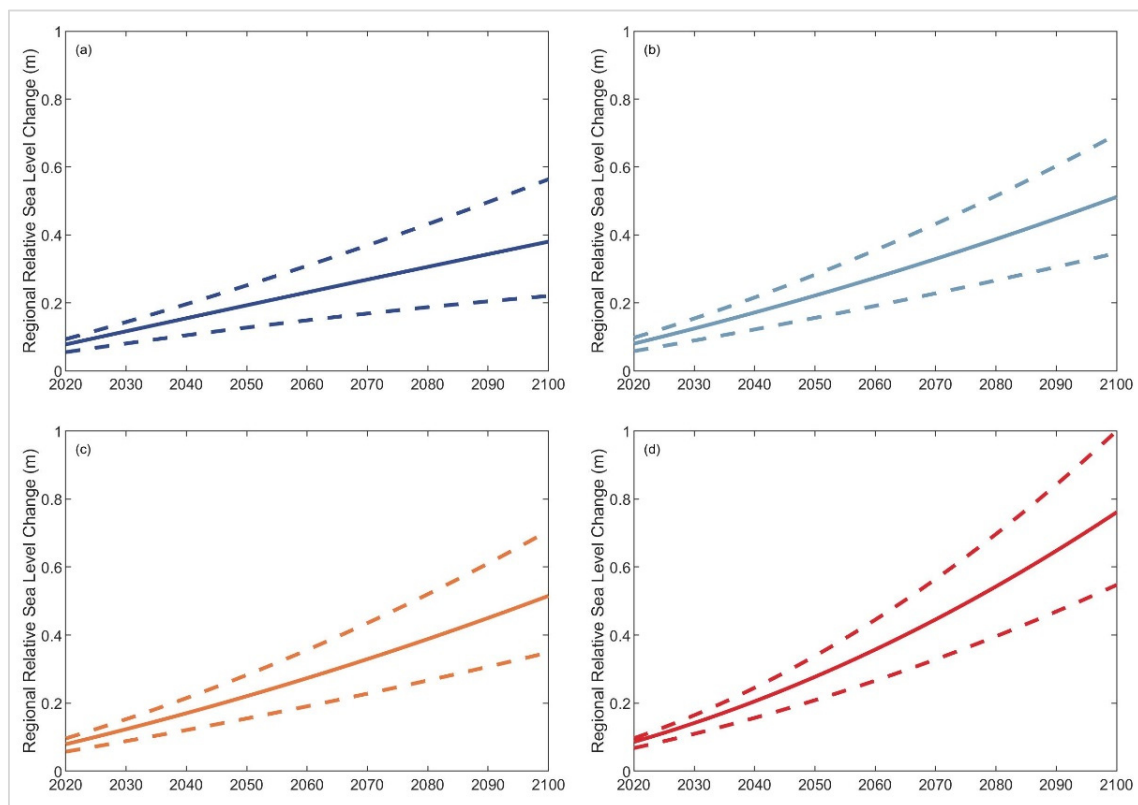


Figure 3-21: Projected changes in regional relative sea level at the Kalu estuary, Sri Lanka. Subplots (a), (b), (c), and (d) are for the RCPs 2.6, 4.5, 6.0, and 8.5, respectively. The solid line indicates the mean change, while the two dashed lines indicate the maximum and minimum variations of ΔRSL .

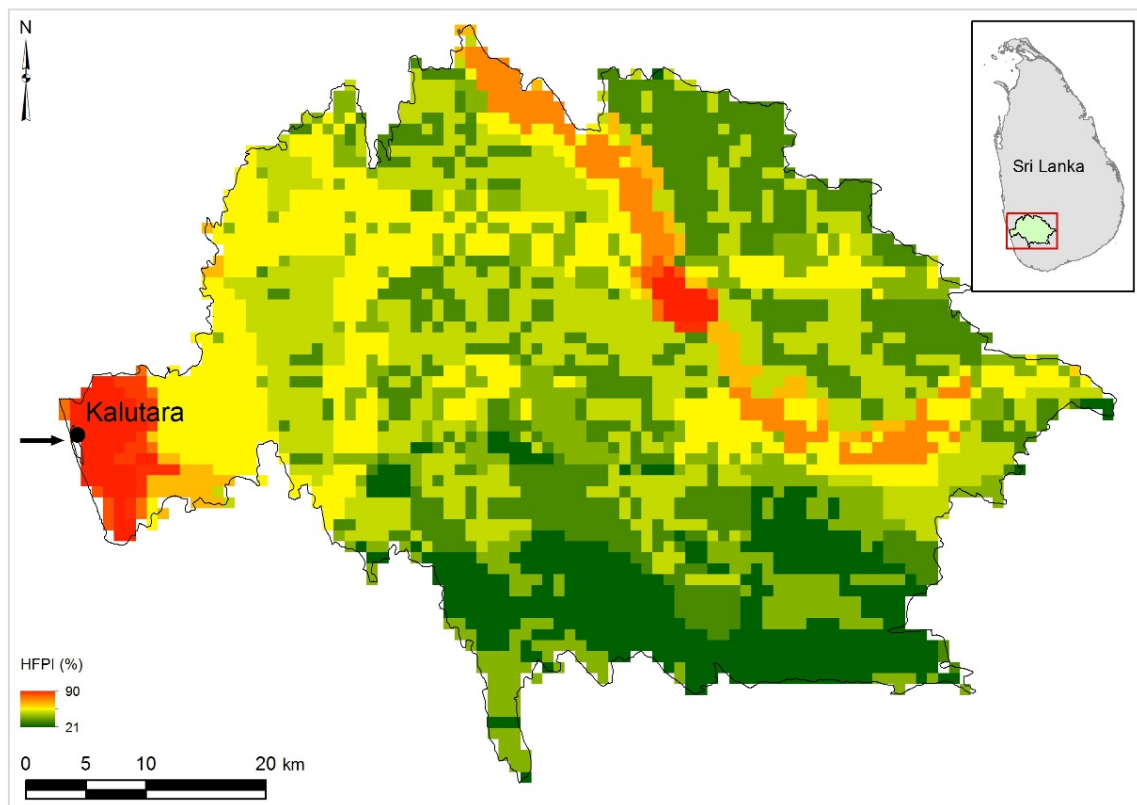


Figure 3-22: Human FootPrint Index (HFPI) of the Kalu River catchment, Sri Lanka. The black arrow in the main figure shows the inlet locations, while the catchment area is shaded in green within the insert location maps.

Figure 3-22 shows the Human FootPrint (HFPI) of the Kalu river catchment, Sri Lanka, which was used to compute the changes in fluvial sediment supply.

Results of the reduced-complexity model application to Kalutara estuary are presented in sub-section 3.5.2 (Future variations of change in total sediment volume exchange between the estuary and the inlet-affected coast) and sub-section 3.5.3 (Projected changes in coastline position).

3.5.2 Future variations of change in total sediment volume exchange between the estuary and the inlet-affected coast

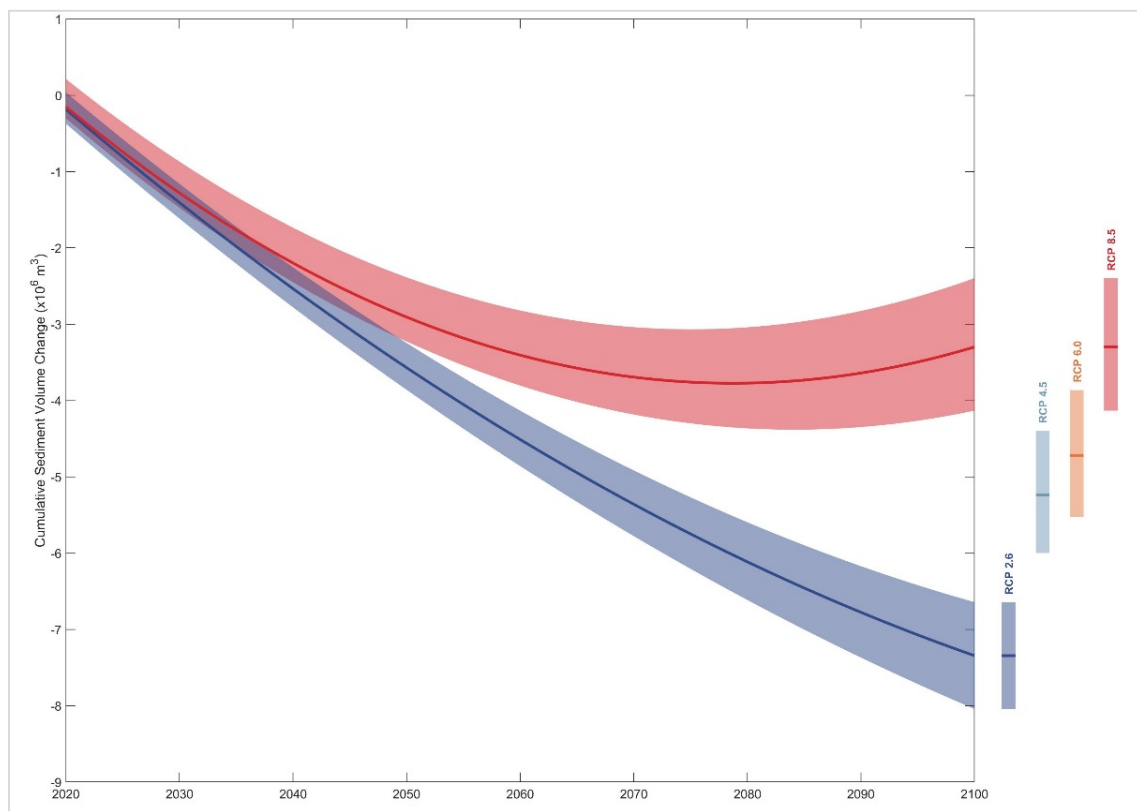


Figure 3-23: Projected variations of change in total sediment volume exchange (ΔV_T) between the Kalurata estuary and its inlet-interrupted coast over the 21st century. The projected ranges between the 10th and 90th percentile are shown as shaded bands with the variation of the 50th percentile values indicated by solid lines for RCP 2.6 (blue) and RCP 8.5 (red). Vertical bars indicate the projected ranges between the same percentiles by 2100 for all RCPs with the 50th percentile values indicated as horizontal lines.

The above figure (Figure 3-23) shows the projected variations in the change in total sediment volume exchange (ΔV_T) between the Kalurata estuary and its inlet-interrupted coast over the 21st century.

According to these results, the 50th percentile value and the uncertainty of ΔV_T will increase gradually over the 21st century. The same percentile value for RCP 8.5 also increases until the mid-century and then decreases towards the end-century period, while the uncertainty increases gradually over the 21st century. The largest and the smallest magnitudes of the projected 50th percentile value of ΔV_T by 2100 are ~ 7.5 MCM and ~ 3.5 MCM for RCP 2.6 and 8.5, respectively. The above variations in ΔV_T are closely related to the differences in projected sea level, annual mean temperature, and annual cumulative river discharge values among the different RCPs, and are discussed in more detail below.

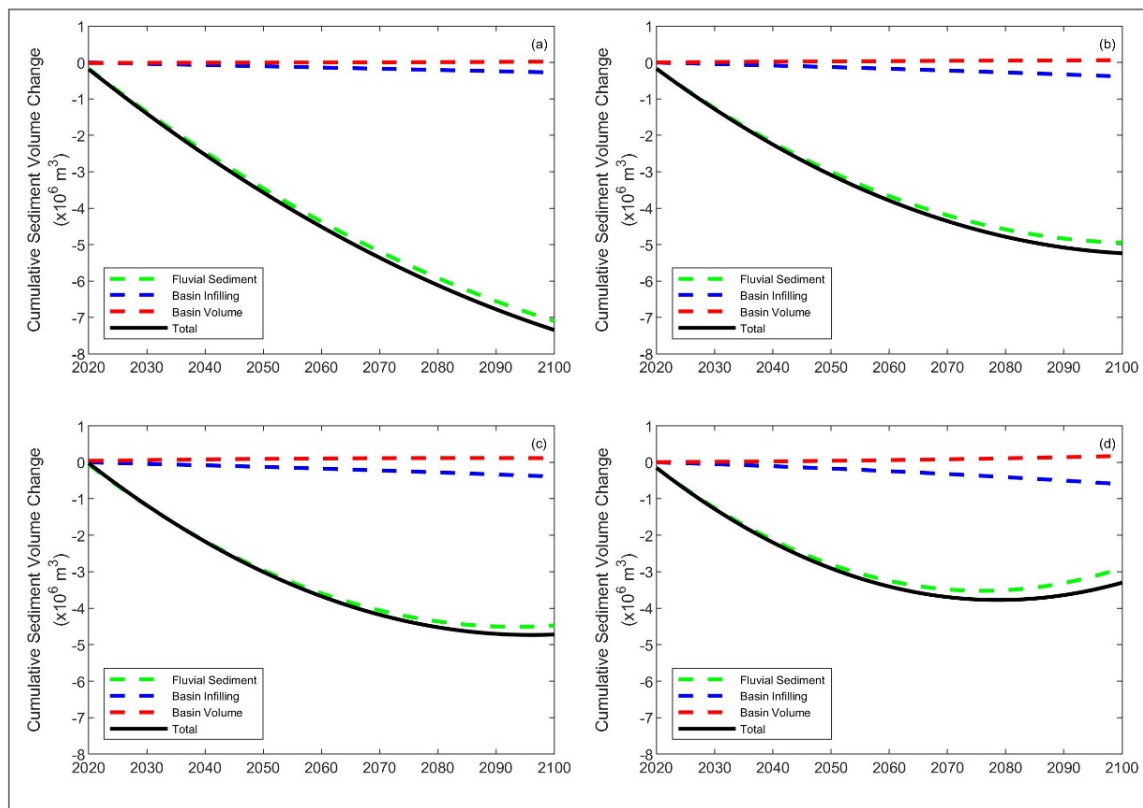


Figure 3-24: Variations of the projected 50th percentile values of change in total sediment volume exchange (ΔV_T) and the different contributing processes at the Kalurata estuary over the 21st century. Subplots (a), (b), (c), and (d) are for the RCPs 2.6, 4.5, 6.0, and 8.5, respectively.

Figure 3-24 shows the variations of the projected 50th percentile values of change in total sediment volume exchange (ΔV_T) and the different contributing processes (basin infilling volume (ΔV_{BI}), basin volume change (ΔV_{BV}) and change in fluvial sediment supply (ΔV_{FS})) at the Kalutara estuary for the entire study period 2021-2100 under all RCPs. The results presented in the above figure indicate that ΔV_T at the Kalutara estuary system is governed by the fluvial sediment supply (ΔV_{FS}) for all RCPs. The results also indicate that the projected variations of ΔV_{BI} and ΔV_{BV} have trivial impact on ΔV_T for all RCPs.

The most significant 50th percentile cumulative sediment volume deficit by 2100 is projected to be ~7.0 MCM for RCP 2.6. This is driven by the reduction in fluvial sediment delivery due to river sand mining, since the projected increases in fluvial sediment supply due to increased T (Figure 3-19) and Q (Figure 3-20) under RCP2.6 do not compensate for this at any time in the 21st century. Despite the same reduction in fluvial sediment due to river sand mining, riverine sediment throughput for RCP 8.5 is projected to increase rapidly towards the end of this century, resulting in ΔV_T of ~-3.5 MCM by 2100 (relative to 2020) under RCP 8.5.

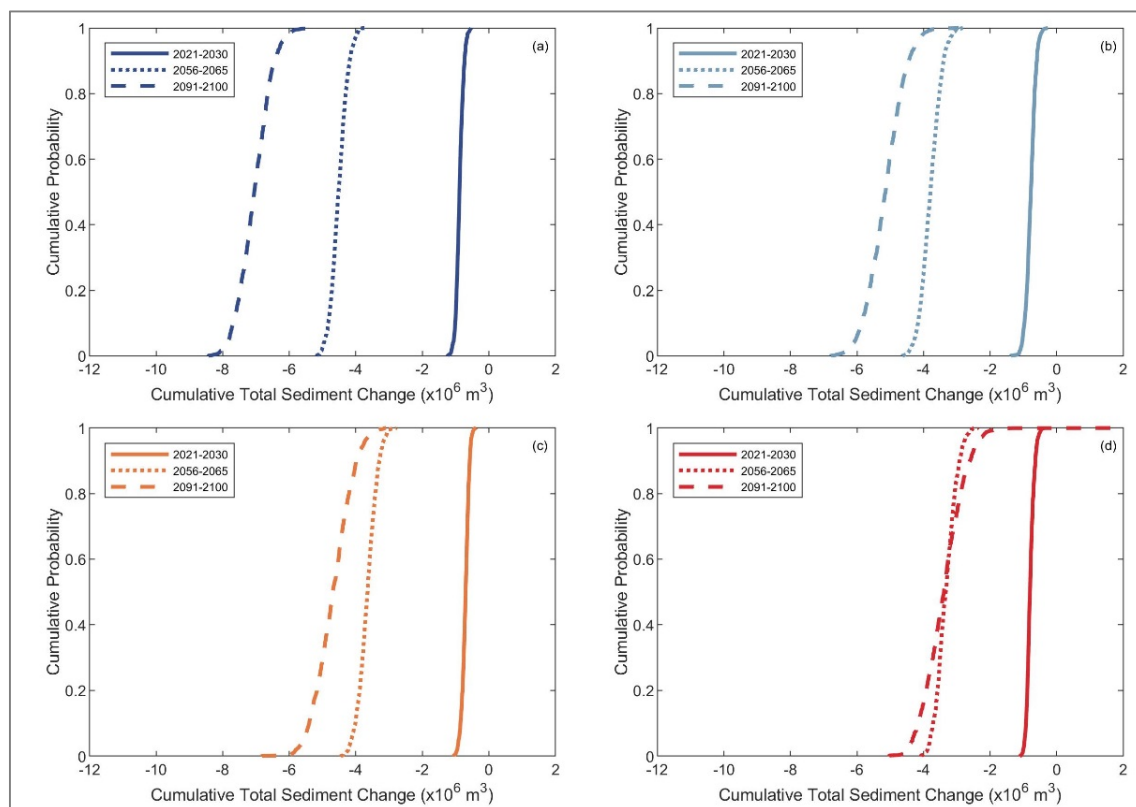


Figure 3-25: Empirical cumulative distributions of the projected change in total sediment volume exchange between the Kalutara estuary and its inlet-interrupted coast. Subplots (a), (b), (c), and (d) are for the RCPs 2.6, 4.5, 6.0, and 8.5, respectively.

Figure 3-25 shows the empirical cumulative distributions (CDFs) of the projected change in total sediment volume exchange (ΔV_T) at Kalutara estuary over the three decadal periods considered (2021-2030, 2056-2065, and 2091-2100) for all RCPs.

During the first decadal period, ΔV_T at this inlet-estuary system shows very little uncertainty under all four RCPs. These uncertainties increase slightly over the mid-century period for all RCPs (~ 1.0 MCM), increasing to considerable uncertainties by the end-century period, in which the largest (~ 5.0 MCM) variation by 2100 was projected for RCP 8.5.

The coastline changes associated with the 50th percentile values of ΔV_T for Kalutara inlet are presented in the following sub-section.

3.5.3 Projected changes in coastline position

The projected 50th percentile cumulative change in total sediment volume exchange (ΔV_T) between the estuary and its adjacent coast by the same periods are presented in Table 3-7. These projections of ΔV_T indicate that the Kalutara estuary is likely to import sediment from its adjacent coast during the periods considered (i.e., by 2040, 2060, 2080, and 2100) for all RCPs. The only exception for this behaviour is projected for RCP 8.5 for 2100, where the estuary is projected to export sediment to its adjacent coast. Therefore, the down-drift coast will undergo additional coastal recession driven by the change in total sediment volume exchange (ΔV_T), on top of that due to the Bruun effect. The extent of additional coastal recession along the down-drift coastline will correspond to the estuarine sediment demand (Table 3-7).

The coastline change for RCP 8.5 by 2100 could be projected as Type-A behaviour (i.e., estuary exports sediment to the adjacent coast; described in Section 2.4.1). Therefore, the down-drift coast at Kalutara estuary is projected to prograde after 2080 under RCP 8.5 during 2081-2100 period due to the change in total sediment volume exchange (ΔV_T). However, this coastline progradation is less than the projected coastline recession due to the Bruun effect over the same period. Therefore, the cumulative effect of these two contributions results in coastline recession along the down-drift coast. The up-drift coast is only affected by the coastline recession due to the Bruun effect.

Table 3-7: The 50th percentile values of the cumulative change in total sediment volume exchange considered for coastline change projections at the Kalutara estuary. Note: Negative signs denote sediment demand into the estuary.

| Year | Cumulative Change in Total Sediment Volume ($\Delta V_T \times 10^6 \text{ m}^3$) | | | |
|------|---|---------|---------|---------|
| | RCP 2.6 | RCP 4.5 | RCP 6.0 | RCP 8.5 |
| 2040 | -2.54 | -2.25 | -2.17 | -2.20 |
| 2060 | -4.51 | -3.79 | -3.67 | -3.41 |
| 2080 | -6.12 | -4.79 | -4.52 | -3.77 |
| 2100 | -7.34 | -5.24 | -4.72 | -3.30 |

Projected 50th percentile changes of the inlet-affected coastline at the Kalutara estuary are shown in Figure 3-26.

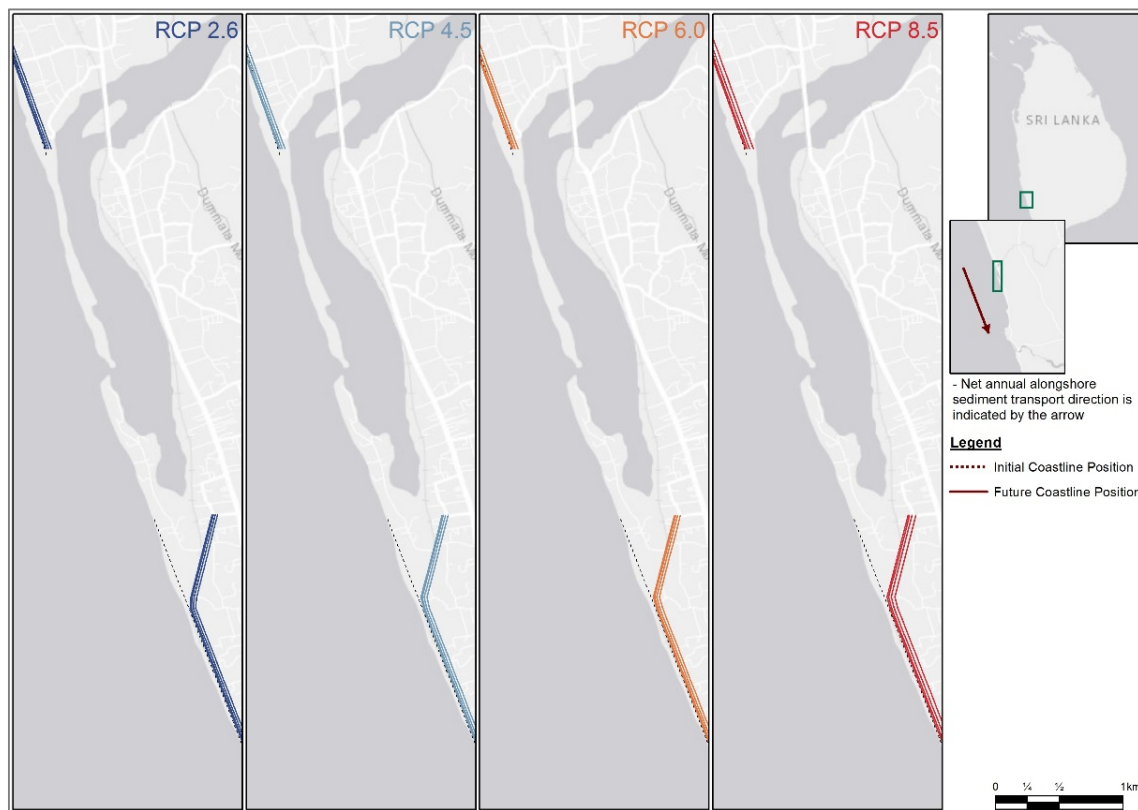


Figure 3-26: Projected changes of the inlet-affected coastline at Kalutara estuary. The four solid lines in each subplot represent the final coastline position by 2040, 2060, 2080 and 2100 (in the same order, moving landward from the most seaward line).

The model results indicate that the down-drift coast at the Kalutara inlet may erode by ~92 m (RCP 2.6) to ~105 m (RCP 8.5) by 2100 (i.e., ~-1.5 m/yr rate of erosion). The up-drift coast is only affected by the coastal recession due to the Bruun effect and hence projected to erode by ~50 m (RCP 2.6) to ~67 m (RCP 8.5) by 2100 (i.e., ~-0.5 m/yr rate of erosion). The coastline change projections presented by Vousdoukas et al. (2020), which excludes the effects of the estuary, indicate ~150 m erosion along both up-and down-drift coast by 2100 for RCP 8.5. According to the model results presented in Table 3-7, the Kalurata inlet-estuary system will export sediment to the coast by 2100 for RCP 8.5, which in turn will reduce the coastal recession due to the Bruun effect. Therefore, the 2100 coastline change projected by the presented modelling technique is less than that projected by Vousdoukas et al. (2020).

3.5.4 Future variations of change in total sediment volume exchange between the estuary and the inlet-affected coast (Excluding river sand mining effect)

All results presented in Section 3.5.2 and 3.5.3 have considered the effect of sand mining in the river on the fluvial sediment supply by the Kalu River. A second set of simulations was also undertaken to investigate the impact of river sand mining along the Kalu River on the predicted change in total sediment volume exchange (ΔV_T), by removing the impact of sand mining from both the reference and future projections of fluvial sediment supply. The findings are presented in this sub-section (Section 3.5.4).

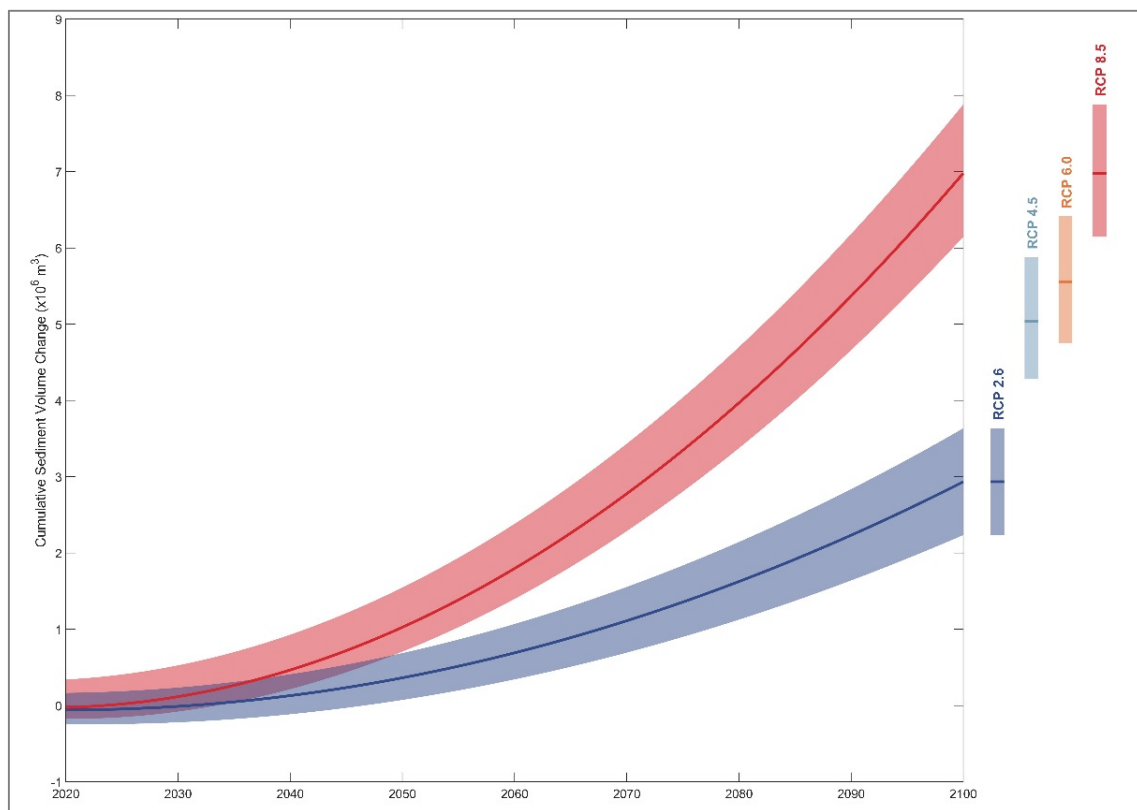


Figure 3-27: Projected variations of change in total sediment volume exchange (ΔV_T) between the Kalutara estuary and its inlet-interrupted coast over the 21st century (excluding the river sand mining). The projected ranges between the 10th and 90th percentile are shown as shaded bands with the variation of the 50th percentile values indicated by solid lines for RCP 2.6 (blue) and RCP 8.5 (red). Vertical bars indicate the projected ranges between the same percentiles by 2100 for all RCPs with the 50th percentile values indicated as horizontal lines.

Figure 3-27 illustrates that the variation in total sediment volume at Kalutara inlet is entirely overwhelmed by the anthropogenic impacts (i.e., river sand mining). Contrasting with the projected behaviour when accounting for river sand mining (Figure 3-23), positive values for the 50th percentiles of ΔV_T are projected for RCP 2.6 and 8.5 during the entire study period. The lowest and the highest magnitudes of the 50th percentile value of ΔV_T by 2100 are projected to be ~3 MCM and ~7 MCM for RCP 2.6 and 8.5, respectively. The above variations in ΔV_T are closely related to the differences in projected sea level,

annual mean temperature, and annual cumulative river discharge values among the different RCPs, and are discussed in more detail below.

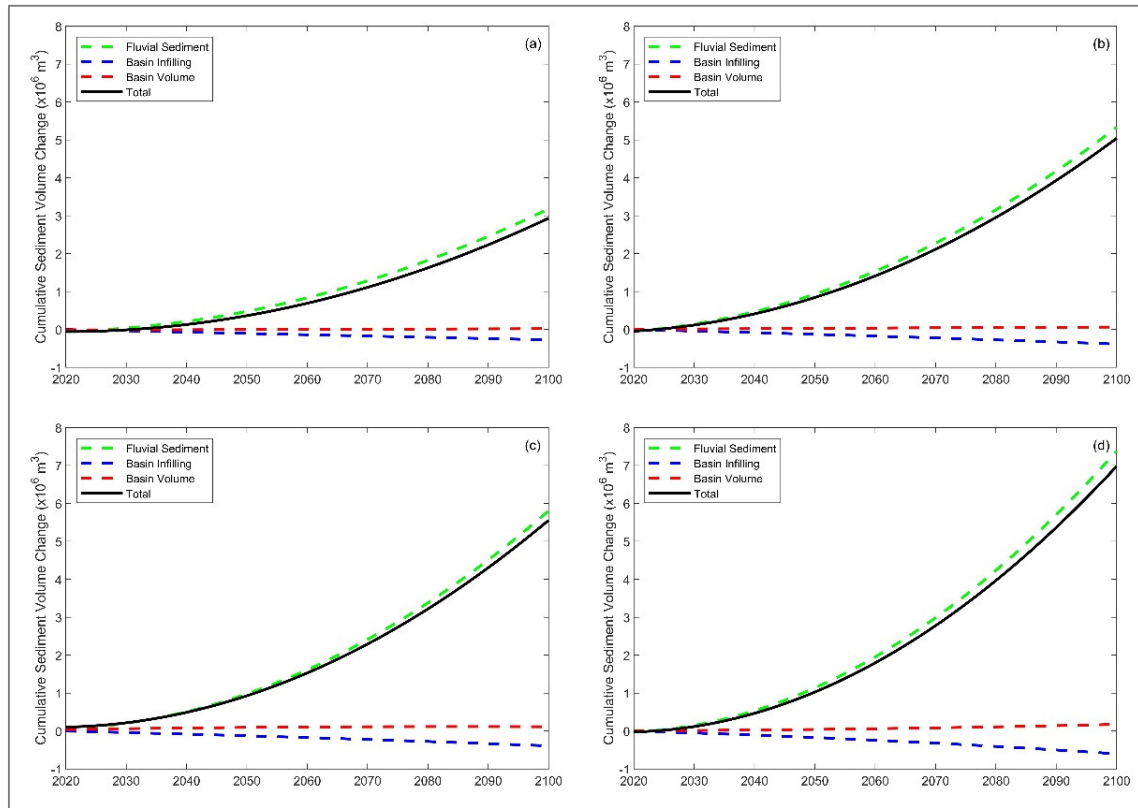


Figure 3-28: Variations of the projected 50th percentile values of change in total sediment volume exchange (ΔV_T) and the different contributing processes at the Kalurata estuary over the 21st century (excluding river sand mining). Subplots (a), (b), (c), and (d) are for the RCPs 2.6, 4.5, 6.0, and 8.5, respectively.

Figure 3-28 shows the variation of the projected 50th percentile values of change in the total sediment volume exchange (ΔV_T) and the different contributing processes (basin infilling volume (ΔV_{BI}), basin volume change (ΔV_{BV}) and change in fluvial sediment supply (ΔV_{FS})) at the Kalutara estuary for the entire study period of 2021-2100 under all RCPs. The results presented in the above figure indicate that ΔV_T at Kalutara estuary system is governed by the fluvial sediment supply (ΔV_{FS}) for all RCPs. The above figure indicates that the variation of ΔV_T at this inlet-estuary system is dominated by fluvial sediment supply when the river sand mining effect is excluded. Thus, the anthropogenic impact (i.e., river sand mining) appears to overwhelm the natural behaviour of this system if it continues into the future. A significant reduction in fluvial sediment supply along the river systems due to anthropogenic impacts is foreshadowed to be a significant concern for inlet-estuary systems (Ranasinghe et al., 2019b; Syvitski and Milliman, 2007; Vörösmarty et al., 2003), and the Kalutara inlet appears to be no exception in this regard.

3.6 Swan River System

3.6.1 Stochastic Model Inputs

The stochastic model inputs of annual mean temperature and annual cumulative river discharge were generated from the fitted joint probability distributions (as described in Section 2.3). Input for the joint probability distributions was obtained from 4 GCMs with daily/monthly projections of temperature and runoff over the Swan River catchment. These projections were yearly averaged to compute the input of the above fitted joint probability distributions. Details of the GCMs used are provided in Annex A.1.

Figure 3-29 shows the projected variations of the annual mean temperature at the Swan River catchment over the three decadal periods considered (2021-2030, 2056-2065, and 2091-2100). Unlike to the globally-averaged temperature variation published by Stocker et al. (2013), the 50th percentile annual mean temperature values for the Swan River catchment show differences during the mid- and end-century periods for RCP 2.6, in which the latter period (i.e., 2091-2100) projection is ~0.25°C warmer than the former duration. The projected maximum and minimum increments of the 50th percentile annual mean temperature values by 2100 are ~3.0°C and <0.5°C for RCP 8.5 and 2.6, respectively. The projected increments of the 50th percentile annual mean temperature values for RCP 4.5 and 6.0 by 2100 are ~1.0°C and ~1.5°C, respectively.

Figure 3-30 shows the projected variation in annual cumulative river discharges of the Swan River over the same three decadal periods, indicating a decrease in river discharge over the 21st century for all RCPs. The annual cumulative river discharges over the mid- and end-century periods are projected to be similar for all but RCP 8.5. The projection of cumulative river discharge for RCP 8.5 over the end-century period is greater than the predicted values over the mid-century period. The projected maximum and minimum reductions in the 50th percentile values by 2100 are ~0.75 km³/yr (for RCP 2.6 and 6.0) and ~0.50 km³/yr (for RCP 8.5).

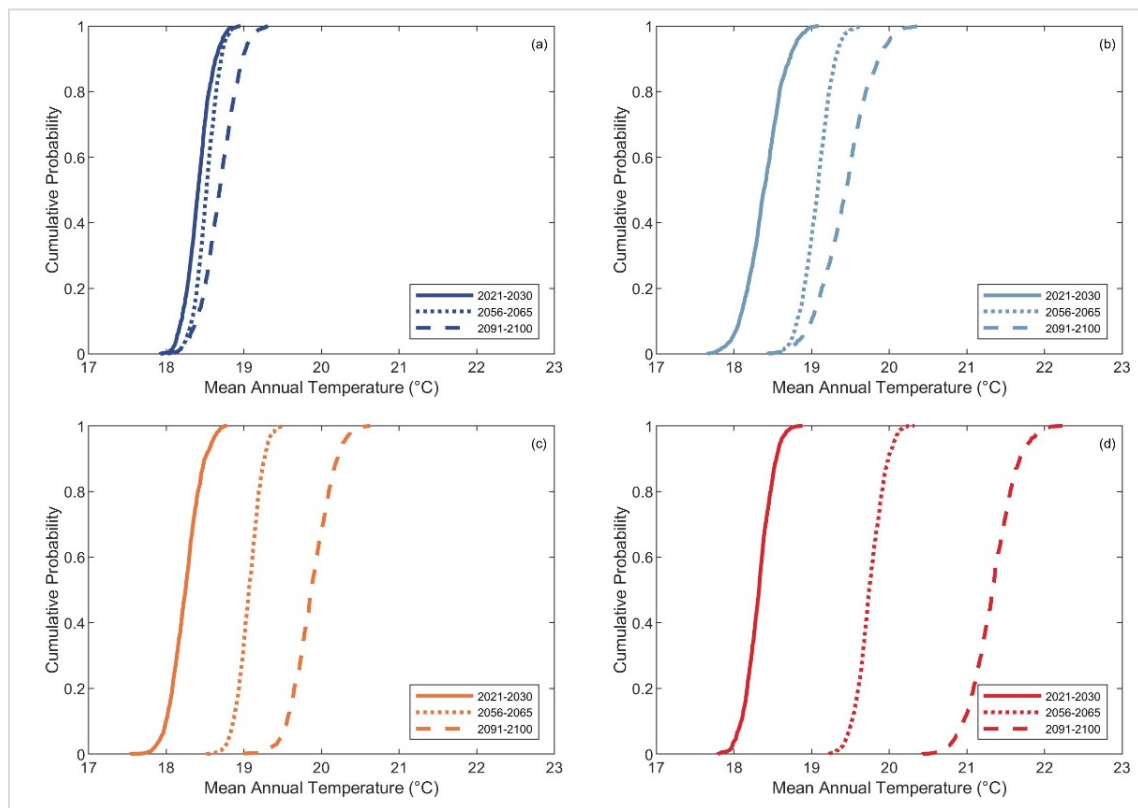


Figure 3-29: Empirical cumulative distributions of averaged annual mean temperature at the Swan River catchment, Australia. Subplots (a), (b), (c), and (d) are for the RCPs 2.6, 4.5, 6.0, and 8.5, respectively.

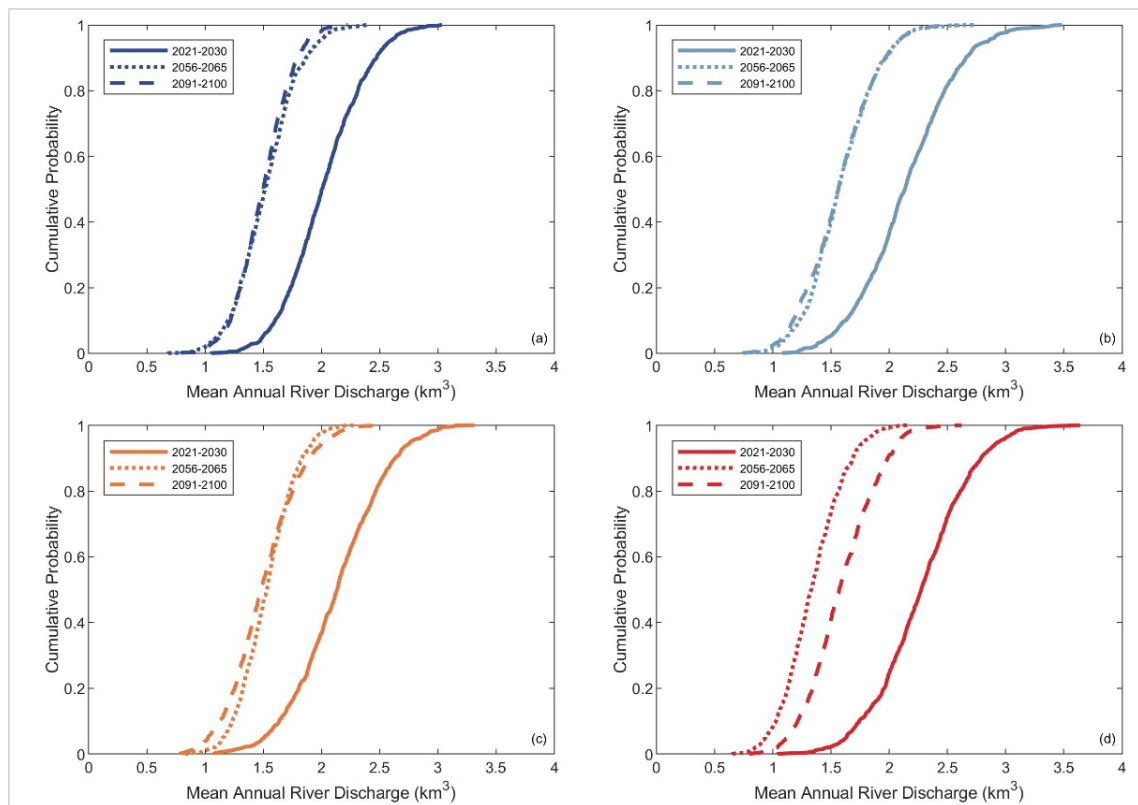


Figure 3-30: Empirical cumulative distributions of averaged annual cumulative river discharge at the Swan River, Australia. Subplots (a), (b), (c), and (d) are for the RCPs 2.6, 4.5, 6.0, and 8.5, respectively.

Figure 3-31 shows the projected regional relative sea-level changes (ΔRSL) in the vicinity of the Swan River estuary for 2021-2100 period. The projected maximum and minimum changes in mean ΔRSL by 2100 are ~ 0.65 m, and ~ 0.40 m for RCP 8.5 and 2.6, respectively.

Table 3-8: Projected changes in regional relative sea-level change and its components considered at the vicinity of Swan River inlet by 2100.

| | RCP 2.6 | RPC 4.5 | RCP 6.0 | RCP 8.5 |
|---|---------|---------|---------|---------|
| Global mean sea level change (ΔSL_G in m) | 0.40 | 0.47 | 0.48 | 0.63 |
| Regional variation (ΔSL_{RM} in m) | 0.05 | -0.02 | 0.07 | 0.02 |
| Regional relative sea level change (ΔRSL in m) | 0.45 | 0.45 | 0.55 | 0.65 |

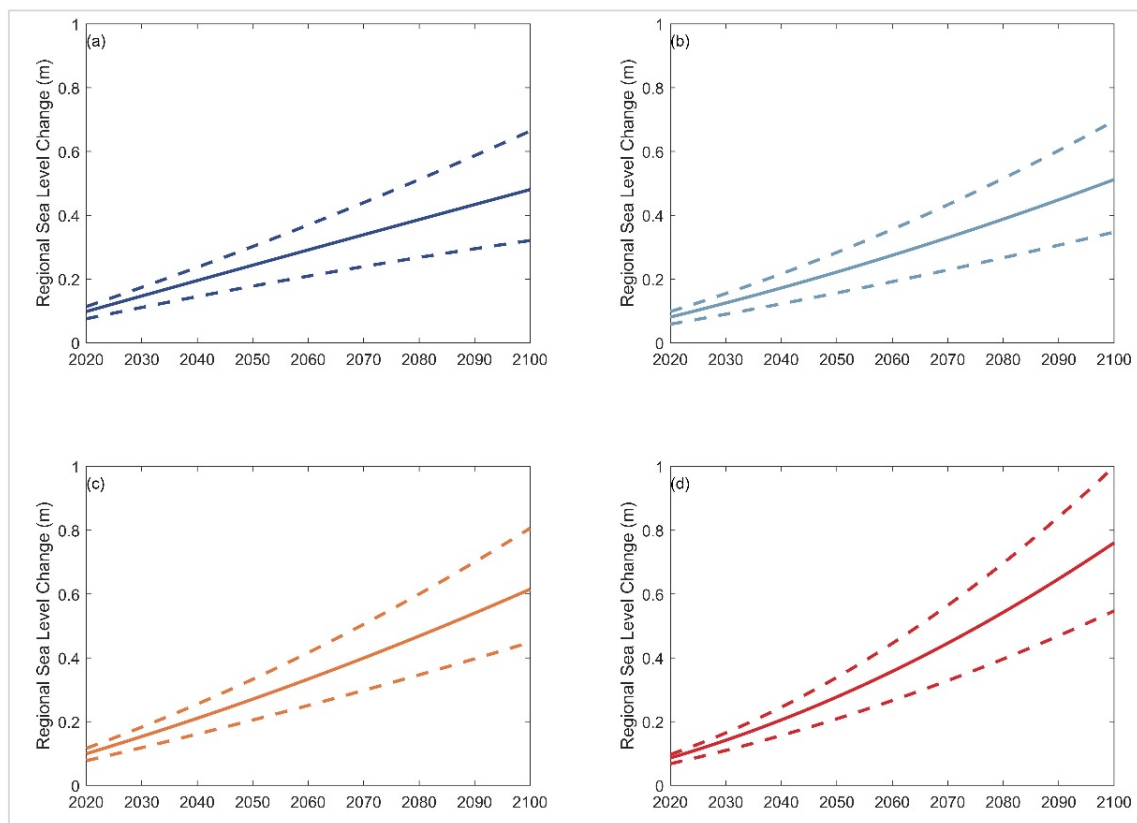


Figure 3-31: Projected changes in regional relative sea level at the Swan estuary, Australia. Subplots (a), (b), (c), and (d) are for the RCPs 2.6, 4.5, 6.0, and 8.5, respectively. The solid line indicates the mean change, while the two dashed lines denote the maximum and minimum variations of ΔRSL .

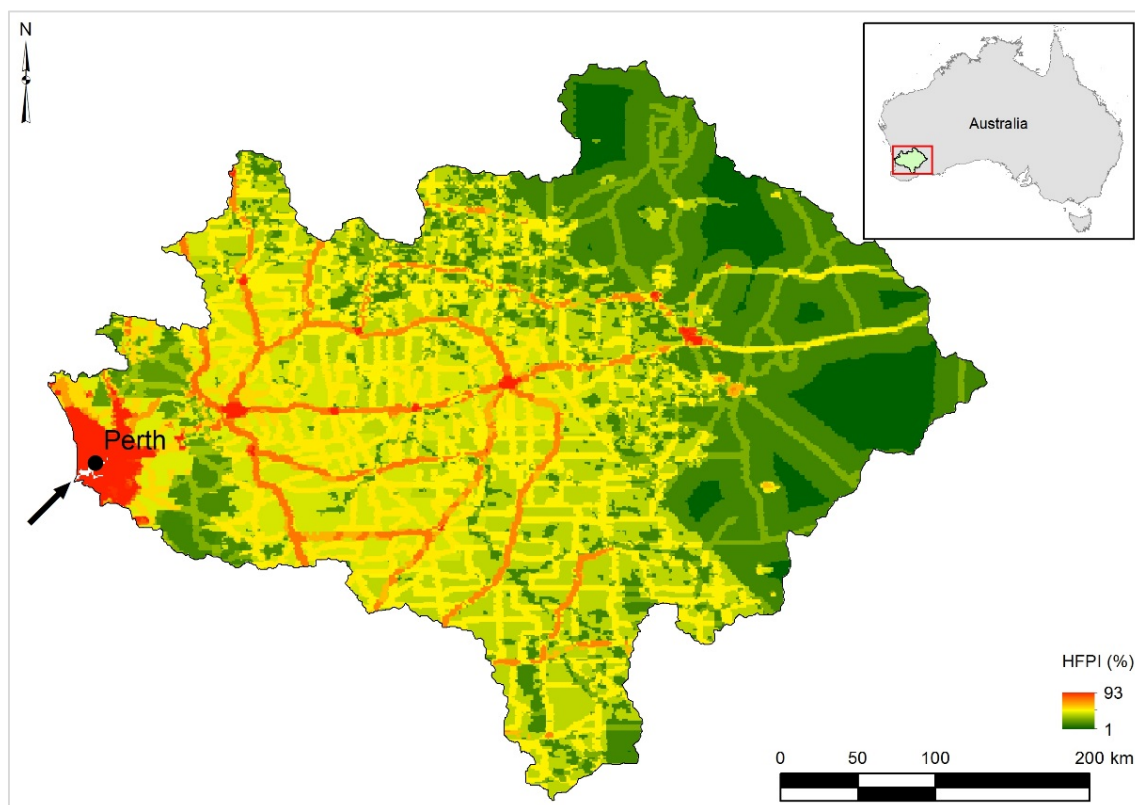


Figure 3-32: Human FootPrint Index (HFPI) of the Swan River catchment, Australia. The black arrow in the main figure shows the inlet locations, while the catchment area is shaded in green within the insert location maps

Figure 3-32 shows the Human FootPrint (HFPI) of the Swan River catchment, Australia, which was used to compute the changes in fluvial sediment supply.

Results of the reduced complexity model application at the Swan River are presented in sub-section 3.6.2 (Future variations of change in total sediment volume exchange between the estuary and the inlet-affected coast) and sub-section 3.6.3 (Projected changes in coastline position).

3.6.2 Future variations of change in total sediment volume exchange between the estuary and the inlet-affected coast

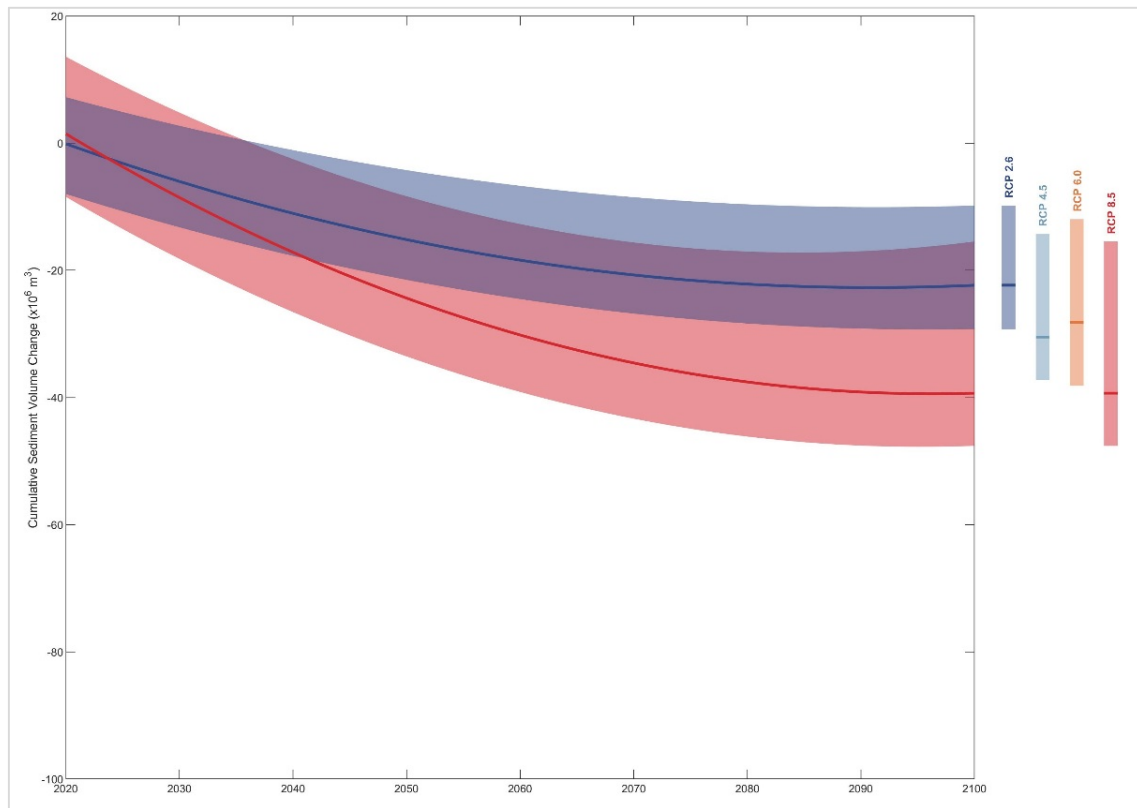


Figure 3-33: Projected variations of change in total sediment volume exchange (ΔV_T) between the Swan River estuary and its inlet-interrupted coast over the 21st century. The projected ranges between the 10th and 90th percentile are shown as shaded bands with the variation of the 50th percentile values indicated by solid lines for RCP 2.6 (blue) and RCP 8.5 (red). Vertical bars indicate the projected ranges between the same percentiles by 2100 for all RCPs with the 50th percentile values indicated as horizontal lines.

The above figure (Figure 3-33) shows the projected variations in the change in total sediment volume exchange (ΔV_T) between the Swan river estuary and its inlet-interrupted coast over the 21st century.

According to these results, the projected 50th percentile value and the uncertainty of ΔV_T for RCP 2.6 and 8.5 increase over 2020-2060 period and gradually stabilise over the end-century period. The largest and the smallest magnitudes of the projected 50th percentile value of ΔV_T by 2100 are for RCP 8.5 (~40 MCM) and 2.6 (~20 MCM), respectively. The projected 50th percentile value of ΔV_T by 2100 for RCP 4.5 and 6.0 is ~30 MCM. The above variations in ΔV_T are closely related to the differences in projected sea level, annual mean temperature, and annual cumulative river discharge values among the different RCPs, and are discussed in more detail below.

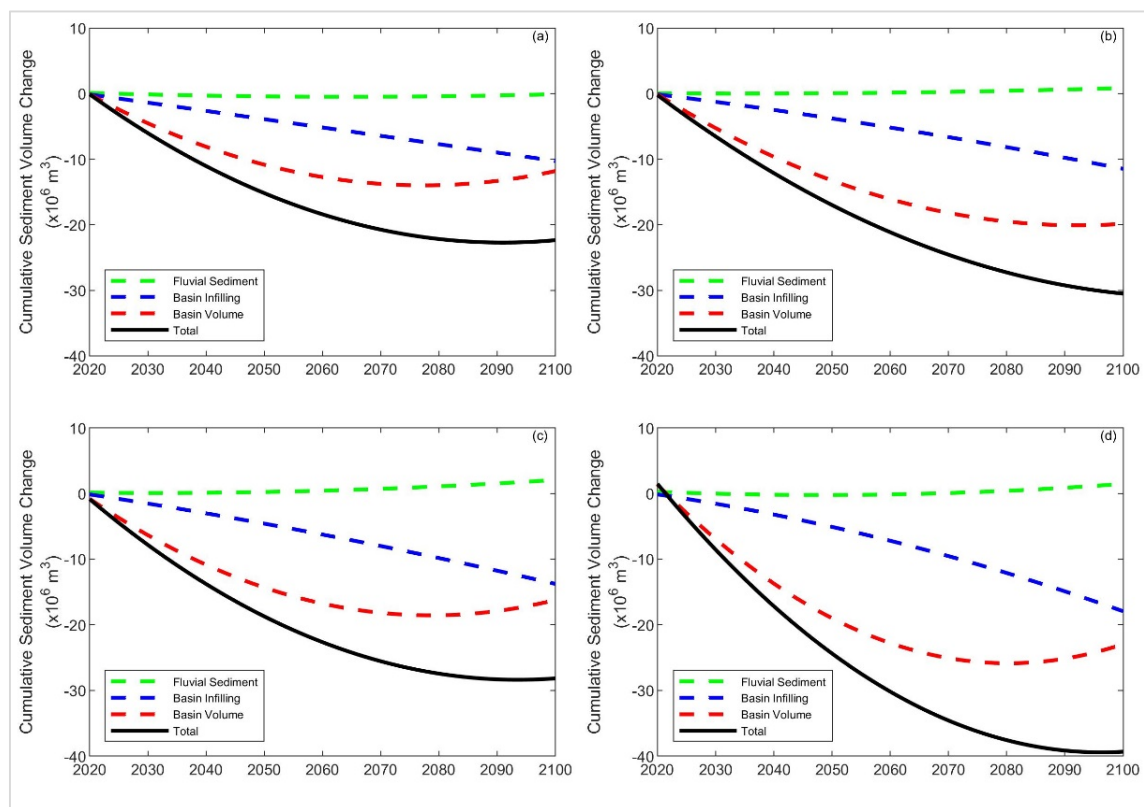


Figure 3-34: Variations of the projected 50th percentile values of change in total sediment volume exchange (ΔV_T) and the different contributing processes at the Swan River over the 21st century. Subplots (a), (b), (c), and (d) are for the RCPs 2.6, 4.5, 6.0, and 8.5, respectively.

Figure 3-34 shows the variations of the projected 50th percentile values of change in total sediment volume exchange (ΔV_T) and the different contributing processes (basin infilling volume (ΔV_{BI}), basin volume change (ΔV_{BV}) and change in fluvial sediment supply (ΔV_{FS})) at the Swan River for the entire study period of 2021-2100 under all RCPs. The results presented in the above figure indicate that ΔV_T at Swan river is governed by the basin volume change (ΔV_{BV}) for all RCPs. The results also indicate that the projected variations of ΔV_{FS} have trivial impacts on ΔV_T for all RCPs.

The sediment demand due to basin volume change (ΔV_{BV}) is projected to increase rapidly under all RCPs over 2020-2060 period and reduce over the late 21st century. The above-projected behaviour is closely related to the projected changes in river discharge (Figure 3-30). The projected variations in ΔV_{BI} also increase over the 21st century for all RCPs, thus increasing the total estuarine sediment demand at this location.

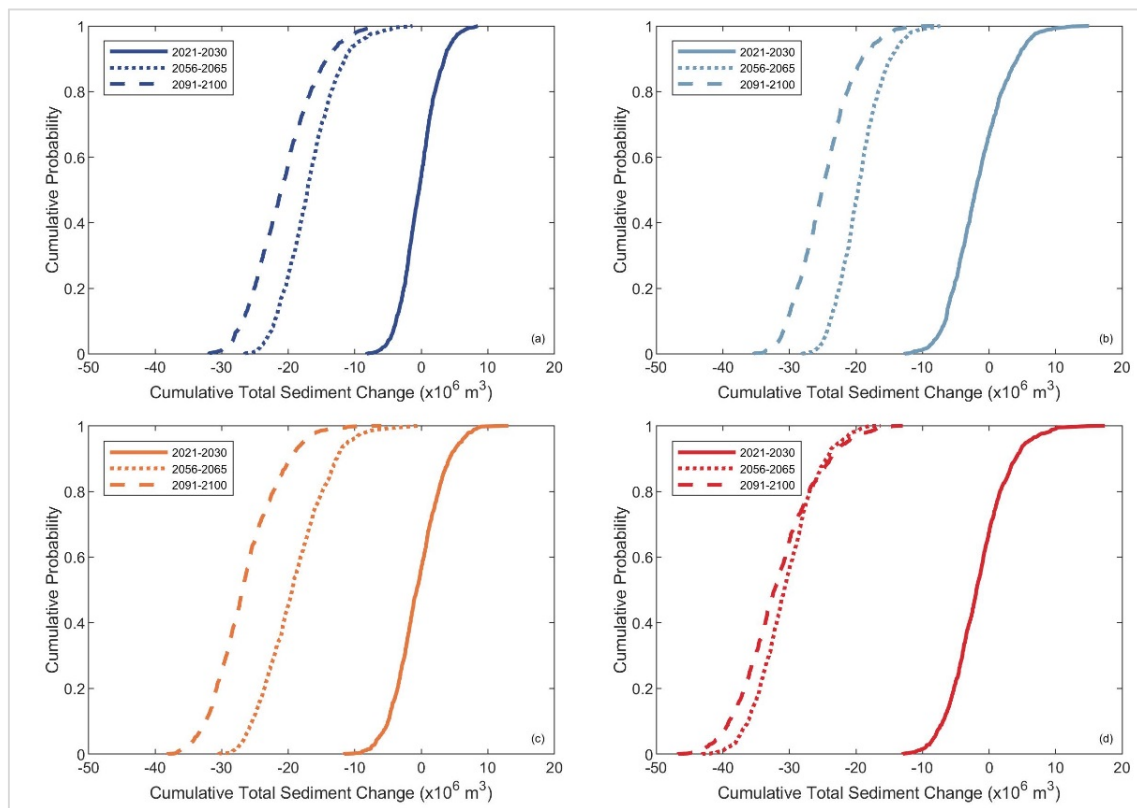


Figure 3-35: Empirical cumulative distributions of the projected change in total sediment volume exchange between the Swan River and its inlet-interrupted coast. Subplots (a), (b), (c), and (d) are for the RCPs 2.6, 4.5, 6.0, and 8.5, respectively.

Figure 3-35 shows the empirical cumulative distributions (CDFs) of the projected change in total sediment volume exchange (ΔV_T) at the Swan River system over the three decadal periods considered (2021-2030, 2056-2065, and 2091-2100) for all RCPs.

Unlike the projected results at the other three case study locations ΔV_T at this inlet-estuary system show significant uncertainties under all four RCPs over the first decadal period. The above uncertainties are driven by the projected changes in river discharge (Figure 3-30). These uncertainties increase slightly over the mid-century period for all RCPs (~ 30 MCM), increasing to considerable uncertainties by the end-century period, in which the most (~ 40 MCM) uncertainty by 2100 was projected for RCP 8.5.

The coastline changes associated with the 50th percentile values of ΔV_T for the Swan River system are presented in the following sub-section.

3.6.3 Projected changes in coastline position

The projected cumulative change in total sediment volume exchange (ΔV_T) between the estuary and its adjacent coast are presented in Table 3-9. Those projections of ΔV_T indicate that the Swan River system is likely to import sediment from its adjacent coast during the periods considered (i.e., by 2040, 2060, 2080, and 2100) for all RCPs. A comparison of the above ΔV_T and the net annual longshore sediment transport capacity near the inlet indicates that the coastline evolution at Swan River could be projected as Type-C behaviour (i.e., LST is less than the sediment volume demand by the estuary; described in Section 2.4.1). Therefore, both the up- and the down-drift coast will be subjected to additional coastal recession driven by the change in total sediment volume exchange (ΔV_T), in addition to that due to the Bruun effect. The extent of additional coastal recession along the down-drift coastline is constrained by the longshore sediment transport capacity. The additional coastal erosion along the up-drift coast corresponds to the deficit of sediment volume (i.e., the difference between the estuarine sediment demand (Table 3-9) and longshore sediment transport capacity; as described in Section 2.4.1).

Table 3-9: The 50th percentile values of the cumulative change in total sediment volume exchange considered for coastline change projections at the Swan River system. Note: Negative signs denote sediment demand in the estuary.

| Year | Cumulative Change in Total Sediment Volume ($\Delta V_T \times 10^7 \text{ m}^3$) | | | |
|------|---|---------|---------|---------|
| | RCP 2.6 | RCP 4.5 | RCP 6.0 | RCP 8.5 |
| 2040 | -1.10 | -1.21 | -1.38 | -1.72 |
| 2060 | -1.84 | -2.11 | -2.74 | -3.02 |
| 2080 | -2.21 | -2.73 | -2.74 | -3.76 |
| 2100 | -2.24 | -3.05 | -2.82 | -3.93 |

The projected 50th percentile changes of the inlet-affected coastline at the Swan Rive inlet are shown in Figure 3-36.

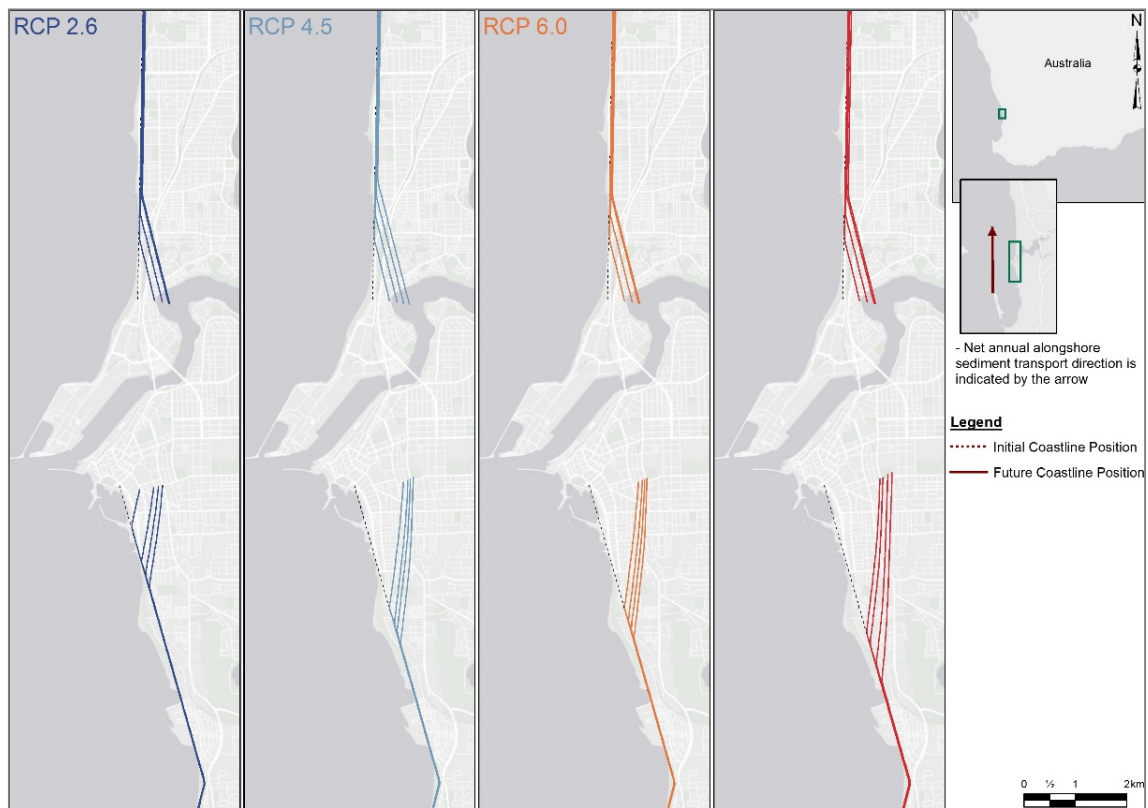


Figure 3-36: Projected changes of the inlet-affected coastline at the Swan River system. The four solid lines in each subplot represent the final coastline position by 2040, 2060, 2080 and 2100 (in the same order, moving landward from the most seaward line).

The model results indicate that the down-drift coast at the Swan river may erode by ~85 m (RCP 2.6) to ~102 m (RCP 8.5) by 2100 (i.e., ~-1 m/yr rate of erosion). However, the up-drift coast is projected to be eroded between ~163 m (RCP 2.6) and ~355 m (RCP 8.5) by 2100 (i.e., ~-4 m/yr rate of erosion). The coastline change projections presented by Vousdoukas et al. (2020), which excludes the effects of the estuary, indicate ~200 m erosion along both up-and down-drift coast by 2100 for RCP 8.5. Hence, the model projections are in reasonable agreement with the coastline changes presented by Vousdoukas et al. (2020). The SMIC application results presented by Ranasinghe et al. (2013) indicate 180 m of erosion of the down-drift coast by 2100, which is ~50% ($\pm 5\%$) of the model projections presented herein for the same period.

3.7 Comparison of the modelled results at the barrier-estuary systems

Application of the newly developed reduced-complexity model at the four barrier estuary case-study locations indicates that macro-time-scale evolution of catchment-estuary-coastal systems under the influence of climate change-driven impacts and anthropogenic activities would vary markedly. Although the coastlines at all four case study sites are projected to erode by the end of this century, the governing processes are very different from one site to another.

The most widely known impact of future climate change, i.e., sea-level rise, has substantial implications on the behaviour of all but the Kalutara inlet system, which has a relatively small estuary surface area. The overall variation of ΔV_T at Kalutara estuary is governed by the change in fluvial sediment supply. The effect of sand mining in the river catchment dominates the entire fluvial sediment supply process, in which favourable climatic forcing is projected to make marginal differences in fluvial sediment supply during the end century periods. Variation in basin volume has trivial impacts on the overall behaviour of Kalutara inlet, which is also true for both the Alsea and Dyfi estuary systems. However, the behaviour of the Swan river system is dominated by the sediment demand due to basin volume variation.

The Swan river system is also affected by the sediment demands due to basin infilling. However, the model projections indicate that variations in ΔV_{BV} govern the overall behaviour of this system. The relatively large estuary surface area and basin volume are the main reasons for the projected variations of ΔV_T at Swan river system. Despite having a vast river catchment, the arid nature of the Swan river catchment does not result in large fluvial sediment supply. Thus, changes in fluvial sediment supply hardly contribute to the variation of ΔV_T of this system.

Both the Alsea and Dyfi estuary systems are governed by the sediment demands due to basin infilling, although, the Alsea inlet system is partially influenced by fluvial sediment supply as well. This fluvial influence becomes significant only by the end-century when increased temperatures are projected to generate a surplus of fluvial sediment that results in a reduction of the overall sediment demand by the estuary. Owing to their relatively small basin volumes, both these systems are not affected by the sediment demands due to variations in basin volume size.

3.8 Chandeleur Islands

3.8.1 Stochastic model inputs and other input parameters

The change in sea level is considered to be the primary stochastic variable that governs the evolution of barrier-island systems in the model presented in Section 2.5 and 2.6. Here, the model was applied at a 20-year time step, starting in 2020, hence producing projections at 2040, 2060, 2080, and 2100. The stochastic variables of ΔRSL were created in a similar way to that of barrier-estuary systems (presented in Section 2.3).

In addition to ΔRSL , barrier-island system evolution is also restricted by a maximum barrier migration rate (m/yr). This threshold value depends on various factors, such as the barrier-island volume and crest width, and aeolian transport in the area (Section 2.4). Therefore, the determination of a suitable barrier-migration rate at a given system is associated with significant uncertainties. To account for these uncertainties, a triangular distribution was adopted for the barrier-migration threshold at the Chandeleur Islands with a minimum, median, and maximum values of 10, 15, and 20, respectively (in m/yr) (Morton and Miller, 2005; Twichell et al., 2013). This fitted distribution provided the second set of stochastic model input to determine the evolution of the Chandeleur Islands over the 21st century.

Figure 3-37 shows the projected regional relative sea-level changes (ΔRSL) in the vicinity of the Chandeleur Islands for 2021-2100 period. Intermediate values for mean, maximum, and minimum relative regional sea-level changes (Figure 3-37) were computed using the values shown in Table 3-10. The projected maximum and minimum changes in mean ΔRSL by 2100 are ~0.65 m, and ~0.35 m for RCP 8.5 and 2.6, respectively.

Table 3-10: Projected regional relative sea-level changes and its components considered for the Chandeleur Islands by 2100.

| | RCP 2.6 | RPC 4.5 | RCP 6.0 | RCP 8.5 |
|--|---------|---------|---------|---------|
| Global mean sea level change (ΔSL_G in m) | 0.43 | 0.53 | 0.54 | 0.74 |
| Regional variation (ΔSL_{RM} in m) | 0.02 | 0.02 | 0.01 | 0.01 |
| Regional relative sea level change (ΔRSL in m) | 0.45 | 0.55 | 0.55 | 0.75 |

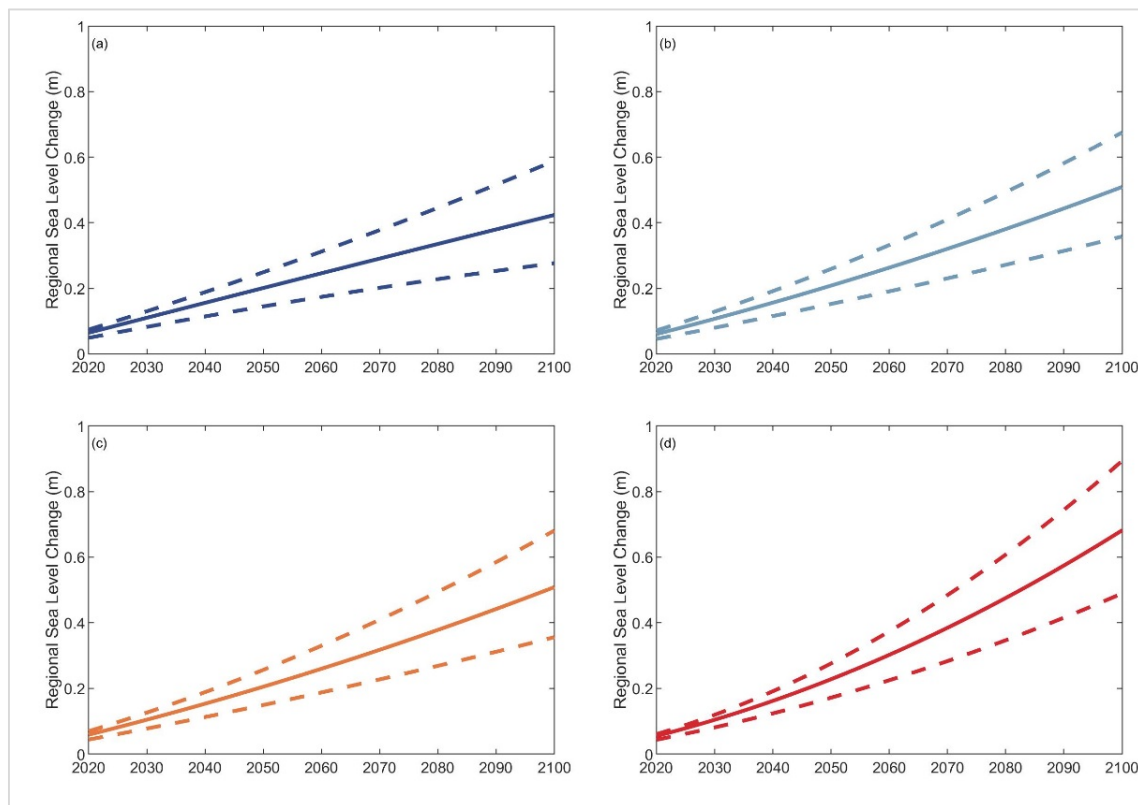


Figure 3-37: Projected changes in regional relative sea level at the Chandeleur Islands, LA, USA. Subplots (a), (b), (c), and (d) are for the RCPs 2.6, 4.5, 6.0, and 8.5, respectively. The solid line indicates the mean change, while the two dashed lines indicate the maximum and minimum variations of ΔRSL .

Other relevant characteristics of the Chandeleur Island are presented in Table 3-11.

Table 3-11: Characteristics of the Chandeleur Island. Source: Lavoie (2009).

| Parameter | Value |
|---|---------|
| Representative equilibrium profile volume (m^3/m) | 27,250 |
| Mean barrier island crest width (m) | 2,000 |
| Freeboard (m) | 2.27 |
| Marine sediment supply ($m^3/m/yr$) | 5.7 |
| Total barrier island length (km) | 80 |
| Back-barrier estuary surface area (km^2) | 1,750 |
| Mean barrier profile slope | ~0.001 |
| Mean underline base slope | ~0.0004 |

3.8.2 Projected changes in the barrier island

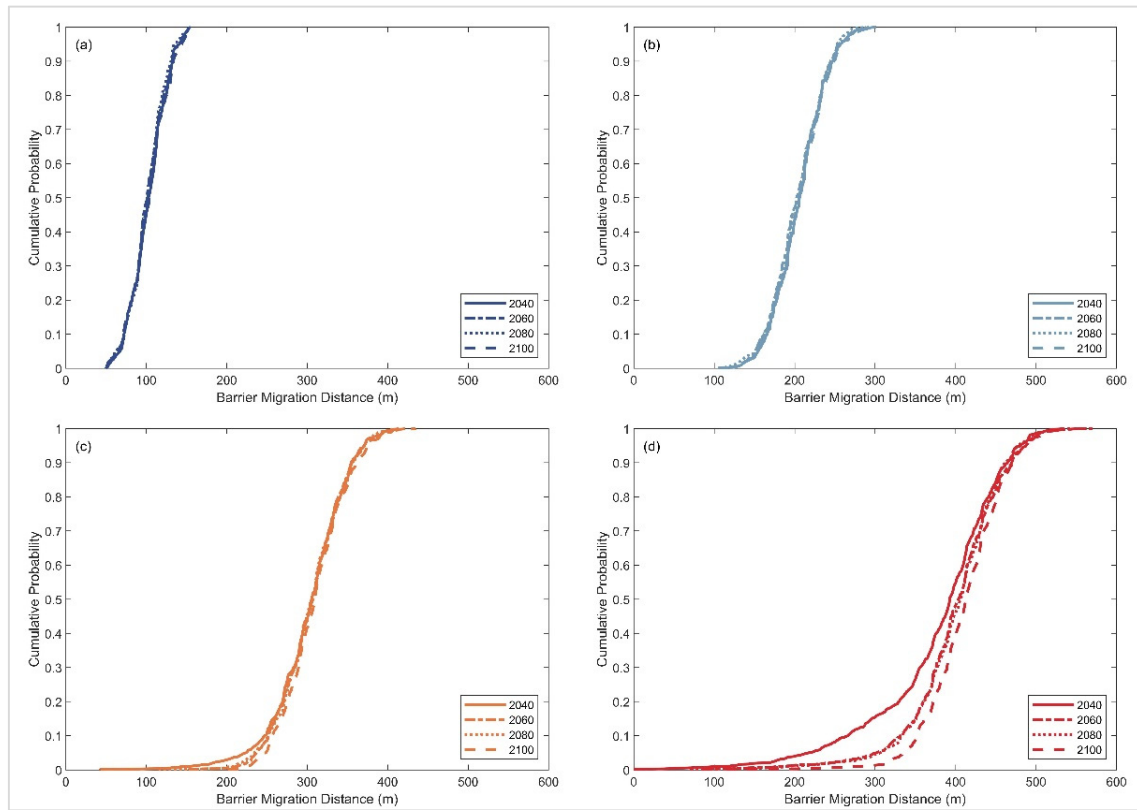


Figure 3-38: Empirical cumulative distributions of the projected barrier island migration distances of the Chandeleur Islands. Subplots (a), (b), (c), and (d) are for the RCPs 2.6, 4.5, 6.0, and 8.5, respectively.

Figure 3-38 shows the empirical cumulative distributions (CDFs) of the projected migration distances for the Chandeleur Islands by 2040, 2060, 2080, and 2100 for all RCPs. These CDF plots incorporate the total uncertainty associated with the projected barrier-island migration distances. Figure 3-38 indicates that the projected distributions of barrier-island migration distances are almost identical for RCP 2.6, 4.5 and 6.0 over the time period considered. The maximum and minimum values of the projected 50th percentile-barrier island migration distance by 2100 are ~450 m and ~100 m for RCP 8.5 and 2.6, respectively.

The historical shoreline variations presented by Luijendijk et al. (2018) indicate ~3 m/yr erosion at the Chandeleur Islands. Moore et al. (2014) have shown that the shoreline change at the Chandeleur Islands is about 668 m between 1920 and 2005. Twichell et al. (2013) have indicated a long-term shoreline change rate of ~13 m/yr for the Chandeleur Islands, whereas Morton and Miller (2005) have determined an average long-term shoreline change rate of 18.6 m/yr.

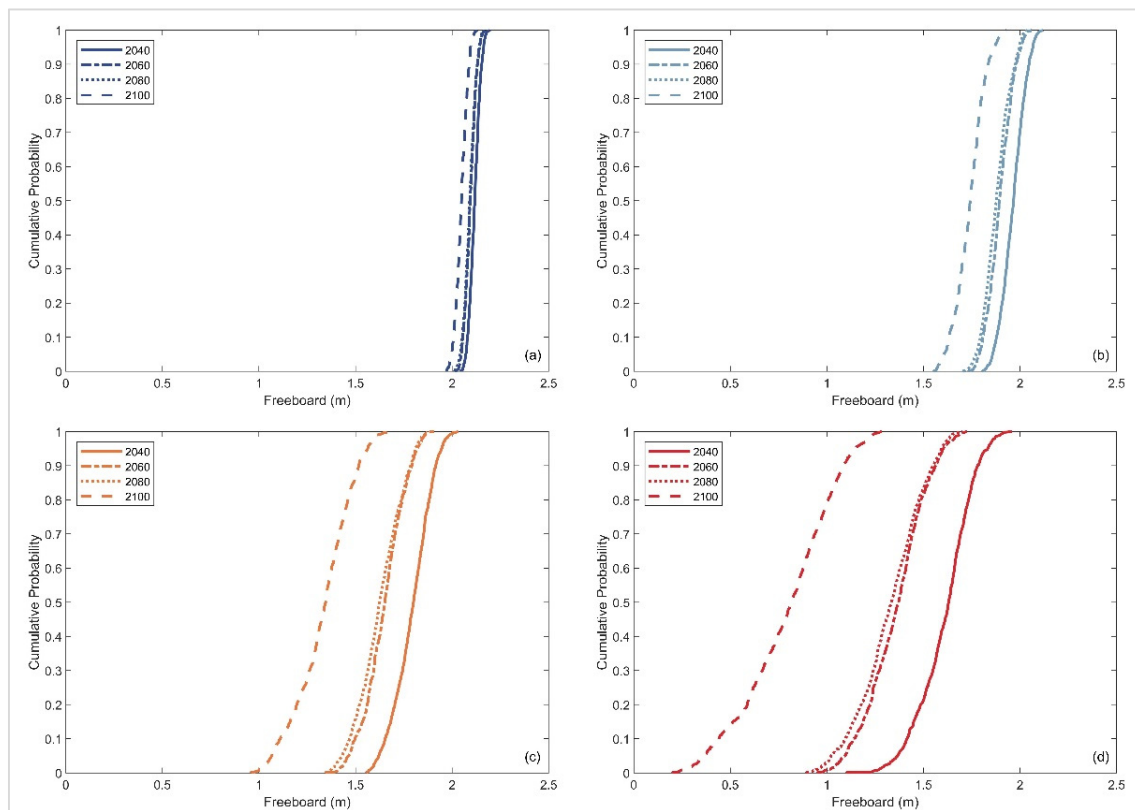


Figure 3-39: Empirical cumulative distributions of the projected barrier island freeboard for the Chandeleur Islands. Subplots (a), (b), (c), and (d) are for the RCPs 2.6, 4.5, 6.0, and 8.5, respectively.

Figure 3-39 shows the empirical cumulative distributions (CDFs) of the projected barrier island freeboard at the Chandeleur Islands by 2040, 2060, 2080, and 2100 for all RCPs. These CDF plots incorporate the total uncertainty associated with the projected barrier-island freeboard. Figure 3-39 indicates that the uncertainties in the projected barrier-islands freeboard for RCP 2.6 are similar for all the periods considered (~ 0.25 m). The maximum and minimum values of the projected 50th percentile barrier-island freeboard by 2100 are ~ 2.0 m and ~ 0.75 m for RCP 2.6 and 8.5, respectively. The results also indicate that there is a $\sim 90\%$ probability of the barrier-island freeboard being less than 1.0 m by 2100 for RCP 8.5.

In addition to the above simulations, a second set of model settings was used to investigate the possibility of barrier drowning. For this purpose, hypothetical initial barrier-island characteristics were considered, which include zero marine sediment supply (i.e., no gradient in longshore sediment transport), lower thresholds for the maximum barrier-migration rate, and reduced barrier freeboard. Such hypothetical initial conditions were considered to investigate the most influential system characteristic that would cause the barrier island to drown under the projected sea-level changes over the 21st century.

3.8.3 Projected changes of the barrier island under hypothetical initial conditions

Under the hypothetical initial conditions, it was first assumed that there is no gradient in longshore sediment transportation across the Chandeleur Islands (neglecting the existing gradient of $5.7 \text{ m}^3/\text{m}/\text{yr}$). However, this restriction of marine sediment supply alone did not result in drowning the barrier island by 2100. Hence, secondly, (in addition to the changes made to the marine sediment supply), the thresholds for maximum migration rates were also reduced. The new thresholds of maximum, mean, and minimum migration rates (in m/yr) were assumed to be 10, 7.5, and 5, respectively. These hypothetical initial conditions only resulted in a quite trivial probability ($< 1\%$) of barrier drowning by 2100 under RCP 8.5. Hence, thirdly, the initial barrier freeboard was also reduced (in addition to the two assumptions made above) to investigate the probability of barrier drowning by 2100, and the results are presented herewith. These results indicate that the initial barrier freeboard is the critical factor in preventing the drowning of this barrier island under the projected sea-level rise over the 21st century.

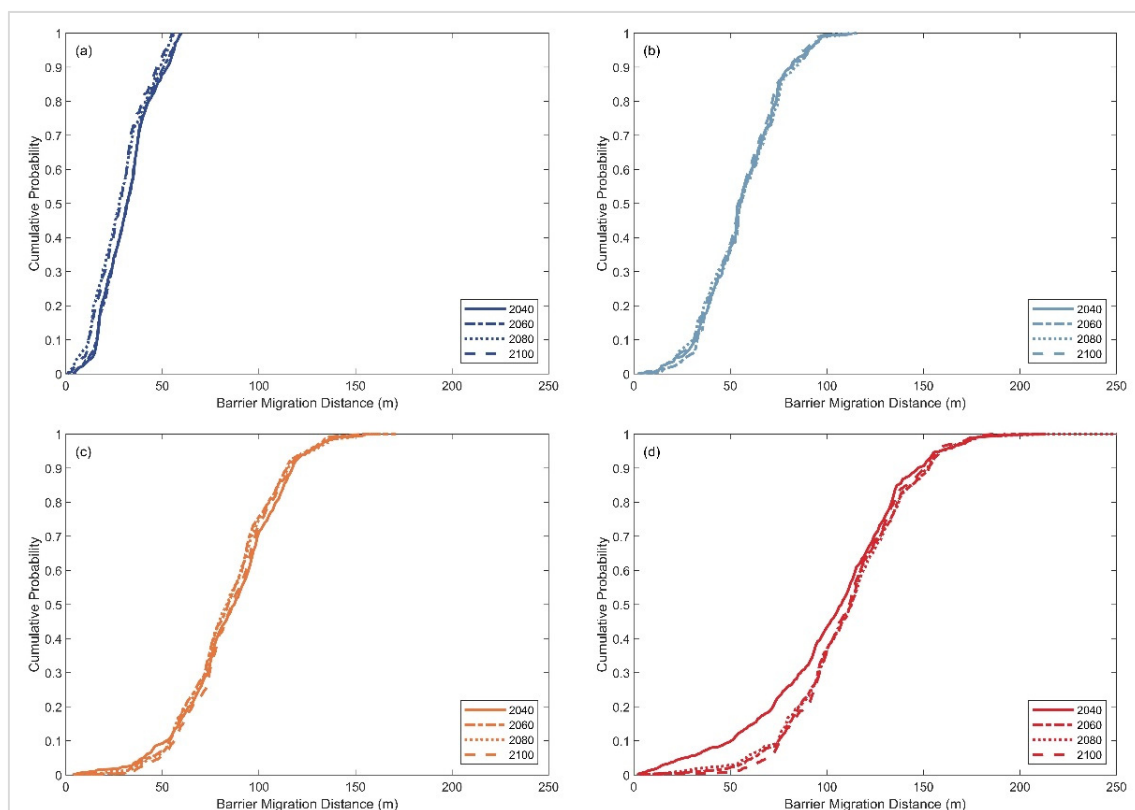


Figure 3-40: Empirical cumulative distributions of projected barrier-island migration distances for the Chandeleur Islands under hypothetical initial conditions. (zero marine sediment supply, reduced maximum barrier-migration rate threshold distribution with the minimum, mean, and maximum values of 5, 7.5, and 10, respectively (in m/yr), and reduced barrier freeboard of 1.0 m). Subplots (a), (b), (c), and (d) are corresponding to RCPs 2.6, 4.5, 6.0, and 8.5, respectively.

Figure 3-40 shows the empirical cumulative distributions of projected barrier island migration distances under the assumed initial conditions for the Chandeleur Islands for the different periods considered (by the year 2040, 2060, 2080, and 2100). The above results indicate that the projected distributions of barrier-island migration distances are almost identical for RCP 4.5 and 6.0 over the four periods considered. The maximum and minimum values of the projected 50th percentile barrier-island migration distance by 2100 ~125 m and ~25 m for RCP 8.5 and 2.6, respectively.

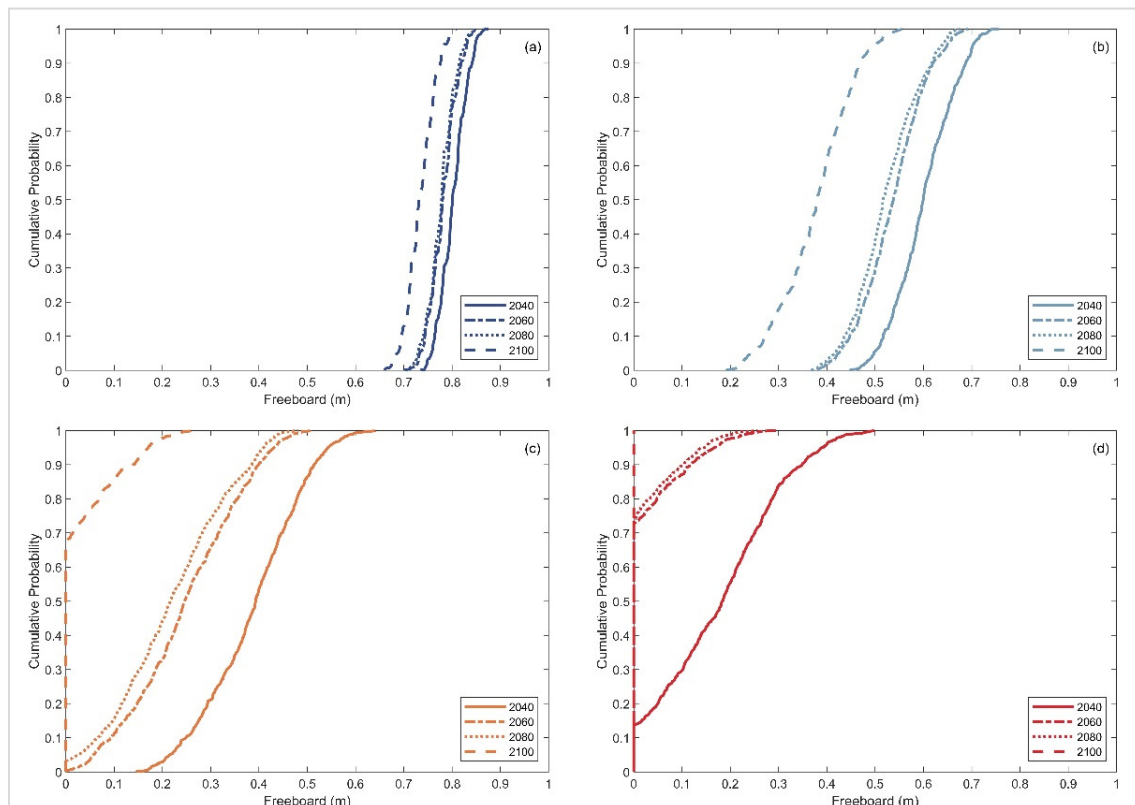


Figure 3-41: Empirical cumulative distributions of projected barrier island freeboard for the Chandeleur Islands under hypothetical initial conditions. (zero marine sediment supply, reduced maximum barrier-migration rate threshold distribution with minimum, mean, and maximum values of 5, 7.5, and 10, respectively (in m/yr), and a reduced barrier freeboard of 1.0 m). Subplots (a), (b), (c), and (d) are corresponding to RCP 2.6, 4.5, 6.0, and 8.5, respectively.

Figure 3-41 shows the empirical cumulative distributions of projected barrier-island freeboard under the assumed initial conditions for the Chandeleur Islands during the different periods considered (by the year 2040, 2060, 2080, and 2100). The results indicate that there are no considered circumstances under which the barrier island will be inundated by the rising sea level projections for both RCP 2.6 and 4.5. Figure 3-41 also indicates a probability of about 70% of barrier drowning for RCP 6.0 by 2100. However, the projected probability of barrier drowning by 2080 is less than 5% for RCP 6.0. This is due to the projected variation in ΔRSL over the time period considered, in which the change in sea level over the last 20 years is almost equal to that over the first 60 years (i.e., 2020-2080; Figure 3-37). The projected probabilities of barrier drowning are significant for RCP

8.5. Results show that sea-level rise under RCP 8.5 is likely to completely drown the barrier island by 2100, while the probability of drowning by 2060 is ~75%.

3.9 Summary and conclusions

A reduced-complexity modelling technique has been developed and applied to probabilistically assess climate change-driven evolution of inlet-interrupted coasts at time scales of 50 to 100 years while taking into account the contributions from Catchment-Estuary-Coastal (CEC) systems in a holistic manner. Attention was given to develop a modelling technique that provides probabilistic estimates of the long-term evolution of inlet-interrupted coasts under climate-change impacts and anthropogenic activities, which enables the quantification of the uncertainties associated in projected coastline change. The model was applied to four case-study sites attached to barrier estuary systems (small tidal inlets; Kalutara inlet, Sri Lanka and Swan river system, Australia and estuaries with low-lying margins; Alsea estuary, Oregon, USA and Dyfi estuary, Wales, UK) and a barrier-island coast (Chandeleur Islands, Louisiana, USA) over the period 2020-2100.

Climate change forcing was obtained from the GCMs that are suitable for each case study location. Yearly stochastic variables for annual mean temperature and cumulative river discharge were obtained through fitted joint probability models. Yearly stochastic variables for regional relative sea-level change (ΔRSL) were obtained through fitted triangular distributions of the minimum, mean and maximum projections of ΔRSL given by Stocker et al. (2013). The Human-induced soil erosion at the catchment scale (E_h) was approximated by the rescaled Human FootPrint Index (HFPI) values over the respective watersheds. The stochastic variables of human-induced erosion were obtained from fitted triangular distributions, in which linearly increasing minimum, mean, and maximum values of E_h were assumed over the study period. These four stochastic variables were used in a Monte-Carlo framework to determine variations of change in total sediment volume exchange (ΔV_T) at the selected mainland barrier inlet-estuary systems, which could be used to determine the long-term evolution of inlet-interrupted coasts. A physics-based one-dimensional coastline model was developed to demonstrate the impacts of the projected variation in ΔV_T along the inlet-affected coastline, and the subsequent total coastline variation, which includes the coastal recession due to the so-called Bruun effect as well.

The stochastic variables of maximum barrier island migration rate were obtained from a fitted triangular distribution. Yearly stochastic variables for regional relative sea-level change (ΔRSL) were obtained through fitted triangular distributions (as described above). These two stochastic variables were used in the Monte-Carlo framework that investigates the evolution of the Chandeleur Islands over the 21st century. Hypothetical initial barrier island characteristics were used to investigate the possibility of barrier island inundation

under the projected sea-level rise over the 21st century. The main findings of the model applications described in this chapter are:

- 1) Depending on the characteristics of mainland barrier estuary inlet-estuary systems considered, variation of the change in total sediment volume exchange (ΔV_T) at tidal inlets is governed by one or two of its contributing components (i.e., basin infilling (ΔV_{BI}), basin volume (ΔV_{BV}), and fluvial sedimentation (ΔV_{FS})).
- 2) Irrespective of the magnitude of climate change-driven variations in annual cumulative river discharges (Q), the influence of basin volume variation (ΔV_{BV}) to the change in total sediment volume exchange (ΔV_T) at tidal inlets is mostly negligible (e.g., Alesa estuary, Dyfi estuary, and Kalutara inlet) with the exception of systems with large estuary volume (e.g., Swan River system). Hence, it is possible to determine a priori whether it is necessary to consider the contribution of ΔV_{BV} to ΔV_T by inspecting the characteristics of the inlet-estuary system considered.
- 3) At inlet-estuary systems located in non-arid river catchments, future increases in fluvial sediment supply (ΔV_{FS}) could decrease the sediment demand due to basin infilling (ΔV_{BI}), and subsequently, decrease the change in total sediment volume exchange (ΔV_T) at tidal inlets (e.g., Alesa estuary and Kalutara inlet) or may even export sediment to the adjacent coast (e.g., Kalutara inlet). Hence, it is necessary to carefully investigate the contribution of ΔV_{FS} when assessing shoreline variations in the vicinity of tidal inlets, which has been routinely neglected in most studies on coastline change at the inlet-interrupted coastline.
- 4) The estuarine sediment demand due to basin infilling (ΔV_{BI}) is the process that is most likely to dictate the variation of change in total sediment volume exchange (ΔV_T) at systems with large estuary surface areas (e.g., Alesa estuary and Dyfi estuary). Thus, for the systems containing small, arid river catchments and large but shallow estuaries, it may be sufficient only to consider ΔV_{BI} to assess the long-term evolution of their adjacent coastline (e.g., Dyfi estuary).
- 5) The extent of the long-term evolution of coastline due to changes in total sediment volume exchange (ΔV_T) at tidal inlets varies with both the magnitude and direction of the net annual longshore sediment transport (LST) in its vicinity. When the aforementioned properties of LST and ΔV_T magnitude are known, it is possible to judge whether the sediment volume variation driven coastline changes would only affect the down-drift coast or both the up- and down-drift coasts.

- 6) Barrier islands with a large initial sediment volume and freeboard may not drown under the projected changes in sea level over the 21st century (e.g., Chandeleur Islands). Model simulations with different initial conditions (i.e., different magnitudes for initial barrier freeboard, maximum barrier-island migration rate, and marine sediment availability) indicate that the initial barrier freeboard is the critical factor in preventing the drowning of the selected barrier island by the projected sea-level rise over the 21st century.

3.10 A note on the uncertainties associated with the model projections

As mentioned in Section 1.1, there are two major sources of uncertainties associated with the model projections presented here: (1) uncertainties arising from the modelling technique adopted (i.e., model uncertainties) and (2) uncertainties arising from the variation in the model input parameters (i.e., input uncertainties). In the modelling framework adopted in this study, model uncertainties may arise from: (1) uncertainties in the fluvial sediment supply values obtained through the BQART model, (2) uncertainties in the basin infilling sediment demand calculation due to the hysteresis relation between sea-level rise (hydrodynamic forcing) and its associated infilling volume (morphological response), and (3) uncertainties associated with the approximations made in the simplified one-line coastline change model.

The river basin database used to develop the BQART model comprises 488 river basins across 63% of the world's drainage area. Therefore, the data source of BQART model development represents most of the climatic, geological, and socio-economic conditions of the world's river basins. Furthermore, the model has been shown to successfully account for 96% of the fluvial sediment variation across six orders of magnitudes in observed values with a 3% bias (Syvitski and Milliman, 2007). Therefore, fluvial sediment projections obtained from the BQART model appear to be robust.

The hysteresis relation between hydrodynamic forcing and its associated morphological response is another potential source of model uncertainty. Here, this hysteresis behaviour is accounted for with a lag factor of 0.5 in all the basin infilling volume calculations, following Ranasinghe et al.'s (2013) argumentation for small tidal inlets. However, this factor may vary with estuary geometries and sea-level rise rates, and hence the projected magnitude of basin infill volume.

The simplified one-line coastline change model adopted in this study only provides preliminary (i.e., first-order) estimates of variations along the inlet-interrupted coasts. This simplified model uses a relatively shallow profile (up to the depth of closure) and does not account for any local changes in coastline orientation (i.e., straight shoreline segments are

assumed) or the presence of any coastal structures. Furthermore, this simplified model does not take into account potential changes in future LST due to the climate-change driven variations in wave climate. Incorporation of such changes in LST is presented as a future research direction in Section 5.3.

The climatic inputs (i.e., T and Q) are obtained from CMIP5 GCMs. There are unavoidable uncertainties associated with GCM projections. Similarly, the values obtained from different GCMs for the same RCP vary among themselves. Despite the inherent uncertainties among different GCM projections, many climate change impact assessment studies use GCM outputs to obtain future climatic projections. Projections of sea-level change also contain uncertainties. Thus, there are three equations presented by Nicholls et al. (2014) to calculate the mean, minimum, and maximum changes in sea-level rise projections. Human activities that may exert changes to the natural environment vary along various dimensions (e.g., population growth, urbanization, and economic development). Therefore, the future projection of human-induced impacts on fluvial sediment supply also contains significant uncertainty.

In this study, the focus was limited to quantifying the uncertainties associated with model input variables (i.e., only input uncertainties not model uncertainties). Given that all GCM projections of T and Q and SLR projections are based on the Representative Concentration Pathways (RCPs) adopted by the IPCC, this study quantifies the differences in model projections obtained for the four IPCC RCPs. Thus, this study provides a quantification of the uncertainties in its outputs due to the variations in the model inputs (i.e., uncertainties in temperature (T), runoff (Q), regional relative sea-level change (ΔRSL), and human-induced erosion factor (E_h), represented by the Human FootPrint Index (HFPI).

However, it should be noted that the uncertainties presented in this study are those associated with the single RC model presented here. To quantify “model uncertainty” it would be necessary to derive projections from several different coastline change models (i.e., a multi-model ensemble). This is recommended as a possible future direction. The result of such a multi-model ensemble is required to determine the likelihood ranges as adopted by the IPCC, which, as a precursor needs a high level of confidence (Cubasch et al., 2013). Therefore, the 10-90% ranges presented in the results only correspond to the output variability due to the model input uncertainties, and cannot be taken as an indication of likelihoods of the projections. As the results of the model are probabilistic, another interesting analysis that would be possible is the evaluation of the contribution of each uncertain input variable to the total variance of the projected coastline change. This could be achieved via the global sensitivity analysis approach presented by Sobol' (2001). One application of this method to coastline projection is presented by Le Cozannet et al. (2019). However, due to time limitations, such an analysis could not be completed in the present study, and this is recommended as a Future research direction in Section 5.3.

Chapter 4

Global applications of the model

4.1 Introduction

In this chapter, the reduced-complexity modelling technique presented in Sections 2.2 and 2.3 is applied at a global scale, consisting of 41 individual mainland barrier estuaries from across all continents of the world.

The content of this chapter is structured as follows: Section 4.2 presents the different data sources and introduces the selected 41 mainland barrier-estuary systems. Section 4.3 presents the average change in total sediment volume exchange (ΔV_T) over the 2091-2100 period (relative to the reference conditions (2010-2019 period) presented in Section 2.2.4), followed by a first-order assessment of inlet-affected coastline changes over the same period (Section 4.4). Section 4.5 presents the summary and conclusions of this chapter.

4.2 Data sources

The barrier-estuary systems considered in this analysis were selected from three global data sets: (1) the global estuary dataset presented by Hinkel et al. (2013) for the DIVA framework (consisting of 200 systems), (2) the enhanced UK estuary database published by Manning (2012) (consisting of 163 estuary systems, but some with partial information), and the New South Wales estuary database published by Office of Environment and Heritage-New South Wales (2017) (consisting of 182 estuaries). A subset of barrier

estuaries was carefully chosen for this global application by considering the existence of tidal inlets and adjacent inlet-interrupted sandy coastlines. In this global application, 22, 8, and 4 estuary systems were selected from the DIVA, New South Wales, and the UK estuary databases, respectively. The four case-study sites (mainland barrier estuaries) considered in the previous Chapter were also included in this global analysis. Finally, two of the four small tidal-inlet systems presented in the SMIC applications by Ranasinghe et al. (2013) and one of the estuary-inlet systems in Liberia were also included in the analysis. The estuarine and catchment data for the Liberian case -site were obtained from the Norwegian Water Resources and Energy Directorate and Liberian Hydrological Service: Ministry of Lands Mines and Energy, (2019) and Liberian Hydrological Service: Ministry of Lands Mines and Energy and Norwegian Water Resources and Energy Directorate (2016).

The locations of the selected mainland inlet-estuary systems are shown in Figure 4-1.

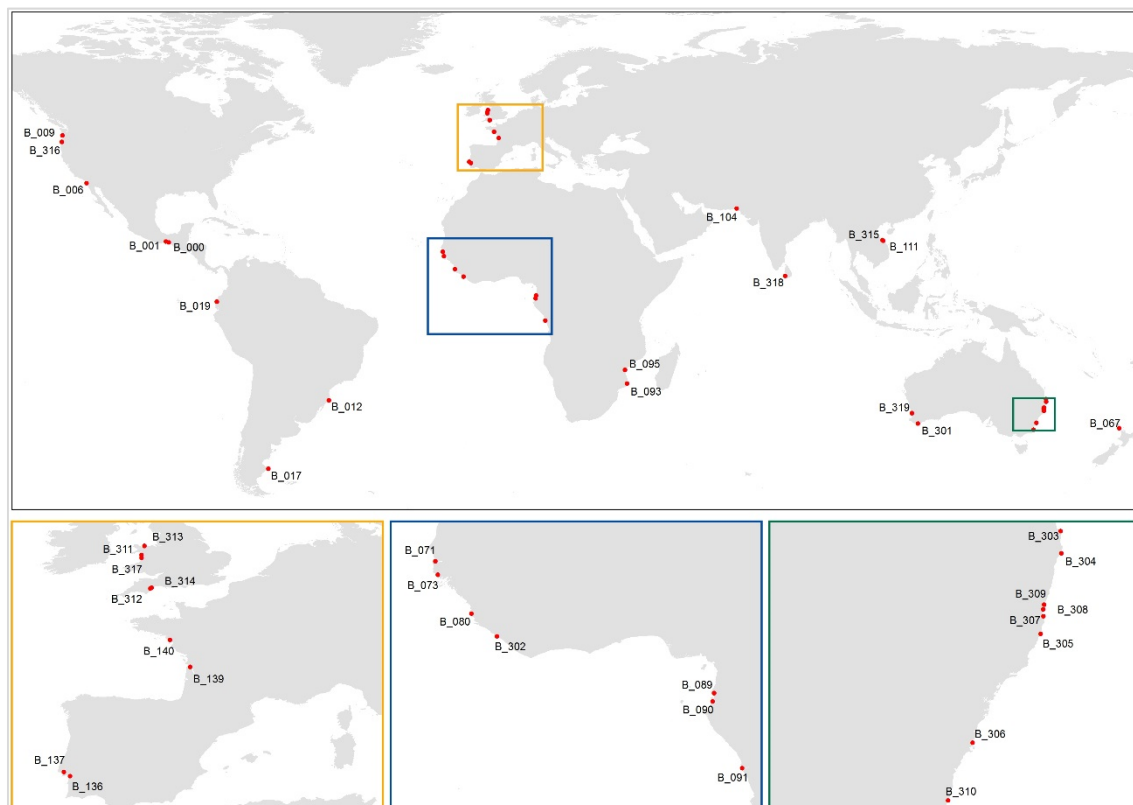


Figure 4-1: Locations of the selected mainland inlet-estuary systems. Original data sources of the above systems are as follows: systems B_303 to B_310 are from the estuary database published by Office of Environment and Heritage-New South Wales (2017); systems B_311 to B_314 are from Manning (2012); systems B_301 and B_315 are from Ranasinghe et al. (2013); system B_302 is from Liberian Hydrological Service: Ministry of Lands Mines and Energy and Norwegian Water Resources and Energy Directorate (2016) and Norwegian Water Resources and Energy Directorate and Liberian Hydrological Service: Ministry of Lands Mines and Energy (2019); systems B_316 to B_319 are the selected case study sites presented in Chapter 3; all other systems are from the DIVA application dataset published by Hinkel et al. (2013).

Once the inlet locations were selected, the connecting river catchment areas were determined from the river network and basin information presented by Lehner et al. (2008). These river basin extents were then used in conjunction with one arc-second resolution digital elevation models obtained from USGS Earth Explorer tool (Farr et al., 2007) and Human FootPrint Index data given in Wildlife Conservation Society - WCS and Center for International Earth Science Information Network - CIESIN - Columbia University (2005) to determine the catchment relief (R) and human-induced erosion factor (E_h) values, respectively. The yearly stochastic model inputs of E_h for the 2021-2100 period were generated by following the methodology adopted for the four case-study sites (Section 2.3).

The annual average tidal amplitude and the annual number of tidal cycles at the selected inlet-estuary systems were obtained from the harmonic analysis of the TOPEX-POSEIDON global inverse solutions (Egbert and Erofeeva, 2002). Catchment-averaged lithological factors (L) for the selected systems were obtained from Syvitski and Milliman (2007). The depth of closure and the active coastal-profile slope values at the selected inlets-estuary systems were obtained from Athanasiou et al. (2019). Catchment relief (R) values for the selected systems were obtained from the one arc-second resolution digital elevation models obtained from USGS Earth Explorer tool (Farr et al., 2007).

Catchment wide mean annual temperature and annual cumulative runoff values for the period 2010-2100 were extracted from 4 GCMs (GFDL-CM3, GFDL-ESM2G, GFDL-ESM2M, and IPSL-CM5A-MR; details presented in the Annex A.1). The selection of the above four GCMs was based on the availability of temperature and runoff projections for all RCPs over the 2010-2100 interval, the spatial resolution ($<2.5^\circ$), and available literature on the suitability of GCMs for different regions (e.g., CSIRO and Bureau of Meteorology (2015) for Australia). The annual mean temperature (T) and annual cumulative runoff (Q) values obtained from the above GCMs were then used to fit yearly joint probability distributions and to generate stochastic model input. The T and Q model inputs were generated by following the same procedure described in Section 2.3. The yearly stochastic model inputs for global sea-level change were also calculated using the method presented in Section 2.3.

Two of the three components (i.e., basin infilling volume (ΔV_{BI}) and basin volume change (ΔV_{BV})) that contribute to the computation of the changes in total sediment volume exchange (ΔV_T) at tidal-inlets are influenced by the estuary surface area (equation [2-2] and [2-3]). Thus, the accuracy of the estuary surface area of the selected systems was carefully examined to improve the model projections. This scrutiny was undertaken by comparing the estuary surface-area values of the selected systems (obtained through the DIVA dataset, the estuary databases from NSW, Australia, and the UK, and other published literature (mentioned above)) with the global estuary information database published by Alder (2003) and Watson et al. (2004). For instances where significant

discrepancies were observed between the two data sources, the water surface areas were further checked against Google Earth observations and measurements. After all these checks, a database of estuary surface areas that could confidently be used in computations was developed.

The contribution of basin volume change (ΔV_{BV}) to the change in total sediment volume exchange (ΔV_T) at tidal-inlets is also influenced by the estuarine volume (equation [2-3]). Therefore, it is necessary to have this information for all the selected barrier-estuary systems. However, the DIVA dataset does not include information about the basin volume. Thus, it was necessary to determine the estuary basin-volume magnitude by the use of other, more readily-available estuary characteristics, such as the surface area and tidal-amplitude. In this regard, a linear regression model was developed to project the basin-volume magnitude based on the estuary surface area and the tidal amplitude.

The input dataset needed for the development of the linear regression model (i.e., basin volume, estuary surface area, and tidal amplitude) was compiled by the use of two of the aforementioned estuary datasets (i.e., UK and Australian estuary databases) and the information on 138 estuaries in the USA published by Engle et al. (2007). These three datasets together contain information of 483 estuary systems. In order to optimise the performance of the fitted linear regression model, it was necessary to remove the estuary systems with significantly larger basin volumes compared to the rest from the dataset (i.e., removal of probable outliers from the dataset). This refinement resulted in a final input dataset of 324 estuaries to develop and train a linear regression model that can estimate the basin-volume magnitude, given estuary surface area and tidal amplitude. This regression model was subsequently used to determine the basin volumes of all 41 selected barrier-estuary systems.

These data and the stochastic model input (i.e., annual mean temperature (T), annual cumulative river discharge (Q), global sea-level change (ΔSL_G), and human-induced erosion factor (E_h)) were used in the reduced-complexity modelling technique presented in Section 2.2 and Section 2.3, to determine the change in total sediment volume exchange (ΔV_T) at the 41 selected barrier-estuary systems over the 2020-2100 period. In this global application, all estuaries were considered as small tidal inlets, so that the basin surface area remains constant under the rising sea level. This simplification was made because of the limitations in the spatial resolution and vertical accuracy of the digital elevation model used in this global application. The anthropogenic activities within the river catchments were represented only by the variations in human-induced erosion factor (E_h). The main findings of this global application are presented in Sections 4.3 and 4.4, and the key model inputs are presented in Annex A.2.

4.3 Projected change in total sediment volume exchange between the estuary and the inlet-affected coast by 2100

The projected change in total sediment volume exchange (ΔV_T) between the estuary-inlet systems and adjacent coasts over the 2091-2100 period is shown in Figure 4-2 (for RCP 2.6) and Figure 4-3 (for RCP 8.5). These figures were created based on the time-averaged 50th percentile values of ΔV_T for the end of the century period (2091-2100). The time-averaged 10th and 90th percentile values of ΔV_T over this period are presented in Annex A.3 for comparison purposes.

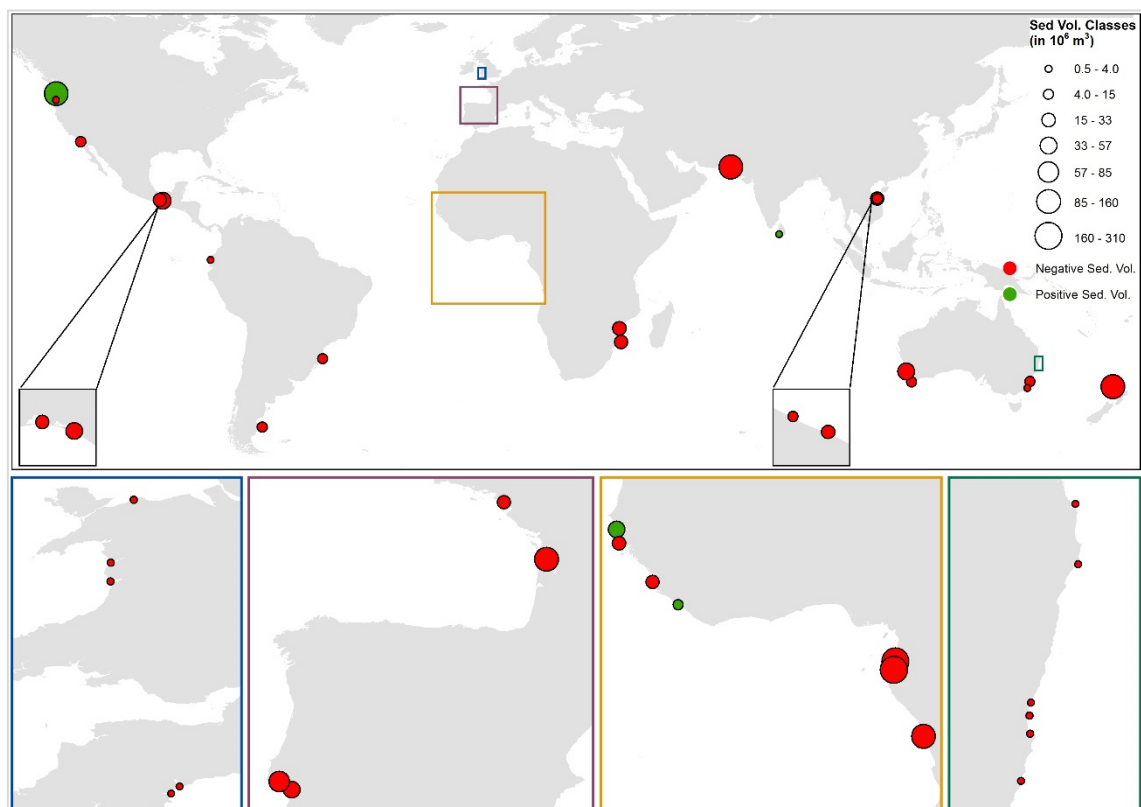


Figure 4-2: The projected change in the time-averaged 50th percentile values of the total sediment volume exchange (ΔV_T) between the estuary system and its adjacent coast over the 2091-2100 period for RCP 2.6. The mean change in total sediment volume exchange during the end-century was obtained by averaging the 50th percentile values of ΔV_T over the 2091-2100 time period. Negative and positive values of ΔV_T indicate sediment imported to the estuary from the adjacent coast and sediment exported from the estuary to the adjacent coast, respectively. Insert boxes, and subplots below the main figure show expanded views of areas that contain several closely located systems and as such are not discernible in the main figure.

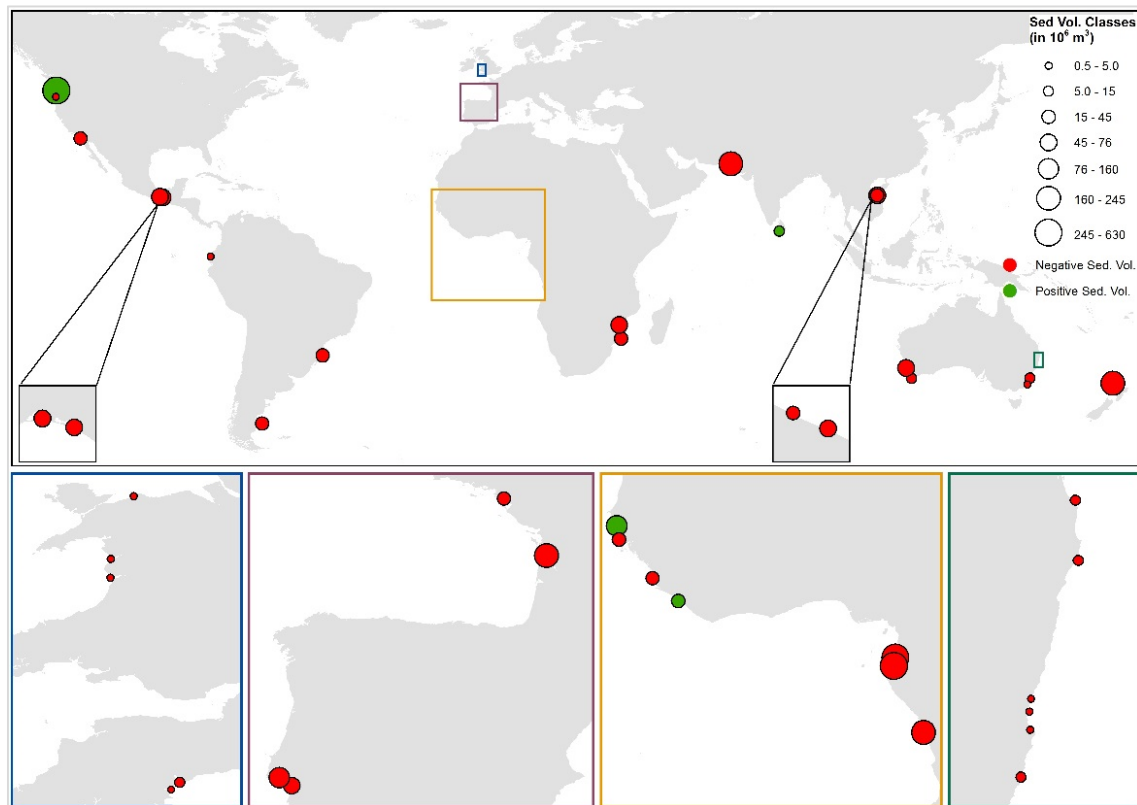


Figure 4-3: The projected change in the time-averaged 50th percentile values of the total sediment volume exchange (ΔV_T) between the estuary system and its adjacent coast over the 2091-2100 period for RCP 8.5. The mean change in total sediment volume exchange during the end-century was obtained by averaging the 50th percentile values of ΔV_T over the 2091-2100 time period. Negative and positive values of ΔV_T indicate sediment imported to the estuary from the adjacent coast and sediment exported from the estuary to the adjacent coast, respectively. Insert boxes, and subplots below the main figure show expanded views of areas that contain several closely located systems and as such are not discernible in the main figure.

The above figures (Figure 4-2 and Figure 4-3) and the table presented in Annex B indicate that only four systems (Colombia River, Canada/USA; Gambia River, Senegal/Guinea; St. Paul, Liberia/Guinea; and Kalutara, Sri Lanka) are projected to export sediment to the adjacent coast (for all RCPs) at the end of the century. Among these four systems, only the Gambia inlet-estuary is governed by both fluvial sediment (FS) and basin infilling (BI) sediment components. The projected change in total sediment volume exchange (ΔV_T) at other systems is governed by the fluvial sediment supply (FS) component. The Colombia system is projected to export the largest amounts to the adjacent inlet-interrupted coast (160, 321, 372, and 628 MCM for RCP 2.6, 4.5, 6.0, and 8.5, respectively). The projected increments in temperature and river discharge are the main reasons for such a large increase in fluvial sediment supply from the Colombia River. However, it should be noted that anthropogenic sediment retention along the Colombia River was not considered in this study.

All other systems considered in this analysis are projected to import sediment into the estuary by the end of this century. Among these sediment importing systems, the two largest magnitudes of ΔV_T (for all RCPs) are projected at the Muni (in Equatorial

Guinea/Gabon; -310, -398, -407, -573 MCM for RCP 2.6, 4.5, 6.0, and 8.5) and Gabon systems (in Gabon; -253, -324, -333, and -467 MCM for RCP 2.6, 4.5, 6.0, and 8.5), respectively. Both these systems comprise extensive estuary surface areas, thus the change in total sediment volume exchange (ΔV_T) at these systems is governed by the sediment demand caused by the basin infilling (BI) volume. There are only four systems that have ΔV_T less than -100 MCM for all RCPs by the end of this century (Kaipara, New Zealand; Zaire, DRC/Angola; Miani Hor, Pakistan; and Gironde, France). Among the above four systems, Kaipara is the only system where ΔV_T is governed by the basin infilling volume (BI), while the other three are influenced by fluvial sediment supply (FS) as well.

At several of the studied inlet-estuary systems, both basin infilling (BI) and fluvial sediment supply (FS) exert almost equal but opposite influences to the change in total sediment volume exchange (ΔV_T) over the end-century period (e.g., Tubarao Lagoon, Brazil and Rio Chone, Ecuador). All these inlet-estuary systems are attached to relatively large, non-arid river catchments and hence, the estuarine sediment demand due to basin infilling is decreased by the fluvial sediment received from its river system.

The projected ΔV_T and the relative contributions of basin infilling and fluvial sediment supply were further analysed to determine a threshold at which the fluvial sediment supply could make a significant influence on the total change in sediment volume exchange (ΔV_T) between the estuary and its adjacent coast. In these calculations, the estuary surface area and the river catchment area were used as proxies for basin infilling volume and fluvial sediment supply, respectively. The ratio between the estuary surface area and the river catchment was considered as an indicator (from hereon referred to as the first-order approximation ratio (i.e., FOAR)) to investigate the relative contributions of basin infilling and fluvial sediment supply to the projected change in total sediment volume exchange (ΔV_T).

In this regard, in order to identify the dominant contributors to the change in total sediment exchange (ΔV_T), the variation of the projected 50th percentile values of ΔV_T and the contributing processes (i.e., basin infilling (BI), fluvial sediment supply (FS), and basin volume change (BV)) at the 41 selected barrier-estuary systems over the 21st century were examined (e.g., Figure 4-4 and Figure 4-5). The identified dominant processes at each of the barrier-estuary systems were then compared with the corresponding first-order approximation ratios (mentioned above). The results indicate that, if the ratio between the estuary surface area and the river catchment area is greater than 0.01, the variation of projected ΔV_T is likely to be governed by the sediment demand due to basin infilling (Figure 4-5; Table 4-1). For the barrier-estuary systems in non-arid catchments, the contribution of fluvial sediment supply to the variation in ΔV_T is likely to be significant (i.e., cannot be neglected) when the above ratio is less than 0.01 (Figure 4-4; Table 4-1). In arid catchments, the first-order approximation threshold analysis shows that ΔV_T at inlet-estuary systems are likely to be governed only by the basin volume sediment demands.

Since the coastline change at tidal inlets is directly affected by the change in total sediment volume exchange (ΔV_T) with the inlet-estuary systems (Section 2.1), the above ratio can be used as an indicator to predict the contributing processes that may affect the long-term behaviour of inlet-interrupted coasts.

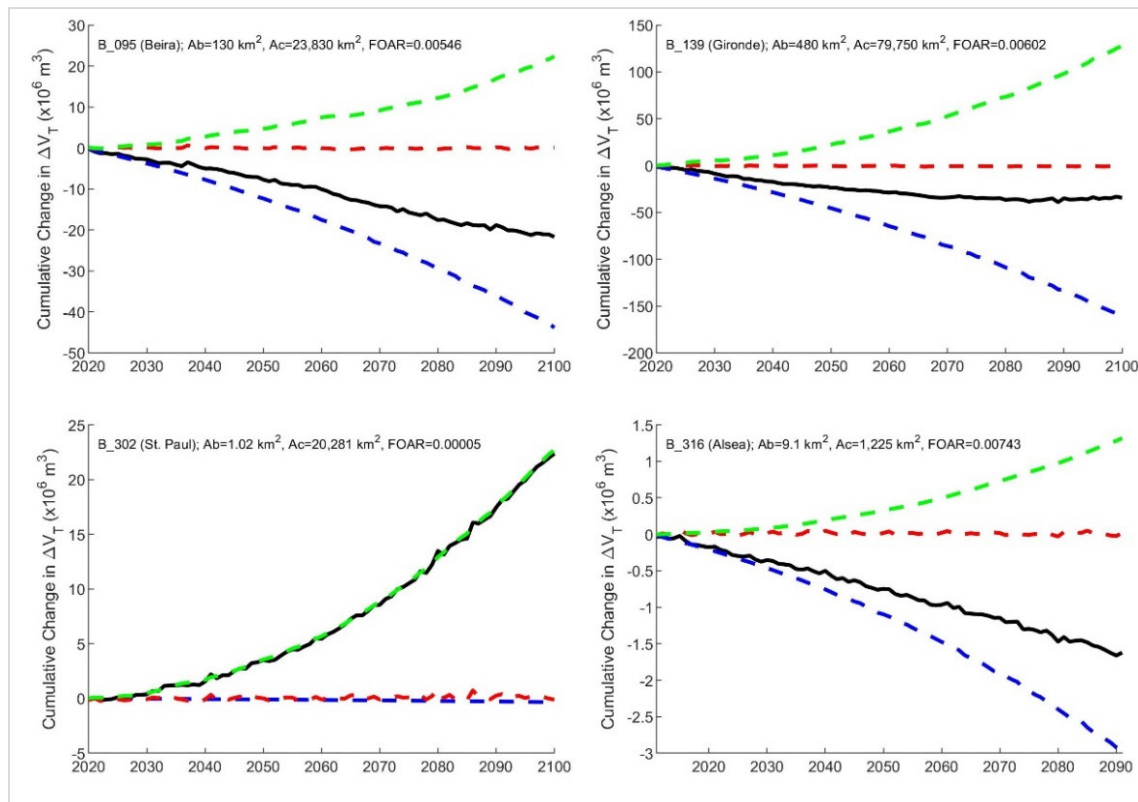


Figure 4-4: An exemplary plot of the variations of the projected 50th percentile values of change in total sediment volume exchange (ΔV_T) and the different contributing processes at four different barrier estuary systems with First-Order Approximation Ratio (FOAR) less than 0.01 for RCP 8.5. The solid black line indicates the variation of ΔV_T , while the dashed blue, red and green lines indicate the variations of basin infilling (BI), basin volume change (BV) and fluvial sediment supply (FS), respectively.

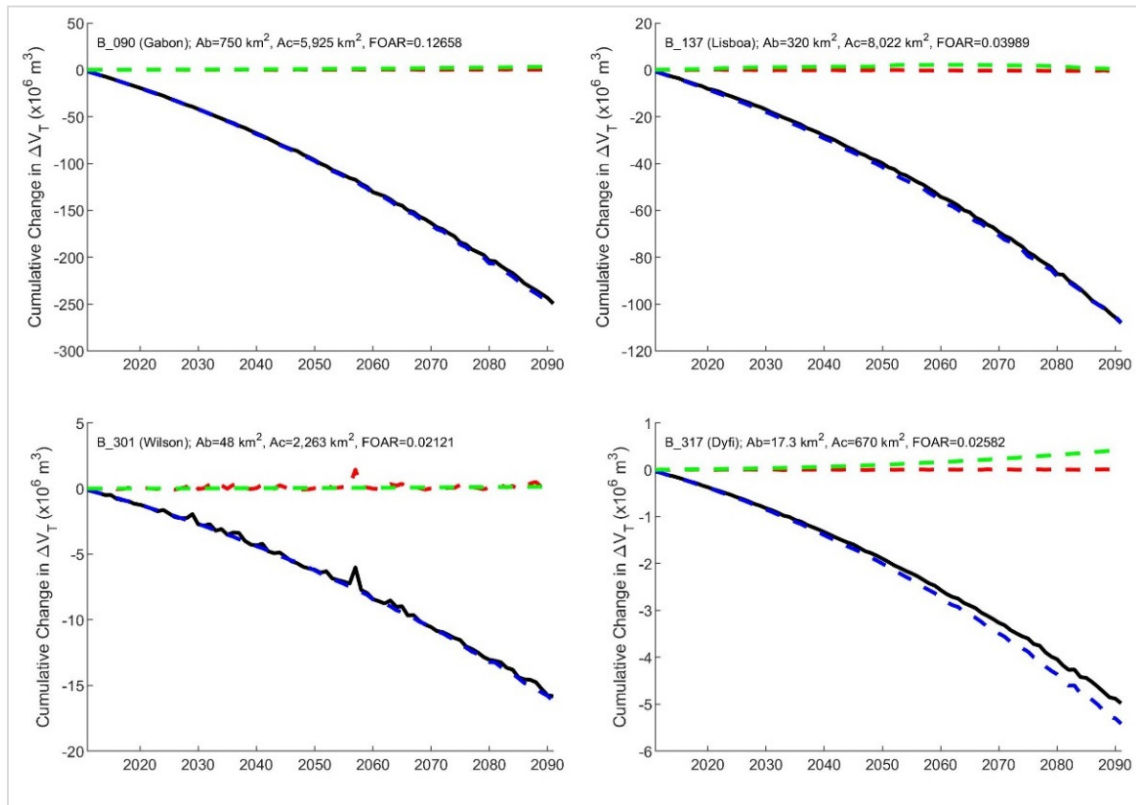


Figure 4-5: An exemplary plot of the variations of the projected 50th percentile values of change in total sediment volume exchange (ΔV_T) and the different contributing processes at four different barrier estuary systems with First-Order Approximation Ratio (FOAR) greater than 0.01 for RCP 8.5. The solid black line indicates the variation of ΔV_T , while the dashed blue, red and green lines indicate the variations of basin infilling (BI), basin volume change (BV) and fluvial sediment supply (FS), respectively.

Table 4-1: Comparison of the first-order approximation ratio (FOAR) and the dominant contributing processes to the total sediment volume exchange (ΔV_T) at the selected barrier estuary systems. Note: The FOAR is the ratio between the estuary surface area and the river catchment area. Dominant contributing processes to ΔV_T were identified by examining the variations of the projected 50th percentile values of ΔV_T and the contributing processes (i.e., basin infilling (BI), basin volume change (BV), and fluvial sediment supply (FS)).

| Label | System Name | Estuary Surface Area (km ²) | Catchment Area (km ²) | First Order Approximation Ratio (FOAR) | Dominantly contributing processes to ΔV_T | | |
|-------|-----------------|---|-----------------------------------|--|---|----|----|
| | | | | | BI | BV | FS |
| B_000 | Mar Muerto | 247 | 1,448 | 0.17058 | X | 0 | 0 |
| B_067 | Kaipara | 780 | 5,392 | 0.14466 | X | 0 | 0 |
| B_090 | Gabon | 750 | 5,925 | 0.12658 | X | 0 | 0 |
| B_001 | Lugana Superior | 220 | 2,028 | 0.10848 | X | 0 | 0 |
| B_006 | San Diego | 107 | 1,167 | 0.09169 | X | 0 | 0 |
| B_111 | Hue | 100 | 1,783 | 0.05609 | X | 0 | 0 |
| B_093 | Inhambane | 110 | 2,377 | 0.04628 | X | 0 | 0 |
| B_137 | Lisboa | 320 | 8,022 | 0.03989 | X | 0 | 0 |
| B_315 | Thuan | 110 | 3,800 | 0.02895 | X | 0 | 0 |
| B_104 | Miani Hor | 314 | 11,066 | 0.02838 | X | 0 | 0 |
| B_317 | Dyfi | 17.3 | 670 | 0.02582 | X | 0 | 0 |
| B_089 | Muni | 185 | 7,995 | 0.02314 | X | 0 | 0 |
| B_073 | Cacheu | 130 | 5,797 | 0.02243 | X | 0 | 0 |
| B_303 | Tweed River | 22.7 | 1,066 | 0.02129 | X | 0 | 0 |
| B_012 | Tubarao Lagoon | 120 | 5,636 | 0.02129 | X | 0 | X |
| B_301 | Wilson | 48 | 2,263 | 0.02121 | X | 0 | 0 |
| B_080 | Freetown | 206 | 11,110 | 0.01854 | X | 0 | X |
| B_136 | Setubal | 110 | 6,516 | 0.01688 | X | 0 | 0 |
| B_019 | Rio Chone | 32 | 2,311 | 0.01385 | X | 0 | X |
| B_312 | Exe | 19.2 | 1,402 | 0.01368 | X | 0 | 0 |
| B_091 | Zaire | 520 | 40,989 | 0.01269 | X | 0 | 0 |

| Label | System Name | Estuary Surface Area (km ²) | Catchment Area (km ²) | First Order Approximation Ratio (FOAR) | Dominantly contributing processes to ΔV_T | | |
|-------|-----------------|---|-----------------------------------|--|---|----|----|
| | | | | | BI | BV | FS |
| B_311 | Mawddach | 3.65 | 314 | 0.01160 | X | 0 | 0 |
| B_308 | Nambucca River | 12.6 | 1,090 | 0.01156 | X | 0 | 0 |
| B_313 | Conwy | 5.6 | 502 | 0.01107 | X | 0 | 0 |
| B_305 | Hastings River | 30 | 3,594 | 0.00835 | X | 0 | X |
| B_314 | Teign | 4.04 | 487 | 0.00830 | X | 0 | X |
| B_316 | Alsea | 9.1 | 1,225 | 0.00743 | X | 0 | X |
| B_309 | Bellinger River | 8.2 | 1,152 | 0.00712 | X | 0 | X |
| B_139 | Gironde | 480 | 79,750 | 0.00602 | X | 0 | X |
| B_304 | Richmond River | 38.4 | 6,924 | 0.00555 | X | 0 | X |
| B_095 | Beira | 130 | 23,830 | 0.00546 | X | 0 | X |
| B_306 | Shoalhaven | 31.9 | 7,087 | 0.00450 | X | 0 | 0 |
| B_307 | Macleay River | 31.6 | 11,347 | 0.00278 | X | 0 | X |
| B_017 | Rio Deseado | 90 | 38,743 | 0.00232 | X | 0 | 0 |
| B_310 | Bega River | 3.8 | 1,870 | 0.00203 | X | 0 | 0 |
| B_071 | Gambia | 120 | 70,018 | 0.00171 | 0 | 0 | X |
| B_318 | Kalutara | 1.75 | 2,778 | 0.00063 | 0 | 0 | X |
| B_140 | Loire | 55 | 103,552 | 0.00053 | 0 | 0 | X |
| B_009 | Colombia River | 340 | 669,403 | 0.00051 | 0 | 0 | X |
| B_319 | Swan | 52 | 121,000 | 0.00043 | X | X | 0 |
| B_302 | St Paul | 1.02 | 20,281 | 0.00005 | 0 | 0 | X |

4.4 Approximated inlet-affected coastline changes

As mentioned in Section 2.1, the total coastline change at tidal inlets is driven by two components: (1) coastline recession/progradation due to changes in total sediment volume exchanged between the inlet-estuary systems and its adjacent coast (ΔV_T), and (2) coastline retreat due to the Bruun effect. Section 2.4 of this dissertation introduced a conceptual framework to determine the extent and magnitude of ΔV_T -driven coastline changes, which requires site specific information on longshore sediment transport and breaking-wave conditions. Thus, applying the same methodology at all the inlet-estuary systems considered in this chapter becomes quite a challenging task.

In the SMIC application, Ranasinghe et al. (2013) adopted another simplified technique to assess the sediment volume change-driven variations of inlet-affected coastlines. Within this SMIC methodology, change in total sediment volume exchange (ΔV_T) is distributed uniformly along both up- and down-drift coasts, which are presumed to be affected by the inlet-estuary system. Subsequently, this coastline variation due to the total sediment volume change is assumed to shift the entire active coastal profile along the inlet-affected coast. This simple geometric relationship can be expressed as:

$$dx_V = \frac{\Delta V_T}{L_{AC}D} \quad [4-1]$$

where dx_V is coastline variation due to total sediment volume change (m), ΔV_T is total sediment volume change (m^3), L_{AC} is the total length of inlet-affected coastline (m), and D is the depth of closure (m).

This method provides a first-order approximation of coastline variation due to the change in total sediment volume exchange (ΔV_T) at tidal inlets. This approach has been applied to the 41 inlet-estuary systems considered in this study. The 50th percentile values of the projected time-averaged ΔV_T over the 2091-2100 period were used to determine the coastline variation due to the change in total sediment volume exchange.

The final coastline positions of these inlet-interrupted coasts were determined by superimposing the coastal recession due to Bruun effect. The extent of coastline recession due to the Bruun effect was determined based on the method presented by Vousdoukas et al. (2020), which can be expressed as:

$$dx_{BE} = E \frac{1}{\tan \beta} SLR \quad [4-2]$$

where dx_{BE} is the coastal recession due to Bruun effect (m), E is a correction factor for the Bruun effect that varies randomly within a fitted triangular distribution of minimum, maximum, and median values of 0.1, 1.0, and 0.75, respectively, $\tan \beta$ is the active profile slope, and SLR is the projected sea-level rise (here SL_G was used in all computations).

In this study, the median value of E (0.75) was used to determine the coastal recession due to the Bruun effect. The projected total coastline changes by 2100 under RCP 2.6 and 8.5

are shown in Figure 4-6 and Figure 4-7, respectively. The figures were created based on the time-averaged 50th percentile values of ΔV_T over the end-century period (2091-2100). The projected coastline change based on the time-averaged 10th and 90th percentile values of ΔV_T over same period are presented in Annex A.4 for comparison purposes. The largest range of coastline change for 10th and 90th percentile values of ΔV_T was projected at the Muni system for all RCPs (122 m, 125 m, 129 m, and 168 m for RCP 2.6, 4.5, 6.0, and 8.5, respectively). The minimum ranges in coastline variations were projected at Alesa (OR, USA) and Mawddach (Wales, the UK) systems for all RCPs (2 m for RCP 2.6, 4.5, and 6.0, respectively and 3 m for RCP 8.5).

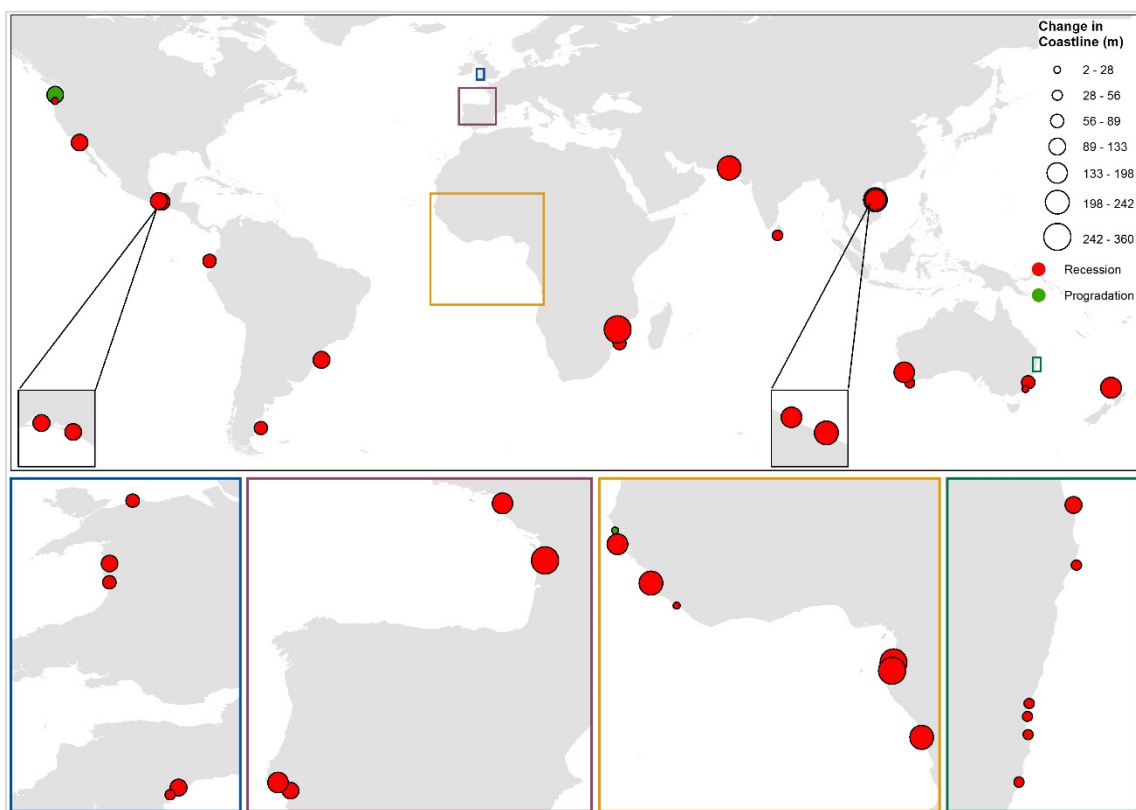


Figure 4-6: The projected total change in inlet-affected coastlines by 2100 for RCP 2.6. The projected coastline change shown is that associated with time-averaged values of the 50th percentiles of the total sediment volume exchange (ΔV_T) between the estuary system and its adjacent coast over the 2091-2100 period plus the coastal recession due to the Bruun effect by 2100.

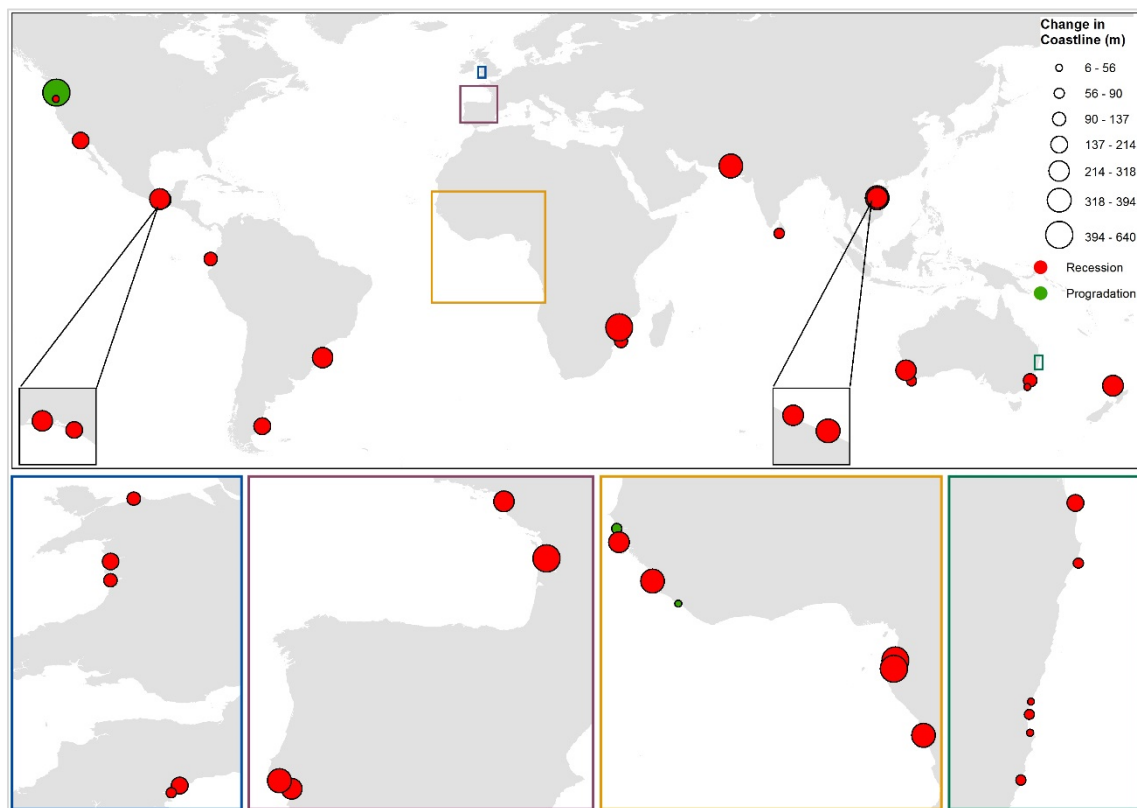


Figure 4-7: The projected total change in inlet-affected coastlines by 2100 for RCP 8.5. The projected coastline change shown is that associated with time-averaged values of the 50th percentiles of the total sediment volume exchange (ΔV_T) between the estuary system and its adjacent coast over the 2091-2100 period plus the coastal recession due to the Bruun effect by 2100.

The coastline changes by 2100 projected here were compared with the findings of a study that investigates the world's sandy shoreline evolution under rising sea level. The following table (Table 4-2) shows the comparison of the projected coastline change with the median changes in shoreline presented by Vousdoukas et al. (2020) for RCP 4.5 and 8.5 by 2100. The selected 41 systems are clustered into different continents/countries for convenience in comparison.

The comparison of the model results indicates that the coastline changes projected here are mostly larger than the projections made by Vousdoukas et al. (2020) for the eroding coasts. This is likely due to the fact that Vousdoukas et al.'s (2020) projections do not account for the estuarine sediment demand when assessing the future coastline positions. In the applications of the SMIC model for four case studies from different parts of the world, Ranasinghe et al. (2013) concluded that the coastline recession due to the Bruun effect only accounts for ~25 to 50 percent of the total coastline change at small tidal inlets, which explains the larger recession amounts projected by the present application.

A significant difference in the two sets of projections can be observed at the Colombia, Gambia, and St. Paul systems, where coastline progradation is projected by the present application, while Vousdoukas et al.'s (2020) projections indicate coastline recession. This can be explained by the fact that while the present application does take fluvial sediment

supply and future changes therein (i.e., the main driver of coastline progradation) into account, Vousdoukas et al.'s (2020) approach does not.

Table 4-2: Comparison of projected coastline change by 2100 with the results of Vousdoukas et al. (2020). Positive and negative values of coastline change indicate coastal progradation and recession, respectively. The 50th percentile values of the projected coastline change by Vousdoukas et al. (2020) in the vicinities of the 41 selected inlet-estuary systems are used in this comparison.

| Label | System Name | Projected coastline change (m) by 2100: present application | | Region/ Country | Projected coastline change (m) by 2100: (Vousdoukas et al., 2020) | |
|-------|----------------|--|---------|-------------------------|--|---------|
| | | RCP 4.5 | RCP 8.5 | | RCP 4.5 | RCP 8.5 |
| B_000 | Mar Muerto | -145 | -210 | Central America | -100 | -150 |
| B_001 | Lugana | -169 | -238 | | | |
| B_006 | San Diego | -128 | -182 | West USA | -50 | -100 |
| B_009 | Colombia River | 251 | 534 | Northwest USA | -50 | -50 |
| B_012 | Tubarao | -134 | -255 | East-mid South America | -100 | -150 |
| B_017 | Rio Deseado | -122 | -164 | East-low. South America | -100 | -150 |
| B_019 | Rio Chone | -84 | -105 | Northwest South America | -100 | -100 |
| B_067 | Kaipara | -209 | -296 | New Zealand | -200 | -200 |
| B_071 | Gambia | 73 | 60 | | | |
| B_073 | Cacheu | -233 | -318 | | | |
| B_080 | Freetown | -272 | -370 | Western Africa | -200 | -200 |
| B_089 | Muni | -449 | -635 | | | |
| B_090 | Gabon | -358 | -508 | | | |
| B_091 | Zaire | -267 | -378 | | | |

A Holistic Modelling Approach to Simulate Catchment-Estuary-Coastal System Behaviour at Macro Time Scales

| Label | System Name | Projected coastline change (m) by 2100: present application | | Region/ Country | Projected coastline change (m) by 2100: (Vousdoukas et al., 2020) | |
|-------|------------------|--|---------|-----------------------|--|---------|
| | | RCP 4.5 | RCP 8.5 | | RCP 4.5 | RCP 8.5 |
| B_093 | Inhambane | -96 | -138 | Eastern Africa | -150 | -150 |
| B_095 | Beira | -350 | -509 | | | |
| B_104 | Miani Hor | -297 | -395 | Central Asia | -150 | -200 |
| B_111 | Hue | -269 | -370 | Mid-Vietnam | -200 | -200 |
| B_136 | Setubal | -168 | -245 | Southwest of Portugal | -100 | -150 |
| B_137 | Lisboa | -230 | -339 | | | |
| B_139 | Gironde | -349 | -481 | Northwest of France | -200 | -200 |
| B_140 | Loire | -195 | -306 | | | |
| B_301 | Wilson | -54 | -75 | Western Australia | -50 | -50 |
| B_302 | St Paul | -12 | 7 | West Africa | -50 | -50 |
| B_303 | Tweed River | -151 | -214 | | | |
| B_304 | Richmond River | -58 | -86 | | | |
| B_305 | Hastings River | -64 | -91 | | | |
| B_306 | Shoalhaven River | -106 | -132 | NSW (Australia) | -50 | -100 |
| B_307 | Macleay River | -38 | -56 | | | |
| B_308 | Nambucca | -49 | -67 | | | |
| B_309 | Bellinger River | -38 | -52 | | | |
| B_310 | Bega River | -34 | -43 | | | |

| Label | System Name | Projected coastline change (m) by 2100: present application | | Region/ Country | Projected coastline change (m) by 2100: (Vousdoukas et al., 2020) | |
|-------|-------------|--|---------|-------------------------|--|---------|
| | | RCP 4.5 | RCP 8.5 | | RCP 4.5 | RCP 8.5 |
| B_311 | Mawddach | -123 | -165 | | | |
| B_312 | Exe | -129 | -180 | West and south of UK | -100 | -100 |
| B_313 | Conwy | -77 | -105 | | -100 | -100 |
| B_314 | Teign | -64 | -87 | | | |
| B_315 | Thuan | -212 | -293 | Mid-Vietnam | -200 | -200 |
| B_316 | Alsea | -33 | -44 | West of USA | -50 | -50 |
| B_317 | Dyfi | -79 | -106 | West of UK | -100 | -100 |
| B_318 | Kalutara | -49 | -64 | West of Sri Lanka | -100 | -150 |
| B_319 | Swan | -213 | -269 | Western Australia | -150 | -200 |

4.5 Summary and conclusions

The reduced-complexity modelling technique that was developed in this study to probabilistically assess climate change-driven variations of inlet-interrupted coast at macro (50-100 year) time scales, while taking into account the contributions from Catchment-Estuary-Coastal (CEC) systems in a holistic manner, was applied to 41 mainland inlet-estuary systems located across all continents.

Data of the barrier-estuary systems considered in this chapter were obtained from three global datasets (the DIVA dataset presented by Hinkel et al. (2013), the enhanced UK estuary database presented by Manning (2012), and the New South Wales (Australia) estuary database obtained from Office of Environment and Heritage-New South Wales (2017)). The estuary surface-area values were checked against a global estuary dataset published by Alder (2003) and Watson et al. (2004), to ensure the reliability of the estuary surface-area values used in the model applications, as this parameter affects two of the three components (i.e., basin infilling volume and basin volume change) of the total sediment volume exchange (ΔV_T) calculations in the model. As the DIVA dataset did not contain basin volume information, the basin volume values required for sediment volume calculation were obtained through a fitted linear regression model that estimates basin-volume magnitude given estuary surface area and tidal amplitude values. The input (i.e., basin volume, estuary surface area, and tidal amplitude) for the linear regression model development were obtained by combining three estuary databases from the UK (Manning, 2012), USA (Engle et al., 2007), and NSW, Australia (Office of Environment and Heritage-New South Wales, 2017). The final combined dataset used for regression model development contained 324 estuary systems.

The climatic input required for model forcing were obtained from 4 selected CMIP5 GCMs. Yearly stochastic model input for annual mean temperature (T) and cumulative river discharge (Q) were derived from fitted joint probability models. Yearly stochastic model input for global sea-level change (ΔSL_G) was obtained by fitting triangular distributions to the minimum, median and maximum projections of global mean sea-level rise presented by Stocker et al. (2013). The human-induced erosion at the catchment scale (E_h) was approximated using the rescaled Human FootPrint Index (HFPI) values (Wildlife Conservation Society - WCS and Center for International Earth Science Information Network - CIESIN - Columbia University, 2005) over the watersheds. The stochastic model inputs of human-induced erosion were generated from fitted triangular distributions, in which linearly increasing minimum, median, and maximum values of E_h were assumed over the study period. These four stochastic model inputs were used in a Monte-Carlo framework to obtain fully probabilistic projections of the change in total sediment volume exchange (ΔV_T) at the 41 selected barrier estuary systems. The main findings of this model applications are summarized below.

- 1) Most of the world's inlet-interrupted coasts may erode under changing climate conditions. Depending on the projected climatic conditions (i.e., arid or non-arid conditions) and the characteristics of the attached river catchment, both basin infilling and fluvial sediment supply could influence the future evolution of the inlet-interrupted coasts.
- 2) Based on the projected results of the 41 barrier estuary systems, an indicative threshold was derived to predict the behaviour of the inlet-estuary systems. This first-order approximation indicates that the long-term evolution of inlet-interrupted coasts in non-arid river catchments is affected by both basin infilling and fluvial sediment supply if the ratio between the estuary surface area and the river catchment area is less than 0.01. On the other hand, both the inlet-estuary systems attached to arid river catchments and for those with first-order approximation ratio greater than 0.01 are likely to be influenced only by the basin infilling sediment demands of the estuary.

Chapter 5

General conclusions

5.1 Introduction

The preceding chapters provided probabilistic projections of inlet-interrupted coastlines under climate change-driven impacts at macro (50-100 year) time scales, while taking into account the contributions from Catchment-Estuary-Coastal (CEC) systems in a holistic manner. To achieve the overarching research objective of this dissertation, a reduced-complexity modelling technique has been developed and subsequently applied at four mainland barrier-estuary systems (viz., Alesha estuary, Oregon, USA; Dyfi estuary, Wales, UK; Kalutara Inlet, Sri Lanka; and Swan River system, Australia), and one barrier island (Chandeleur Islands, Louisiana, USA). The future variation of the world's inlet-interrupted costs was also investigated via a global application of the newly developed reduced-complexity model by applying the model to 41 barrier-estuary systems across six continents. This chapter presents a synthesis of the preceding chapters and the main general conclusions of the study, which also comprises descriptions of relative contributions of the different physical processes governing the long-term evolution of inlet-interrupted coasts (Section 5.2). The final section of this chapter (Section 5.3) outlines the limitations of the proposed reduced-complexity modelling technique and provides suggestions for future developments that may enhance our understanding of the long-term evolution of inlet-interrupted coasts.

5.2 Synthesis and main conclusions of this study

Probabilistically modelling of climate change driven the evolution of inlet-interrupted coasts at macro (50-100 year) time scales, while taking into account the various contributions from the catchment-estuary-coastal (CEC) systems in a holistic manner, can be accomplished by the use of physics-based reduced-complexity (RC) modelling technique. Such a modelling technique needs to encapsulate the main physical processes that govern the variations of the change in total sediment volume exchange between the estuary system and its inlet-interrupted coasts under climate change-driven impacts and anthropogenic activities. The RC model developed here can be applied at longer time scales (i.e., multi-decadal, up to 50~100 years) to obtain projections of coastline change (5~25 km alongshore) at CEC systems with relatively large (i.e., several hundreds of km²) river catchments.

Changes in total sediment volume exchange consist of three key components (as factors in a demand-supply balance): (1) basin volume change caused by sea-level rise, and (2) basin fill change caused by variation in river discharge. Sea level rise causes an increase in accommodation space in the estuary that will result in an extra sediment demand. The river supply will partly fill that extra volume. The rest has to come from the coast, causing recession of the coastline. This comes on top of the sediment demand caused by the Bruun effect along the coast, and (3) fluctuation of the fill volume in the estuary with water discharge of the river. A significant increase in river flow will scour the channel beds and cause the export of sediment to the sea. In a later stage part of that sediment might be imported into the estuary again after reduction of the river flow. Hence, the estuarine fill 'breathes' with the river discharge. These sediment volume components are in turn driven by four main drivers: annual mean temperature, annual cumulative river discharge, regional relative sea-level rise, and anthropogenic activities.

First, a modelling technique that deterministically estimates the variation in total sediment volume exchange is presented in Section 2.2 of this dissertation. Herein, the temperature is considered as the main driver, while river discharge and sea level are considered to vary with the future changes in temperature. Future changes in anthropogenic activities are considered as an independent driver.

Secondly, the above-mentioned deterministic model is extended into a fully probabilistic model and demonstrated at four strategically selected case study sites (viz., Alsea estuary, Oregon, USA; Dyfi estuary, Wales, UK; Kalutara Inlet, Sri Lanka; and Swan river system, Australia). Here, the stochastic model inputs of the aforementioned four system drivers are first constructed using available data. Yearly stochastic model input for anthropogenic impacts are obtained from fitted triangular distributions, where the minimum, median, and maximum increments by 2100 were assumed to be 10, 15, and 20 percent of present value, respectively. Yearly stochastic model inputs for temperature and river discharge are

obtained from the fitted joint probability distributions. Inputs for these fitted joint probability distributions are obtained from the selected CMIP5 GCMs that are most suited for the case study locations. Yearly stochastic variables for regional relative sea-level change are also obtained from fitted triangular distributions. These yearly triangular distributions were fitted from computed minimum, mean, and maximum changes in regional relative sea-level projections (Section 1.4.3). The application of the model with these inputs, within a Monte Carlo framework (100,000 model realisations per year) yields probabilistic estimates of the change in total sediment volume exchange between the estuary system and the adjacent inlet-interrupted coast. A conceptual framework to distribute the impacts of the above-computed variations of change in total sediment volume exchange (ΔV_T) along the inlet-interrupted coastline is presented in Section 2.4. Probabilistic estimates of the computed variations of ΔV_T enables total projection uncertainty driven selection of a sediment volume, which can be subsequently distributed along the inlet-affected coastline. This sediment volume distribution is a function of the net annual longshore sediment transport capacity at the vicinity of the estuary systems. The final coastline position can be estimated by superimposing the coastline recession due to the Bruun effect to the above-computed sediment volume variation-driven coastline change. This final coastline position provides a first-order estimation of the future evolution of inlet-interrupted coasts under climate change-driven impacts and anthropogenic activities.

Model results at the case study sites indicate that, although mainland inlet-interrupted coasts (i.e., coastlines with barrier estuaries) are likely to import sediment from the coast by the end of this century, the governing processes and the relative contributions of different processes (i.e., change in fluvial sediment, basin infilling volume, and basin volume change) may vary markedly depending on the inter-site differences in geomorphic settings and climate change projections.

The change in total sediment volume exchange at the Alsea estuary (USA) and its inlet-interrupted coast in Oregon, USA is affected by both the sediment demand due to basin infilling and the variation in fluvial sediment supply, in which the former governs the overall behaviour of the system. Increased fluvial sediment supply towards the end of the 21st century may reduce the total sediment demand by the estuary due to basin infilling, which is likely to reduce the total coastal recession along its inlet-interrupted coasts. These processes are closely linked with climatic forcing, in which the projected temperature increases the fluvial sediment supply, especially towards the end of the 21st century. The projected variations in river discharge at the Alsea river catchment are trivial, and hence its potential contribution to the change in fluvial sediment supply is minimal. Therefore, the combined effects of temperature and anthropogenic activities by 2100 are the main contributors to the increased fluvial sediment supply from the Alsea river catchment. The sediment volume demand due to basin infilling is directly affected by the regional relative sea-level change. As a result, the variation of sediment volume demand closely follows the

projected change in sea level. The net effect of these two processes results in eroding the inlet-interrupted coast along the Alsea estuary, which is exacerbated by the coastal recessions due to the Bruun effect.

The overall behaviour of the inlet-interrupted coast along Dyfi estuary (Wales, UK) is governed by the sediment volume demand due to basin infilling. The projected changes in river discharge at the Dyfi River catchment are trivial, and hence its potential contribution to the fluvial sediment supply is also minimal. Despite the increased temperature and anthropogenic impacts closer to 2100, the Dyfi River catchment may not generate a significant volume of fluvial sediment to compensate for the basin infilling demand driven by sea-level rise. As a result, the total sediment volume demand to the Dyfi estuary increases throughout the century following the projected regional relative sea level, leading to increased coastal recession along its inlet-interrupted coast. This coastal recession is further increased by the Bruun effect driven erosions throughout the century.

The evolution of the inlet-interrupted coast adjacent to Kalutara inlet (Sri Lanka) is mostly affected by the changes in fluvial sediment supply. The projected variations in temperature, river discharge, and increments in anthropogenic impacts may increase the fluvial sediment supply from the river catchment throughout the 21st century. However, extensive sand mining activities along the river significantly reduce the potential fluvial sediment supply to the coast, thus eroding the inlet-interrupted coast adjacent to the estuary throughout the century. However, during the end-century period (2091-2100), significantly increased temperature and river discharge values are projected under RCP 8.5. These climatic inputs, together with the anthropogenic impacts by 2100, are sufficiently large to provide a surplus of sediment to the coast. However, coastline progradation due to this sediment surplus is smaller than the coastal recession due to the Bruun effect over the same period. As a result, the net change (by 2100) of the coast adjacent to Kalutara inlet expected to be a recession. If the impacts of sand mining activities are removed from the sediment volume calculations, the fluvial sediment supply to the coast by the Kalu River catchment will be significantly larger than the sediment volume demand due to basin infilling. As a result, inlet-interrupted coast along Kalutara estuary could prograde throughout the 21st century. This result highlights the significant impact of river sand mining on the future evolution of coastline adjacent to Kalutara inlet.

The inlet-interrupted coast adjacent to the Swan River inlet (Western Australia) is affected by both basin volume change and basin infilling, with the former governing the overall sediment volume exchange between the estuary and the coast. The projected change in fluvial sediment supply from the river catchment is minimal, and thus has a trivial impact on the evolution of the inlet-interrupted coast. The sediment volume demand due to basin volume change is directly affected by changes in river flow, and thus follow the projected variations of river discharge. The sediment volume demand due to basin infilling increases with the projected changes in regional relative sea level, leading to an increase in the total

sediment volume demand by the estuary. Owing to this sediment volume demand, the coastline adjacent to the Swan River inlet is projected to erode throughout the 21st century. This coastal recession is further increased by the Bruun effect driven erosions as well.

The evolution of the barrier island coast along the Chandeleur Islands (Louisiana, USA) is governed by the sediment volume demand due to basin infilling, and hence its variation follows the projected regional relative sea-level change. However, the maximum barrier-migration distance was found to be restricted by the maximum migration threshold, which forces the barrier island to reduce its freeboard under rising sea level. The projected changes of Chadeleur Island over the 21st century indicate that the barrier island could survive without drowning under projected sea-level rise scenarios. Model simulations under hypothetical conditions (i.e., zero marine sediment supply, reduced initial barrier freeboard, and reduced threshold for maximum migration-distance) indicate that future drowning of this barrier island is closely linked with its initial freeboard.

There are significant uncertainties in the projections of coastline change obtained for all case study sites. These uncertainties emphasize the need for probabilistic modelling techniques when investigating long-term coastline evolutions so that risk-based information can be provided to the coastal zone planners/managers and decision makers to manage/mitigate socio-economic losses due to future climate change impacts and anthropogenic activities.

Application of the reduced-complexity model developed here at 41 barrier-estuary systems spanning in six different continents shows that 93% of the studied inlet-interrupted coasts may erode under changing climate conditions. Results show that, depending on the projected climatic conditions (i.e., arid or non-arid conditions) and the characteristics of the river catchment, basin infilling and fluvial sediment supply are likely to be the main processes governing the future evolution of the inlet-interrupted coasts. Only 2 of the studied inlet-interrupted coasts are projected to prograde due to surpluses of fluvial sediment supply from the river catchments where significant increments are projected for river discharge and temperature. The findings of this study show that the evolution of inlet-interrupted coastlines at macro time scales may not always be governed by the climate change-induced sea-level rise, as commonly believed.

Further scrutiny of the global application results indicates that, to a first-order, the ratio between estuary surface area and river catchment area identifies the key processes governing the future evolution of inlet-interrupted coasts. For systems with non-arid catchments, when this ratio is less than 0.01, the coastline evolution is controlled by the interaction between sea-level rise driven basin infilling and changes in fluvial sediment supply. When the ratio is greater than 0.01, only the basin infilling (i.e., sea-level rise) needs to be considered to understand coastline evolution. For systems in arid catchments, coastline evolution is likely to be controlled by sea-level rise driven basin infilling in all cases.

5.3 Implications of the study and possible future research initiatives

The reduced-complexity modelling technique presented in this study enables the probabilistic simulation of the future evolution of inlet-interrupted coasts at macro (50-100 year) time scales. The findings of this study show that the evolution of inlet-interrupted coastlines at macro time scales may not always be governed by the climate change-induced sea-level rise, as commonly believed. Although this general expectation does hold for many of the case studies considered, at some systems, other processes such as fluvial sediment supply (e.g., Kalutara inlet, Sri Lanka and Alsea estuary, USA) and future variations in river flow (e.g., Swan river inlet, Australia) govern the future coastline change.

Due to the time limitations, this study was not extended to investigate the contribution of each of the uncertain model inputs (i.e., temperature (T), runoff (Q), regional relative sea-level change (ΔRSL), and human-induced erosion factor (E_h)) to the total variance of the projected coastline change. One future research directions would be to evaluate the contribution of the individual model inputs to the total uncertainty of the model projections by the use of global sensitivity analysis approach presented by Sobol' (2001). An application of this method with respect to shoreline change projection is presented by Le Cozannet et al. (2019).

Future research in this area could benefit from improving the representation of the anthropogenic activities within the river catchments. In this study, the human footprint index (HFPI) was used to quantify (in a rather aggregated way) the contemporary anthropogenic impacts at the catchment scale, and a linear increment of HFPI was assumed to represent future changes in human activities that affect fluvial sediment supply. However, it is known that the human-induced impacts have substantially modified the sediment generation and transportation at catchment scale (Dunn et al., 2019, 2018; Ranasinghe et al., 2019b; Syvitski et al., 2009; Syvitski and Milliman, 2007). Furthermore, human-induced impacts on the environment vary along various dimensions (e.g., population growth, urbanization, and economic development). Hence, better representation and translation of future human activities, such as changes in land use pattern, reservoir sediment trapping, and introduction of flood controlling/water diversion structures could improve the assessment of projected change in fluvial sediment supply at the catchment scale.

Improving the representation of river discharge at the catchment scale is another research area that could improve projections of the long-term evolution of inlet-interrupted coasts. In this study, fluvial sediment supply to the coast was computed as a direct function of mean annual temperature, cumulative annual river discharge, and human-induced erosion (i.e., anthropogenic impacts). In doing so, the cumulative annual river discharge values

were approximated with the surface runoff projections of the watershed areas. As the fluvial sediment volume changes were calculated at annual time steps, here it was assumed that the cumulative river discharge is equal to the cumulative surface runoff volume. This approximation eliminates the contribution from groundwater inputs to riverflow (i.e., baseflow) and all water volume reductions of surface flow (e.g., detention losses, evaporation, water extraction, and seepage). More detailed representation of riverflow will improve assessments of fluvial sediment supply.

The proposed reduced-complexity modelling technique does not account for potential changes in net annual longshore sediment transport capacity when assessing future changes along the inlet-interrupted coasts. Many studies have indicated potential changes in future wave climate under changing climatic conditions (Casas-Prat et al., 2018; Hemer et al., 2013; Mori et al., 2010; Morim et al., 2019; Semedo et al., 2013). Such changes in wave conditions (i.e., changes in significant wave height, wave direction, and wave period) have the potential to change the net annual longshore sediment transport capacity, which could subsequently affect the evolution of inlet-interrupted coasts. Therefore, incorporating the changes in longshore sediment transport capacity may also improve the projections of inlet-interrupted coastline evolution under changing climatic conditions.

Future research initiatives are also needed to enhance the understanding of the hysteresis effect between hydrodynamic forcing and morphological response related to the sea-level-rise driven basin infilling volume computations. In this study, the above computation was based on a lag factor adopted in a similar study (i.e., SMIC application by Ranasinghe et al. (2013)). A detailed, process-based investigation of this hysteresis behaviour under different rates of sea-level rise and estuary geometries could substantially strengthen the validity of the presently adopted lag factor (Section 2.2.1; *Basin infilling volume due to sea-level rise-induced increase in accommodation space*).

It is also desirable to apply the proposed modelling technique at different barrier islands. Such a modelling exercise will provide better insights and more conclusive outcomes on whether the reduced-complexity barrier island model presented in this study can be generically used for assessing the long-term evolution of barrier-island coasts worldwide.

A Annexes

A.1 The GCMs used in the study

Table A-1: Details of the GCMs used in this study. Note: All the GCMs were used to obtain the temperature and runoff data for the model applications at Alsea estuary, OR, USA; Dyfi estuary, Wales, UK; and Kalutara Inlet, Sri Lanka. Only the first four GCMs (highlighted) were used in the model applications at Swan river system, Australia. The global application of the model presented in Chapter 4 was also undertaken by the temperature and runoff data obtained from the first four GCMs listed below.

| GCM model ID | Institute | Spatial resolution (Lon. X Lat. in deg.) |
|--------------|---|---|
| GFDL-CM3 | NOAA GFDL, USA | 2.5x2.0 |
| GFDL-ESM2G | NOAA GFDL, USA | 2.5x2.0 |
| GFDL-ESM2M | NOAA GFDL, USA | 2.5x2.0 |
| IPSL-CM5A-MR | Institut Pierre-Simon Laplace, France | 2.5x1.258 |
| HadGEM2-AO | National Institute of Meteorological Research, UK and South Korean Meteorological Administration | 1.875x1.241 |
| MRI-CGCM3 | Meteorological Research Institute, Japan | 1.125x1.125 |
| MIROC5 | Atmosphere and Ocean Research Institute (The University of Tokyo) and the National Institute for Environmental Studies, and Japan Agency for Marine-Earth Science and Technology, Japan | 1.406x1.406 |

A.2 Properties of the selected barrier estuary systems

Table A-2. Properties of the selected barrier estuary systems for global application of the model. Note: Estuary surface area values are available with the original datasets (i.e., global estuary dataset presented by Hinkel et al. (2013) for the DIVA framework, The enhanced UK estuary database published by Manning (2012), The New South Wales estuary database published by Office of Environment and Heritage-New South Wales (2017), SMIC application dataset by Ranasinghe et al. (2013), and Liberian Hydrological Service: Ministry of Lands Mines and Energy and Norwegian Water Resources and Energy Directorate (2016)); Basin volume values were derived through the linear regression model developed in this study to project the basin volume magnitude based on the estuary surface area and the tidal amplitude; Lithology factors of the catchment areas are from (Syvitski and Milliman, 2007); Catchment relief values were calculated from the one arc second resolution digital elevation models obtained from USGS earth explorer tool Farr et al. (2007); Huma induced erosion factor was calculated from the Human FootPrint Index (HFPI) data given in Wildlife Conservation Society - WCS and Center for International Earth Science Information Network - CIESIN - Columbia University. (2005); Depth of closure and breach profile slope values were obtained from Vousdoukas et al. (2020).

| Label | System Name | Catchment Area (km ²) | Estuary Area (km ²) | Basin volume (MCM) | Lithology factor (L) | Catchment relief (km) | Anthropogenic factor (Eh) | Depth of closure (m) | Beach profile Slope |
|-------|-----------------|-----------------------------------|---------------------------------|--------------------|----------------------|-----------------------|---------------------------|----------------------|---------------------|
| B_000 | Mar Muerto | 1,448 | 247 | 456.3 | 1 | 2.478 | 1.0219 | 8 | 0.013 |
| B_001 | Lugana Superior | 2,028 | 220 | 406.4 | 1.5 | 2.26 | 0.8538 | 8 | 0.004 |
| B_006 | San Diego | 1,167 | 107 | 197.7 | 1.5 | 1.75 | 1.1160 | 12 | 0.008 |
| B_009 | Colombia River | 669,403 | 340 | 628.1 | 0.75 | 4.18 | 0.5757 | 20 | 0.005 |
| B_012 | Tubarao Lagoon | 5,636 | 120 | 221.7 | 1.5 | 1.8 | 0.7990 | 13 | 0.007 |
| B_017 | Rio Deseado | 38,743 | 90 | 166.3 | 1 | 2.4 | 0.4821 | 15 | 0.005 |
| B_019 | Rio Chone | 2,311 | 32 | 59.1 | 1.5 | 0.67 | 0.9383 | 8 | 0.006 |
| B_067 | Kaipara | 5,392 | 780 | 1,441.1 | 2 | 0.77 | 0.8925 | 17 | 0.007 |
| B_071 | Gambia | 70,018 | 120 | 221.7 | 2 | 1.54 | 0.7335 | 19 | 0.002 |
| B_073 | Cacheu | 5,797 | 130 | 240.2 | 2 | 0.08 | 0.8172 | 19 | 0.002 |
| B_080 | Freetown | 11,110 | 206 | 380.6 | 1.5 | 0.98 | 0.8627 | 20 | 0.002 |

| Label | System Name | Catchment Area (km ²) | Estuary Area (km ²) | Basin volume (MCM) | Lithology factor (L) | Catchment relief (km) | Anthropogenic factor (Eh) | Depth of closure (m) | Beach profile Slope |
|-------|------------------|-----------------------------------|---------------------------------|--------------------|----------------------|-----------------------|---------------------------|----------------------|---------------------|
| B_089 | Muni | 7,995 | 185 | 341.8 | 0.5 | 1.15 | 0.5803 | 20 | 0.003 |
| B_090 | Gabon | 5,925 | 750 | 1385.6 | 0.5 | 0.92 | 0.4684 | 20 | 0.004 |
| B_091 | Zaire | 40,989 | 520 | 960.7 | 0.5 | 1.08 | 0.6847 | 15 | 0.005 |
| B_093 | Inhambane | 2,377 | 110 | 203.2 | 2 | 0.24 | 0.7744 | 11 | 0.013 |
| B_095 | Beira | 23,830 | 130 | 240.2 | 0.75 | 1.85 | 0.6543 | 9 | 0.002 |
| B_104 | Miami Hor | 11,066 | 314 | 580.1 | 2 | 2.33 | 0.7718 | 10 | 0.006 |
| B_111 | Hue | 1,783 | 100 | 122.0 | 1 | 1.45 | 0.8541 | 20 | 0.002 |
| B_136 | Setubal | 6,516 | 110 | 203.2 | 1 | 0.44 | 0.9200 | 14 | 0.018 |
| B_137 | Lisboa | 8,022 | 320 | 591.2 | 1.5 | 0.98 | 0.9504 | 15 | 0.015 |
| B_139 | Gitonde | 79,750 | 480 | 886.8 | 1 | 3.19 | 0.9072 | 15 | 0.003 |
| B_140 | Loire | 103,552 | 55 | 101.6 | 1 | 1.86 | 0.9413 | 15 | 0.003 |
| B_301 | Wilson | 2,263 | 48 | 85.0 | 0.5 | 0.474 | 0.5570 | 19 | 0.02 |
| B_302 | St Paul | 20,281 | 1.02 | 1.9 | 0.5 | 1.649 | 0.7945 | 10 | 0.005 |
| B_303 | Tweed River | 1,066 | 22.7 | 41.9 | 1 | 1.171 | 0.8227 | 13 | 0.004 |
| B_304 | Richmond River | 6,924 | 38.4 | 70.9 | 1 | 1.152 | 0.6756 | 13 | 0.012 |
| B_305 | Hastings River | 3,594 | 30 | 55.4 | 1 | 1.245 | 0.7627 | 13 | 0.009 |
| B_306 | Shoalhaven River | 7,087 | 31.9 | 58.9 | 1.5 | 1.475 | 0.6265 | 13 | 0.008 |

| Label | System Name | Catchment Area (km ²) | Estuary Area (km ²) | Basin volume (MCM) | Lithology factor (L) | Catchment relief (km) | Anthropogenic factor (Eh) | Depth of closure (m) | Beach profile Slope |
|-------|-----------------|-----------------------------------|---------------------------------|--------------------|----------------------|-----------------------|---------------------------|----------------------|---------------------|
| B_307 | Macleay River | 11,347 | 31.6 | 58.4 | 1 | 1.583 | 0.6076 | 14 | 0.01 |
| B_308 | Nambucca River | 1,090 | 12.6 | 23.3 | 1 | 1.08 | 0.7677 | 14 | 0.01 |
| B_309 | Bellinger River | 1,152 | 8.2 | 15.1 | 1 | 1.558 | 0.7283 | 14 | 0.01 |
| B_310 | Bega River | 1,870 | 3.8 | 7.0 | 0.5 | 1.3 | 0.6637 | 14 | 0.017 |
| B_311 | Mawddach | 314 | 3.642 | 6.7 | 0.5 | 0.878 | 0.9425 | 10 | 0.003 |
| B_312 | Exe | 1,402 | 19.185 | 35.4 | 0.5 | 0.517 | 1.0585 | 11 | 0.006 |
| B_313 | Conwy | 502 | 5.556 | 10.3 | 0.5 | 0.863 | 0.8714 | 8 | 0.006 |
| B_314 | Teign | 487 | 4.041 | 7.5 | 0.5 | 0.589 | 1.0471 | 11 | 0.007 |
| B_315 | Thuan | 3,800 | 110 | 178.0 | 1 | 1.2 | 0.8200 | 20 | 0.003 |
| B_316 | Alsea | 1,225 | 9.1 | 20.0 | 1 | 1.25 | 0.6100 | 22 | 0.012 |
| B_317 | Dyfi | 670 | 17.3 | 45.0 | 0.75 | 0.66 | 0.9200 | 10 | 0.007 |
| B_318 | Kalutara | 2,778 | 1.75 | 5.3 | 0.5 | 2.25 | 0.9300 | 7 | 0.005 |
| B_319 | Swan | 121,000 | 52 | 312.0 | 0.5 | 0.8 | 0.5800 | 17 | 0.003 |

A.3 Projected change in total sediment volume exchange at the selected barrier estuary systems

Table A-3: Different percentiles of mean change in total sediment volume exchange (ΔV_T) at the selected barrier estuary systems during 2091-2100 period. Note: The mean values of change in total sediment volume exchange were computed by averaging the projected 10th, 50th, and 90th percentile values of ΔV_T over 2091-2100 time period; BI, BV, and FS denote Basin Infilling, Basin Volume, and Fluvial Sediment, respectively; negative signs denote sediment imported into the estuary.

| Label | System Name | Mean values of the change in total sediment volume exchange (ΔV_T) over 2091-2100 period ($\times 10^6 \text{ m}^3$) | | | | | | | | | | | |
|-------|-----------------|--|------------------|------------------|------------------|------------------|------------------|------------------|------------------|------------------|------------------|------------------|------------------|
| | | RCP 2.6 | | | RCP 4.5 | | | RCP 6.0 | | | RCP 8.5 | | |
| | | 10 th | 50 th | 90 th | 10 th | 50 th | 90 th | 10 th | 50 th | 90 th | 10 th | 50 th | 90 th |
| B_000 | Mar Muerto | -45.5 | -35.5 | -26.3 | -57.6 | -47.3 | -37.9 | -58.3 | -47.8 | -38.0 | -83.4 | -69.5 | -56.7 |
| B_001 | Lugana Superior | -37.0 | -28.1 | -19.8 | -47.9 | -38.7 | -30.3 | -47.9 | -38.6 | -29.8 | -70.0 | -57.7 | -46.2 |
| B_006 | San Diego | -19.1 | -14.8 | -10.8 | -24.6 | -20.1 | -16.1 | -22.2 | -17.7 | -13.4 | -35.6 | -29.5 | -24.0 |
| B_009 | Colombia River | 120.4 | 160.6 | 202.9 | 273.7 | 321.5 | 371.1 | 330.0 | 371.6 | 416.7 | 569.3 | 628.3 | 686.2 |
| B_012 | Tubarao Lagoon | -15.6 | -10.4 | -5.7 | -16.3 | -10.9 | -5.8 | -18.9 | -13.3 | -8.0 | -31.9 | -24.3 | -16.7 |
| B_017 | Rio Deseado | -17.0 | -13.2 | -9.6 | -27.1 | -23.1 | -19.4 | -26.4 | -22.3 | -18.5 | -37.0 | -31.4 | -26.3 |
| B_019 | Rio Chone | -3.1 | -1.8 | -0.5 | -4.5 | -3.1 | -1.8 | -3.2 | -1.7 | -0.3 | -5.1 | -3.2 | -1.4 |
| B_067 | Kaipara | -158.0 | -126.1 | -97.3 | -194.6 | -162.0 | -132.2 | -199.1 | -165.9 | -134.3 | -277.2 | -233.3 | -192.8 |
| B_071 | Gambia | 45.2 | 57.8 | 70.1 | 82.0 | 94.6 | 107.6 | 85.8 | 98.0 | 110.5 | 98.0 | 112.5 | 127.3 |
| B_073 | Cacheu | -26.5 | -21.2 | -16.3 | -32.3 | -26.9 | -22.0 | -33.3 | -27.7 | -22.5 | -46.4 | -39.0 | -32.3 |
| B_080 | Freetown | -31.3 | -22.6 | -14.7 | -37.5 | -28.6 | -20.5 | -35.8 | -26.8 | -18.2 | -51.9 | -40.2 | -29.1 |
| B_089 | Muni | -386.6 | -310.3 | -240.8 | -475.0 | -397.5 | -326.3 | -486.5 | -406.8 | -331.3 | -677.7 | -572.5 | -475.6 |

Mean values of the change in total sediment volume exchange (ΔV_T) over 2091-2100 period ($\times 10^6 \text{ m}^3$)

| Label | System Name | RCP 2.6 | | | RCP 4.5 | | | RCP 6.0 | | | RCP 8.5 | | |
|-------|------------------|------------------|------------------|------------------|------------------|------------------|------------------|------------------|------------------|------------------|------------------|------------------|------------------|
| | | 10 th | 50 th | 90 th | 10 th | 50 th | 90 th | 10 th | 50 th | 90 th | 10 th | 50 th | 90 th |
| B_090 | Gabon | -315.2 | -253.1 | -196.6 | -387.0 | -323.9 | -266.1 | -397.0 | -332.2 | -270.9 | -552.8 | -467.4 | -388.5 |
| B_091 | Zaire | -144.4 | -114.2 | -86.5 | -178.5 | -147.4 | -119.2 | -182.3 | -150.6 | -121.1 | -254.3 | -212.3 | -173.9 |
| B_093 | Inhambane | -22.6 | -18.1 | -14.0 | -27.4 | -22.8 | -18.6 | -28.6 | -23.9 | -19.5 | -39.7 | -33.5 | -27.8 |
| B_095 | Beira | -44.1 | -33.2 | -23.4 | -50.1 | -39.0 | -28.9 | -50.1 | -38.9 | -28.4 | -76.0 | -61.3 | -47.4 |
| B_104 | Miani Hor | -144.6 | -115.7 | -89.4 | -172.1 | -142.8 | -115.8 | -170.5 | -140.5 | -112.3 | -229.2 | -189.6 | -152.7 |
| B_111 | Hue | -36.2 | -28.5 | -21.3 | -45.1 | -37.1 | -29.8 | -45.9 | -37.7 | -30.0 | -64.4 | -53.6 | -43.6 |
| B_136 | Setubal | -50.8 | -40.7 | -31.6 | -62.3 | -52.1 | -42.6 | -64.6 | -54.0 | -43.9 | -90.5 | -76.7 | -63.7 |
| B_137 | Lisboa | -106.0 | -84.8 | -65.4 | -129.9 | -108.2 | -88.3 | -135.1 | -112.5 | -91.2 | -190.5 | -161.4 | -134.3 |
| B_139 | Gironde | -180.3 | -132.9 | -89.5 | -222.8 | -174.0 | -129.4 | -214.4 | -165.6 | -119.6 | -307.4 | -243.0 | -182.6 |
| B_140 | Loire | -38.4 | -22.9 | -8.3 | -38.7 | -23.1 | -8.8 | -25.1 | -9.7 | 5.1 | -64.0 | -44.5 | -25.8 |
| B_301 | Wilson | -10.0 | -8.0 | -6.1 | -12.6 | -10.2 | -8.4 | -12.4 | -10.4 | -8.4 | -17.2 | -14.6 | -12.1 |
| B_302 | St Paul | 9.1 | 11.1 | 13.2 | 9.6 | 11.7 | 13.8 | 12.8 | 15.0 | 17.2 | 18.0 | 20.2 | 22.7 |
| B_303 | Tweed River | -4.0 | -3.1 | -2.2 | -5.1 | -4.1 | -3.2 | -5.2 | -4.2 | -3.3 | -7.5 | -6.3 | -5.1 |
| B_304 | Richmond River | -5.4 | -3.8 | -2.3 | -7.2 | -5.5 | -4.0 | -7.3 | -5.6 | -3.9 | -11.3 | -9.1 | -7.0 |
| B_305 | Hastings River | -4.8 | -3.5 | -2.3 | -5.2 | -3.9 | -2.8 | -5.3 | -4.0 | -2.8 | -7.7 | -6.0 | -4.4 |
| B_306 | Shoalhaven River | -8.0 | -6.6 | -5.3 | -9.5 | -8.0 | -6.7 | -7.3 | -5.8 | -4.4 | -11.3 | -9.4 | -7.6 |

Mean values of the change in total sediment volume exchange (ΔV_T) over 2091-2100 period ($\times 10^6 \text{ m}^3$)

| Label | System Name | RCP 2.6 | | | RCP 4.5 | | | RCP 6.0 | | | RCP 8.5 | | |
|-------|-----------------|------------------|------------------|------------------|------------------|------------------|------------------|------------------|------------------|------------------|------------------|------------------|------------------|
| | | 10 th | 50 th | 90 th | 10 th | 50 th | 90 th | 10 th | 50 th | 90 th | 10 th | 50 th | 90 th |
| B_307 | Macleay River | -2.9 | -1.4 | 0.1 | -1.9 | -0.4 | 1.0 | -1.8 | -0.3 | 1.2 | -3.3 | -1.3 | 0.6 |
| B_308 | Nambucca River | -2.1 | -1.6 | -1.1 | -2.4 | -1.9 | -1.4 | -2.5 | -1.9 | -1.4 | -3.5 | -2.8 | -2.1 |
| B_309 | Bellinger River | -1.2 | -0.8 | -0.4 | -0.9 | -0.5 | -0.1 | -1.1 | -0.7 | -0.3 | -1.3 | -0.8 | -0.4 |
| B_310 | Bega River | -0.8 | -0.7 | -0.5 | -1.1 | -0.9 | -0.7 | -0.8 | -0.6 | -0.4 | -1.3 | -1.0 | -0.8 |
| B_311 | Mawddach | -0.7 | -0.5 | -0.4 | -0.8 | -0.7 | -0.5 | -0.8 | -0.7 | -0.5 | -1.1 | -0.9 | -0.8 |
| B_312 | Exe | -3.8 | -3.1 | -2.4 | -4.6 | -3.8 | -3.1 | -4.8 | -3.9 | -3.2 | -6.6 | -5.6 | -4.6 |
| B_313 | Conwy | -1.1 | -0.8 | -0.6 | -1.2 | -1.0 | -0.8 | -1.3 | -1.0 | -0.8 | -1.8 | -1.5 | -1.2 |
| B_314 | Teign | -0.8 | -0.6 | -0.5 | -0.9 | -0.7 | -0.6 | -0.9 | -0.8 | -0.6 | -1.3 | -1.1 | -0.9 |
| B_315 | Thuan | -18.5 | -14.0 | -9.9 | -23.5 | -18.9 | -14.7 | -23.5 | -18.8 | -14.3 | -33.4 | -27.1 | -21.4 |
| B_316 | Aalsea | -1.5 | -1.1 | -0.7 | -1.7 | -1.3 | -0.9 | -1.6 | -1.1 | -0.7 | -2.1 | -1.5 | -1.0 |
| B_317 | Dyfi | -3.2 | -2.4 | -1.8 | -4.2 | -3.4 | -2.7 | -4.2 | -3.4 | -2.8 | -5.6 | -4.6 | -3.6 |
| B_318 | Kalutara | 2.1 | 2.7 | 3.3 | 3.9 | 4.6 | 5.4 | 4.3 | 5.1 | 5.8 | 5.5 | 6.3 | 7.2 |
| B_319 | Swan | -59.4 | -49.9 | -28.3 | -57.8 | -48.5 | -25.1 | -61.7 | -49.0 | -24.1 | -70.2 | -56.9 | -22.9 |

A.4 Projected inlet-affected coastline change adjacent to the selected barrier estuary system

Table A-4: The projected different percentiles of shoreline variation along the inlet-affected coastlines adjacent to the selected barrier estuary systems during 2091-2100 period. Note: The 10th, 50th, and 90th percentiles of coastline change were calculated for the same percentiles of mean change in total sediment volume exchange (ΔV_T) over 2091-2100 time period (Table A-3). The coastal recession due to Bruun effect was calculated for the mean change in sea level by 2100.

| Label | System Name | Projected change in coastline 2091-2100 (m) | | | | | | | | | | | |
|-------|-----------------|---|------------------|------------------|------------------|------------------|------------------|------------------|------------------|------------------|------------------|------------------|------------------|
| | | RCP 2.6 | | | RCP 4.5 | | | RCP 6.0 | | | RCP 8.5 | | |
| | | 10 th | 50 th | 90 th | 10 th | 50 th | 90 th | 10 th | 50 th | 90 th | 10 th | 50 th | 90 th |
| B_000 | Mar Muerto | -137 | -112 | -89 | -171 | -145 | -122 | -173 | -147 | -123 | -245 | -210 | -178 |
| B_001 | Lugana Superior | -152 | -133 | -116 | -188 | -169 | -151 | -190 | -170 | -152 | -264 | -238 | -214 |
| B_006 | San Diego | -117 | -99 | -82 | -147 | -128 | -111 | -138 | -119 | -101 | -207 | -182 | -159 |
| B_009 | Colombia River | 60 | 101 | 143 | 203 | 251 | 301 | 258 | 300 | 345 | 475 | 534 | 592 |
| B_012 | Tubarao Lagoon | -163 | -123 | -86 | -176 | -134 | -95 | -197 | -154 | -113 | -313 | -255 | -196 |
| B_017 | Rio Deseado | -98 | -89 | -81 | -131 | -122 | -114 | -131 | -122 | -113 | -177 | -164 | -153 |
| B_019 | Rio Chone | -76 | -65 | -54 | -96 | -84 | -73 | -87 | -74 | -63 | -121 | -105 | -91 |
| B_067 | Kaipara | -198 | -167 | -138 | -241 | -209 | -180 | -247 | -214 | -183 | -339 | -296 | -257 |
| B_071 | Gambia | -31 | 2 | 34 | 40 | 73 | 107 | 46 | 78 | 111 | 22 | 60 | 99 |
| B_073 | Cacheu | -206 | -195 | -184 | -244 | -233 | -222 | -250 | -238 | -227 | -334 | -318 | -304 |
| B_080 | Freetown | -254 | -225 | -199 | -301 | -272 | -245 | -299 | -269 | -241 | -409 | -370 | -333 |
| B_089 | Muni | -422 | -359 | -301 | -513 | -449 | -389 | -525 | -459 | -396 | -722 | -635 | -554 |

Projected change in coastline 2091-2100 (m)

| Label | System Name | RCP 2.6 | | | RCP 4.5 | | | RCP 6.0 | | | RCP 8.5 | | |
|-------|------------------|------------------|------------------|------------------|------------------|------------------|------------------|------------------|------------------|------------------|------------------|------------------|------------------|
| | | 10 th | 50 th | 90 th | 10 th | 50 th | 90 th | 10 th | 50 th | 90 th | 10 th | 50 th | 90 th |
| B_090 | Gabon | -338 | -286 | -239 | -411 | -358 | -310 | -421 | -367 | -316 | -579 | -508 | -442 |
| B_091 | Zaire | -252 | -212 | -175 | -308 | -267 | -229 | -315 | -273 | -233 | -434 | -378 | -326 |
| B_093 | Inhambane | -91 | -78 | -66 | -110 | -96 | -84 | -114 | -100 | -87 | -157 | -138 | -121 |
| B_095 | Beira | -346 | -298 | -254 | -399 | -350 | -305 | -403 | -353 | -306 | -574 | -509 | -447 |
| B_104 | Miani Hor | -291 | -243 | -199 | -346 | -297 | -252 | -344 | -294 | -247 | -461 | -395 | -333 |
| B_111 | Hue | -241 | -221 | -203 | -289 | -269 | -251 | -295 | -274 | -255 | -397 | -370 | -345 |
| B_136 | Setubal | -162 | -133 | -107 | -198 | -168 | -141 | -205 | -174 | -145 | -285 | -245 | -208 |
| B_137 | Lisboa | -222 | -181 | -145 | -271 | -230 | -192 | -281 | -238 | -198 | -394 | -339 | -287 |
| B_139 | Gironde | -340 | -277 | -219 | -415 | -349 | -290 | -406 | -341 | -279 | -567 | -481 | -401 |
| B_140 | Loire | -228 | -176 | -128 | -246 | -195 | -147 | -204 | -152 | -103 | -371 | -306 | -243 |
| B_301 | Wilson | -50 | -43 | -37 | -62 | -54 | -47 | -62 | -54 | -48 | -84 | -75 | -66 |
| B_302 | St Paul | -15 | -4 | 6 | -22 | -12 | -1 | -8 | 3 | 14 | -5 | 7 | 19 |
| B_303 | Tweed River | -137 | -122 | -109 | -166 | -151 | -138 | -170 | -155 | -140 | -234 | -214 | -196 |
| B_304 | Richmond River | -53 | -44 | -37 | -66 | -58 | -50 | -67 | -59 | -50 | -97 | -86 | -75 |
| B_305 | Hastings River | -64 | -56 | -48 | -73 | -64 | -57 | -74 | -66 | -58 | -102 | -91 | -81 |
| B_306 | Shoalhaven River | -99 | -89 | -78 | -117 | -106 | -95 | -101 | -90 | -79 | -146 | -132 | -117 |

Projected change in coastline 2091-2100 (m)

| Label | System Name | RCP 2.6 | | | RCP 4.5 | | | RCP 6.0 | | | RCP 8.5 | | |
|-------|-----------------|------------------|------------------|------------------|------------------|------------------|------------------|------------------|------------------|------------------|------------------|------------------|------------------|
| | | 10 th | 50 th | 90 th | 10 th | 50 th | 90 th | 10 th | 50 th | 90 th | 10 th | 50 th | 90 th |
| B_307 | Macleay River | -51 | -40 | -30 | -49 | -38 | -28 | -49 | -38 | -28 | -70 | -56 | -43 |
| B_308 | Nambucca River | -45 | -41 | -38 | -52 | -49 | -45 | -54 | -50 | -46 | -72 | -67 | -63 |
| B_309 | Bellinger River | -37 | -35 | -33 | -40 | -38 | -36 | -42 | -40 | -38 | -55 | -52 | -49 |
| B_310 | Bega River | -30 | -27 | -25 | -37 | -34 | -31 | -32 | -30 | -27 | -46 | -43 | -40 |
| B_311 | Mawddach | -106 | -104 | -103 | -124 | -123 | -122 | -127 | -126 | -124 | -167 | -165 | -164 |
| B_312 | Exe | -120 | -106 | -93 | -143 | -129 | -115 | -147 | -132 | -118 | -199 | -180 | -162 |
| B_313 | Conwy | -69 | -65 | -61 | -81 | -77 | -73 | -83 | -78 | -75 | -111 | -105 | -100 |
| B_314 | Teign | -57 | -54 | -51 | -67 | -64 | -61 | -68 | -65 | -62 | -91 | -87 | -83 |
| B_315 | Thuan | -192 | -170 | -149 | -235 | -212 | -191 | -238 | -214 | -192 | -324 | -293 | -264 |
| B_316 | Aalsea | -30 | -28 | -27 | -35 | -33 | -32 | -35 | -33 | -32 | -46 | -44 | -42 |
| B_317 | Dyfi | -69 | -63 | -58 | -85 | -79 | -73 | -87 | -80 | -74 | -114 | -106 | -98 |
| B_318 | Kalutara | -50 | -47 | -44 | -52 | -49 | -45 | -51 | -48 | -44 | -68 | -64 | -60 |
| B_319 | Swan | -217 | -198 | -156 | -231 | -213 | -167 | -241 | -216 | -167 | -295 | -269 | -202 |

B Bibliography

- Alder, J., 2003. Putting the coast in the 'Sea Around Us'. *Sea Around Us Newslette* 15 (1–2).
- Angamuthu, B., Darby, S.E., Nicholls, R.J., 2018. Impacts of natural and human drivers on the multi-decadal morphological evolution of tidally-influenced deltas, *Proceedings of the Royal Society A: Mathematical, Physical and Engineering Sciences*.
- Anthony, E.J., Brunier, G., Besset, M., Goichot, M., Dussouillez, P., Nguyen, V.L., 2015. Linking rapid erosion of the Mekong River delta to human activities. *Sci. Rep.* 5, 14745.
- Athanasiou, P., van Dongeren, A., Giardino, A., Vousdoukas, M., Gaytan-Aguilar, S., Ranasinghe, R., 2019. Global distribution of nearshore slopes with implications for coastal retreat. *Earth Syst. Sci. Data Discuss.* 2019, 1–29.
- Aubrey, D.G., Weishar, L. (Eds.), 1988. *Hydrodynamics and Sediment Dynamics of Tidal Inlets, Lecture Notes on Coastal and Estuarine Studies*. Springer New York, New York, NY.
- Balthazar, V., Vanacker, V., Girma, A., Poesen, J., Golla, S., 2013. Human impact on sediment fluxes within the Blue Nile and Atbara River basins. *Geomorphology* 180–181, 231–241.
- Bamunawala, J., Maskey, S., Duong, T., van der Spek, A., 2018a. Significance of Fluvial Sediment Supply in Coastline Modelling at Tidal Inlets. *J. Mar. Sci. Eng.* 6, 79.
- Bamunawala, J., Ranasinghe, R., van der Spek, A., Maskey, S., Udo, K., 2018b. Assessing Future Coastline Change in the Vicinity of Tidal Inlets via Reduced Complexity Modelling. *J. Coast. Res.* 85, 636–640.
- Bayram, A., Larson, M., Hanson, H., 2007. A new formula for the total longshore sediment transport rate. *Coast. Eng.* 54, 700–710.
- Besset, M., Anthony, E.J., Bouchette, F., 2019. Multi-decadal variations in delta shorelines and their relationship to river sediment supply: An assessment and review. *Earth-Science Rev.* 193, 199–219.
- Bowen, A.J., Inman, D.L., 1966. Budget of littoral sands in the vicinity of Point Arguello, California. U.S. Army Corps of Engineers, Coastal Engineering Research Center, Technical Memorandum No. 19, 56pp.
- Brown, S., Nicholls, R.J., Hanson, S., Brundrit, G., Dearing, J.A., Dickson, M.E., Gallop, S.L., Gao, S., Haigh, I.D., Hinkel, J., Jiménez, J.A., Klein, R.J.T., Kron, W., Lázár, A.N., Neves, C.F., Newton, A., Pattiaratchi, C., Payo, A., Pye, K., Sánchez-Arcilla, A., Siddall, M., Shareef, A., Tompkins, E.L., Vafeidis, A.T., van Maanen, B., Ward, P.J., Woodroffe, C.D., 2014. Shifting perspectives on coastal impacts and adaptation. *Nat. Clim. Chang.* 4, 752–755.
- Bruun, P.M., 1962. Sea-Level Rise as a Cause of Shore Erosion. *Am. Soc. Civ. Eng. Proceeding, J. Waterw. Harb. Div.* 88, 117–132.
- Casas-Prat, M., Wang, X.L., Swart, N., 2018. CMIP5-based global wave climate projections including the entire Arctic Ocean. *Ocean Model.* 123, 66–85.

- CERC, 1984. Shore Protection Manual. Washington, DC, USA.
- Chu, Z., 2014. The dramatic changes and anthropogenic causes of erosion and deposition in the lower Yellow (Huanghe) River since 1952. *Geomorphology* 216, 171–179.
- Collins, M., Knutti, R., Arblaster, J., Dufresne, J.-L., Fichet, T., Friedlingstein, P., Gao, X., Gutowski, W.J., Johns, T., Krinner, G., Shongwe, M., Tebaldi, C., Weaver, A.J., Wehner, M., 2013. Long-term Climate Change: Projections, Commitments and Irreversibility. In: Stocker, T.F., Qin, D., Plattner, G.-K., Tignor, M., Allen, S.K., Boschung, J., Nauels, A., Xia, Y., Bex, V., Midgley, P.M. (Eds.), *Climate Change 2013: The Physical Science Basis. Contribution of Working Group I to the Fifth Assessment Report of the Intergovernmental Panel on Climate Change*. Cambridge University Press, Cambridge, United Kingdom and New York, NY, USA.
- Cooper, J.A.G., Pilkey, O.H., 2004. Sea-level rise and shoreline retreat: time to abandon the Bruun Rule. *Glob. Planet. Change* 43, 157–171.
- Cowell, P.J., Stive, M.J.F., Niedoroda, A.W., De-Vriend, H.J., Swift, D.J.P., Kaminsky, G.M., Capobianco, M., 2003. The Coastal-Tract (Part 1): A Conceptual Approach to Aggregated Modeling of Low-Order Coastal Change. *J. Coast. Res.* 19, 812–827.
- CSIRO, Bureau of Meteorology, 2015. *Climate Change in Australia Information for Australia's Natural Resource Management Regions: Technical Report*, CSIRO and Bureau of Meteorology, Australia.
- Cubasch, U., Wuebbles, D., Chen, D., Facchini, M.C., Frame, D., Mahowald, N., Winther, J.-G., 2013. Introduction. In: Stocker, T.F., Qin, D., Plattner, G.-K., Tignor, M., Allen, S.K., Boschung, J., Nauels, A., Xia, Y., Bex, V., Midgley, P.M. (Eds.), *Climate Change 2013: The Physical Science Basis. Contribution of Working Group I to the Fifth Assessment Report of the Intergovernmental Panel on Climate Change*. Cambridge University Press, Cambridge, United Kingdom and New York, NY, USA.
- Dastgheib, A., 2012. Long-term process-based morphological modeling of large tidal basins. Delft University of Technology.
- Dastgheib, A., Jongejan, R., Wickramanayake, M., Ranasinghe, R., 2018. Regional Scale Risk-Informed Land-Use Planning Using Probabilistic Coastline Recession Modelling and Economical Optimisation: East Coast of Sri Lanka. *J. Mar. Sci. Eng.*
- Dastgheib, A., Martinez, C., Udo, K., Ranasinghe, R., 2020. Projecting CC driven coastline change on sandy beaches: a comparison of deterministic and probabilistic approaches at Hasaki Beach Japan. *J. Coast. Eng.*
- Davenport, J., Davenport, J.L., 2006. The impact of tourism and personal leisure transport on coastal environments: A review. *Estuar. Coast. Shelf Sci.* 67, 280–292.
- Davis-Jr., R.A., Fitzgerald, D.M., 2003. *Beaches and Coasts*. Wiley-Blackwell.
- Dronkers, J.J., 1964. *Tidal computations in rivers and coastal waters*. North-Holland Pub. Co. ; New York : Interscience Publishers, Amsterdam.
- Dunn, F.E., Darby, S.E., Nicholls, R.J., Cohen, S., Zarfl, C., Fekete, B.M., 2019. Projections of declining fluvial sediment delivery to major deltas worldwide in response to climate change and anthropogenic stress. *Environ. Res. Lett.* 14, 84034.
- Dunn, F.E., Nicholls, R.J., Darby, S.E., Cohen, S., Zarfl, C., Fekete, B.M., 2018.

- Projections of historical and 21st century fluvial sediment delivery to the Ganges-Brahmaputra-Meghna, Mahanadi, and Volta deltas. *Sci. Total Environ.* 642, 105–116.
- Duong, T.M., Ranasinghe, R., Walstra, D., Roelvink, D., 2016. Assessing climate change impacts on the stability of small tidal inlet systems: Why and how? *Earth-Science Rev.* 154, 369–380.
- Egbert, G.D., Erofeeva, S.Y., 2002. Efficient Inverse Modeling of Barotropic Ocean Tides. *J. Atmos. Ocean. Technol.* 19, 183–204.
- Engle, V.D., Kurtz, J.C., Smith, L.M., Chancy, C., Bourgeois, P., 2007. A Classification of U.S. Estuaries Based on Physical and Hydrologic Attributes. *Environ. Monit. Assess.* 129, 397–412.
- Fanos, A.M., 1995. The Impact of Human Activities on the Erosion and Accretion of the Nile Delta Coast. *J. Coast. Res.* 11, 821–833.
- Farr, T.G., Rosen, P.A., Caro, E., Crippen, R., Duren, R., Hensley, S., Kobrick, M., Paller, M., Rodriguez, E., Roth, L., Seal, D., Shaffer, S., Shimada, J., Umland, J., Werner, M., Oskin, M., Burbank, D., Alsdorf, D., 2007. The Shuttle Radar Topography Mission. *Rev. Geophys.* 45, RG2004.
- FitzGerald, D., Georgiou, I., Miner, M., 2015. Estuaries and Tidal Inlets. In: Masselink, G., Gehrels, R. (Eds.), *Coastal Environments and Global Change*, Wiley Online Books. John Wiley & Sons, Ltd, Chichester, UK, pp. 268–298.
- FitzGerald, D.M., Fenster, M.S., Argow, B. a., Buynevich, I. V., 2008. Coastal Impacts Due to Sea-Level Rise. *Annu. Rev. Earth Planet. Sci.* 36, 601–647.
- FitzGerald, D.M., Georgiou, I., Miner, M., 2014. Estuaries and Tidal Inlets. In: Masselink, G., Gehrels, R. (Eds.), *Coastal Environments and Global Change*. John Wiley & Sons, Ltd and American Geophysical Union, Sussex, UK, pp. 268–298.
- Green, M.O., 2013. Catchment sediment load limits to achieve estuary sedimentation targets. *New Zeal. J. Mar. Freshw. Res.* 47, 153–180.
- Guo, L., van der Wegen, M., Roelvink, D., He, Q., 2015. Exploration of the impact of seasonal river discharge variations on long-term estuarine morphodynamic behavior. *Coast. Eng.* 95, 105–116.
- Hallegette, S., Green, C., Nicholls, R.J., Corfee-Morlot, J., 2013. Future flood losses in major coastal cities. *Nat. Clim. Chang.* 3, 802.
- Hemer, M.A., Fan, Y., Mori, N., Semedo, A., Wang, X.L., 2013. Projected changes in wave climate from a multi-model ensemble. *Nat. Clim. Chang.* 3, 471–476.
- Hinkel, J., Nicholls, R.J., Tol, R.S.J., Wang, Z.B., Hamilton, J.M., Boot, G., Vafeidis, A.T., McFadden, L., Ganopolski, A., Klein, R.J.T., 2013. A global analysis of erosion of sandy beaches and sea-level rise: An application of DIVA. *Glob. Planet. Change* 111, 150–158.
- Jongejan, R., Ranasinghe, R., Wainwright, D., Callaghan, D.P., Reyns, J., 2016. Drawing the line on coastline recession risk. *Ocean Coast. Manag.* 122, 87–94.
- Kamphuis, J.W., 1991. Alongshore Sediment Transport Rate. *J. Waterw. Port, Coastal, Ocean Eng.* 117, 624–640.

- Kana, T.W., 1995. A mesoscale sediment budget for Long Island, New York. *Mar. Geol.* 126, 87–110.
- Kettner, A.J., Gomez, B., Hutton, E.W.H., Syvitski, J.P.M., 2009. Late Holocene dispersal and accumulation of terrigenous sediment on Poverty Shelf, New Zealand. *Basin Res.* 21, 253–267.
- Kettner, A.J., Syvitski, J.P., Gomez, B., 2005. Simulating the Effects of Natural Events and Anthropogenic Activity on Sediment Discharge to the Poverty Shelf, New Zealand during the late Holocene. In: *Eos Trans. AGU*, 86(52), Fall Meet. Suppl. p. Abstract H51C-0388.
- Keulegan, G.H., 1951. Report No. 1146: Third Progress Report on Tidal Flow in Entrances, Water Level Fluctuations of Basins in Communication with Seas. Washington D.C, USA.
- Komar, P.D., 1976. Beach processes and sedimentation. Prentice Hall, NJ.
- Komar, P.D., 1998. Beach processes and sedimentation, 2nd edition. Prentice Hall, NJ.
- Larson, M., Hanson, H., Kraus, N.C., 1987. Analytical solutions of the one-line model of shoreline change. Washington, DC, USA.
- Larson, M., Kraus, N.C., Connell, K.J., 2007. Modeling Sediment Storage and Transfer for Simulating Regional Coastal Evolution. In: Smith, J.M. (Ed.), *Coastal Engineering 2006*. World Scientific Publishing Company, San Diego, California, USA, pp. 3924–3936.
- Larson, M., Kraus, N.C., Hanson, H., 2003. Simulation of regional longshore sediment transport and coastal evolution - The “CASCADE” model. In: Smith, J.M. (Ed.), *28th International Conference on Coastal Engineering 2002*. World Scientific Publishing Company, Cardiff, Wales, UK, pp. 2612–2624.
- Lavoie, D. (ed), 2009. Sand resources, regional geology, and coastal processes of the Chandeaur Islands coastal system-an evaluation of the Breton National Wildlife Refuge: U.S. Geological Survey Scientific Investigations Report 2009–5252, 180 p.
- Le Cozannet, G., Bulteau, T., Castelle, B., Ranasinghe, R., Wöppelmann, G., Rohmer, J., Bernon, N., Idier, D., Louisor, J., Salas-y-Mélie, D., 2019. Quantifying uncertainties of sandy shoreline change projections as sea level rises. *Sci. Rep.* 9, 42.
- Lehner, B., Verdin, K., Jarvis, A., 2008. New Global Hydrography Derived From Spaceborne Elevation Data. *Eos, Trans. Am. Geophys. Union* 89, 93–94.
- Lesser, G., 2009. An Approach to Medium-term Coastal Morphological Modeling. UNESCO-IHE/Delft University of Technology.
- Liberian Hydrological Service: Ministry of Lands Mines and Energy, Norwegian Water Resources and Energy Directorate, 2016. Liberia River Basins: Drainage Divisions and river Basin Boundaries.
- Luijendijk, A., Hagenaars, G., Ranasinghe, R., Baart, F., Donchyts, G., Aarninkhof, S., 2018. The State of the World’s Beaches. *Sci. Rep.* 8, 6641.
- Manning, A.J., 2012. TR167 – Enhanced UK Estuaries database: explanatory notes and metadata. HR Wallingford Report DDY0427-RT002-R02-00.

- McBride, R.A., Byrnes, M.R., Hiland, M.W., 1995. Geomorphic response-type model for barrier coastlines: a regional perspective. *Mar. Geol.* 126, 143–159.
- McGranahan, G., Balk, D., Anderson, B., 2007. The rising tide: assessing the risks of climate change and human settlements in low elevation coastal zones. *Environ. Urban.* 19, 17–37.
- McSweeney, S.L., Kennedy, D.M., Rutherford, I.D., Stout, J.C., 2017. Intermittently Closed/Open Lakes and Lagoons: Their global distribution and boundary conditions. *Geomorphology* 292, 142–152.
- Mehvar, A., Dastgheib, A., Ranasinghe, R., 2016. Relative Sea Level Rise Scenarios: Central Coast of Bangladesh. Delft. The Netherlands.
- Mil-Homens, J., Ranasinghe, R., van Thiel de Vries, J.S.M., Stive, M.J.F., 2013. Re-evaluation and improvement of three commonly used bulk longshore sediment transport formulas. *Coast. Eng.* 75, 29–39.
- Moore, L.J., List, J.H., Williams, S.J., Stolper, D., 2007. Modelling barrier island response to sea-level rise in the outer banks, North Carolina. In: Kraus, N.C., Rosati, J.D. (Eds.), *Coastal Sediments '07: Sixth International Symposium on Coastal Engineering and Science of Coastal Sediment Process*. American Society of Civil Engineers, New Orleans, Louisiana, USA., pp. 1153–1164.
- Moore, L.J., Patsch, K., List, J.H., Williams, S.J., 2014. The potential for sea-level-rise-induced barrier island loss: Insights from the Chandeleur Islands, Louisiana, USA. *Mar. Geol.* 355, 244–259.
- Mori, N., Yasuda, T., Mase, H., Tom, T., Oku, Y., 2010. Projection of Extreme Wave Climate Change under Global Warming. *Hydrol. Res. Lett.* 4, 15–19.
- Morim, J., Hemer, M., Wang, X.L., Cartwright, N., Trenham, C., Semedo, A., Young, I., Briceno, L., Camus, P., Casas-Prat, M., Erikson, L., Mentaschi, L., Mori, N., Shimura, T., Timmermans, B., Aarnes, O., Breivik, Ø., Behrens, A., Dobrynin, M., Menendez, M., Staneva, J., Wehner, M., Wolf, J., Kamranzad, B., Webb, A., Stopa, J., Andutta, F., 2019. Robustness and uncertainties in global multivariate wind-wave climate projections. *Nat. Clim. Chang.* 9, 711–718.
- Morton, R.A., Miller, T.L., 2005. National Assessment Of Shoreline Change: Part 2, Historical Shoreline Changes And Associated Coastal Land Loss Along The U.S. Southeast Atlantic Coast, Open-File Report.
- Motyka, J.M., Brampton, A.H., 1993. Coastal Management: Mapping of littoral cells.
- Neumann, B., Vafeidis, A.T., Zimmermann, J., Nicholls, R.J., 2015. Future Coastal Population Growth and Exposure to Sea-Level Rise and Coastal Flooding - A Global Assessment. *PLoS One* 10, e0118571.
- Nicholls, R.J., Hanson, S.E., Lowe, J.A., Warrick, R.A., Lu, X., Long, A.J., 2014. Sea-level scenarios for evaluating coastal impacts. *Wiley Interdiscip. Rev. Clim. Chang.* 5, 129–150.
- Norwegian Water Resources and Energy Directorate, Liberian Hydrological Service: Ministry of Lands Mines and Energy, 2019. Liberian Hydrological Services [WWW Document]. URL <http://lhsliberia.com/> (accessed 11.23.18).

- O'Brien, M.P., 1969. Equilibrium flow areas of tidal inlets on sandy coasts. *J. Waterw. Harb. Div.* 95, 43–52.
- Office of Environment and Heritage-New South Wales, 2017. Estuaries of NSW [WWW Document]. Retrieved from <https://www.environment.nsw.gov.au/topics/water/estuaries/estuaries-of-nsw>.
- Oppenheimer, M., Glavovic, B.C., Hinkel, J., Van-de-Wal, R., Magnan, A.K., Abd-Elgawad, A., Cai, R., Cifuentes-Jara, M., DeConto, R.M., Ghosh, T., Hay, J., Isla, F., Marzeion, B., Meyssignac, B., Sebesvari, Z., 2019. Sea Level Rise and Implications for Low-Lying Islands, Coasts and Communities. In: Pörtner, H.-O., Roberts, D.C., Masson-Delmotte, V., Zhai, P., Tignor, M., Poloczanska, E., Mintenbeck, K., Alegría, A., Nicolai, M., Okem, A., Petzold, J., Rama, B., Weyer, N.M. (Eds.), IPCC Special Report on the Ocean and Cryosphere in a Changing Climate. In Press.
- Overeem, I., Kettner, A.J., Syvitski, J.P.M., 2013. Impacts of Humans on River Fluxes and Morphology. In: *Treatise on Geomorphology*. Elsevier, pp. 828–842.
- Overeem, I., Syvitski, J.P.M., 2009. Dynamics and Vulnerability of Delta Systems. LOICZ Reports & Studies No. 35. GKSS Research Center, Geesthacht.
- Palmer, M.A., Liermann, C.A.R., Nilsson, C., Flörke, M., Alcamo, J., Lake, P.S., Bond, N., 2008. Climate Change and the World's River Basins: Anticipating Management Options. *Front. Ecol. Environ.* 6, 81–89.
- Patsch, K., Griggs, G., 2008. A sand budget for the Santa Barbara Littoral Cell, California. *Mar. Geol.* 252, 50–61.
- Ranasinghe, R., 2016. Assessing climate change impacts on open sandy coasts: A review. *Earth-Science Rev.* 160, 320–332.
- Ranasinghe, R., Callaghan, D., Stive, M.J.F., 2012. Estimating coastal recession due to sea level rise: beyond the Bruun rule. *Clim. Change* 110, 561–574.
- Ranasinghe, R., Duong, T., Boer, W. de, Vroeg, H. de, 2019a. Modelling of natural and coastal structure modified longshore sediment transport: Stage I - South and West coasts (Mount Lavinia to Galle). Delft. The Netherlands.
- Ranasinghe, R., Duong, T.M., Uhlenbrook, S., Roelvink, D., Stive, M., 2013. Climate-change impact assessment for inlet-interrupted coastlines. *Nat. Clim. Chang.* 3, 83–87.
- Ranasinghe, R., Stive, M.J.F., 2009. Rising seas and retreating coastlines. *Clim. Change* 97, 465.
- Ranasinghe, R., Wu, C.S., Conallin, J., Duong, T.M., Anthony, E.J., 2019b. Disentangling the relative impacts of climate change and human activities on fluvial sediment supply to the coast by the world's large rivers: Pearl River Basin, China. *Sci. Rep.* 9, 9236.
- Roelvink, D., Reniers, A., 2011. *A Guide to Modeling Coastal Morphology*, Advances in Coastal and Ocean Engineering. World Scientific Press.
- Rosati, J.D., 2005. Concepts in Sediment Budgets. *J. Coast. Res.* 212, 307–322.
- Ruggiero, P., Kratzmann, M.G., Himmelstoss, E.A., Reid, D., Allan, J., Kaminsky, G., 2013. National assessment of shoreline change-Historical shoreline change along the

- Pacific Northwest coast: U.S. Geological Survey Open-File Report 2012–1007, 62 p.
- Samaras, A.G., Koutitas, C.G., 2014. Modeling the impact of climate change on sediment transport and morphology in coupled watershed-coast systems: A case study using an integrated approach. *Int. J. Sediment Res.* 29, 304–315.
- Sanderson, E.W., Jaiteh, M., Levy, M., Redford, K.H., Wannebo, A.V., Woolmer, G., 2002. The Human Footprint and the Last of the Wild. *Bioscience* 52, 891–904.
- Semedo, A., Weisse, R., Behrens, A., Sterl, A., Bengtsson, L., Günther, H., 2013. Projection of Global Wave Climate Change toward the End of the Twenty-First Century. *J. Clim.* 26, 8269–8288.
- Shennan, I., Coulthard, T., Flather, R., Horton, B., Macklin, M., Rees, J., Wright, M., 2003. Integration of shelf evolution and river basin models to simulate Holocene sediment dynamics of the Humber Estuary during periods of sea-level change and variations in catchment sediment supply. *Sci. Total Environ.* 314–316, 737–754.
- Shrestha, B., Babel, M.S., Maskey, S., van Griensven, A., Uhlenbrook, S., Green, A., Akkharath, I., 2013. Impact of climate change on sediment yield in the Mekong River basin: a case study of the Nam Ou basin, Lao PDR. *Hydrol. Earth Syst. Sci.* 17, 1–20.
- Smith, R.K., 1988. Poverty Bay, New Zealand: A case of coastal accretion 1886–1975. *New Zeal. J. Mar. Freshw. Res.* 22, 135–142.
- Sobol', I.M., 2001. Global sensitivity indices for nonlinear mathematical models and their Monte Carlo estimates. *Math. Comput. Simul.* 55, 271–280.
- Spencer, T., Schuerch, M., Nicholls, R.J., Hinkel, J., Lincke, D., Vafeidis, A.T., Reef, R., McFadden, L., Brown, S., 2016. Global coastal wetland change under sea-level rise and related stresses: The DIVA Wetland Change Model. *Glob. Planet. Change* 139, 15–30.
- Stive, M.J.F., 2004. How Important is Global Warming for Coastal Erosion? *Clim. Change* 64, 27–39.
- Stive, M.J.F., Capobianco, M., Wang, Z.B., Ruol, P., Buijsman, M.C., 1998. Morphodynamics of a tidal lagoon and the adjacent Coast. In: Dronkers, J., Scheffers, M. (Eds.), *Physics of Estuaries and Coastal Seas*. A. A. Balkema, Rotterdam, pp. 397–407.
- Stive, M.J.F., Roelvink, J.A., de Vriend, H.J., 1990. Large-Scale Coastal Evolution Concept. In: 22nd International Conference on Coastal Engineering, Proceedings. Delft, The Netherlands, pp. 1962–1974.
- Stocker, T.F., Qin, D., Plattner, G.-K., Alexander, L. V., Allen, S.K., Bindoff, N.L., Bréon, F.-M., Church, J.A., Cubasch, U., Emori, S., Forster, P., Friedlingstein, P., Gillett, N., Gregory, J.M., Hartmann, D.L., Jansen, E., Kirtman, B., Knutti, R., Kumar, K.K., Lemke, P., Marotzke, J., Masson-Delmotte, V., Meehl, G.A., Mokhov, I.I., Piao, S., Ramaswamy, V., Randall, D., Rhein, M., Rojas, M., Sabine, C., Shindell, D., Talley, L.D., Vaughan, D.G., Xie, S.-P., 2013a. Technical Summary. In: Stocker, T.F., Qin, D., Plattner, G.-K., Tignor, M., Allen, S.K., Boschung, J., Nauels, A., Xia, Y., Bex, V., Midgley, P.M. (Eds.), *Climate Change 2013: The Physical Science Basis. Contribution of Working Group I to the Fifth Assessment Report of the Intergovernmental Panel on Climate Change*. Cambridge University Press,

Cambridge, United Kingdom and New York, NY, USA.

- Stocker, T.F., Qin, D., Plattner, G.-K., Tignor, M., Allen, S.K., Boschung, J., Nauels, A., Xia, Y., Bex, V., Midgley, P.M. (Eds.), 2013b. IPCC, 2013: Summary for Policymakers. In: *Climate Change 2013: The Physical Science Basis. Contribution of Working Group I to the Fifth Assessment Report of the Intergovernmental Panel on Climate Change*. Cambridge University Press, Cambridge, United Kingdom and New York, NY, USA.
- Stolper, D., List, J.H., Thieler, E.R., 2005. Simulating the evolution of coastal morphology and stratigraphy with a new morphological-behaviour model (GEOMBEST). *Mar. Geol.* 218, 17–36.
- Stutz, M.L., Pilkey, O.H., 2011. Open-Ocean Barrier Islands: Global Influence of Climatic, Oceanographic, and Depositional Settings. *J. Coast. Res.* 72, 207–222.
- Syvitski, J.P.M., 2003. Supply and flux of sediment along hydrological pathways: research for the 21st century. *Glob. Planet. Change* 39, 1–11.
- Syvitski, J.P.M., 2005. Impact of Humans on the Flux of Terrestrial Sediment to the Global Coastal Ocean. *Science* (80-.). 308, 376–380.
- Syvitski, J.P.M., Kettner, A.J., 2008. Scaling sediment flux across landscapes. Sediment dynamics in changing environments. In: Jochen Schmidt, Tom Cochrane, Chris Phillips, Sandy Elliott, T.D.& L.B. (Ed.), *IAHS Publ. IAHS Publications*, Christchurch, New Zealand, pp. 149–156.
- Syvitski, J.P.M., Kettner, A.J., Overeem, I., Hutton, E.W.H., Hannon, M.T., Brakenridge, G.R., Day, J., Vörösmarty, C., Saito, Y., Giosan, L., Nicholls, R.J., 2009. Sinking deltas due to human activities. *Nat. Geosci.* 2, 681–686.
- Syvitski, J.P.M., Milliman, J.D., 2007. Geology, Geography, and Humans Battle for Dominance over the Delivery of Fluvial Sediment to the Coastal Ocean. *J. Geol.* 115, 1–19.
- Syvitski, J.P.M., Peckham, S.D., Hilberman, R., Mulder, T., 2003. Predicting the terrestrial flux of sediment to the global ocean: a planetary perspective. *Sediment. Geol.* 162, 5–24.
- Syvitski, J.P.M., Saito, Y., 2007. Morphodynamics of deltas under the influence of humans. *Glob. Planet. Change* 57, 261–282.
- Toimil, A., Losada, I.J., Camus, P., Díaz-Simal, P., 2017. Managing coastal erosion under climate change at the regional scale. *Coast. Eng.* 128, 106–122.
- Townend, I., Whitehead, P., 2003. A preliminary net sediment budget for the Humber Estuary. *Sci. Total Environ.* 314–316, 755–767.
- Twichell, D.C., Flocks, J.G., Pendleton, E. a, Baldwin, W.E., 2013. Geologic Controls on Regional and Local Erosion Rates of Three Northern Gulf of Mexico Barrier-Island Systems. *J. Coast. Res.* SI, 32–45.
- United Nations, 2015. *World Urbanization Prospects: The 2014 Revision*, (ST/ESA/SER.A/366).
- Vafeidis, A., Neumann, B., Zimmermann, J., Nicholls, R.J., 2011. MR9: Analysis of land area and population in the low-elevation coastal zone (LE CZ). In: *UK Government's*

- Foresight Project, Migration and Global Environmental Change. London, UK, p. 172.
- van Heteren, S., 2014. Barrier Systems. In: Masselink, G., Gehrels, R. (Eds.), Coastal Environments and Global Change. John Wiley & Sons, Ltd and American Geophysical Union, Sussex, UK, pp. 194–226.
- van Maanen, B., Nicholls, R.J., French, J.R., Barkwith, A., Bonaldo, D., Burningham, H., Murray, B.A., Payo, A., Sutherland, J., Thornhill, G., Townend, I.H., van der Wegen, M., Walkden, M.J.A., 2016. Simulating mesoscale coastal evolution for decadal coastal management: A new framework integrating multiple, complementary modelling approaches. *Geomorphology* 256, 68–80.
- Veerbeek, W., 2017. Estimating the Impacts of Urban Growth on Future Flood Risk: A Comparative Study. The Delft University of Technology.
- Verstraeten, G., Poesen, J., 2001. Factors controlling sediment yield from small intensively cultivated catchments in a temperate humid climate. *Geomorphology* 40, 123–144.
- Vitousek, S., Barnard, P.L., Limber, P., Erikson, L., Cole, B., 2017. A model integrating longshore and cross-shore processes for predicting long-term shoreline response to climate change. *J. Geophys. Res. Earth Surf.* 122, 782–806.
- Vörösmarty, C.J., Meybeck, M., Fekete, B., Sharma, K., Green, P., Syvitski, J.P.M., 2003. Anthropogenic sediment retention: major global impact from registered river impoundments. *Glob. Planet. Change* 39, 169–190.
- Vousdoukas, M.I., Ranasinghe, R., Mentaschi, L., Plomaritis, T.A., Athanasiou, P., Luijendijk, A., Feyen, L., 2020. Sandy coastlines under threat of erosion. *Nat. Clim. Chang.* 10, 260–263.
- Walling, D.E., 1999. Linking land use, erosion and sediment yields in river basins. *Hydrobiologia* 410, 223–240.
- Watson, R., Alder, J., Booth, S., Christensen, V., Kaschner, K., Kitchingman, A., Lai, S., Palmares, M.L.D., Valdez, F., Pauly, D., 2004. Welcome to www.seaaroundus.org: launching our ‘product’ on the web. *Sea Around Us Newsl.* 22 (1–8).
- Wildlife Conservation Society (WCS) and Center for International Earth Science Information Network (CIESIN) - Columbia University., 2005. Last of the Wild Project, Version 2, 2005 (LWP-2): Global Human Footprint Dataset (Geographic).
- Wong, P.P., Losada, I.J., Gattuso, J.-P., Hinkel, J., Khattabi, A., McInnes, K.L., Saito, Y., Sallenger, A., 2014. Coastal systems and low-lying areas. In: Field, C.B., Barros, V.R., Dokken, D.J., Mach, K.J., Mastrandrea, M.D., Bilir, T.E., Chatterjee, M., Ebi, K.L., Estrada, Y.O., Genova, R.C., Girma, B., Kissel, E.S., Levy, A.N., MacCracken, S., Mastrandrea, P.R., White, L.L. (Eds.), *Climate Change 2014: Impacts, Adaptation, and Vulnerability. Part A: Global and Sectoral Aspects. Contribution of Working Group II to the Fifth Assessment Report of the Intergovernmental Panel on Climate Change*. Cambridge University Press, Cambridge, United Kingdom and New York, NY, USA, pp. 361–409.
- Woodroffe, C.D., 2003. *Coasts: form, process and evolution*, First. ed. Cambridge University Press, Cambridge, UK.
- Woodruff, J.D., Irish, J.L., Camargo, S.J., 2013. Coastal flooding by tropical cyclones and

sea-level rise. *Nature* 504, 44–52.

World Bank, 2010. *World Development Report 2010 : Development and Climate Change*. Washington, DC, USA.

Zhang, K., Douglas, B.C., Leatherman, S.P., 2004. Global Warming and Coastal Erosion. *Clim. Change* 64, 41.

C List of figures

| | |
|---|----|
| Figure 1-1: Schematic representation of the sediment pathway from its source to the coast (adjacent to a mainland barrier estuary). | 5 |
| Figure 1-2: Different modes of barrier island behaviour | 9 |
| Figure 1-3: A definitional figure of the coastal types considered in this study. | 11 |
| Figure 1-4: Projected average of annual mean surface air temperature change (relative to 1986–2005) for the four RCPs. | 12 |
| Figure 1-5: Projected change in annual mean runoff for 2081–2100 (relative to 1986–2005). | 13 |
| Figure 1-6: Projections of global mean sea-level rise over the 21 st century (relative to 1986–2005). | 14 |
| Figure 1-7: Projected maximum, mean and minimum global sea-level changes for 2020–2100 (relative to 1986–2005). | 15 |
| Figure 1-8: Regional relative sea-level change for 2081–2100 (relative to 1986–2005). | 16 |
| Figure 1-9: Global map of Human FootPrint Index (HFPI). | 17 |
| Figure 2-1: Schematic illustration of the connections between sediment volume components associated with the change in total sediment-volume exchange (ΔV_T) between inlet-estuary system and its adjacent coast. | 25 |
| Figure 2-2: Flowchart of the iteration procedure to determine equilibrium tidal prism at estuaries with low-lying margins. | 27 |
| Figure 2-3: Flowchart of the proposed modelling approach of determining the change in total sediment volume exchange between a barrier-estuary system and its adjacent inlet-interrupted coast. | 31 |
| Figure 2-4: Conceptual framework for distributing a positive sediment budget. | 36 |
| Figure 2-5: Conceptual framework for distributing a negative sediment budget (case 1). | 37 |
| Figure 2-6: Conceptual framework for distributing a negative sediment budget (case 2). | 38 |
| Figure 2-7: Schematic illustration of a hypothetical equilibrium cross-shore profile | 39 |
| Figure 2-8: Flowchart of the conceptual modelling framework for determining the final coastline position along inlet-interrupted coastlines. | 43 |
| Figure 2-9: An illustrative plot of the Initial equilibrium barrier island profile and the present-day sea level. | 46 |

| | |
|--|----|
| Figure 2-10: An illustrative plot of the intermediate barrier island profile under future sea-level conditions (computed without a threshold on maximum barrier migration rate). | 46 |
| Figure 2-11: An illustrative plot of the final barrier island profile under future sea-level conditions (computed with a threshold on maximum barrier migration rate). | 47 |
| Figure 2-12: Flowchart of the proposed probabilistic modelling framework to determine future changes in barrier islands | 48 |
| Figure 3-1: Locations of the selected mainland inlet-estuary systems | 54 |
| Figure 3-2: Location of the selected barrier-island system (Chandeleur Islands) in Louisiana, USA | 55 |
| Figure 3-3: Empirical cumulative distributions of averaged annual mean temperature in the Alsea river catchment, OR, USA. | 57 |
| Figure 3-4: Empirical cumulative distributions of averaged annual cumulative river discharge at the Alsea estuary, OR, USA. | 57 |
| Figure 3-5: Projected changes in regional relative sea level at the Alsea estuary, OR, USA. | 58 |
| Figure 3-6: Human FootPrint Index (HFPI) of the Alsea river catchment, OR, USA. | 59 |
| Figure 3-7: Projected variations of change in total sediment volume exchange (ΔV_T) between the Alsea estuary and its inlet-interrupted coast over the 21 st century. | 60 |
| Figure 3-8: Variations of the projected 50 th percentile values of change in total sediment volume exchange (ΔV_T) and the different contributing processes at the Alsea estuary over the 21 st century. | 61 |
| Figure 3-9: Empirical cumulative distributions of the projected change in total sediment volume exchange between the Alsea estuary and its inlet-interrupted coast. | 62 |
| Figure 3-10: Projected changes of the inlet-affected coastline at the Alsea estuary. | 64 |
| Figure 3-11: Empirical cumulative distributions of averaged annual mean temperature in the Dyfi river catchment, Wales, UK. | 66 |
| Figure 3-12: Empirical cumulative distributions of averaged annual cumulative river discharge at the Dyfi estuary, Wales, UK. | 66 |
| Figure 3-13: Projected changes in regional relative sea level at the Dyfi estuary, Wales, UK. | 67 |
| Figure 3-14: Human FootPrint Index (HFPI) of the Dyfi river catchment, Wales, UK. | 68 |
| Figure 3-15: Projected variations of change in total sediment volume exchange (ΔV_T) between the Dyfi estuary and its inlet-interrupted coast over the 21 st century. | 69 |

| | |
|--|----|
| Figure 3-16: Variations of the projected 50 th percentile values of change in total sediment volume exchange (ΔV_T) and the different contributing processes at the Dyfi estuary over the 21 st century. | 70 |
| Figure 3-17: Empirical cumulative distributions of the projected change in total sediment volume exchange between the Dyfi estuary and its inlet-interrupted coast. | 71 |
| Figure 3-18: Projected changes of the inlet-affected coastline at the Dyfi estuary. | 73 |
| Figure 3-19: Empirical cumulative distributions of averaged annual mean temperature in the Kalu river catchment, Sri Lanka. | 75 |
| Figure 3-20: Empirical cumulative distributions of averaged annual cumulative river discharge at the Kalutara estuary, Sri Lanka. | 75 |
| Figure 3-21: Projected changes in regional relative sea level at the Kalu estuary, Sri Lanka. | 76 |
| Figure 3-22: Human FootPrint Index (HFPI) of the Kalu River catchment, Sri Lanka. | 77 |
| Figure 3-23: Projected variations of change in total sediment volume exchange (ΔV_T) between the Kalutara estuary and its inlet-interrupted coast over the 21 st century. | 78 |
| Figure 3-24: Variations of the projected 50 th percentile values of change in total sediment volume exchange (ΔV_T) and the different contributing processes at the Kalurata estuary over the 21 st century. | 79 |
| Figure 3-25: Empirical cumulative distributions of the projected change in total sediment volume exchange between the Kalutara estuary and its inlet-interrupted coast. | 80 |
| Figure 3-26: Projected changes of the inlet-affected coastline at Kalutara estuary. | 82 |
| Figure 3-27: Projected variations of change in total sediment volume exchange (ΔV_T) between the Kalutara estuary and its inlet-interrupted coast over the 21 st century (excluding the river sand mining). | 83 |
| Figure 3-28: Variations of the projected 50 th percentile values of change in total sediment volume exchange (ΔV_T) and the different contributing processes at the Kalurata estuary over the 21 st century (excluding river sand mining). | 84 |
| Figure 3-29: Empirical cumulative distributions of averaged annual mean temperature at the Swan River catchment, Australia. | 86 |
| Figure 3-30: Empirical cumulative distributions of averaged annual cumulative river discharge at the Swan River, Australia. | 86 |
| Figure 3-31: Projected changes in regional relative sea level at the Swan estuary, Australia. | 87 |
| Figure 3-32: Human FootPrint Index (HFPI) of the Swan River catchment, Australia. | 88 |

| | |
|--|-----|
| Figure 3-33: Projected variations of change in total sediment volume exchange (ΔV_T) between the Swan River estuary and its inlet-interrupted coast over the 21 st century. | 89 |
| Figure 3-34: Variations of the projected 50 th percentile values of change in total sediment volume exchange (ΔV_T) and the different contributing processes at the Swan River over the 21 st century. | 90 |
| Figure 3-35: Empirical cumulative distributions of the projected change in total sediment volume exchange between the Swan River and its inlet-interrupted coast. | 91 |
| Figure 3-36: Projected changes of the inlet-affected coastline at the Swan River system. | 93 |
| Figure 3-37: Projected changes in regional relative sea level at the Chandeleur Islands, LA, USA. | 96 |
| Figure 3-38: Empirical cumulative distributions of the projected barrier island migration distances of the Chandeleur Islands. | 97 |
| Figure 3-39: Empirical cumulative distributions of the projected barrier island freeboard for the Chandeleur Islands. | 98 |
| Figure 3-40: Empirical cumulative distributions of projected barrier-island migration distances for the Chandeleur Islands under hypothetical initial conditions. | 99 |
| Figure 3-41: Empirical cumulative distributions of projected barrier island freeboard for the Chandeleur Islands under hypothetical initial conditions. | 100 |
| Figure 4-1: Locations of the selected mainland inlet-estuary systems. | 106 |
| Figure 4-2: The projected change in the time-averaged 50 th percentile values of the total sediment volume exchange (ΔV_T) between the estuary system and its adjacent coast over the 2091-2100 period for RCP 2.6. | 109 |
| Figure 4-3: The projected change in the time-averaged 50 th percentile values of the total sediment volume exchange (ΔV_T) between the estuary system and its adjacent coast over the 2091-2100 period for RCP 8.5. | 110 |
| Figure 4-4: An exemplary plot of the variations of the projected 50 th percentile values of change in total sediment volume exchange (ΔV_T) and the different contributing processes at four different barrier estuary systems with First-Order Approximation Ratio (FOAR) less than 0.01 for RCP 8.5. | 112 |
| Figure 4-5: An exemplary plot of the variations of the projected 50 th percentile values of change in total sediment volume exchange (ΔV_T) and the different contributing processes at four different barrier estuary systems with First-Order Approximation Ratio (FOAR) greater than 0.01 for RCP 8.5. | 113 |
| Figure 4-6: The projected total change in inlet-affected coastlines by 2100 for RCP 2.6. | 117 |

Figure 4-7: The projected total change in inlet-affected coastlines by 2100 for RCP 8.5.

118

D List of tables

| | |
|---|-----|
| Table 1-1: Trends and rate of change in trends of global sea-level rise for IPCC RCP scenarios | 15 |
| Table 2-1: Comparison of the hindcasts rates of coastline change over 1986-2005 with the observed rates of coastline change obtained from Luijendijk et al. (2018). | 50 |
| Table 3-1: Properties of the selected mainland inlet-estuary systems | 53 |
| Table 3-2: Projected changes in regional relative sea-level change and its components in the vicinity of Alsea estuary by 2100 | 58 |
| Table 3-3: The 50 th percentile values of the cumulative change in total sediment volume exchange considered for coastline change projections at the Alsea estuary. | 63 |
| Table 3-4: Projected changes in regional relative sea-level change and its components considered at the vicinity of the Dyfi estuary by 2100. | 67 |
| Table 3-5: The 50 th percentile values of the cumulative change in total sediment volume exchange considered for coastline change projections at the Dyfi estuary. | 72 |
| Table 3-6: Projected changes in regional relative sea-level change and its components considered at the vicinity of Kalutara estuary by 2100 | 76 |
| Table 3-7: The 50 th percentile values of the cumulative change in total sediment volume exchange considered for coastline change projections at the Kalutara estuary. | 81 |
| Table 3-8: Projected changes in regional relative sea-level change and its components considered at the vicinity of Swan River inlet by 2100. | 87 |
| Table 3-9: The 50 th percentile values of the cumulative change in total sediment volume exchange considered for coastline change projections at the Swan River system. | 92 |
| Table 3-10: Projected regional relative sea-level changes and its components considered for the Chandeleur Islands by 2100. | 95 |
| Table 3-11: Characteristics of the Chandeleur Island. | 96 |
| Table 4-1: Comparison of the first-order approximation ratio (FOAR) and the dominant contributing processes to the total sediment volume exchange (ΔV_T) at the selected barrier estuary systems. | 114 |
| Table 4-2: Comparison of projected coastline change by 2100 with the results of Vousdoukas et al. (2020). | 119 |
| Table A-1: Details of the GCMs used in this study. | 134 |
| Table A-2: Properties of the selected barrier estuary systems for global application of the model. | 135 |

Table A-3: Different percentiles of mean change in total sediment volume exchange (ΔV_T) at the selected barrier estuary systems during 2091-2100 period. 138

Table A-4: The projected different percentiles of shoreline variation along the inlet-affected coastlines adjacent to the selected barrier estuary systems during 2091-2100 period. 141



*Netherlands Research School for the
Socio-Economic and Natural Sciences of the Environment*

D I P L O M A

For specialised PhD training

The Netherlands Research School for the
Socio-Economic and Natural Sciences of the Environment
(SENSE) declares that

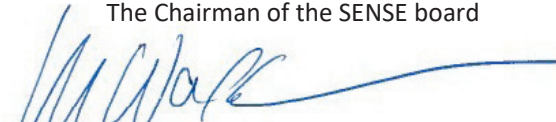
***Rajapaksha Mudiyanseelage
Janaka Bamunawala***

born on 6 September 1984 in Kurunegala, Sri Lanka

has successfully fulfilled all requirements of the
Educational Programme of SENSE.

Enschede, 16 April 2020

The Chairman of the SENSE board



Prof. dr. Martin Wassen

the SENSE Director of Education



Dr. Ad van Dommelen

The SENSE Research School has been accredited by the Royal Netherlands Academy of Arts and Sciences (KNAW)



K O N I N K L I J K E N E D E R L A N D S E
A K A D E M I E V A N W E T E N S C H A P P E N



The SENSE Research School declares that **Mr Rajapaksha Mudiyansele Janaka Bamunawala** has successfully fulfilled all requirements of the Educational PhD Programme of SENSE with a work load of 33.2 EC, including the following activities:

SENSE PhD Courses

- o Environmental research in context (2016)
- o Research in context activity: 'Contributing to the Content and Practical aspects of Regional Workshop on: Coastal Hazard Assessment: Applications in Risk Assessment, Management and Mitigation For Western Indian Ocean Countries, 7-11 March 2016 at Victoria, Seychelles'

Other PhD and Advanced MSc Courses

- o NCK Summer School 2017, Netherlands Centre for Coastal Research (2017)
- o Workshop on 1D and 2D water systems and watershed modelling with US EPA SWMM5 and PCSWMM Europe, IHE Delft (2018)

Management and Didactic Skills Training

- o Coordinating AXA Climate Change and Coastal Risk Science and Networking Meeting at IHE Delft on 4-October-2017
- o Coordination and organizing a stakeholder meeting and networking at University of Moratuwa, Katubedda, Sri Lanka from 7-9 December 2016
- o Coordination and organizing a stakeholder meeting and networking at the offices of Coast Conservation Department and Urban Development Authority, Trincomalee, Sri Lanka 3-5 December 2016
- o Coordinating and co-organizing stakeholder meetings with the General Manager and other delegates from the Coast Conservation Department, Sri Lanka at Den Haag and Delft, 17-18 June 2016

Oral Presentations

- o *Impacts of Climate Change on Extreme Wave Climate Along the Western Coast of Sri Lanka*. ICE Coastal Conference 2015, 7-9 September 2015, Amsterdam, The Netherlands
- o *Assessing Fluvial Sediment supplies to coasts using reduced complexity models*. IX PIANC-International Conference on Coastal and Port Engineering in Developing Countries (COPEDEC), 16-21 October 2016, Rio de Janeiro, Brazil
- o *Assessing Future Coastline Change in the Vicinity of Tidal Inlets via Reduced Complexity Modelling*. 15th International Coastal Symposium, 13-18 May 2018, Busan, South Korea
- o *Assessing the Fate of Inlet-Affected Coastlines under Climate Change and Anthropogenic Impacts*. PhD Symposium-2018 (IHE Delft), 1-2 October 2018, Delft, The Netherlands

SENSE Coordinator PhD Education

Dr. Peter Vermeulen



UNIVERSITY OF TWENTE.

Probabilistic assessment of the long-term evolution of inlet-interrupted coasts has always been a challenge, thus continuing to remain a significant knowledge gap. Therefore, this research study was undertaken to gain new insights into the climate change (CC) driven evolution of inlet-interrupted coasts at macro time scales in a probabilistic manner, while giving due consideration to terrestrial and oceanic processes. Here, this was achieved through the development and application of a reduced-complexity (RC) model at a number of locations around the world. Application of this RC model to four sites in USA, UK, Sri Lanka and Australia shows that the long-term evolution of coastlines

would vary markedly. These variations are linked to the catchment size, basin surface area and arid/non-arid nature of CC projection. Broader application of the RC model to 41 inlet systems worldwide shows that 93% of the inlet-interrupted coasts will erode under changing climate. The projections also show that the long-term evolution of inlet-interrupted coastlines may not always be governed by the CC-induced sea-level rise, as commonly believed, but may at some locations be governed by the terrestrial processes. Uncertainties in the model projections emphasize the need for probabilistic approaches to investigate the long-term evolution of inlet-interrupted coasts.